XIX CONGRESSO DI SCIENZE PLANETARIE

5-9 FEBBRAIO 2024, SALA CONGRESSI DEL COMPLESSO DI BORMIO TERME

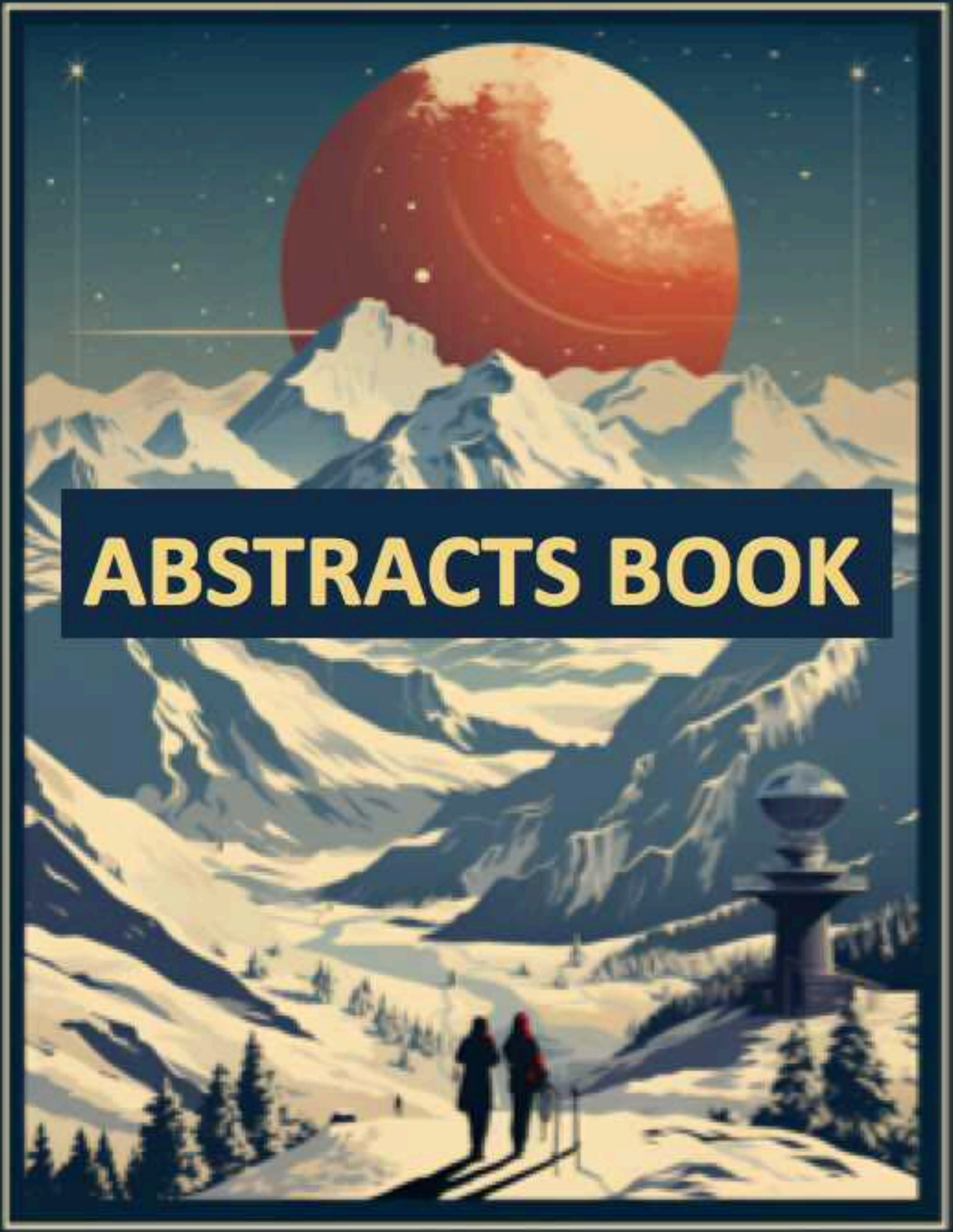

ABSTRACTS BOOK

ORAL PROGRAM

5 Febbraio, Lunedì

09.00-10:00	Iscrizione	
10:00-10:30	Introduzione - Logistica	
10:30-11:00	**Coffee Break gestito dalla Scuola Alberghiera "Alberti"**	
Sessione 1: Pianeti e Satelliti - MARTE I		
Chair: Enrico Flamini		
11:00-11:12	Under a faint sun: the role of seasonal thaws in explaining the liquid water on the Boachian and Hesperian Mars	P. Simonetti
11:12-11:24	Scientific insights on the mechanical properties of Martian subsurface from Rosalind Franklin rover drill telemetry data	L. Rossi
11:24-11:36	Quasi-periodic Fe/Mg clay enrichment within sulfate beds of equatorial layered deposits in Meridiani Planum	B.Baschetti
11:36-11:48	Study of the seasonal water ice in the ejecta of a small crater on Mars	F. Furnari
11:48-12:00	Analysis of ice sublimation and boulder size frequency distribution on the fresh Martian crater S1094B	F. Tusberti
12:00-12:12	Spatial distribution and orientational trends of fractures on Oxia Planum	A. Apuzzo
12:12-12:30	Discussione	
12:30-14:00	**Pranzo**	

Sessione 2: Pianeti e Satelliti – MERCURIO		
Chair: Gabriele Cremonese		
14:00-14:12	Insights on triggering processes for explosive volcanism on Mercury throughout a global correlation study	M. Mirino
14:12-14:24	Insights into Mercury's tectonic history: a structural analysis of the Discovery quadrangle	A. Sepe
14:24-14:36	Perturbative Analysis of the MORE Geodesy Experiment During BepiColombo's Orbital Phase	A. Zurria
14:36-14:48	Seasonal variation of Ca and Ca-bearing molecules in Mercury's exosphere as product of micro-meteoroids and comet stream particles impact	M. Moroni
14:48-15:00	Discussione	
Sessione 3: Pianeti e Satelliti		
Chair: Federico Tosi		
15:00-15:12	Spectral analysis of mare Ingenii Basin (lunar farside).	G. Salari
15:12-15:24	The joint NASA-ESA Venus science coordination (VESCOOR) group	L. Marinangeli
15:24-15:30	Discussione	
15:30-16:00	**Coffee Break + Sessione poster**	
Sessione 4: Pianeti e Satelliti - Pianeti e Satelliti – Jupiter seen by JUNO/JIRAM		
CHAIR: Federico Tosi		
16:00-16:12	Ellipticity of the polar cyclones of Jupiter through vorticity field	P. Scarica
16:12-16:24	Modelling of the CH_4 limb radiance measured by	C. Castagnoli

	Juno/JIRAM at Jupiter’s equatorial latitudes	
16:24-16:36	Detection of pure ammonia clouds in a Jupiter high-latitude region based on an analysis of Juno/JIRAM infrared spectral data	F. Biagiotti
16:36-16:45	Discussione	
Sessione 5: Astrobiologia e Astrochimica		
CHAIR: Nadia Balucani		
16:45-16:57	Tracing the universal evolution’s operator in prebiotic chemistry and origins of life.	R. Saladino
16:57-17:09	Differential composition and metabolic profiles of soils and rocks microbial communities in Antarctic deserts as a model for Mars explorations	F. Canini
17:09-17:21	Extreme environments: cryoconite holes	F. Pittino
17:21-17:33	Ethanolamine ices in simulated space conditions	S. Biancalani
17:33-17:45	Sulfur reactivity on interstellar water ice surface	G. Di Genova
17:45-18:00	Discussione	
19:00	**Aperitivo di benvenuto presso l’Hotel Baita dei Pini**	

6 Febbraio, Martedì

Sessione 6: Pianeti e Satelliti - Focus *La nostra Luna*		
CHAIR: Francesca Zambon		
09:00-09:12	ANTHELIA - ANalysis of illumination and THermal Environment of Lunar pIts and lavA tubes	P. Cambianica
09:12-09:24	Moon multisEnsor and LabOratory Data analysis (MELODY): PRELIMINARY RESULTS	F. Tosi
09:24 -09:36	Combining numerical and machine learning models for the detection of landslides inside lunar craters	V. Yordanov
09:36-09:45	Discussione	
Sessione 7: Piccoli Corpi - Focus *La popolazione dei NEO*		
CHAIR: Simone Ieva		
09:45 - 09:57	3200 Phaethon, an active asteroid: surface alterations and expectations for Destiny^{+} space mission	M. Angrisani
09:57 - 10:09	Spectral and photometric characterization of (98943) 2001 cc21, fly-by target of Hayabusa2	J. Bourdelle de Micas
10:09 - 10:21	LICIACUBE: the light Italian Cubesat for imaging of asteroids in support to the NASA mission DART	E. Dotto
10:21 - 10:30	Discussione	
10:30 - 11:15	**Coffee Break + Sessione poster**	
Sessione 8: Astrobiologia e Astrochimica / Focus *Coevoluzione geosfera-biosfera, Geobiologia*		

CHAIR: Luca Tonietti		
11:15-11:27	Spectroscopic investigation of a potential Mars analog site: Lake “Bagno dell’acqua”, Pantelleria, Italy	E. Bruschini
11:27 – 11:39	Trace element availability and the evolution of biogeochemistry: a planetary perspective	D. Giovannelli
11:39 – 11:51	A multidisciplinary approach to explore how life might origin and perpetuate on Mars using planetary field analogues: a comparison between three projects	M. Pedone
11:51 – 12:00	Discussione	
Sessione 9: Pianeti e Satelliti / Focus *Mars Sample Return*		
CHAIR: Francesca Altieri		
12:00-12:12	Organic or not organic? updates from the NASA Mars 2020 mission	T. Fornaro
12:12-12:24	The Pantelleria “Bagno dell'acqua” lake: a new Mars-like environment as a reactor for prebiotic chemistry	G. Costanzo
12:24-12:36	Hyperspectral imaging in the VNIR of NWA13367 Martian Shergottite	S. De Angelis
12:36-12:45	Discussione	
12:45-14:15	**Pranzo**	
Sessione 10: Pianeti e Satelliti - MARTE II		
CHAIR: Filippo Giacomo Carrozzo		
14:15-14:27	Spectral survey on clay deposits & possible carbonates along the Martian crustal dichotomy, in context with the ExoMars rover mission	J. Brossier
14:27-14:39	Analysis of the OMEGA 0.4-2.5 µm spectra of the Martian satellite Phobos	J. Beccarelli

14:39-14:51	Investigating the origin and formation mechanisms of Martian Recurring Slope Lineae (RSL) from TGO/CaSSIS 4-band spectrophotometry	G. Munaretto
14:51-15:03	TGO/NOMAD UVIS and LNO channels combined nadir datasets' analysis: Martian dust characterization.	F. Oliva
15:03-15:15	Discussione	
Sessione 11: Pianeti e Satelliti - Outer Planets and Satellites I		
CHAIR: Aalessandro Mura		
15:15-15:27	A bayesian inference framework to determine the internal structure of terrestrial planets and icy moons	A. Genova
15:27-15:39	Ongoing investigation of ice analogs of the Solar System icy moons using laboratory facilities	A. Migliorini
15:39 – 15:45	Discussione	
15:45-16:15	**Coffee Break + Sessione poster**	
Sessione 12: Pianeti e Satelliti - Outer Planets and Satellites II		
CHAIR: Alessandro Mura		
16:15-16:27	Infrared analysis of the surface of Jupiter's galilean icy moons with Juno/JIRAM data	E. Di Mico
16:27-16:39	Mid-sized saturnian icy satellites investigation by spectral modeling (missis): the case of Rhea	M. Ciarniello
16:39 – 16:45	Discussione	
Sessione 13: Pianeti e Satelliti - Focus *Tettonica, Vulcanesimo e Fratturazione nel Sistema Solare*		
CHAIR: Riccardo Pozzobon		
16:45-16:57	The role of graphite in thrust faults formation on Mercury.	N.A. Vergara

16:57-17:09	Mercury’s crustal structure modelling	S. Buoninfante
17:09-17:21	Lava lakes on Io	A. Mura
17:21-17:30	Discussione	
Sessione 14: Planetologia sperimentale e di laboratorio I		
CHAIR: Stefano Rubino		
17:30-17:42	Preliminary results from laboratory investigations into electromagnetic properties of Ganymede icy crust analogues	A. Brin
17:42-17:54	Experimental results on the H_2-H_2 and H_2-He collisional-induced absorption coefficients at typical Jupiter’s upper tropospheric conditions.	F. Vitali
17:54 – 18:00	Discussione	
Sessione 15: Piccoli Corpi/Focus *Space Weathering dei corpi senza atmosfera*		
CHAIR: Marianna Angrisani		
18:00 - 18:12	Space-weathering on primitive bodies: a multi-scale laboratory study on weathered grains	S. Rubino
18:12 - 18:24	Constraining the lifetime of organics on planetary surfaces	R. G. Urso
18:24 - 18:30	Discussione	

7 Febbraio, Mercoledì

09:00– 10:00	**Sessione ASI : Il sistema solare dallo spazio**	
09:00 - 9:15	Il GdL Sistema Solare: verso una Roadmap per il contributo ASI alle Scienze Planetarie	A.Olivieri
09:15– 09:30	Esplorazione robotica dello spazio. Attività di esplorazione, infrastrutture orbitanti e di superficie	R. Mugnuolo
09:00 – 10:00	Discussione	
Sessione 16: Piccoli Corpi/ Risultati della missione DART/LICIACube I		
CHAIR: Pedro Hasselmann		
10:00 - 10:12	Reconstruction of the 3D ejecta structure of the DART impact on Dimorphos	Jasinghege Don P.D.
10:12 - 10:24	Long term dynamics around the Didymos-Dimorphos binary asteroid of boulders ejected by the DART impact	A. Rossi
10:24 - 10:36	Fracturing by thermal fatigue on Dimorphos	A. Lucchetti
10:36 - 10:45	Discussione	
10:45 - 11:15	**Coffee Break + Sessione poster**	
Sessione 17: Piccoli Corpi/ Risultati della missione DART/LICIACube II		
CHAIR: Jasinghege Don P.D.		
11:15 - 11:27	The Didymos and Dimorphos global boulder size-frequency distributions: implications on their mutual origin	M. Pajola
11:27 - 11:39	The Unusual Brightness Phase Curve of Didymos	P. H. Hasselmann
11:39 - 11:51	Dust clumps dynamics of the Dimorphos ejecta plume	S. Ivanovski

11:51-12:00	Discussione	
Sessione 18: Piccoli Corpi		
CHAIR: Davide Perna		
12:00-12:12	Comparing Didymos and Dinkinesh asteroid binary systems: collisional history and orbital evolution	A. Campo Bagatin
12:12-12:24	Granular surface artifact contacts modeling in support of small bodies landing operations design	M. Lavagna
12:24-12:36	Thermal analysis of the Comet 67P/CG	E. Rognini
12:36-12:48	the EU H2020 Programme NEOROCKS	E. Mazzotta Epifani
12:48-13:00	Mineralogical mapping of Ceres as revealed by the 1 μm absorption	G.F. Carrozzo
13:00-13:15	Discussione	
13:15-20:00	**Pomeriggio Libero**	
20:00	**Cena sociale presso l’hotel Baita dei Pini**	

8 Febbraio, Giovedì

Sessione 19: Pianeti e Sistemi Planetari I		
CHAIR: Michele Maris		
09:00 – 09:12	The diversity of Neptune-sized Exoplanets	L. Mancini
09:12 – 09:24	Global architecture of planetary systems (GAPS): searching for and characterizing exoplanets with TNG	R. Claudi
09:24 – 09:36	Are planets with large Earth-similarity index really habitable?	E. Bisesi
09:36 – 09:48	3D simulations of circumstellar disks in binaries: dust evolution and mass accretion	F. Marzari
09:48 – 10:00	Potential climates on GL514 b: a super-Earth exoplanet with high eccentricity.	L. Biasiotti
10:00 – 10:12	Search for thermal emission of protoplanets with VLT/ERIS - initial results	D. Fedele
10:12-10:30	Discussione	
10:30-11:00	**Coffee Break + Sessione poster**	
Sessione 20: Pianeti e Sistemi Planetari II		
CHAIR: Lorenzo Biasiotti		
11:00-11:12	Refraction in transiting habitable exoplanets	M. Maris
11:12-11:26	The impact of planets and flybys on the evolution of solar system analogs, the debris disk systems	V. Roccatagliata
11:24-11:30	Discussione	
Sessione 21: Pianeti e Sistemi Planetari - Focus/ *Studio dei corpi del Sistema Solare con tecniche esoplanetarie*		

CHAIR: M. Rainer		
11:30 – 11:42	Commissioning and first scientific results of LOCNES: a specialized small telescope designed for the investigation of the Sun-as-a-star spectra in the Near Infrared.	L. Cabona
11:42 – 11:54	Mars as a terrestrial exoplanet: insight from atmospheric CO_2 measurements	E. Balbi
11:54 – 12:00	Discussione	
Sessione 22: Meteore, Meteoriti e Polvere interplanetaria / Focus *Impattiti ed effetti di shock in materiale extraterrestre*		
CHAIR: Anna Barbaro		
12:00-12:12	Tektites and microtektites iron oxidation state and water content	G. Giuli
12:12-12:24	Target–projectile interaction in large-scale impacts on earth: clues form the australasian microtektites	L. Folco
12:24 -12:36	$\delta^{13}C$ values of the largest extraterrestrial microdiamond found in Ureilite NWA6871 — implications on its origin.	O. Christ
12:36-12:45	Discussione	
12:45-14:15	**Pranzo**	
Sessione 23: Meteore, Meteoriti e Polvere interplanetaria / Focus *Polveri nel Sistema Solare*		
CHAIR: Giuseppe Massa		
14:15-14:27	A new piezoeletric crystal microbalance device as a dust electrostatic collector (DEC) in the moon environment	E. Nardi
14:27-14:39	Primary dust lifting and electrification in the Makgadikgadi salt pans as Martian analogue	G. Franzese
14:39-14:51	The dust and gas analysis at 67P/Churyumov-	G. Rinaldi

	Gerasimenko sheds light on cometary activity.	
14:51-15:00	Discussione	
Sessione 24: Meteore, Meteoriti e Polvere interplanetaria I		
CHAIR: Oliver Christ		
15:00-15:12	From micro- to meter-scale: new laboratory investigations on grain size and mineral mixing in support of space mission remote sensing interpretation	G. Poggiali
15:12-15:24	The recovery of the Matera meteorite thanks to the observation of the 2023 Valentine's Day bolide by the PRISMA fireball network.	D. Barghini
15:24-15:36	Multi-analytical investigations of two Ryugu particles	M. Ferrari
15:36 – 15:45	Discussione	
15:45-16:15	**Coffee Break + Sessione poster**	
Sessione 25: Meteore, Meteoriti e Polvere interplanetaria II		
CHAIR: Marco Ferrari		
16:15 – 16:27	A new spectral parameter to detect Olivines and Pyroxenes: application to ordinary chondrites.	G. Massa
16:27-16:39	Characterizing physical properties of meteoroids using machine learning: a case study using high-resolution observations by the canadian automated meteor observatory	M. Vovk
16:39-16:45	Discussione	
Sessione 26: Planetologia sperimentale e di laboratorio II		
CHAIR: Francesca Ferri		
16:45-16:57	Near Infrared Spectroscopy and Mass	E. La

	Spectrometry of Ammonium Salts at controlled P-T conditions	Francesca
16:57-17:09	The radar signal propagation through the icy crust of Jovian moons	G. Turchetti
17:09-17:21	The new a-central model for the geometrical calibration of Daedalus lunar eyes for lava tube exploration.	E. Simioni
17:21 – 17:30	Discussione	
Sessione 27: Sviluppo di Strumentazione I		
CHAIR: Andrea Longobardo		
17:30-17:42	The ANIME cubesat for near-earth asteroids exploration	D. Perna
17:42-17:54	Establishing a common ground for radiative transfer in earth and planetary atmospheres: recent efforts	G. Liuzzi
17:54-18:06	Italian potential contribution to NASA Uranus flagship and new frontiers 5 missions	G. Sindoni
18:06-18:15	Discussione	

9 Febbraio, Venerdì

Sessione 28: Sviluppo di Strumentazione - Focus *Strumentazione Spaziale Miniaturizzata*		
CHAIR: Chiara Gisellu		
09:00-09:12	TASTE - a cubesat mission to Deimos	A. Meneghin
09:12-09:24	the VISTA instrument onboard Milani cubesat for HERA mission.	F. Dirri
09:24-09:36	Preliminary performance assessment of customized piezoelectric crystal microbalances for space applications	C. Gisellu
09:36-09:45	Discussione	
Sessione 29: Sviluppo di Strumentazione / Focus *Gestione dati in Planetologia*		
CHAIR: Angelo Zinzi		
09:45-09:57	NEO data management: from awareness to operations	E. Perozzi
09:57-10:09	VO-compliant planetary analogue spectral catalogues at ASI-SSDC	A. Zinzi
10:09-10:21	Europlanet Gmap: tools, services, and training support for planetary geologic mapping	R. Pozzobon
10:21-10:30	Discussione	
10:30-11:00	**Coffee Break**	
Sessione 30: Sviluppo di Strumentazione II		
CHAIR: Giuseppe Sindoni		
11:00-11:12	Laboratory spectral characterization of the didymium and polystyrene filters used in the internal calibration unit of MAJIS	S. Stefani

11:12-11:24	VENOM: venture the extraction of organic molecules – preliminary design of the instrument	G. Colombatti
11:24-11:36	Explore L-EXPLO & L-HEX: open-source scientific applications for lunar cartography	G. Nodjoumi
11:36-11:48	The Tianwen2 mission and the DIANA instrument	A. Longobardo
11:48-12:00	Pansharpening in planetary exploration studies: development of tools and applications	A. Tullo
12:00-12:15	Discussione	
Sessione 31: Sviluppo strumentazione / Focus *Ruolo dei Piccoli Osservatori nelle Scienze Planetarie*		
CHAIR: Mario Di Martino		
12:15 - 12:30	The contribution and the facilities of the Gal Hassin astronomical center in planetary science – toward a network of wide-field telescopes in Sicily	A.Nastasi
12:30 – 12.45	Telescope Array eNabling Debris Monitoring (TANDEM)	D. Gallieni
12:45 - 13:00	**Premiazione Miglior Poster e Migliore Presentazione**	
13:00 – 13:15	**Saluto del Sindaco di Bormio S. Cavazzi**	
13:15-14:30	**Pranzo**	
14:30-18:00	**ASSEMBLEA SISP**	

POSTER PROGRAM

	Astrobiologia e Astrochimica	
1	Bacterial and algal communities of cryoconite, differences between antarctica and three alpine glacier (Morteratsch, Forni, and Adamello)	M. Plotti
2	Laboratory investigation of the O(3p,1d) + small aromatics reactions: the role of oxygen atoms in space organic chemistry	N. Balucani
3	Multi-omic characterization of antarctic cryptoendolithic communities as proxy for searching life on Mars - cryptomars.	L. Selbmann
4	Prokaryotic life in hypersaline brines from cryosystems of the northern victoria land	A. Lo Giudice
5	Bacterial and archeal communities in an antarctic salt efflorescences from the boulder clay glacier (northern victoria land).	M. Azzaro
6	Extreme habitat of volcanic lakes for the astrobiological exploration (HELENA)	B. Cavalazzi L. Marinangeli
	Meteore, Meteoriti e Polvere interplanetaria	
7	VNIR spectral characterization of brachinites and ungrouped brachinites-like in comparison with S-Type parental bodies, in support of the HERA mission	C. Carli
8	first find of Wadsleyite and Ringwoodite in the Alfianello L6 ordinary chondrite.	L. Carone
9	Mineralogical characterization of the fusion crust of the Cavezzo L5 anomalous chondrite	M. Rondinelli
10	XPS, SEM, and micro-raman investigations of Tagish Lake (C2-ung) meteorite fusion crust	X. Shehaj
11	Transmission electron microscopy, X-ray diffraction and micro-raman spectroscopy investigation of extraterrestrial ureilitic carbon	A. Barbaro
12	Redox conditions from XAS spectroscopy on brachinites and brachinite-like ungrouped achondrites	T. Cuppone
13	Cosmic Dust II (PRIN2022 project): cosmochemistry and space tweezers technologies for solar system science and exploration	L. Folco
14	The dust and gas analysis at 67/P Churyumov-Gerasimenko shed light on cometary activity	G. Rinaldi
14	Insights on the chemical composition of Morasko meteorite by non invasive analyses: the contribution of M-XRF data and implications on the NASA-Psyche mission.	P. Manzari
	Pianeti e Satelliti	
15	Love numbers for an andrade planet	A. Consorzi

16	Planetary space weather in the context of solar system exploration	C. Plainaki
17	Constraining roughness and thermal inertia of planetary surfaces: a statistical multi-facet approach.	A. Raponi
	Pianeti e Satelliti - MARTE	
18	Antarctic cryptoendolithic communities: a natural benchmark for searching life on the red planet	C. Del Franco
19	Ice and fire: the possible interaction between periglacial and volcanic activity in the formation of a floor fractured crater, Terra Sirenum, MARS.	S. Bertoli
20	The need of a standardized geological and geomorphological mapping on MARS: central Arabia Terra craters as test sites for an objective map	I. Di Pietro
21	Investigating martian ripple formation in the Aarhus mars simulation wind tunnel.	S. Silvestro
22	A study of terrestrial volcanic Leachates: implications for Mars aqueous alterations	C. Popa
23	Production and spectroscopic investigation of martian analog mixtures	E. Bruschini
24	Development of an open source tool to perform unsupervised clustering of CRISM/MRO data on Mars: first results	B. Baschetti
25	Multi-instrument and multi-approach carbon isotopic studies on Mars	G. Liuzzi
25a	Spatial distribution and orientational trends of fractures on Oxia Planum	A. Apuzzo
	Pianeti e Satelliti - MERCURIO	
26	Geological and structural features of the Michelangelo (h12) quadrangle.	S. Buoninfante
27	Hollows on Mercury: a global perspective	B. De Toffoli
28	Minero-petrologic investigation of Boninites from Cyprus island as potential analogues of Mercury lavas	A. I. Landi
29	Exploring the thermal behavior of craters with permanent shadowed areas in the north pole of Mercury	S. Bertoli
30	Mega lava doming and collapse upon inherited tectonic structures in Caloris planitia, Mercury	G. Schmidt
31	Photometric modelling of MESSENGER/MDIS observations : insights on Mercury surface features and applications for SIMBIO-SYS on Bepicolombo	G. Munaretto
32	Mercury's crustal thickness estimation with Bepicolombo MORE investigation	I. Di Stefano
33	The thermal impact of the self-heating effect on the permanently shadowed regions of Mercury's north pole craters	P. Cambianica
	Pianeti e Satelliti - MOON	

34	Mapping data fusion: a geostratigraphic map for the lunar Tsiolkovskiy crater	G. Tognon
35	Hyperspectral characterization of the Flakstadøy anorthositic complex (Lofoten islands, Norway) as analog site of lunar highlands: preliminary results.	R. Chirico
36	moon space weathering integrated analysis	F. Zambon
	Pianeti e Satelliti – Outer Planets and Satellites	
37	Spectral properties of clear areas in Jupiter atmosphere from JIRAM / Juno data	D. Grassi
38	JANUS: the scientific camera onboard the ESA Juice mission. In-flight and on-ground activities in preparation of the science phase	C. Tubiana A. Lucchetti
39	Cyclic deformation events in the region of Gula and Achelous craters, Ganymede	C. Rossi
40	Rayleigh-Benard convection in the deep interior of Ganymede	S. Pagnoscin
41	Dione's surface composition from VIS-IR spectral modeling	B. Gorga
42	Reconstruction of localized gravity anomalies of Callisto with 3GM gravity experiment	P. Cappuccio
	Pianeti e Satelliti – VENUS	
43	HECATE PROJECT: THE EVOLUTION OF VENUS: CORONAE, SUBSURFACE STRUCTURE AND VOLCANO-TECTONICS	B. De Toffoli
44	THE DETERMINATION OF VENUS GRAVITY FIELD WITH VERITAS	F. Giuliani
	Pianeti e Sistemi Planetari	
45	Dynamical stability of highly inclined planets in binary star systems	F. Marzari
46	Collisional statistics in debris disks: preliminary results and comparison with analytical theory	A. Dell'Oro
47	Star-spot activity, orbital obliquity, transmission spectrum and TTVS of the HATS-2 planetary system	F. Biagiotti
	Piccoli Corpi	
48	ON THE ROLE OF THE LUNAR EJECTA IN THE MINIMOON POPULATION.	E. M. Alessi
49	FULL EUROPEAN RADAR OBSERVATION OF THE BINARY ASTEROID 2005 LW3	G. Pupillo
50	SEARCH FOR SPECTRAL SIGNATURES OF ORGANICS ON THE DWARF PLANET CERES: ANALYSIS OF DATA FROM VIR SPECTOMETER OF NASA'S DAWN MISSION	S. D'Urzo
51	The dust environment of distant Long Period Comets: a study in support to ESA Comet Interceptor space mission	E. Mazzotta Epifani
52	NEOROCKS: "Early-response" spectroscopy of small NEAs	V. Petropoulou

53	On the similarity of rotational motion of dust particles in the inner atmosphere of comets	S. Ivanovski
54	Computation of a possible Tunkuska's strewn field.	A. Carbognani / Di Martino
55	Scattering encounters and the predictability horizon of near earth asteroids	G. Tommei
56	Dimorphos plume profiles after DART impact: an experimental analysis	S. Caporali
57	The dynamics of the ejecta plume following the DART impact	A. Rossi
58	Near-infrared spectral homogeneity of the Didymos system before and after the DART impact	S. Ieva
59	VADER: constraining the shape of Dimorphos with LICIACUBE Luke images	A. Zinzi
60	Photometric properties of Ryugu and its artificial impact crater	A. Longobardo
	Planetologia Sperimentale e di Laboratorio	
61	Laboratory analyses of organo-sulphate samples to support MARS2020 and ExoMars rovers organic detections	A. Alberini
62	Infrared characterisation and stability studies under UV radiation of Lhistidine in Saponite to assist Mars missions in biosignature detection	C. Garcia Florentino / A. Alberini
63	Interlaboratory hub for handling and characterization of sample return and extraterrestrial materials	E. Palomba
64	Spectral acquisitions of mixtures with martian simulants and water ice	N. Costa
65	Hyperspectral analysis of terrestrial planetary-analog sites: preliminary results from ancient fluvial environments in the Gobi area.	P. Manzari
65a	The importance of terrestrial analogue sites for *in-situ* planetary exploration	E. Flamini
	Sviluppo di Strumentazione	
66	Laboratory spectral characterization of the didymium and polystyrene filters used in the internal calibration unit of MAJIS	S. Stefani
67	DaedalusNAV: a software package to display immersive images of lunar caves	C. Pernechele
68	Physical effects of ionizing gamma radiations on IR optical fibers and IR sources for the TRIS project	E. La Francesca
69	JIRAM: discovering the galileian moons.	R. Sordini
70	Deployable optics for remote sensing applications: performances of the deployment mechanism	I. Di Varano
71	Accelerated ion-ena beam for planetary space weather	E. De Angelis
72	Empowering researchers with open-source tools: a JupyterHub and docker-integrated planetary data processing environment	G. Nodjoumi
73	Expected climates for terrestrial exoplanets using Exoplan3t-	F. Manni

	ARTECS EPN-TAP connections	
	Terza Missione	
74	Exploration of the Moon between communication and science	B. Ambrosio
75	From Earth to the Moon and Mars: a virtual walk on the planetary surfaces. a CISAS-UniPd outreach activity in planetary geology	G. Tognon
76	Space Twinkles: why do we go in the space?	A. Longobardo
77	Europlanet Society and Italian Regional Hub	S. Ivanovski

Under a Faint Sun: the role of seasonal thaws in explaining the liquid water on the Noachian and Hesperian Mars

Paolo Simonetti[1], Giovanni Vladilo[1], Stavro Ivanovski[1], Laura Silva[1,2], Lorenzo Biasiotti[1,3], Michele Maris[1,2,4], Giuseppe Murante[1,2,4,5], Erica Bisesi[1,5] and Sergio Monai[1], [1]INAF/OATs – Trieste (paolo.simonetti@inaf.it), [2]IFPU - Trieste, [3]Università degli Studi di Trieste, [4]Fondazione ICSC – Casalecchio di Reno (BO) [5]CNR/IGG – Pisa

Introduction: An open problem of planetary science, with strong astrobiological ramifications, is the so-called Faint Young Sun (FYS) Paradox [1]. This comes from the contrast between established stellar evolutionary models, which predict the slow but constant brightening of G-type stars during the Main Sequence Phase [2], and the presence of liquid water traces already at around 4 Gyr before present both on the Earth [3] and Mars [4], when the Sun's bolometric flux was ~25% lower than today. Concerning the former, an atmospheric CO_2 concentration moderately larger than today (and even expected from indirect clues) is sufficient to keep the planet unfrozen [5]. Concerning the latter, a completely satisfactory solution is still missing [6].

Explaining the Martian FYS Paradox can be done by invoking either a Warm and Wet climate [7], which necessitates a sufficiently strong greenhouse effect (provided e.g. by a thick CO_2-H_2 atmosphere [8]), or a Cold and Icy one [9] coupled with transient and frequent heat-injecting phenomena (like asteroid impacts [10] or volcanic eruptions [11]). However, both answers come with a range of related issues. For example, the surface pressure of the Noachian Mars seems limited below ~2 bars by the distribution of crater diameters [12] and it is uncertain if the redox state of the mantle is able to support large concentrations of atmospheric H_2 [13]. Samely, post-impact rainfall simulations are apparently unable to explain the observed distribution of dendritic valleys [14].

A third possible solution can be seasonal thaws on an otherwise glaciated Mars [15]. Sufficiently strong seasonal temperature variations are necessary in order to drive these thaws, which in turn are possible only for certain combinations of orbital, atmospheric and planetary parameters. On the other hand, the same temperature variations might cause vigorous condensation of the CO_2 at surface, possibly starting a runaway collapse of the atmosphere [16]. Large variations of the obliquity and eccentricity of Mars are predicted by dynamical models on Myr timescales [17]. This idea has already been explored by means of non-diffusive latitudinal energy balance models (EBMs) and for a limited set of input parameters [18].

Methods: In [19] we performed a new analysis of this idea employing ESTM [20,21], an EBM with enhanced prescriptions for the meridional heat diffusion, and EOS [22], a fast radiative transfer model. We mapped the seasonal thermal maximum and its duration for a wide range of obliquity, eccentricity, argument of perihelion, surface pressure, surface land albedo and cloud cover fraction. The parameter space exploration has been repeated for five different CO_2-dominated atmospheric mixtures, using three possible concentrations of CH_4 (0, 0.1 and 1%) and three values of H_2O relative humidity (0, 20 and 40%). These choices are justified by assumptions on the average climatology, which we assumed to be akin to that of Earth deserts, and on the outgassing of reduced carbon from the interior. We also tested the impact of three possible ocean configurations, related to specific global equivalent layer (GEL) levels (0, 150 [23] and 550 m [24]). In all cases, we checked for the presence of CO_2 condensation during each hemisphere's winter and included the effects of the so-called martian dichotomy on the surface temperature via a latitudinally-averaged altimetry. These choices resulted in ~10^4 individual climate simulations like the one showed in Fig.1.

Results: We concluded that: (i) greenhouse gases other than CO_2 are not strictly needed for seasonal thaws, provided the obliquity and the surface pressure are sufficiently large, (ii) a 1% concentration of CH_4 allows for thaws even on the southern highlands already at ~1 bar, (iii) the impact of the ocean cover fraction and land albedo are small, even for rather extreme values and (iv) if ice melting is possible, then the temperate season lasts for at least 15% of the martian year. Our maps provide specific relationships between orbital parameters and surface pressure for pure water and NaCl-saturated brine runoffs. Finally, we underline how an even lower pressure (~0.3 bar) solution for deglaciation exists, but is accompanied by surface CO_2 condensation. Further investigations with 3D climate models are needed to establish if this might cause the collapse of the atmosphere or not.

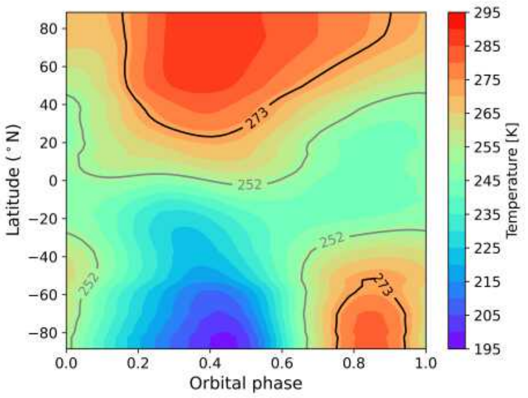

Fig.1: A seasonal-latitudinal map obtained using EOS-ESTM for an atmosphere with 1% CH_4, a surface pressure of 1 bar and an obliquity of 55°. The effects of the latitudinally-averaged altimetry and of a 150 m GEL northern ocean are included. Black and grey lines represent the 273 and 252 K isotherms, respectively. This particular case has a stable atmosphere, i.e. there is no CO_2 surface condensation.

References: [1] Sagan C. & Mullen G. (1972) Sci, 177, 52. [2] Gough D. (1981) SoPhys, 74, 21. [3] Peck W. et al. (2001) GeCoA, 65, 4215. [4] Hoke M. et al. (2011) E&PSL, 312, 1. [5] Charnay B. et al. (2020) SSRev, 5, 90. [6] Wordsworth R. et al. (2016) AREPS, 44, 381. [7] Craddock R. & Howard A. (2002) JGRe, 107, 5111. [8] Ramirez R. (2017) Icar, 297, 71. [9] Squyres S. & Kasting J. (1994) Science, 65, 744. [10] Segura T. et al. (2008) JGRe, 113, E11007. [11] Halevy I. & Head J. (2014) NatGeo, 7, 12. [12] Kite E. et al. (2014) NatGeo, 7, 335. [13] Ramirez R. et al. (2014) NatGeo, 7, 59. [14] Turbet M. et al. (2020) Icar, 335, 113419. [15] Armstrong J. et al. (2004) Icar, 171, 255. [16] Nakamura T & Tajika E. (2003) GeoRL, 30, 1685. [17] Laskar J. et al. (2004) Icar, 170, 343. [18] Kite E. et al. (2013) Icar, 223, 181. [19] Simonetti P. et al. (2023), ApJ, in press. [20] Vladilo G. et al. (2015), ApJ, 804, 50. [21] Biasiotti L. et al. (2022) MNRAS, 514, 5105. [22] Simonetti P. et al. (2022) ApJ, 925, 105. [23] Schmidt F. et al. (2022) PNAS, 119, e2112930118. [24] Di Achille G. & Hynek B. (2010) NatGeo, 3, 459.

Scientific Insights on the Mechanical Properties of Martian Subsurface from Rosalind Franklin Rover Drill Telemetry Data.

L. Rossi[1], F. Altieri[1], A. Frigeri[1], S. De Angelis[1], M.C. De Sanctis[1], M. Ferrari[1], S. Fonte[1], M. Formisano[1], M.P. Clemente[2], L. Cordeschi[2], A. Merlo[3], L. Joudrier[4], E. Sefton-Nash[4], J.L. Vago[4]
[1]INAF-IAPS, Roma, IT (lorenzo.rossi@inaf.it); [2]ALTEC, Torino, IT; [3]TAS-I, Torino, IT;
[4]ESA/ESTEC, Noordwijk, NE

The Drill of the Rosalind Franklin Rover: The Rosalind Franklin rover, set to be launched in 2028, will explore the Martian surface and subsurface at Oxia Planum, Mars. It will be the first rover equipped with a drill system capable of exploring down to a depth of 2 m. It will drill a hole, drive the Ma_MISS miniaturized spectrometer [1], collect a small core sample and deliver it for preparation and investigations using a suite of analytical instruments.

Subsurface Characterization: The study of the subsurface is essential to better understand the environment where the samples are taken from. The rover also has additional instruments besides the ones that study the sample: information about the subsurface will be provided by WISDOM, a ground penetrating radar [2], CLUPI, a close-up imager that can look at drilling fines [3], and the Ma_MISS miniaturized spectrometer collecting reflectance measurements from the borehole walls [1].

The overall picture of the subsurface provided by these instruments can be complemented and improved with information about the mechanical properties of the soil and subsurface rocks. While there is no instrument specifically dedicated to measuring such mechanical properties on board the rover, the drill system itself provides an opportunity to gain important insights about the mechanical behaviour of the rocks it bores through [4,5]. During its operation, the drill provides a wealth of information in the form of telemetry data. Drill telemetry includes data such as readings from torque and force sensors, position resolvers, temperature sensors, and motor currents and speed.

Development of Data Analysis Techniques: To extract useful information from drill telemetry data at Mars, we must develop suitable analysis techniques and validate them before the launch.

GTM Drilling Tests: Here we present telemetry data from drilling tests performed with the rover GTM (Ground Test Model). The GTM is hosted in the MTS (Mars Terrain Simulator) at ALTEC, in Turin, Italy. Drilling tests were performed with the GTM on the MTS' Drilling Facility: a raised platform with a Drilling Well that can be filled with different rocks and sand to simulate a varied stratigraphy. Using data from these tests, together with *a priori* information about the simulated stratigraphy used for each test, we can develop, optimize, and validate data analysis techniques tailored for this specific drill system, trying to extract as much useful information as possible. We are currently focusing on the analysis of data from drilling tests conducted in February 2023. In this case,

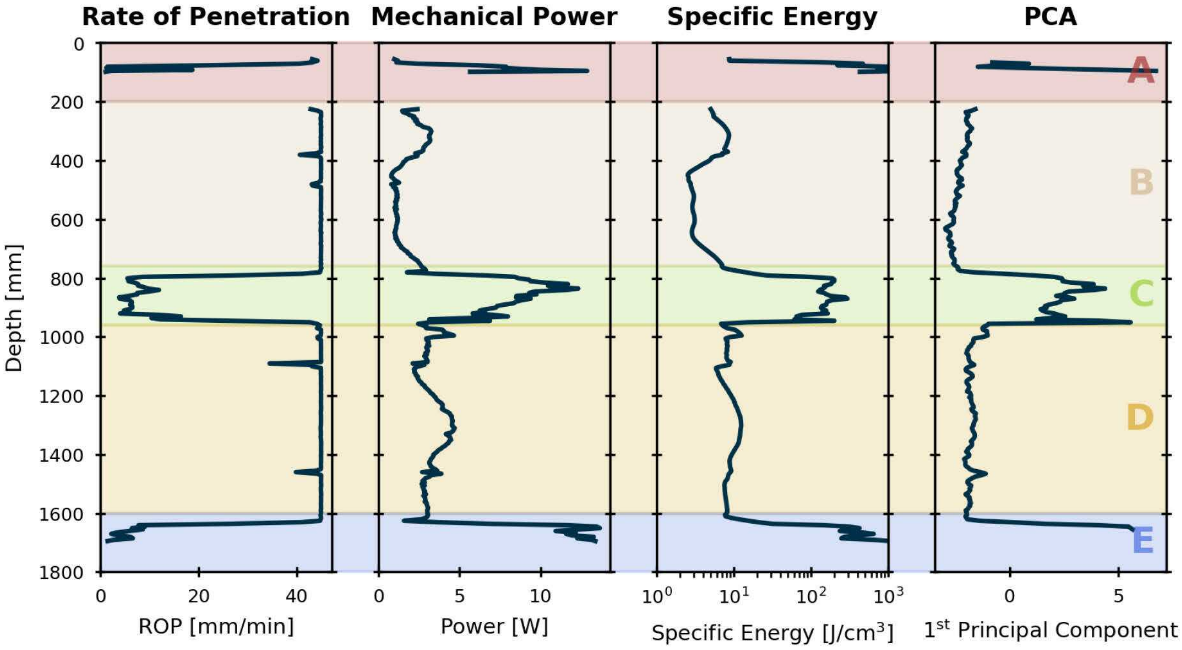

Figure 1. Quantities derived from drill telemetry data from February 2023 GTM drilling tests.

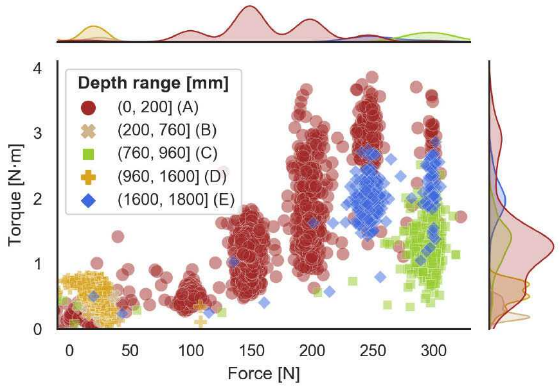

Figure 2. Torque vs WOB in the five stratigraphy layers.

the Drilling Well was filled with five different layers of rocks and sand.

Feature Engineering: We computed characteristic parameters, such as the mechanical power and drilling specific energy (mechanical energy spent per unit of volume excavated) [6], which are useful to distinguish between layers with different properties. We present an example in Figure 1, where some of these quantities are plotted against penetration depth. In the background, the known depth ranges of the five stratigraphy layers used for this test are highlighted as colour bands (labelled A, B, C, D, E). In this case, it is easy to tell apart the five layers by looking at the values of these parameters: the data show that layers B and D were much easier to drill than the others. The scatter plot in Figure 2 shows values of torque and vertical force (often referred to as WOB, Weight On Bit), with each data point coloured as a function of its depth. For the same level of force applied and rotation speed, the various layers reacted with different levels of torque, a property that can be useful to discriminate between different materials or cohesion states.

Unsupervised Learning: To assess the information content of each telemetry parameter and get a lower-dimensional representation of the dataset, a principal component analysis (PCA) was used. The first principal component, shown in the rightmost plot of Figure 1, accounts for about 77% of the variance and highlights the difference in the mechanical response to drilling of the different stratigraphy layers.

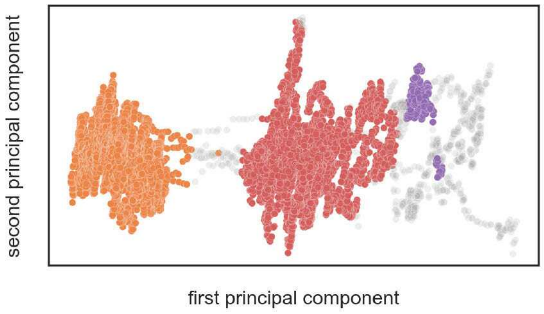

Figure 3. HDBSCAN clustering results. Each cluster is shown in a different colour. Datapoints shown in grey were marked as outliers by HDBSCAN.

In addition, some clustering algorithms were tested on the telemetry dataset. An example of the results of the HDBSCAN algorithm (Hierarchical Density-Based Spatial Clustering of Applications with Noise) are shown in Figure 3. Here, the algorithm identified three clusters in the dataset, and correctly assigned data from layers B and D to the same cluster (they are, indeed, made of the same material).

Neural Network Classifier: In addition, some supervised learning algorithms were also tested on the GTM drill telemetry dataset. For example, a 1-Dimensional Convolutional Neural Network (1D CNN) classification model, which was trained on telemetry timeseries data to recognize different materials, achieved a classification accuracy of approximately 96% on the chosen test set (which had no overlap with the training set).

Way Forward: So far, we have utilised only a limited set of data, stemming from a single test campaign. However, these first results are encouraging. They demonstrate that this technique has good potential to boost our understanding of subsurface material properties. More data are needed to optimize and validate the analysis methods we are developing. It is also crucial to assess the performance and accuracy of this method under various scenarios. Additional GTM drilling tests will be performed soon, and the resulting data will be instrumental in improving our data analysis algorithms. We are also working on extracting informative features that are closely relatable to mechanical properties of the material being drilled and on tuning the supervised learning models, with a more thorough exploration of the hyperparameter space. A larger reference dataset will enable developing methods to correlate drill telemetry data to quantitative estimates of some mechanical properties of subsurface material, such as the uniaxial compressive strength and surface hardness.

References:

[1] M. C. De Sanctis et al., Planetary Science Journal, vol. 3, n. 6 (2022)
[2] Ciarletti, V. et al., Astrobiology, vol 17, n. 6-7(2017)
[3] J.-L. Josset et al., Astrobiology, vol 17, n. 6-7 (2017)
[4] F. Altieri et al., Advances in Space Research (2023)
[5] A. Frigeri et al, abstract #1462 in LPSC 52 (2021)
[6] R. Teale, International Journal of Rock Mechanics and Mining Sciences & Geomechanics, 2, 1 (1965)

QUASIPERIODIC Fe/Mg CLAY ENRICHMENT WITHIN SULFATE BEDS OF EQUATORIAL LAYERED DEPOSITS IN MERIDIANI PLANUM.

B. Baschetti[1,2], A. Tullo[3], M. Massironi[1], F. Altieri[2], C. Carli[2], M. Baroni[1,4], A. Breda[1]. [1]Department of Geosciences, University of Padova, Padova, Italy (beatrice.baschetti@phd.unipd.it); [2]INAF-IAPS, Rome, Italy; [3]INAF-OAPD, Padova, Italy. [4] Department of Physics and Geology, University of Perugia, Perugia, Italy.

Introduction: The area of Meridiani Planum is located near the martian equator, at the south-western end of Arabia Terra. The region is well known for hosting hematite deposits [1], partially overlying extensive layered sediments rich in aqueous minerals such as sulfates and clays [2]. These sediments are usually referred to as “etched unit” [3] due to their appearance and texture, and can be contiguously mapped over a large part of Meridiani. The deposition/erosion time of the etched sediments spans from the Late Noachian to the Early Hesperian [4,5], making them an important record of Mars’ past surface conditions and essential to constrain most of the aqueous activity in the region. Eroded remnants of the etched units are found inside and outside impact craters of the northern part of Meridiani [6], where they display complex layered morphologies such as those observed in Firsoff [7], Kotido [8], Danielson [9], Becquerel [10], Jiji and Sera craters [11] and in many other regions around Meridiani and Arabia Terra. These deposits, due to their presence in the equatorial regions of Mars and because of their peculiar appearance showing repetitive bedding, fall under the general term of Equatorial Layered Deposits (ELDs). From a mineralogical point of view, ELDs are commonly associated with hydrated minerals such as sulfates (e.g.; [12, 13, 14, 6]) and, less commonly, clays [15, 16]. Evidence of mixed clay/sulfate mineralogy has not been reported as today, although assumed in [17]. The study of ELDs is particularly significant as they might retain information about past environmental and climatic conditions of Mars and the quasiperiodic bedding observed indicates cyclic environmental changes during their deposition [18]. In this abstract we report three different cases across Meridiani Planum (Kai crater, Unnamed crater A and B; **Table 1**) where we observe a mixed clay/sulfate mineralogy within ELDs. In all three cases the ELDs are observed inside impact craters.

Name	Coord.	Diameter	CRISM ID
Kai	4°20’N; 2°50’E	18 km	9B5A (FRT)
Unnamed A	5°27’N; 1°50’O	9 km	3E24 (FRT)
Unnamed B	0°40’N; 7°24’E	6 km	11403 (HRL)

Table 1. List of selected craters with ELDs deposits.

Dataset and methods: To characterize in detail the morphology, stratigraphy, bedding attitudes and mineralogy of the layered deposits we make use of the high-resolution grayscale images and stereo pairs from the High Resolution Imaging Experiment (HiRISE) [19], and combine them with the compositional information retrieved through the Compact Reconnaissance Imaging Spectrometer for Mars (CRISM) [20] targeted hyperspectral data. The overall mineralogy is investigated with standard RGB browse products, as defined in [21]. Relevant browse products for this analysis are the HYD (hydrated minerals) and the PHY (phyllosilicates) products. Thanks to the spatial resolution of targeted CRISM observations, which is about 18 m/pixel at its peak, and to the de-noised spectral summary parameters available with the CRISM MTRDR dataset, we are able to characterize the spectral signature of different layers within the ELDs. This further analysis has been specifically carried out investigating the SINDEX2 spectral parameter (see [21] for its mathematical expression), which detects the convexity of the spectrum at 2.29 μm due to the 2.1 and 2.4 μm absorptions of hydrated sulfates. We choose different threshold values of the SINDEX2 parameter, focusing on a portion of the CRISM image that covers the ELDs. With this technique we are able to select different layers, dividing them in three groups, based on whether the SINDEX2 parameter has *low*, *intermediate* or *high* values. The exact values are empirically-determined and observation-dependent but they have comparable magnitude throughout the three images.

Results:

Mineralogy. **Figure 1A** shows the extracted spectra from the ELDs in one of the three craters selected (Kai crater). Each spectrum is the result of a mean of all the pixels within the CRISM scene selected with the SINDEX2 criterion described in the methods section. The three extracted spectra have two major differences: a) they all have a 2.3 μm absorption feature but with different depth, where the band gets deeper as SINDEX2 decreases; b) they have a different spectral contrast in the 2.35-2.4 μm range, where the contrast decreases as SINDEX2 decreases. This exact behavior is observed within the ELDs of all three craters reported here.

Layering. Based on plane fitting using the HiRISE digital elevation model, it seems that the layers in Kai and Unnamed A are almost horizontal. Accurate measurements still have to be performed for Unnamed crater B.

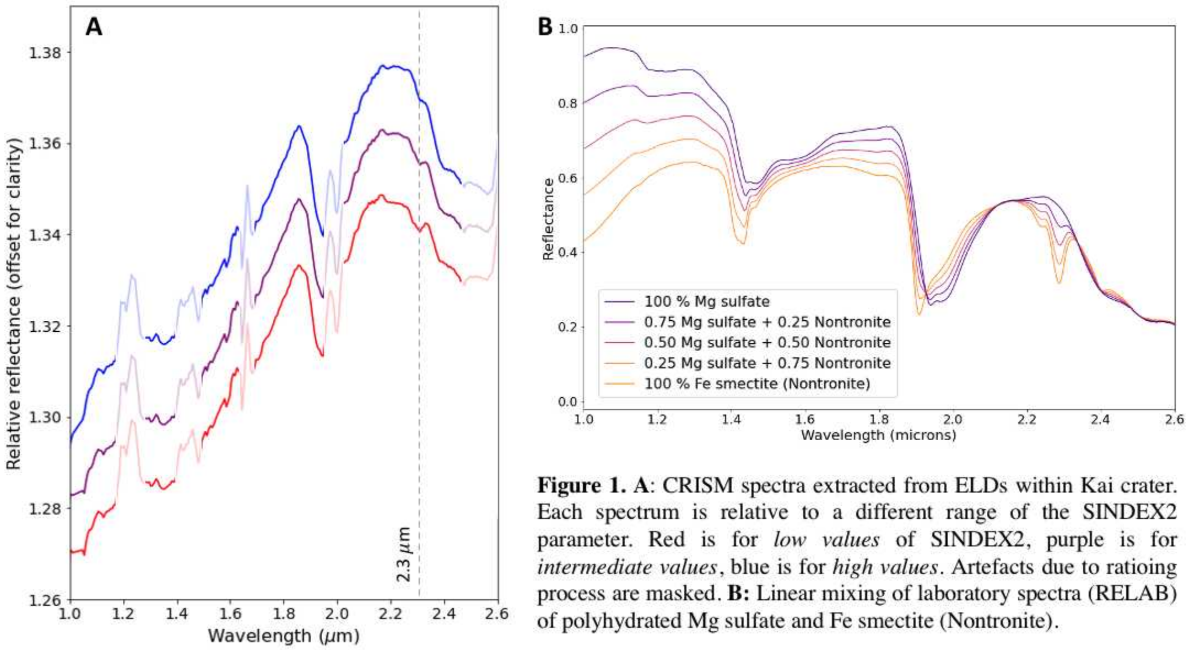

Figure 1. A: CRISM spectra extracted from ELDs within Kai crater. Each spectrum is relative to a different range of the SINDEX2 parameter. Red is for *low values* of SINDEX2, purple is for *intermediate values*, blue is for *high values*. Artefacts due to ratioing process are masked. **B:** Linear mixing of laboratory spectra (RELAB) of polyhydrated Mg sulfate and Fe smectite (Nontronite).

Discussions and conclusions: The observed fluctuations in the intensity of the SINDEX2 parameter throughout the ELDs indicates a varying sulfate content. The extracted spectra then show the presence of a shallow 2.3 µm band. This band is usually associated with Fe/Mg-OH vibrations in Fe/Mg-OH minerals such as Fe/Mg phyllosilicates. The increasing intensity of the 2.3 band correlates with the decreasing of the SINDEX2 parameter, which might indicate different degrees of mixtures between sulfate and clay minerals in the ELDs. Where SINDEX2 is most intense, the 2.3 µm band is shallow, indicating only a small presence of the Fe/Mg phyllosilicates. On the contrary, where the SINDEX2 is less intense, the 2.3 band is deeper and therefore Fe/Mg clays are more present, although sulfates might still dominate the overall composition. This behavior of the spectral shape in sulfate + Fe/Mg phyllosilicate mixtures is also found in linear mixing experiments between a polyhydrated Mg sulfate endmember and Fe/Mg phyllosilicates endmembers (for example, in the case of Nontronite, **Figure 1B**). Unfortunately, none of these techniques allows us to quantitatively constrain the amount of sulfate and clay phases within the layers. Laboratory experiments on reflectance spectra of clay and sulfate mixtures are planned to cover this knowledge gap.

Nevertheless, the results shown here indicate that the mineralogy of some ELDs is more complex than previously thought. The interbedding of layers with different degrees of mixing between sulfates and phyllosilicates is puzzling. A possible explanation could be related to slight and periodic changes of the environmental conditions in which these sediments formed/deposited, resulting in slightly different mineralogical assemblages. Further in depth analysis is planned in order to understand the possible formation mechanisms of these peculiar ELDs in the Meridiani region.

References:

[1] Christensen P. R. et al. (2001) *JGR, 106,* 23873-23885. [2] Flahaut J. et al. (2015) *Icarus, 248*, 269-288. [3] Hynek B. M. et al. (2002), *JGR, 107 (E10)*, 5088. [4] Fassett C. I. and Head J. W (2007), *JGR, 112* (E08002). [5] Zabrusky et al. (2012), *Icarus, 220 (2)*, 311-330. [6] Hynek B. M. and Di Achille G. (2017), USGS Scientific Investigation Map 3356. [7] Pondrelli M. et al. (2015), *GSA Bulletin, 127* (7/8), 1064-1089. [8] Pondrelli M. et al. (2019), *JGR-Planets, 124*, 779-800. [9] Murana A. (2018), *Journal of Maps, 14* (2), 161-172. [10] Schmidt G. et al (2022), *JGR - Planets, 127*, e2022JE007320. [11] Di Pietro I. et al. (2023) *JGR-Planets, 128 (3),* e2022JE007504. [12] Gendrin A. et al. (2005), *Science, 307 (5715)*, 1587-1591. [13] Bibring J.P. et al. (2006) *Science, 312(5772),* 400–404. [14] Murchie S. (2009a), *JGR-Planets, 114 (E2)*. [15] Michalski J. R. and Noe Dobrea E. Z. (2007) *Geology, 35 (10),* 951-954. [16] Noe Dobrea E. Z. (2010) *JGR, 115,* E00D19. [17] Poulet F. et al. (2005) *Nature, 438,* 624-627. [18] Lewis K. W. and Aharonson O. (2014), *JGR-Planets, 119*, 1432-1457. [19] McEwen A. S. et al. (2007), *JGR, 112*, E05S02. [20] Murchie S. et al. (2007) *JGR, 112 (E5)*, E05S03. [21] Viviano-Beck C. E. et al. (2014) *JGR Planets, 119*, 1403-1431.

Acknowledgements: CRISM and HiRSE images and stereo pairs were downloaded through the PDS Geosciences Node Orbital Data Explorer (ODE). Laboratory spectra of Mg sulfate and Fe smectite are from the RELAB spectral library (product IDs: CJB366 and CBJB26, respectively). This project is partially funded by Europlanet RI20-24 GMAP project (research grant agreement No. 871149).

STUDY OF THE SEASONAL WATER ICE IN THE EJECTA OF A SMALL CRATER ON MARS.

F. Furnari[1,2], F. Altieri[1], A. Raponi[1], M.C. De Sanctis[1], A. Frigeri[1], J. Brossier[1], [1]Istituto di Astrofisica e Planetologia (IAPS), Istituto Nazionale di Astrofisica (INAF), Via del Fosso del Cavaliere 100, 00133 Roma, Italy, [2]Dipartimento di Fisica, Sapienza Università di Roma, Roma, Italy (furnari.1796897@studenti.uniroma1.it)

Introduction: Although Mars is very similar to Earth in terms of its rotational axis inclination and rotational period, which allows for the existence of seasons, it is quite different in other ways. On Mars, temperature and pressure values are always below the triple point of water, and that's why water is present only in vapor and solid phase, for example as ice in the polar caps. The cycle of condensation of water ice on the Martian surface is seasonal and daily, due to the very high thermal excursion between day and night [1]. Here, we focus on the characterization of the water ice present on the ejecta of a small crater on Mars (LON = 301.6°, LAT = 43.9°), located in the northern hemisphere between the Acidalia Planitia and Chryse Planitia regions by means of the CRISM/MRO data [2,3]. The crater, shown in Figure 1, has the particularity of radial ejecta characterized by a larger abundance of water ice than the surroundings, which cannot apparently be explained by altimetry or morphology of the terrain. The water ice is clearly present only in the winter season (CRISM data at Solar Longitude, Ls = 322.7°), while in autumn (Ls = 210.9°) it's almost completely absent. The aim of this work is to estimate the abundance, grain size and temperature of water ice in order to figure out the cause of the stronger spectral features of the ice on the radial ejecta of the crater.

Figure 1: RGB image of the CRISM cube taken at Ls = 322.7 ° (winter) in the VNIR spectral range (400 - 1000 nm). CRISM observation: frt00007f64

Data and methods: The two data cubes analyzed, the autumn and winter ones, were taken by the CRISM instrument [2], onboard the Mars Reconnaissance Orbiter [3], with a spatial resolution of 18.4 m/pixel, and a spectral resolution of 6.55 nm/channel. The cubes were first preprocessed with the CAT ENVI toolkit for atmospheric and photometric corrections. Corrected cubes were then denoised to reduce noise and residual atmospheric contributions. We analyzed the spectrum of each pixel of the cubes in the IR spectral range (1-4 μm), which comprises key features for water ice [4]. Examples of CRISM spectra of the area of study are shown in Figure 2. In particular, for each pixel, we computed spectral parameters such as the slope in the continuum between 1.4 and 2.3 μm, as well as band depth and band area for the absorption bands at 1.5 and 2 μm to evaluate the spatial distribution of water ice and producing maps of these spectral parameters.

Then, we applied the Hapke's equation [5] to model the spectra of each pixel as a mixture of Martian dark terrain (the spectrum is the mean spectrum of a ROI of the autumn cube), and water ice (the spectrum is modelled by using water ice optical constant). For the mixture we considered both areal and intimate cases [6]. Through this model, we retrieved the maps for abundance and grain size of water ice over the whole winter cube, both for areal and intimate mixture, at different temperatures between 166 K and 196 K (with a ΔT of 10 K), choosing for each pixel the best fit for both abundance and grain size. We noticed a degeneration between the two parameters and a small variation of the grain size over the whole cube. For this reason, we realized a map of the abundance of water ice at fixed grain size for each temperature. At this point, by comparing the chi-square values of each pixel we were able to determine which type of mixture is the most fitting. Finally, we obtained a map of temperatures with a continuous gradient, even though ice optical constants are available at only four temperatures (166 K, 176 K, 186 K, and 196 K).

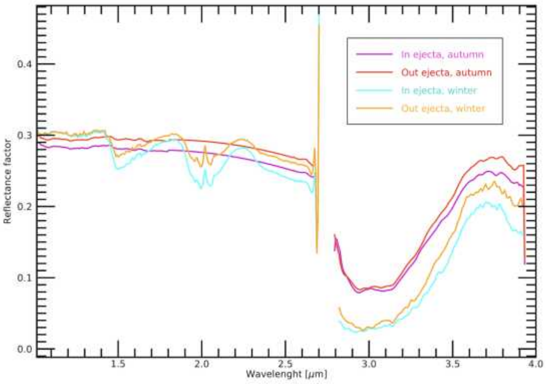

Figure 2: Selected spectra of the autumn cube (magenta inside the ejecta, red outside the ejecta) and of the winter cube (cyan inside the ejecta, orange outside the ejecta) reported as Reflectance Factors. A spike in the winter spectra is evident.

Results: The maximum values found for the abundance inside and outside the ejecta are of about, respectively, 20% and 15% for the areal mixture, while they drop to 13% and 8% for the intimate one, confirming that the ejecta are characterized by a higher abundance of water ice. This result is in line with what we expected from the spectral parameter maps, in particular the band area at 1.5 µm. On the other hand, the grain size seems to have a very small variation between inside and outside the ejecta, so we decided to fix it at its median value inside the cube, which is around 60 µm for the areal mixture and 300 µm for the intimate one.

Moreover, we find that the intimate mixture is the one that provides the best fits. The abundance map at 1.5 µm is shown in Figure 3. Finally, the comparison between the chi-square values of the four abundance maps with fixed grain size, at different temperatures, shows that the temperature on the ejecta is lower than the surroundings, with a variation all over the cube of about 15-20 K (Figure 4).

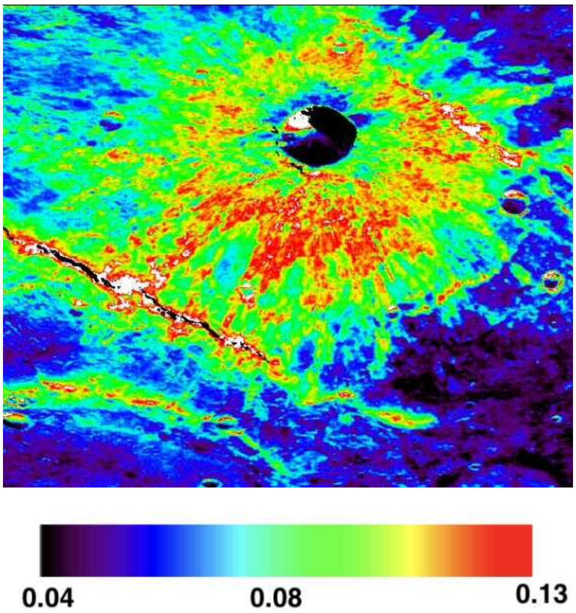

Figure 3: Map of the abundances at fixed grain size (300 µm) and fixed temperature (176 K) for the intimate mixture, with relative colour ramp.

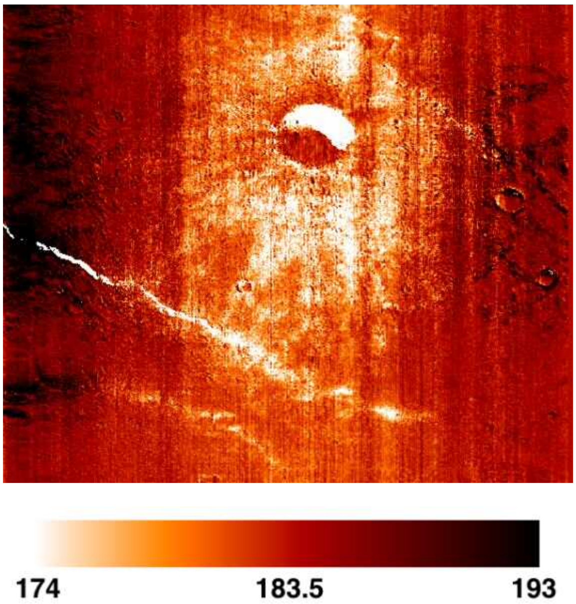

Figure 4: Map of the temperatures with relative colour ramp in K units.

Conclusions: The purpose of this study is to better understand the deposition of seasonal water ice on the radial ejecta of a crater at LON= 301.6° and LAT= 43.9° on Mars. CRISM spectral parameters used to detect water ice indicate a difference in the quantity of water ice between inside and outside the ejecta. Through the modelling of the spectra, we were able to estimate the abundance and grain size all over the CRISM cube, to assert that the mixture between water ice and Martian dark terrain is intimate, and to produce a map of the temperatures as well.

We find that on the ejecta, water ice is more abundant than in the surroundings, while the grain size seems to be constant all over the region covered by the CRISM observation, within the sensitivity of the model. Another important outcome of our study is that the ejecta are characterized by a lower temperature (around 174 K) than the surroundings (around 193 K), a fact that could explain the major abundance of water ice. Thermal inertia data from the THEMIS instrument as well as high resolution images from HiRISE are under evaluation to better understand the role of texture and/or subsurface properties of the ejecta in trapping a higher amount of water ice.

Acknowledgments - This work is supported by the Italian Space Agency (ASI) [Grant ASI-INAF n.2023-3-HH.0]

References: [1] Altieri F., Hauber E., Orosei R. (2021) *Encyclopedy of geology (Second edition),* 94-104. [2] Murchie S. et al. (2007) *JGR Pl.* [3] Zurek R.W. et al. (2007) *JGR Pl.* [4] Carrozzo F.G., et al. (2009) *Icarus 203.2,* 406-420 . [5] Hapke (2012) *Cambridge University Press*. [6] Raponi A., et al. (2016) *MNRAS 426.1,* 476-490 .

ANALYSIS OF ICE SUBLIMATION AND BOULDER SIZE FREQUENCY DISTRIBUTION ON THE FRESH MARTIAN CRATER S1094b.

[1]Tusberti, F, [1]Pajola M., [1]Munaretto, G., [1]Lucchetti A., [1,2]Beccarelli J., [1]Penasa L., [1]Rossi, C., [3]Pozzobon R., [3]Massironi M.

[1]INAF-OAPD Astronomical Observatory of Padova, Padova, Italy (filippo.tusberti@inaf.it); [2]Centro di Ateneo di Studi e Attività Spaziali – Giuseppe Colombo (CISAS), Padova, via Venezia 15, 35131 Padova,Italy. [3]University of Padova, Department of Geoscience, Padova, Italy.

Introduction: On December 24, 2021, a new crater named S1094b formed on Mars [1]. It was localized at the coordinates 34.8°N, 189.92°E, through the contemporary exploitation of InSight seismic data [2,3] and MRO HiRISE images [4]. The impact occurred in the northern part of the Amazonis Planitia region, which is a flat area mainly composed of rugged lava flows and pyroclastic materials [5,6]. The projectile likely traveled from southwest to northeast, at an inferred azimuth of ~60°. The resulting S1094b crater has a diameter of ~155 m and a depth of ~20÷23 m [1]. The lack of up-range ejecta indicates an oblique impact (~30°) coming from SW [1,6,7]. The most interesting feature about S1094b crater is that the impact which formed it, exhumed and ejected water-ice rich material, showing patches among its proximal ejecta. To date, this is the lowest latitude (35°N) where water-ice has been exposed [8]. In this work, we i) analyze the geology of the crater, its ejecta and the surrounding area providing a large-scale geologic map; ii) study the Size Frequency Distribution (SFD) of the rocky and icy boulders freshly ejected by the impact; and iii) provide a quantitative estimation of the ice volume exhumed by the impact. Moreover, we exploit an additional dataset obtained ~9 months later in order to analyze the changes of the ejecta with time, providing a multitemporal analysis of both the volume of ice and the boulder SFD.

Datasets and Methods: We exploited two images, called ESP_073077_2155 and ESP_076677_2155 taken by the High Resolution Imaging Science Experiment (HiRISE) camera onboard Mars Reconnaissance Orbiter (MRO) [4,9]. The first one dates back to 27 February 2022 while the second one was taken on 5 December 2022. Specifically, we used the RED channel images (0.25 m/px) in combination with the HiRISE Digital Terrain Model (DTM) (1 m/px) and the merged RGB images (0.5 m/px). We chose such datasets because of their similar illumination and geometrical properties, hence, reducing the observational bias.

Geologic Mapping: We distinguished the different geologic units, features and landforms, on the basis of their RGB colors, morphology, texture, and stratigraphic order. The mapping process was made through the *Qgis* software and well-established methods [e.g. 10,11].

Boulder Size Frequency Distribution: All the boulders present in the study area have been manually mapped in both datasets, distinguishing the icy boulders from the rocky ones. In order to consider the minimum three pixels sampling rule [12], and to reduce observational biases, [13,14] we used only boulders with diameter ≥ 0.75 m for our statistics. All boulder diameters were used to calculate the SFD, finding a power-law fit for each dataset. We then validated the existence of the power-law fit through the [15] methodology which provides the scaling parameter α, also called power-law index. Furthermore, this methodology allows to identify the completeness limit x_{min} (i.e. the threshold value above which the power-law exists), through the Kolmogorov-Smirnoff (KS) statistics. Finally, the KS statistics also provides the p-value, which confirms above the significance level of 0.10 if the dataset comes from a power-law distribution.

Ice estimation: By exploiting the two mentioned images we identified any surface changes in the ice content. Since the ice around S1094b is present in two forms, i.e. single boulders and stripes, we mapped the icy boulders as circles and the stripes as polygons in the investigated area.
To estimate the volume of the ice boulders, we approximated them as spheres with a diameter equal to that of the respective boulder. Conversely, we approximated the stripes as irregular prisms and we estimated their thickness. We then compared the values of the February and December datasets, providing an ice volume loss estimation.

Results and Discussions: We provide a 1:10000 scale geologic map of S1094b, where 5 geologic units and 4 landforms have been identified (Fig. 1). This geologic map shows the morphology of S1094b and its ejecta. Given the geologic context of the northern Amazonis Planitia and the crater's depth of ~21 m, it is unlikely that the impact exhumed other material except for the most surficial geologic unit. Moreover, this map highlights potential forbidden areas in the down-range direction. This would lower the impact angle from ~30° to ~15÷20°.

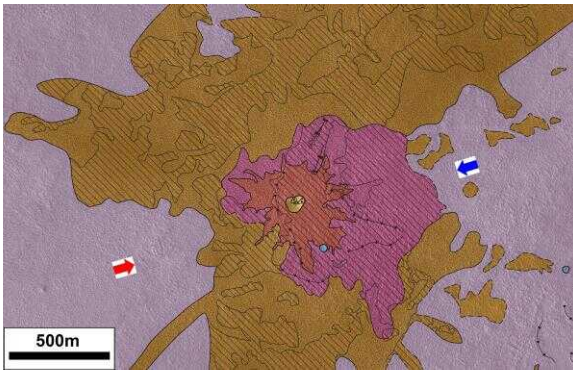

Fig. 1: a closeup of the geologic map, the red arrow indicates the up-range forbidden zone, the blue arrow the down-range forbidden zone identified in this work.

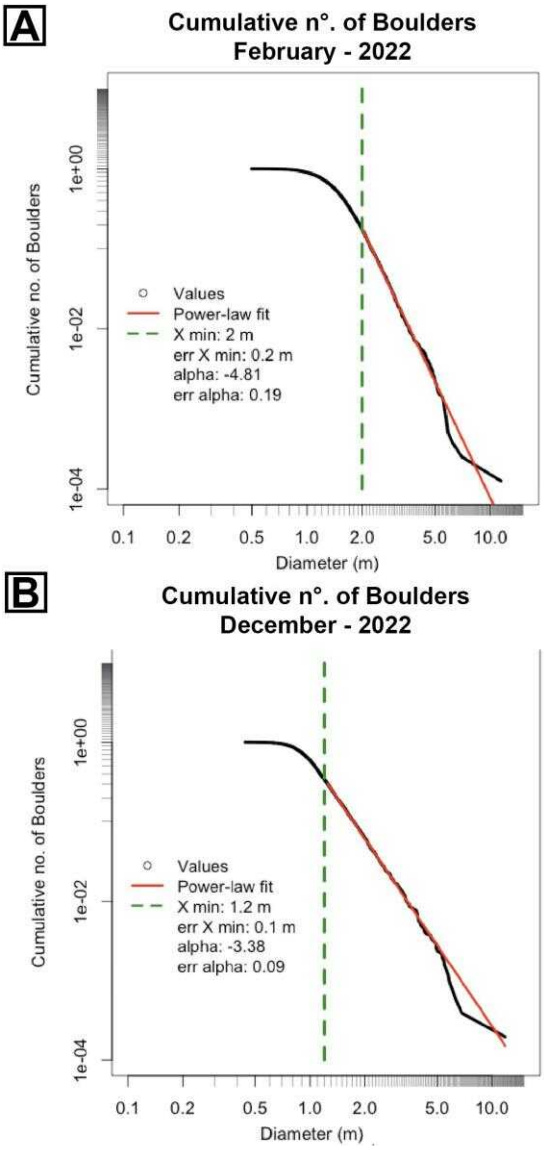

Fig. 2: comparison between the boulder SFD of February (A) and December (B). Is possible to see the slight flattening of the fit, going from α = -4.81 to -3.38.

We counted on the February dataset a total of 7989 boulders, 3470 icy while 4519 rocky. On the December dataset we counted a total of 5138 boulders, 1096 icy and 4042 rocky. The SFD of both datastets resulted in a power-law fit, with a x_{min} of 2 m in the February dataset, while a x_{min} of 1.2 m in the December one. In 9 months the α value changed from a -4.81 to a -3.38. This flattening is likely due to the loss of the smallest sizes of the dataset. Thus, we applied the same methodology to only the icy and rocky boulders components separately. When comparing the results of February with those of December, a flattening in both of the curves becomes noticeable. The α value of the rocky boulders decreased from -4.37 to -3.38 (a difference of 0.99), while the power-law index of the icy boulders changed from -5.51 to -3.56 (a difference of 1.95). These results indicate that most of the small-boulder loss can be attributed to the icy sublimation.

We then estimated the ice loss from February to December computing a difference of ~7313 m^3, i.e. a value of about 60%, from the February case of ~20274 m^3, to the December one of ~7951 m^3. Such evidence suggests that a clear sublimation process occurred during the 281 considered days.

Acknowledgements: This study has been supported by the Italian Space Agency (ASI) through the ASI-INAF agreement no. 2020-17-HH.0

References: [1] Posiolova, L. et al., (2022) *Science*, *378*(6618), 412-417. [2] R. F. Garcia et al., (2022) *Nat. Geosci*., 15(10), 774. [3] Tanaka, K. L., et al., (2005) *US Department of the Interior*, USGS. [4] McEwen, A. S. et al., (2007) *JGR: Planets*, *112*(E5). [5] Tanaka, K.L. et al., (2014) *USGS Scientific Investigations* Map 3292, pamphlet 43. [6] Gault, D. E., et al., (1978) *New York, Pergamon Press*, Vol. 9 p. 3843. [7] Kenkmann, T. et al., (2014) *JSG*, vol 62, p. 156. [8] C. M. Dundas et al., (2021) *J. Geophys. Res. Planets* 126, e2020JE006617. [9] Zurek, R. W., and Smrekar, S. E. (2007) *JGR: Planets*, *112*(E5). [10] Galluzzi, V., L. et al., (2016) Journal of Maps 12 (sup1): 227–38. [11] Tusberti F., et al., (2024). *GFT&M*, vol. 16, 1-19 https://doi.org/10.3301/GFT.2024.01. [12] Nyquist, H., (1928) *Trans. Am. Inst. Elect. Eng*. 47, 617. [13] Golombek M. and Rapp D., (1997) *s. JGR.* 102, 4117–4129. [14] Golombek, M.P., et al., (2003) *JGR.* 27, 8086. [15] Clauset, A., et al., (2009) *SIAM Rev. 51*, 661-703.

Insights on triggering processes for explosive volcanism on Mercury troughouth a global correlation study.

M. Mirino[1,2], M. Massironi[1] and R. Pozzobon[1]
[1] Università degli studi di Padova (melissa.mirino@unipd.it), [2]Centro di Ateneo di Studi e Attività Spaziali "Giuseppe Colombo" - **CISAS**

Introduction: The NASA-MESSENGER mission investigated the planet Mercury highlighting three main geological processes which shaped the surface: (i) volcanism, (ii) global contraction with consequent formation of tectonic-compressive features, and (iii) impact cratering with consequent formation of basins or minor craters [e.g., 1, 2, 3]. However, it is still unclear if the tectonic induced by impact basins and later tectonic re-activation have influenced later volcanism and for how long. Thus, we investigated the presence and the absence of a correlation between the various volcanic features and their geological context (e.g., inside craters and/or basins, relationship with tectonic structures) to understand how the primary or secondary triggering activities could have influenced the volcanic activity of the planet.

Methodology: The study was developed primarily using the ESRI ArcGIS (Geographic Information System) software package. The MDIS data and base maps used in the main part of the project come from the MESSENGER mission. To carry out the correlation study on a global scale, a new GIS database was created in which all the candidate volcanic emission centres identified so far on Mercury, their morphological characteristics and their associations with various other tectonic (e.g., thrust faults) or volcanic features (e.g., faculae) were specified. 346 samples were included: (i) volcanic vents and their morphological classification [4, 5], (ii) presumed volcanic cones [5, 6, 7], and (iii) irregular pitted terrains [8, 9]. Once this global database was created, the study was divided into two parts. The first part was based on the study of the global distribution and statistics of the volcanic structures studied with respect to impact basins [10], minor craters and tectonic features due to global tectonics [11]. This part allowed to identify any patterns and areas of interest for more detailed observations and analyses. The second part was focused on evaluating the presence of a proper correlation between the different parameters [12], characteristics and geological contexts considered. The correlation of the volcanic centers with the tectonic features has been evaluated by splitting them by types (wrinkle ridges, thrust faults and compressional features) and by distances from the candidate emission centers. We classified at distance 0 the tectonic features which are crossed or are crossing the candidate volcanic centers and the hosting minor crater. Features at a distance $\geq$ 50 km are classified as proximal, from 50 km <distance $\geq$ 100 km are classified as relatively distant and, when the distance is > 100 km, the tectonic feature has been classified as distant.

Observations and Results: The 66% of the volcanic features in the database was found within minor impact craters (81% on the crater floor and the 19% on the crater rim or in adjacent areas to the rim). However, form Fig. 1 is clear how the majority of the features is developed at the margin of the major impact basins wherever those are considered certain or probable.The distribution is not random but the craters hosting the candidate volcanic centres present a proper semi-circular trend, which follow the basins'rim(or possible rim when the basins are less evident or covered by subsequent events) or emulates the approximate boundaries of the basins in the case of the probable basins. The strong connection with this type of pattern is confirmed by the correlation study (Fig. 2). Statistical evaluation show that the 15% of the volcanic centers, wherever they are developed within or outside craters, are at distance 0 from a compressive structure, the 55% are proximal, the 10% are relatively distant and the 17% are distant. From the correlation study (Fig. 2) is present a correlation between the volcanic vents and the tectonic features classified as thrust faults. These thrust faults are often proximal to the volcanic centers or are proximal to the craters hosting the volcanic features. Showing that a trend is actually present and occur at a global scale, at least for the 55% of the vents in the database. Pit vents within craters are found on both hanging walls and footwalls of these thust faults or at distance 0 from other closer compressive features. These tectonic features and the craters hosting the vents are often on the rim of a basin or within 200 km from it (a reasonable distance for fracturing of a basin damage zone).

Interpretation: A model that could explain the formation of all the 346 samples is hard to find, since many local factors could have occurred to form or influence the formation of volcanic centers. However, the 55% of the volcanic vents present a recurring pattern which strongly relates vents, minor craters, basins and thrust faults. A possible model to explain this global correlation is as follow: (i) Major impact basins would form on the surface of the planet creating listric internal faults and other external distensivefratures within the damage zone, (ii) magmatic material upward movements would follow the structuresformed by those large impacts, (iii) tectonic reactivation during the compressive stage would form critically stressed thrust faults in prior areas of impact faulting, (iv) the magma propagation along those areas could have been partly impeded by the compressional deformation but v)minor smaller impacts might have released the critical stressed areas allowing explosive eruptions

Conclusions: Correlation and global distribution studies of volcanic features have highlighted how the majority of these centers are distributed on the margins of large basins whether they were formed inside or outside craters. The studied volcanic features are often related to compressive tectonic structures at distances ranging from 10 to 200 km. Explosive volcanic activity on a global scale seems triggered mainly in areas where minor impacts were formed near critically stressed tectonic basin structures reactivated following compression.

References: [1] Denevi, B., et al., (2018), Cambridge Planetary Science, 144-175. [2] Neukum et al., (2001), Volume 49, Issues 14–15, 1507-1521. [3] Rothery et al., (2020), Space Science Reviews, 216, 66 (2020). [4] Pegg et al., (2021), Icarus, Volume 365, 114510. [5] Jozwiak et al., (2018) Icarus Volume 302, 191-212, [6] Ferrari et al., (2021), vEGU21, id.EGU21-15987. [7] Wright et al., (2018), JGR Planets, 123, 952–971. [8] Ru Xu et al. (2022), *Remote Sens.*, *14*(17), 4164.[9] Goudge et al. , (2014), J. Geophys. Res.Planets,119, 635–658. [10] Orgel et al., (2020), Journal of Geophysical Research:Planets,125, e2019JE006212. [11] Byrne et al., (2014), *Nature Geoscience* volume 7, 301–307. [12] Mirino (2022), https://doi.org/10.21954/ou.ro.000148c5.

Acknowledgements: This work was supported by BepiColombo ASI-INAF contract no 2017- 47-H.0.

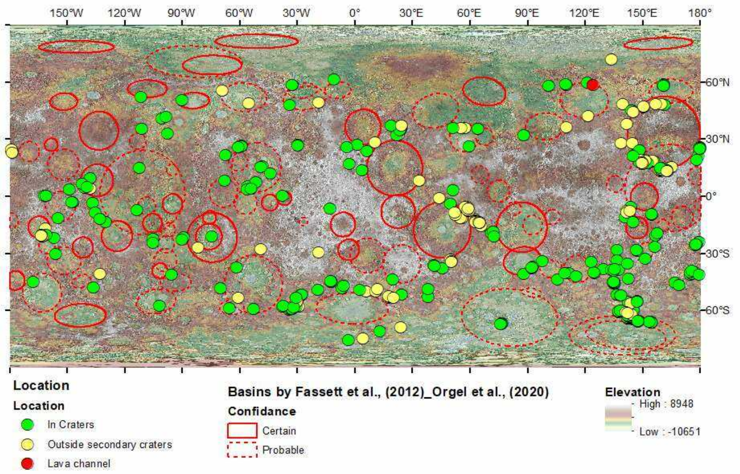

Figure 1: *Global distribution of volcanic features on Mercury indicated with the dots on the map. The features are classified based on their position within (green dots) or outside (yellow dots) of minor craters. It is clear how many of them follow the boundary of both certain and probable basins (red circles). Basemap:Global topographic DEM.*

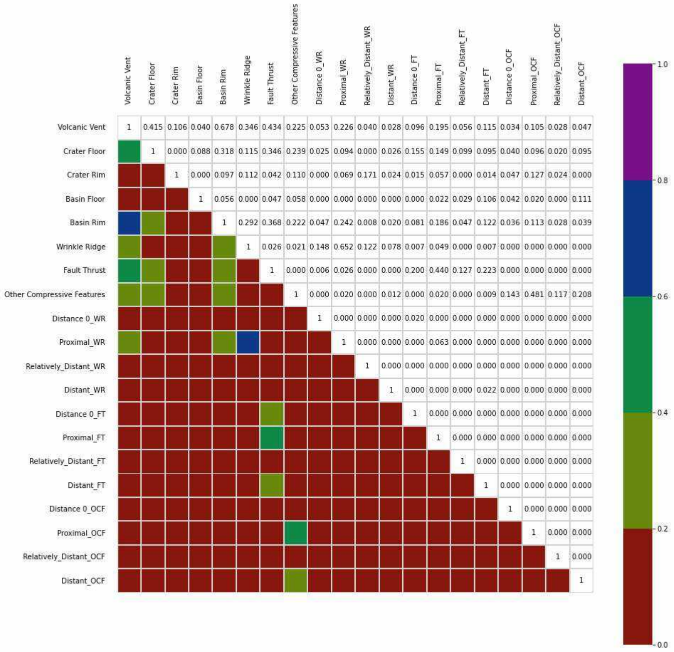

	Volcanic Vent	Crater Floor	Crater Rim	Basin Floor	Basin Rim	Wrinkle Ridge	Fault Thrust	Other Compressive Features	Distance 0_WR	Proximal_WR	Relatively_Distant_WR	Distant_WR	Distance 0_FT	Proximal_FT	Relatively_Distant_FT	Distant_FT	Distance 0_OCF	Proximal_OCF	Relatively_Distant_OCF	Distant_OCF
Volcanic Vent	1	0.415	0.106	0.040	0.678	0.346	0.434	0.225	0.053	0.226	0.040	0.028	0.096	0.195	0.056	0.115	0.034	0.105	0.028	0.047
Crater Floor		1	0.000	0.088	0.318	0.115	0.346	0.239	0.025	0.094	0.000	0.026	0.155	0.149	0.099	0.095	0.040	0.096	0.020	0.095
Crater Rim			1	0.000	0.097	0.112	0.042	0.110	0.000	0.069	0.171	0.024	0.015	0.057	0.000	0.014	0.047	0.127	0.024	0.000
Basin Floor				1	0.056	0.000	0.047	0.058	0.000	0.000	0.000	0.000	0.000	0.022	0.029	0.106	0.042	0.020	0.000	0.111
Basin Rim					1	0.292	0.368	0.222	0.047	0.242	0.008	0.020	0.081	0.186	0.047	0.122	0.036	0.113	0.028	0.039
Wrinkle Ridge						1	0.026	0.021	0.148	0.652	0.122	0.078	0.007	0.049	0.000	0.007	0.000	0.000	0.000	0.000
Fault Thrust							1	0.000	0.006	0.026	0.000	0.000	0.200	0.440	0.127	0.223	0.000	0.000	0.000	0.000
Other Compressive Features								1	0.000	0.020	0.000	0.012	0.000	0.020	0.000	0.009	0.143	0.481	0.117	0.208
Distance 0_WR									1	0.000	0.000	0.000	0.020	0.000	0.000	0.000	0.000	0.000	0.000	0.000
Proximal_WR										1	0.000	0.000	0.000	0.063	0.000	0.000	0.000	0.000	0.000	0.000
Relatively_Distant_WR											1	0.000	0.000	0.000	0.000	0.000	0.000	0.000	0.000	0.000
Distant_WR												1	0.000	0.000	0.000	0.022	0.000	0.000	0.000	0.000
Distance 0_FT													1	0.000	0.000	0.000	0.000	0.000	0.000	0.000
Proximal_FT														1	0.000	0.000	0.000	0.000	0.000	0.000
Relatively_Distant_FT															1	0.000	0.000	0.000	0.000	0.000
Distant_FT																1	0.000	0.000	0.000	0.000
Distance 0_OCF																	1	0.000	0.000	0.000
Proximal_OCF																		1	0.000	0.000
Relatively_Distant_OCF																			1	0.000
Distant_OCF																				1

Figure 2: *Correlation graph of the volcanic vents in the global database and the geological context. The scale bar indicates the correlation number which ranges from 0 (no correlated values) to 1 (perfect correlation). For natural phenomena is hard to find a perfect correlation. For the number of samples we used values from 0.4 and above already indicate a likely correlation between the two considered parameters.*

INSIGHTS INTO MERCURY'S TECTONIC HISTORY: A STRUCTURAL ANALYSIS OF THE DISCOVERY QUADRANGLE

A. Sepe[1,2], L. Ferranti[2,1], V. Galluzzi[1], G.W. Schmidt[1], and P. Palumbo[3,1]
[1]INAF, Istituto di Astrofisica e Planetologia Spaziali (IAPS), Rome, Italy (antonio.sepe@inaf.it)
[2]Dipartimento di Scienze della Terra, dell'Ambiente e delle Risorse, Università degli Studi di Napoli "Federico II", Naples, Italy
[3]Dipartimento di Scienze e Tecnologie, Università degli Studi di Napoli "Parthenope", Naples, Italy

Introduction: Mercury's Discovery quadrangle (H–11) is located at the southern mid-latitudes (22.5°S−65°S and 270°E−360°E) in a heavily cratered region roughly antipodal to the Caloris Basin [1]. It is named after the NE–SW trending Discovery Rupes, one of the longest and highest lobate scarps on the planet (600 km in length and 2 km high). The quadrangle also hosts a probable multi-ring impact basin, informally named Andal–Coleridge [2] or Bramante–Schubert [3], surrounded by a three- to five-ring system.

Here we present an updated high-resolution structural map of the quadrangle that will contribute to the 1:3M quadrangle geological map series in preparation for the BepiColombo mission [4]. In addition, we carried out a structural analysis in order to study the structural framework of the quadrangle and define the multi-ring geometry of the Andal−Coleridge or Bramante−Schubert basin.

Data and methods: We produced a high-resolution structural map of the quadrangle utilizing MESSENGER/MDIS imagery coupled with the digital elevation model (DEM) provided by [5]. Structure azimuths were then plotted in rose diagrams to recognize preferential trends at the regional scale. We also investigated the structural relationships among three main scarps (Discovery, Adventure and Resolution Rupes – DAR), extending over an arc exceeding 1000 km [3], by making several profiles across the scarps and measuring their height (a proxy for the throw). Furthermore, to validate and ascertain the presence of the Andal–Coleridge or Bramante–Schubert basin, we employed gravimetric data and estimated its center via beta-analysis.

Map and trend of structural features: The structural map reveals approximately 500 segments of contractional structures. These structures, including lobate scarps, high-relief ridges and wrinkle ridges, exhibit a circular arrangement at the approximate center of the quadrangle, showing two NW−SE and NE−SW-trending linear systems. The rose diagrams show a general girdle distribution with a NW−SE preferential trend and two less prominent ~N−S and NE−SW trends. Most of these structures encircle a high-density mass concentration (mascon) identified in the Bouguer Anomaly map provided by [6] that roughly coincides with a broad topographic low approximately centered in Schubert crater (43°S, 54°W).

Analysis of the DAR system: For each profile the scarp height (H) was measured and then plotted against its position on the fault trace, corresponding to the fault length (L).

From the analysis of the scarp height, we discerned that the three structures represent segments of two different scarps, the Discovery Rupes and the Adventure−Resolution Rupes. They appear to be kinematically soft-linked, since the cumulative throw falls approximately in the center of the system, consistent with terrestrial fault growth patterns [7].

Mascons as buried basin detectors: The Andal−Coleridge or Bramante−Schubert is a probable multi-ring impact basin proposed in earlier studies due to the roughly circular pattern and strongly arcuate trend of the structures [2][3].

Multiple studies [8–10] have emphasized that the basin-forming impacts would leave distinctive traces in gravity anomaly maps (Free Air or Bouguer), manifesting as large-scale high-density mass concentrations (mascons) characterized by a large central positive gravity anomaly surrounded by minor and/or negative anomalies. The impact event thinned the crust causing the upwelling of mantle plugs, which provided favorable conditions for subsequent volcanism.

In the Bouguer Anomaly map of [7] several mascons are distinctly visible, associated with well-known impact basins such as Caloris, Rachmaninoff, and Raditladi. A specific mascon is present in the area of the Andal–Coleridge or Bramante–Schubert basin, indicating a shallower hermean 'moho', and hence an upwelled mantle plug.

Basin's center estimation: Following the work done for Mercury and Mars by [3] and [11], we estimated the stress field related to the concentric structures via beta-analysis by defining the planes normal to the structures on a Schmidt net and contouring their intersections applying the 1% area method. This approach revealed a roughly bimodal distribution consisting of a primary "bull's-eye" distribution, whose center represents the point from which the causative stress field for faults spread, and thus also corresponds to the geometric center of the basin. A secondary, much less dense, distribution, is also present. The Discovery Rupes aligns concentrically with the primary distribution, while the Adventure−Resolution Rupes exhibits concentric alignment with the secondary distribution. This similarly is roughly coincident with another smaller mascon found in the Rabelais crater area (60°S, 62°W), where another probable impact basin, informally named b78, is hypothesized.

Multi-ring structure of the Andal−Coleridge or Bramante−Schubert basin: The compelling evidence from the roughly circular pattern and strongly arcuate trend of the mapped structures, combined with the presence of a mascon, reinforces the likelihood of the Andal−Coleridge or Bramante−Schubert basin. We proceeded to define the possible multi-ring structure of the basin guided by two key assumptions: 1) since the Discovery Rupes is the highest and longest scarp in the quadrangle, we considered it as part of the so-called "Topographic Rim" that is the morphologically most prominent ring and the one that occurs most frequently; 2) all rings must fit at least two structures to ensure their representativeness. Since there are three potential centers, which are the center of the topographic depression (41.3°S, 53.5°W), the center of the mascon (39.4°S, 55.5°W), and the center of the "bull's eye" distribution (45°S, 54.3°W), we propose three different geometries, one for each point. So, the Andal−Coleridge or Bramante−Schubert could be a multi-ring impact basin surrounded by a four- to five-ring system.

Conclusions and future work: The present work reveals a complex structural framework within Mercury’s Discovery quadrangle. The concentric alignment of structures to both a topographic low and a mascon serves as compelling evidence, further supporting the existence of the Andal–Coleridge or Bramante−Schubert basin. This suggests that the mapped structures may represent the morphological evidence of at least four rings encircling the basin. The concentricity of the Discovery Rupes to the primary distribution identified through beta-analysis reinforces its connection to the basin. In contrast, the Adventure–Resolution Rupes displays concentric alignment with the smaller and likely older b78 impact basin. This observation implies that these two scarps originated from two distinct local-scale processes, i.e., impacts, and were reactivated by Mercury's global contraction as a linked fault system.

The lack of N−S trending structures typical of Mercury’s southern mid-latitudes [12] coupled with the concentric pattern observed, may be attributed to the presence of the Andal−Coleridge or Bramante−Schubert multi-ring basin. This basin likely introduced mechanical discontinuities in the crust, influencing the localization and orientation of thrusts. These thrusts, in turn, represented preferential weak zones along which the global contraction of the planet acted.

We aim at improving the structural map of the quadrangle and investigating the fault reactivation and deformative evolution of the basin in further detail.

Acknowledgements: We gratefully acknowledge funding from the Italian Space Agency (ASI) under ASI-INAF agreement 2017-47-H1.

References: [1] Trask and Dzurisin (1984). USGS, IMAP 1658. [2] Spudis and Strobell (1984). Lunar and Planetary Science Conference, 814-815. [3] Watters et al. (2001). *Planetary and Space Science*, 49(14-15), 1523-1530. [4] Galluzzi et al. (2019). *Journal of Geophysical Research: Planets*, 124(10), 2543-2562. [5] Becker et al. (2016). *47th Annual Lunar and Planetary Science Conference*, p. 2959. [6] Buoninfante et al. (2023). *Scientific Reports*, 13, 19854. [7] Kim and Sanderson (2005). *Earth-Science Reviews*, 68(3-4), 317-334. [8] Muller and Sjogren (1968). *Science*, 161 680 684. [9] Wise and Yates (1970). *Journal of Geophysical Research*, 75(2), 261 268. [10] Zhao et al. (2023). *Space: Science & Technology*, 3:0076. [11] Wise et al. (1979). *Icarus*, 38, 456-472. [12] Byrne et al. (2014). *Nature Geoscience*, 7, 301–307.

PERTURBATIVE ANALYSIS OF THE MORE GEODESY EXPERIMENT DURING BEPICOLOMBO'S ORBITAL PHASE.

A. Zurria[1], P. Cappuccio[1], I. di Stefano[1], U. De Filippis[1], L. Iess[1]
[1] Department of Mechanical and Aerospace Engineering (DIMA), Sapienza University of Rome, Italy
First author email: ariele.zurria@uniroma1.it

Introduction: The BepiColombo mission, designed by ESA/JAXA, was launched in October 2018 and is currently in the cruise phase towards Mercury [1]. The Mercury Orbiter Radio-science Experiment (MORE), one of the scientific investigations of the mission, will exploit a multi-frequency microwave tracking system with an advanced Ka-band transponder to fulfill scientific goals in Mercury's geodesy and fundamental physics [2,3]. In particular, the precise measurements enabled by the state-of-the-art radio tracking system will allow us to estimate the gravity field and rotational state of Mercury, and to perform tests of general relativity through an accurate analysis of the spacecraft orbital motion. In this work we assess the performance of the geodesy investigation addressed by MORE, focusing on the orbital phase, starting in early 2026. We carry out numerical simulations which consist of generating synthetic radio observables and estimating the parameters of interest through a precise orbit determination process. The novelty of this work lies in the inclusion of different sources of mismodelling to reproduce a perturbed dynamical state of the probe. The goal is to assess whether or not these errors introduce biases in the solution. We include errors in the thermo-optical coefficients of the spacecraft, wheel off-loading maneuvers with unbalanced ΔVs, periodic accelerations of unknown magnitude and random fluctuations of solar irradiance, which cannot be modelled or measured by the onboard accelerometer ISA (Italian Spring Accelerometer). In this paper we first provide an overview of the geodesy experiment. Then, we explain the methodology adopted in the numerical simulations. Finally, we report the results based on the latest mission scenario, which foresees a two-year orbital phase starting in 2026. Our results show that the MORE investigation is not affected by the considered mismodelling effects. We show that MORE shall fulfill its scientific goals with an enhanced level of accuracy compared to past missions, improving our knowledge of Mercury's interior.

Geodesy experiment: MORE aims to conduct accurate measurements of Hermean gravity to enhance our understanding of Mercury's interior structure. The onboard radiotracking system enables a precise analysis of the spacecraft's orbital motion, allowing for the retrieval of the static and time-varying gravity field of Mercury. The geodesy and geophysics experiment of MORE mainly focuses on the following areas [3]: the determination of the static gravity field to maximum degree and order ~40; the estimation of the Love number k_2 to investigate tidal variations in the gravity field; the characterization of Mercury's rotational state (pole direction and librations in longitude)

Methodology: The methodology consists of a precise orbit determination (OD) process, implemented through the JPL's MONTE OD code. In this process, the radio observables measured at the ground stations are compared with predictions. The latter are computed by propagating the orbital motion of the spacecraft starting from a reference dynamical model. The result of this comparison is a vector of observation residuals (actual observables minus computed observables). A cost function, defined upon this vector, is minimized by iteratively correcting the spacecraft state and other solved-for parameters in a least-squares fit. A covariance matrix is then extracted to provide the uncertainties of the estimated parameters.

The procedure described above can be decomposed in 2 main steps. The first step is the simulation phase, which produces simulated range and Doppler observables measured at the ground stations, perturbed by a white Gaussian noise. The second step is the estimation process (the least-squares fit), which corrects the solved-for parameters to minimize the discrepancy between the measured and predicted observables.

We process the entire two-years orbital phase, starting in early 2026, with observables in Ka-band from Malargüe station, in Argentina. The Doppler accuracy is 0.017 mm/s and the range accuracy is 1 cm both at 60 seconds integration time [4]. For the gravity field of Mercury we use the MESSENGER field HgM008 [5]. Regarding non-gravitational accelerations, we include solar radiation pressure and a daily wheel off-loading maneuver during the Malargüe pass. In the estimation phase we use a perturbed dynamical model with respect to model used to generate the simulated observables. We add a 20 % relative error in the thermo-optical coefficients of the solar arrays and in the bus panels area, random fluctuations of solar irradiance, daily unbalanced ΔVs with random components due to wheel off-loading maneuvers.

Results: Figure 1 shows the accuracy in the global gravity field solution, together with the corrections to the reference field. As can be seen all the corrections are inside the formal uncertainty, thus, the gravity experiment is not biased by the errors introduced in the dynamical model. Figure 2 shows the degree strength mapped on the surface of Mercury, which indicates the maximum degree of the spherical harmonics expansion of the gravity field that MORE is able to estimate at a particular location. The conversion factor between the degree l of the expansion and the spatial resolution is $\sim\pi R/l$, where R is the reference radius of Mercury ($2440\ km$). As can be seen, MORE is able to estimate up to degree and order ~40 (< 200 km of spatial resolution) in the southern hemisphere without any a priori constraint from previous models. The higher sensitivity in the southern hemisphere is due to drift of the periherm, which reaches low altitudes (~230 km) in those areas during the last months of the mission. This results in a complementary coverage of the planet compared to MESSENGER mission [5].

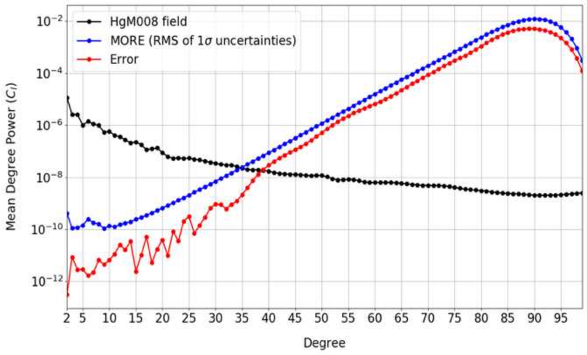

Figure 1. Gravity field power per degree. The black line is the reference field. The blue line is the RMS of the uncertainty in the gravity field coefficients. The red line is the RMS of the errors.

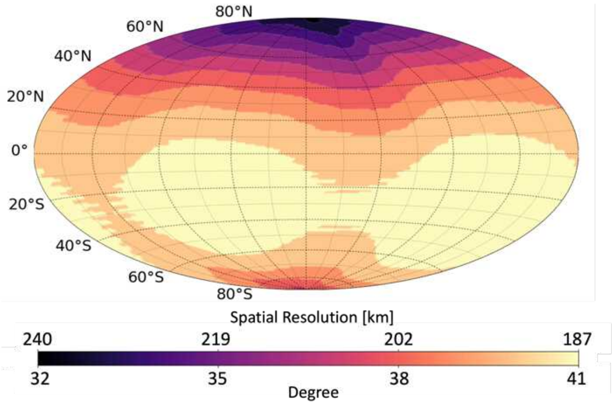

Figure 2. Mercury degree strength and spatial resolution map.

Table 1 compares the estimates of the tidal Love number k_2 and rotational parameters provided by MORE with the MESSENGER solution HgM008. These estimates show improvements by a factor of ~10, allowing an improved characterization of the planet.

Parameter	**Formal uncertainty (HgM008)**	**Formal uncertainty (MORE)**
k_2	**8.3e-03**	**3.7e-04**
Pole RA α [deg]	**3.0e-04**	**3.6e-05**
Pole DEC δ [deg]	**1.0e-04**	**2.8e-05**
Libration amplitude [arcsec]	**2.7**	**0.19**
Obliquity [arcmin]	**9.0e-03**	**1.4e-03**
Moment of Inertia Factor	**1.6e-03**	**2.4e-04**

Table 1. Uncertainties in the tidal and rotational parameters.

Conclusions: In this work we analyse the performance of the geodesy experiment onboard the BepiColombo mission, taking into account different source of errors in the OD process. Results show that the OD filter is able to compensate the mismodelling errors without introducing any bias in the solution (the corrections to the reference values are inside the formal uncertainties). We report the updated expected accuracy of the gravity and rotation experiment for the complete two-years orbital phase. MORE can estimate Mercury gravity field up to degree and order ~40 (spatial resolution better than 200 km) without any a priori constraint from previous models. The estimation of the Love number k_2 can be improved at the level of $3.7\cdot10^{-4}$, allowing to set tighter constraints to the interior structure of Mercury. The estimation of the pole's right ascension and declination can be improved at the level of a few parts in 10^{-5} deg. The amplitude of Mercury's physical librations in longitude can be determined with an accuracy of ~2 m at the equator. Mercury's obliquity can be retrieved with an accuracy of $\sim1.4\cdot10^{-3}$ arcmin, improving the determination of the dimensionless moment of inertia.

References:

[1] Benkhoff et al. (2021), Space Sci Rev 217, 90, https://doi.org/10.1007/s11214-021-00861-4
[2] Iess et al. (2021), Space Sci Rev 217, 21, https://doi.org/10.1007/s11214-021-00800-3
[3] Genova et al. (2021), Space Sci Rev 217, 31, https://doi.org/10.1007/s11214-021-00808-9
[4] Cappuccio et al. (2020), IEEE Transactions on Aerospace and Electronic Systems, vol. 56, no. 6, pp. 4984-4988, DOI: 10.1109/TAES.2020.3008577
[5] Genova et al. (2019), Geophysical Research Letters, doi:10.1029/2018GL08113

SEASONAL VARIATION OF CA AND CA-BEARING MOLECULES IN MERCURY'S EXOSPHERE AS PRODUCT OF MICRO-METEOROIDS AND COMET STREAM PARTICLES IMPACT.

M. Moroni[1], A. Milillo[1], A. Mura[1] , C. Plainaki[2-1], V. Mangano[1], A. Aronica[1], E. De Angelis[1], D. Del Moro[3], P.P. Di Bartolomeo[1], A. Kazakov[1], S. Massetti[1], S. Orsini[1], R. Rispoli[1], R. Sordini[1], M. Stumpo[1]. [1]Istituto Nazionale di Astrofisica – Istituto di Astrofisica e Planetologia Spaziali (INAF – IAPS), Rome, Italy; martina.moroni@inaf.it [2]Agenzia Spaziale Italiana (ASI), Rome, Italy, [3]Department of Physics, University of Rome Tor Vergata, Italy

Introduction

The NASA/MESSENGER (MErcury Surface, Space ENvironment, GEochemistry, and Ranging) mission provided measurements of Mercury's Ca exosphere, allowing the study of its configuration and its seasonal variations. The observed Ca exhibited very high energies, with a scale height consistent with a temperature > 50,000 K, originated mainly on the dawn-side of the planet [1, 2]. It was suggested that the originating process is due to MMIV (Micro-Meteoroids Impact Vaporization), but previous estimations were not able to justify the observed intensity and energy. The most likely origin of this exospheric element may be a combination of different processes involving the release of atomic and molecular surface particles [4, 5].

Methods

In this work we use the exospheric Monte Carlo model by *Mura et al. (2007)* [6] to simulate the 3-D spatial distribution of the Ca-bearing molecule and atomic Ca exospheres generated through the MMIV process. We investigate the possible pathways to produce the high energy observed in the Ca exosphere and discuss about the generating mechanism. Following previous studies [4, 7] we consider that the atomic Ca in Mercury's exosphere may be produced in a sequence of different processes: the exospheric energetic Ca component derives from the shock-induced non-equilibrium dissociative ionization and neutralization of Ca+ during the vapor cloud expansion, while a low energy Ca component is generated later by the photo-dissociation of the CaO molecules released by micro-meteoroid impact vaporization. Since exact temperature, photolysis lifetimes of the produced molecules and excess energy during different photolysis processes are still not well constrained by observations, we investigate different model assumptions. We simulated total Ca distribution in terms of atoms in the exosphere at different TAAs (angle between perihelium and the planet as seen from the Sun) to reproduce the exospheric variability along the planet orbit and compared the results with the MESSENGER/MASCS observations (Fig. 1).

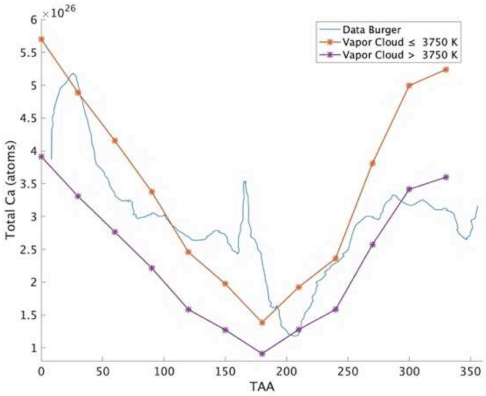

Figure 1: Comparison between the simulations results obtained in the approximation of temperature vapor cloud ≤ 3750 K (red line) and at higher temperatures (purple line) with the observations (blue line, [2]) along the orbit and, hence, TAA

The total Ca content obtained through a best fit to the observations shows excess emission near TAA ~ 25° and TAA ~ 150° that was attributed to the vaporization of surface material induced by the impact of a meteor stream. We investigate the possible contribution due to the crossing of the comet 2P/Encke for explaining the excess Ca emission at that specific orbit positions (Fig.2) [3].

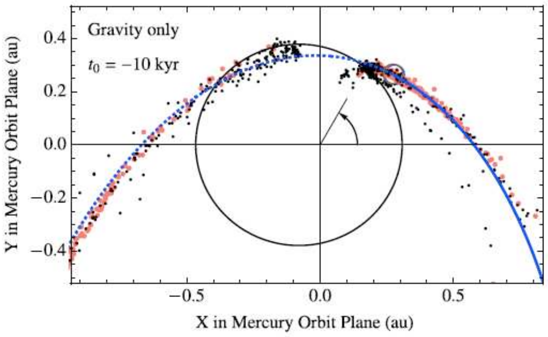

Figure 2. Projection of the comet Encke orbit (blue line) that crosses the Mercury's orbit (black line) [3]

Results

The theoretical calculations agree better with observations at shorter photolysis lifetimes and higher excess energy of Ca atoms obtained during photolysis of Ca-bearing species. In that case we can emphasize the presence of two different Ca components where the energetic Ca component is more intense

than the other at high altitudes, but in the post-dawn low altitudes we can see a substantial contribution of the low energy component to the global Ca exospheric content.
Futhermore, the simulated excess emission along Mercury orbit due to the comet contribution is underestimated compared to the observations at TAA equal to 25° and 150°.
Since the MMIV contribution in refilling the exosphere is strongly dependent on the impact velocity, the total stream mass influx and also the arrival geometry of the meteoroids on planetary surface, these model parameters require further investigation to be consistent with the data.

Conclusions
The results presented in this work can be useful in the exospheric studies and in the interpretation of active surface release processes, as well as in the exosphere observations planning for the ESA-JAXA BepiColombo mission that will start its nominal mission phase in 2026. More specifically, the resulting molecular distributions will be compared to the measurements of the SERENA-STROFIO mass spectrometer that will be the only instrument able to identify the molecular components.

References:

[1] Burger, M.H. et al., “Modeling MESSENGER observations of calcium in Mercury’s exosphere”, J. Geophys. Res. 117, E00L11, (2012)

[2] Burger, M.H. et al., “Seasonal variations in Mercury’s dayside calcium exosphere”, Icarus 238 (2014) 51–58 , (2014)

[3] Christou, A. A., Killen, R. M., & Burger, M. H., 2015, The meteoroid stream of comet Encke at Mercury: Implications for MErcury Surface, Space ENvironment, GEochemistry, and Ranging observations of the exosphere, Geophysical Research Letters, 42(18), 7311-7318

[4] Killen, R. M., 2016, Pathways for energization of Ca in Mercury’s exosphere, Icarus, 268, 32–36

[5] Moroni, M., Mura, A., Milillo, A., Plainaki, C., et al. , 2023, Micro-meteoroids impact vaporization as source for Ca and CaO exosphere along Mercury’s orbit, Icarus, 401, 115616

[6] Mura, A., P. Wurz, H. I. M. Lichtenegger, H. Schleicher, H. Lammer, D. Delcourt, A. Milillo, S. Orsini, S. Massetti, and M. L. Khodachenko, “The sodium exosphere of Mercury: Comparison between observations during Mercury’s transit and model results”,Icarus,200(1),1–11, (2009)

[7] Plainaki C., A. Mura, A. Milillo, S. Orsini, S. Livi, V. Mangano, S. Massetti, R. Rispoli, E. De Angelis, “Investigation of the possible effects of comet Encke’s meteoroid stream on the Ca exosphere of Mercury”, J. Geophys. Res., Planets 122, 1217–1226 (2017)

Tematica:
Pianeti e Satelliti: Analisi dati, Analisi di superfici, atmosfere, esosfere, modellistica

SPECTRAL ANALYSIS OF MARE INGENII BASIN (LUNAR FARSIDE).

Giulia Salari[1], Gloria Tognon[2], Francesca Zambon[1], Cristian Carli[1], Federico Tosi[1], Lorenza Giacomini[1], Jean-Philippe Combe[3], Riccardo Pozzobon[4], Sergio Fonte[1], Matteo Massironi[4,2], Giovanna Rinaldi[1].

[1]Istituto Nazionale di Astrofisica – Istituto di Astrofisica e Planetologia Spaziali (INAF-IAPS), Rome, Italy, giulia.salari@inaf.it, [2]Centro di Ateneo di Studi e Attività Spaziali (CISAS), Università degli Studi di Padova, Padova, Italy, [3]Planetary Science Institute (PSI), Tucson, AZ, USA, [4]Dipartimento di Geoscienze, Università degli Studi di Padova, Padova, Italy.

Introduction: The Ingenii basin is a Pre-Nectarian (i.e. >3.9 Ga; [1]) impact structure situated in the NW border of the South Pole Aitken (SPA) basin, the largest and the deepest impact basin on the Moon and in our Solar System [2]. Ingenii basin is ~315 km in diameter and it encompasses one of the few basaltic maria occurring on the lunar farside. Indeed, Mare Ingenii, which only partially fills the floor of the basin, was likely generated by the impact of two younger craters, Thomson and Thomson M (~120 km and ~100 km in diameter, respectively), lying on the SE portion of the basin.

One of most relevant discoveries regarding Mare Ingenii is its prominent swirl, a high-albedo surface feature whose occurrence seems to be limited to the lunar surface. Its origin is still debated [3], but these twisted morphologies are thought to be likely correlated to crustal magnetic anomalies [3, 4, 5]. Another important feature of the investigated area is a ~130 m diameter irregularly shaped pit likely leading to a cavity which might represent a natural shelter against the space environment, then offering potential locations for future lunar settlements.

A better understanding of the swirl region and its formation mechanisms can be useful to reveal information about the magnetic history of the Moon. Moreover, an in-depth investigation of the mare deposits within the SPA basin could help provide valuable insights about the lunar mantle and crustal compositions.

In this work, we present a spectral analysis of Mare Ingenii. A morpho-stratigraphic map was produced in support of our investigation for better characterizing the geology of Ingenii basin [6]. We then used hyperspectral data to perform a spectral characterization of the mare with the aim to infer its mineralogical composition and provide a valuable resource for improving the knowledge of the evolution of the Moon.

Data and methods: The morpho-stratigraphic map was produced by identifying different units based on their morphology and their relative stratigraphic position within the Ingenii basin. We used data from the Lunar Reconnaissance Orbiter Camera Wide Angle Camera [7], from Lunar Orbiter Laser Altimeter and from Kaguya Terrain Camera merged Digital Elevation Model, [8]. We also considered the Clementine Ultraviolet-Visible Color Ratio mosaic (red: 750/415 nm; green: 750/1000 nm; blue: 415/750 nm) [9], which provided a preliminary spectroscopical discrimination of the different basin materials.

We processed spectral parameters derived from calibrated and photometrically corrected hyperspectral data, acquired in the visible to near-infrared spectral range by the Moon Mineralogy Mapper (M^3) onboard Chandrayaan-1 [10]. We identified 28 Regions Of Interest (ROIs) based on spectral variability and surface morphological elements and grouped them as dark material (basaltic low reflectance smooth plains), swirl material (showing sinuous and heterogeneous aspect with intermediate reflectance values), intermediate regions (showing intermediate albedo values, likely indicating heterogeneous material) and bright material (small young craters). We then derived a set of spectral indices considering the reflectance at 580 nm, the absorption band centers and band depths at 1 and 2 micron (BCI and BCII), the absorption band area ratio (BAR), the global spectral slope and FeO and TiO_2 abundances, with the purpose of investigating the mineralogical variation across Mare Ingenii [6].

Results and discussion:

The morpho-stratigraphic map integrated with multispectral color information highlighted different units in the studied area, which suggest an heterogeneity in the deposits characterizing the Ingenii basin. The dataset acquired by M^3 also reveals a substantial spectral variability, with near-infrared spectra of the investigated ROIs which are mostly characterized by two strong absorption bands centered at 1 and 2 μm (Figure 1), indicating the occurrence of pyroxenes. A general increase in the band center wavelengths is observed from intermediate areas (BCI=0.94-0.96 μm and BCII=1.98-2.01 μm) and swirl regions (BCI=0.96-0.98 μm and BCII=2.07-2.11 μm) to dark mare deposits (BCI=0.96-0.99 μm and BCII=2.03-2.12 μm), suggesting a widespread occurrence of Ca-rich pyroxenes throughout the area (Figure 2). On the other hand, bright material shows absorption band center positions shifted towards shorter wavelengths, more akin to low-Ca or Ca-free pyroxenes (i.e. BCI=0.91-0.94 μm and BCII=1.91-2.04 μm; Figure 2). The BAR spectral parameter, which in general is used to identify olivine on planetary surfaces, indicates that olivine is not consistently abundant in Mare Ingenii area. Yet, a broad range of higher values for the bright material of the small craters suggests a variation in the mineral composition or in the grain size or in the space weathering processes. Indeed, these isolated small craters are located in the outer margin of the SPA basin, which is mainly constituted of ejecta and degraded rim deposits. The SPA basin is spectrally characterized by a widespread mafic component [11, 12, 13], chiefly ascribed to pyroxene occurrence. FeO and TiO_2 abundances of the investigated ROIs support the hypothesis of an overall iron-rich signature throughout the studied area, probably representative of the composition of the deeper section of the lunar crust [13, 14, 15].

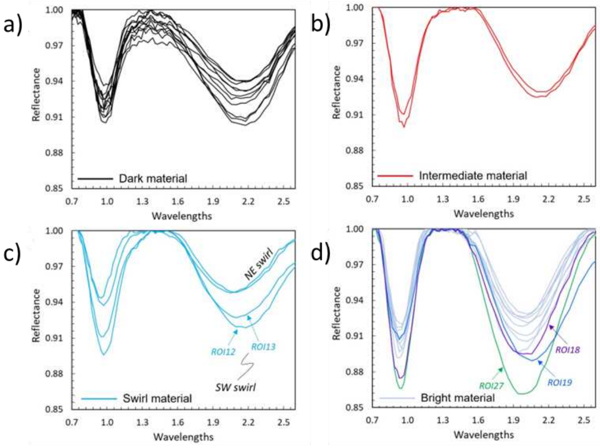

Fig. 1: Continuum-removed spectra of investigated ROIs: a) dark material; b) intermediate regions; c) swirl region and d) bright material. [6]

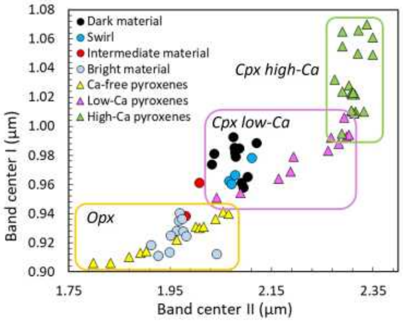

Fig. 2: Absorption band center 1 µm vs absorption band center 2 µm of the investigated ROIs within Mare Ingenii basin. Band centers of Ca-free and Ca-bearing pyroxenes (Klima et al., 2007; 2011) have been plotted for a comparison. [6]

Conclusions: Mare Ingenii reveals a mineralogical variability, mainly dominated by strong pyroxene absorptions. Dark material from Thomson craters' floor indicate compositions close to high-Ca pyroxenes (as well as swirl regions and intermediate albedo areas). The bright material from small craters instead resemble spectral properties of low-Ca or Ca-free pyroxenes, also showing lower FeO and TiO_2 abundances. Moreover, the BAR spectral parameter indicates that olivine is not abundant in the investigated area.

The Ingenii basin is located within the outer border of the South Pole-Aitken basin which is characterized by exposure of iron-rich material. M^3 data suggest a strong contribution of the mafic component in the basin, with dominant pyroxene minerals. These spectral characteristics suggest that Mare Ingenii likely represents mare deposits encompassed in a regional setting of the deeper lunar primordial crust.

Acknowledgements: We acknowledge support from the PRIN INAF (RIC) 2019 project: "MELODY: Moon multisEnsor and LabOratory Data analYsis", selected by the Scientific Directorate of Italy's National Institute for Astrophysics (INAF) on 10 November 2020 and funded with 167,162 euros (INAF grant 1.05.01.85.17).

References: [1] Wilhelms D. (1987). *USGS Prof. Pap*., 1348. [2] Spudis P. D. et al., (1994). *Science*, 266, 1848-1851. [3] Hood L L (2001). *JGR Planets*, 106, 27825-27839. [4] Pinet P. C. (2000). *JGR Planets,* 105, 9457-9475. [5] Garrick-Bethell I. (2011). *Icarus*, 212, 408-492. [6] Salari G. (2023). *JGR Planets*, in press. [7] Robinson M. S. (2010). *Space Sci. Rev*., 150, 81-124. [8] Barker M. K. (2016). *Icarus*, 273, 346-355. [9] Lucey P. G. (2000). *JGR*, 105, 20377-20386. [10] Pieters C. M. (2009). *Current Science*, 96, 500-505. [11] Jolliff B. L. (2000). *JGR Planets,* 105, 4197-4216. [12] Lemelin M. (2019). *Planet. Space Sci*., 165, 230-243. [13] Yamamoto S. (2023). *JGR Planets, 128, e2023JE007817.* [14] Pieters C. M. (1986). *Rev. Geophys*, 24, 557-578. [15] Anbazhagan S. (2021). *Icarus*, 366, 114511.

THE JOINT NASA-ESA VENUS SCIENCE COORDINATION (VESCOOR) GROUP

L. Marinangeli[1], P.J. McGovern[2], G. Alemanno[3], Y. Futaana[4], J.A. Holmes[5], I. López Ruiz-Labranderas[6], A. Piccialli[7], T. Bocanegra-Bahamon[8], L. W. Esposito[9], T. Gregg[10], J.G. O-Rourke[11], J. Rabinovitch[12], J. Garvin[13], J. Helbert[3], S. Smrekar[8], J.Y. Lee[13], T. Widemann[14], L. Hays[15], M. Schulte[15], A.G. Straume-Lindner[16], R. de Paula[15], L. Colangeli[16], [1]Universita G. d'Annunzio, Italy, lucia.marinangeli@unich.it, [2]Lunar Planetary Institute USRA, USA McGovern@lpi.usra.edu, [3]Institute of Planetary Research (DLR), Germany, [4]Swedish Institute of Space Physics, Sweden, [5]The Open University, United Kingdom, [6]Universidad Rey Juan Carlos, Spain, [7]Royal Belgian Institute for Space Aeronomy (BIRA-IASB), Belgium, [8]NASA Jet Propulsion Laboratory, USA, [9]Laboratory of Atmospheric & Space Physics (LAPS), University of Colorado, USA, [10]University of Buffalo, USA, [11]Arizona State University, Tempe, USA, [12]Stevens Institute of Technology, USA, [13]Institute for Basic Science, South Korea, [15] LESIA/Observatoire de Paris/PSL & U.Versailles-St-Quentin/Paris-Saclay, [15]NASA HQ, [16]ESA.

Introduction: With the three new Venus missions (ESA's EnVision and NASA's VERITAS and DAVINCI) planned to observe Venus in the next 10-15 years, ESA and NASA established a joint Venus Science Coordination group (VeSCoor) [1]. VeSCoor is intended as a forum for dialogue within the broader Venus scientific community, in support of the upcoming ESA and NASA missions to Venus.

The NASA VERITAS mission will study the surface and interior with a radar and infrared instrument that provide global topography, imaging, rock type, and targeted surface deformation, plus radio science for interior structure [2].

The NASA DAVINCI mission is a descent probe mission to determine the composition and history of Venus' atmosphere as well as make additional measurements of the planet's surface and atmosphere. DAVINCI consists of a spacecraft hosting a carrier and a descent probe, hosting seven in-situ, imager and spectrometer instruments [3].

EnVision, an ESA orbital mission in collaboration with NASA, will be the first mission to simultaneously investigate Venus' history, activity and climate, from its inner core, to its surface, and further up to its upper atmosphere. EnVision's science payload consists of five instruments (radar, spectrometers, sounding radar and radio science experiment) [4].

These missions will offer an unprecedented complementary view of Venus and determine fundamental characteristics of the planet and its long term evolution [5, 6].

In this scenario, the VeSCoor's primary goals are to identify new, unanticipated scientific approaches and outcomes based on synergies among the missions to Venus and suggest studies to enhance overall scientific return.

It is worthwhile to emphasize that VeSCoor will not evaluate or propose changes to the current mission profiles, scientific objectives, or requirements.

The group kick-off occurred last July and consists of 12 members, 6 selected by ESA and 6 by NASA from the scientific community, plus 3 representatives of the EnVision, VERITAS and DAVINCI missions [2]. VesCoor's membership is initially set for 2 years, but may be renewed at the discretion of NASA and ESA. The detailed info of the members can be found in Table 1 and in the web page [7]. Representatives of the NASA and ESA agencies are also involved as observers to provide support to the group's activities. Furthermore, a scientist from South Korea has been added as an 'observer' due to the on-going discussion on future collaboration for the exploration of Venus.

VeSCoor members' expertises cover different scientific disciplines to provide a comprehensive view of Venus as a planet, and hence, as a complex system. We will evaluate the involvement of experts in fields not covered by the group.

An artist's impression of a volcanic eruption on Venus. Credits: ESA/AOES Medialab

Tasks and Activities: VeSCoor is currently undertaking the task of developing a Rules of the Road (RoR) document, to be approved by ESA and NASA, which is required to establish the *modus operandi* for the group.

We plan a meeting next spring in USA which will be dedicated to start the discussion on scientific complementarity between the future Venus missions.

A second meeting is planned in the fall in Europe, likely in one of ESA's establishments.

Outcomes will be released publicly in the form of presentations and papers with coordination from ESA and NASA.

ESA selected members:

- Lucia Marinangeli (**co-chair**), Universita G. d'Annunzio, Italy
- Giulia Alemanno, Institute of Planetary Research (DLR), Germany
- Yoshifumi Futaana, Swedish Institute of Space Physics, Sweden
- James Holmes, School of Physical Sciences, The Open University, United Kingdom
- Iván López Ruiz-Labranderas, Universidad Rey Juan Carlos, Spain
- Dr. Arianna Piccialli, Royal Belgian Institute for Space Aeronomy (BIRA-IASB), Belgium

NASA selected members:

- Patrick J. Mc Govern (**co-chair**), Lunar Planetary Inst. USRA, USA
- Tatiana Bocanegra-Bahamon, Jet Propulsion Laboratory, USA
- Larry W. Esposito, Laboratory of Atmospheric & Space Physics (LAPS), University of Colorado, USA
- Tracy Gregg, University of Buffalo, USA
- Joseph G. O-Rourke, Arizona State University, Tempe, USA
- Jason Rabinovitch, Stevens Institute of Technology, USA

Mission representatives:

- Jim Garvin (DAVINCI), NASA Goddard Space Flight Center, USA
- Joern Helbert (EnVision), Inst. of Planetary Research (DLR), Germany (to be replaced by Thomas Widemann, Obs. de Paris, France)
- Sue Smrekar (VERITAS), NASA Jet Propulsion Laboratory, USA

NASA and ESA observers:

- Lindsay Hays (NASA HQ, DAVINCI Program Scientist)
- Mitch Schulte (NASA HQ, EnVision and VERITAS Program Scientist)
- Anne Grete Straume-Lindner (ESA, EnVision Project Scientist)
- Ramon de Paula (NASA HQ, EnVision Program Executive)
- Luigi Colangeli (Coordination Office of the ESA Science Programme)

Other observers:

- Yeon Joo Lee, Institute for Basic Science, Korea

Table 1. List of VeSCoor members

References: [1] NASA-ESA Venus Science Coordination (VeSCoor) – Terms of Reference 2022, [2] Smrekar , S.E. et al. (2022) VERITAS (Venus emissivity, radio science, InSAR, topography, and spectroscopy): a discovery mission. In: 2022 IEEE aerospace conference (AERO), pp 1–20. https://doi.org/10.1109/AERO53065. 2022.9843269; [3] Garvin, J.B. et al. (2022) Revealing the mysteries of Venus: the DAVINCI mission. Planet Sci J 3:117. https://doi.org/10.3847/psj/ac63c2 [4] European Space Agency (ESA), EnVision assessment study report. Yellow book, ESA/SCI(2021)1, pages 1-111. https://sci.esa.int/documents/34375/36249/EnVision_YB_final.pdf; [5] O'Rourke et al. Venus, the Planet: Introduction to the Evolution of Earth's Sister Planet. *Space Sci Rev* 219, 10 (2023). https://doi.org/10.1007/s11214-023-00956-0; [6] Widemann, T., Smrekar, S.E., Garvin, J.B. *et al.* Venus Evolution Through Time: Key Science Questions, Selected Mission Concepts and Future Investigations. *Space Sci Rev* 219, 56 (2023). https://doi.org/10.1007/s11214-023-00992-w [7] https://www.cosmos.esa.int/web/envision/vescoor-page

Ellipticity of the polar cyclones of Jupiter through vorticity field. P. Scarica[1], A. Mura[1], D. Grassi[1], C. Plainaki[2], G. Sindoni[2], G. Piccioni[1], A. Adriani[1], F. Biagiotti[1], JIRAM team. [1]Istituto di Astrofisica e Planetologia Spaziali-Istituto Nazionale di Astrofisica, Rome, Italy, [2]Agenzia Spaziale Italiana, Sede di Roma, Rome, Italy

Introduction: Jupiter's South Pole features a stable arrangement of five circumpolar cyclones (CPCs) in a pentagonal pattern, observed consistently during successive Perijove passages of the Juno spacecraft [1][2][3][4].

The mechanism behind the stability of this pattern has been investigated. Shielding due to the presence of an anticyclonic field has been invoked [5][6], as well as vorticity-gradient forces resulting from the reciprocal interactions among cyclones and the latitudinal changes in planetary vorticity [7].

In [7], Gavriel N. & Kaspi Y. (2021) proposed a mechanism to account for both the meridional and the zonal stability of the cyclones. Meridionally, this equilibrium would occur at a specific latitude where the effects of the PC (Polar Cyclone) vorticity and the planetary sphericity balance each other out, stabilizing the CPCs in a dynamic balance. Zonally, it is postulated that the CPCs are sustained by mutual rejection, according to the force derived by their respective vorticity gradients.

In this context, the study conducted by Scarica et al. 2022 [8], generated vorticity maps of Jupiter's southern polar region for several Perijove passages of the Juno spacecraft, providing valuable insights for the present discussion.

Based on these vorticity maps, which are directly related to the motion of the clouds, we can deduce the morphology of the cyclones. Observing the deformation and deviation of the cyclones from a circular shape may offer insights into both zonal and meridional interactions. This study could reveal important information about the underlying physical processes driving the cyclones' behavior.

Method: To analyze cyclone ovalization, a simplified scheme using ellipticity as a parameter of interest was developed. Vorticity maps from [8] were selected for 1000, equally spaced vorticity levels, spanning from a minimum (-1 s^{-1}) to a maximum value (0 s^{-1}). Each of these vorticity values extracts different regions of interest (ROIs) associated with the five southern circumpolar cyclones and the central polar cyclone. As a result, there are 6x1000 different ROIs. ROIs associated with higher values of vorticity (i.e., less-cyclonic regions) have a larger size, while lower vorticity values (i.e., very-cyclonic regions) correspond to smaller ROIs. Thus, we will use the term "ROI size" interchangeably with "ROI index" or “ROI radius”, where an index of 1 corresponds to the smallest size and radius and an index of 1000 corresponds to the largest size and radius.

All the 6x1000 ROIs were fitted with an ellipse to extract the mathematical parameters of each ellipse, primarily the aforementioned ellipticity. It should be noted that the number of points in each ROI is highly variable. Additionally, the selection of the lowest and highest vorticity values to define the ROI range can influence the shape of the ROI, the resulting ellipse and its mathematical parameters. These limitations are inherent to this methodology, which, although quick and effective, is prone to a certain degree of arbitrariness, that should not be underastimated.

Results and discussion: If ellipticity increases with the size of the ROI, it suggests that the cyclone has a more elongated shape as the ROI encompasses a larger area of the cyclone. On the other hand, if ellipticity decreases with the size of the ROI, it suggests that the cyclone is becoming more circular as the ROI is growing. This could be indicative of a more symmetric vortex structure, which may suggest a more stable and longer-lasting cyclone. Figure 1 illustrates the profiles of ellipticity for each of the six cyclones, during Perijove passage 28. In some instances, these profiles exhibit a monotonic trend, but more frequently, they display variations with both maxima and minima.

Local maxima and local minima in Figure 1 suggest the presence of intermediate ROI sizes that could be indicative of characteristic scales of the cyclone's vortex structure. This means that, at that particular ROI size, the ellipticity value is capturing a characteristic aspect of the vortex structure.

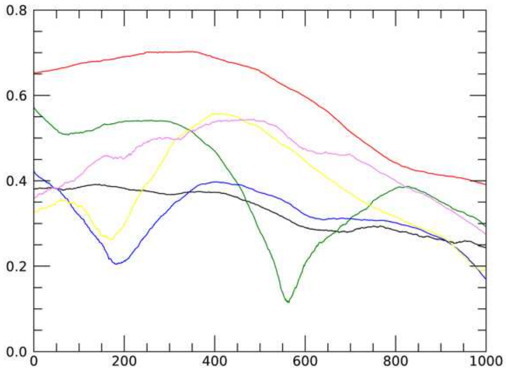

Figure 1 – Ellipticity for different vorticity levels. Black: PC. Red: CPC1. Green: CPC2. Blue: CPC3. Yellow: CPC4. Violet: CPC5.

– PC. This cyclone becomes more circular with increasing radii. The trend is monotonic.

– CPC1. While appearing relatively circular in JIRAM images, this cyclone exhibits some degree of deformation in the vorticity maps (ellipticity 0.7 at smaller radii).

– CPC2. It shows a very deep minimum around ROI 575. However, we cannot determine whether this minimum corresponds to a characteristic length of the cyclone or is rather due to the retrieval process (the vorticity map exhibited significant noise in the core of CPC2).

– CPC3. A local minimum appears at ROI 200, followed by a local maximum at ROI 400. These maxima and minima could be due to the very distinct double-ring morphology of this cyclone.

– CPC4. At ROI 400, which corresponds to -0.6 s^{-1}, this cyclone shows a local maximum that suggests the presence of a characteristic scale. At larger radii, it rapidly becomes more circular.

– CPC5. Similar to CPC4 but with higher ellipticity at larger radii.

Conclusion: The study presented here outlines a potential approach for assessing interactions among Jupiter's polar cyclones using the already-derived wind fields. This work represents an initial phase, with ongoing efforts focused on expanding the analysis to include all vorticity maps provided in [8]. Additionally, a comprehensive examination of other mathematical parameters, such as the position of the centers and orientation angles, is underway. These information will contribute to a deeper understanding of the morphological characteristics of Jupiter's polar cyclones and the extent of their interactions over time.

Acknowledgments: We thank Agenzia Spaziale Italiana (ASI) for the support of the JIRAM contribution to the Juno mission; this work is supported by the ASI–INAF Addendum n. 2016-23-H.3-2023 to grant 2016-23-H.0.

References:

[1] Adriani, A. et al. (2017). JIRAM, the Jovian infrared auroral mapper. *Space Science Reviews, 213(1–4), 393–446. https://doi.org/10.1007/s11214-014-0094-y.*

[2] Adriani, A. et al. (2018). Clusters of cyclones encircling Jupiter's poles. *Nature, 555(7695), 216–219. https://doi.org/10.1038/nature25491.*

[3] Adriani, A. et al. (2020). Two-year observations of the Jupiter polar regions by JIRAM on board Juno. *Journal of Geophysical Research: Planets, 125(6), e06098. https://doi.org/10.1029/2019JE006098.*

[4] Mura, A. et al. (2021). Oscillations and stability of the Jupiter polar cyclones. *Geophysical Research Letters, 48(14), e94235. https://doi.org/10.1029/2021GL094235.*

[5] Li, C. et al. (2020). Modeling the stability of polygonal patterns of vortices at the poles of Jupiter as revealed by the Juno spacecraft. *Proceedings of the National Academy of Sciences, 117(39), 24082–24087.* https://doi.org/10.1073/pnas.2008440117.

[6] Ingersoll, A.P. et al. Vorticity and divergence at scales down to 200 km within and around the polar cyclones of Jupiter. *Nat Astron 6*, *1280–1286 (2022). https://doi.org/10.1038/s41550-022-01774-0.*

[7] Gavriel, N., & Kaspi, Y. (2021). The number and location of Jupiter's circumpolar cyclones explained by vorticity dynamics. *Nature Geoscience, 14(8), 559–563. https://doi.org/10.1038/s41561-021-00781-6.*

[8] Scarica, P. et al. (2022). Stability of the Jupiter southern polar vortices inspected through vorticity using Juno/JIRAM data. *Journal of Geophysical Research: Planets, 127, e2021JE007159. https://doi.org/10.1029/2021JE007159.*

MODELLING OF THE CH_4 LIMB RADIANCE MEASURED BY JUNO/JIRAM AT JUPITER'S EQUATORIAL LATITUDES

Chiara Castagnoli[1,2,3] (chiara.castagnoli@inaf.it), Manuel López-Puertas[4], Bianca Maria Dinelli[2], Alessandra Migliorini[1], Francesca Altieri[1], Alessandro Mura[1], Alberto Adriani[1], Roberto Sordini[1], Federico Tosi[1], and Raffaella Noschese[1]

[1] IAPS-INAF, via Fosso del Cavaliere 100, 00133, Rome, Italy, [2] ISAC-CNR, via Piero Gobetti 101, 40129, Bologna, Italy, [3] University of Tor Vergata, via della Ricerca Scientifica 1, 00133, Rome, Italy, [4] IAA-CSIC, Glorieta de la Astronomía s/n, 18008 Granada, Spain

Introduction: Methane is the most abundant spectroscopically active gas around the Jupiter's μ-bar pressure level, where the stratosphere-thermosphere boundary layer occurs. At these altitudes, the atmospheric energy budget is largely controlled by CH_4 through photochemistry and radiative processes that result in intense emissions at infrared wavelengths. Given the great impact of methane on the dynamics, composition, and thermal profile of Jupiter's upper atmosphere, an accurate estimate of the CH_4 abundance is crucial for understanding the properties involving the highest layers of the planet's atmosphere, still poorly known. In absence of in situ measurements, the first attempts to derive the concentration of methane in the vicinity of the planetary homopause have been performed using daytime nadir measurements at 3.3 μm, sensing the atmosphere between 10^{-1} and 10^{-4} mbar. Due to the limits of this observational geometry, widely different volume mixing ratio profiles have been derived, leaving high uncertainty on the accuracy of these estimates. In more recent years, with the advent of the Juno mission, the Jovian InfraRed Auroral Mapper (JIRAM) has collected several limb measurements of the 3.3-μm CH_4 emission with an unprecedented vertical resolution of a few tens of kilometers. These data provide new insights in the jovian atmosphere and can be exploited to finally resolve the abundance of CH_4 in the upper stratosphere.

Method: In this study, we explore the 27 sequences of limb observations collected by JIRAM at mid- and equatorial latitudes: 3 acquired by the instrument on 27 March 2017 and 24 on 21 December 2018. The measurements exhibit two separate peaks of emission: one linked to the H_3^+ infrared emission, occurring at a tangent height of approximately 500-600 km, and another associated with the non-LTE emission of CH_4 at ~ 200-300 km [1]. We first use the GRANADA (Generic Radiative transfer AnD non-LTE population Algorithm) non-LTE code together with the KOPRA (Karlsruhe Optimized and Precise Radiative Transfer Algorithm) code to reproduce the observed radiance at different tangent heights. We start from the CH_4 non-LTE model that fit the ISO's (Infrared Space Observatory) Short Wavelength Spectrometer (SWS) nadir data [2] and aim at understanding the CH_4 non-LTE populations emitting in several 3.3 μm bands that can explain both the nadir (ISO) and limb (JIRAM) radiances. Later, we explore the pressure-temperatures (p-T) and the CH_4 volume mixing ratio (VMR) profiles that best fit JIRAM radiances.

Results: This work shows the importance of non-LTE to explain the spectral features of CH_4 3.3 μm in the daytime limb atmosphere and the significative contribution of the hot bands to the measured radiance. Consequently, an adeguate spectroscopic line list, including transition from high energetic levels, is required to fit both the nadir and limb radiances. Additionally, we demonstrate the sensitivity of the measured radiances to both the p-T and CH_4 VMR around 200-400 km of altitude. The analysis of JIRAM measurements favours low thermospheric temperatures and rather high CH_4 VMR at the μ-bar pressure level, although the inversion of the CH_4 VMR is required to resolve any degeneracy.

Conclusion: In conclusion, in this work we exploit the high level of information provided by the JIRAM limb spectra to improve the exhisting CH_4 non-LTE model, which, until now, has been limited to explaining only nadir observations. This exploratory study will be eventually used to retrieve the temperature and abundance of CH_4 around the μ-bar pressure level from JIRAM limb data and, consequently, to shed some light on such a key region in terms of dynamics, chemistry, and radiative transport.

Acknowledgments:
We thank Agenzia Spaziale Italiana (ASI) for the support of the JIRAM contribution to the Juno mission; this work is supported by the ASI–INAF Addendum n. 2016-23-H.3-2023 to grant 2016-23-H.0. M. L.-P. acknowledges financial support from the Agencia Estatal de Investigación, MCIN, through grants PID2022-141216NB-I00 and CEX2021-001131-S. We also thank the Società Italiana Scienze Planetarie – Angioletta Coradini (SISP-AC) for the financial support received.

References:

[1] Migliorini, A., Dinelli, B. M., Castagnoli, C., et al. 2023, Journal of Geophysical Research: Planets, 128
[2] Sánchez-López, A., López-Puertas, M., Comas, M. G., et al. 2022

DETECTION OF PURE AMMONIA CLOUDS IN A JUPITER HIGH-LATITUDE REGION BASED ON AN ANALYSIS OF JUNO/JIRAM INFRARED SPECTRAL DATA.

F. Biagiotti[1,2], D. Grassi[2], G. Liuzzi[3], G. Piccioni[2], G. Villanueva[4], F. Oliva[2], E. D'Aversa[2], A. Mura[2], C. Plainaki[5], G. Sindoni[5], A. Adriani, E. Di Mico[2] and the whole JIRAM Team. [1]Department of Physics, University of Rome "La Sapienza", Piazzale Aldo Moro 2, 00185 Rome, Italy, [2]INAF – Istituto di Astrofisica e Planetologia Spaziali (INAF-IAPS), Via Fosso del Cavaliere 100, I-00133, Rome, Italy, [3]Università degli Studi della Basilicata, Potenza, Italy, [4]NASA Goddard Space Flight Center, Greenbelt, MD, USA, [5]Agenzia Spaziale Italiana, Rome, Italy.

Introduction: Ammonia is historically thought to be the main source of condensable species for Jupiter's main cloud layer (0.6-1.1 bar level) [1]. However, measurements from Galileo first [2] and Juno later [3,4], showed that the spectral features connected to ammonia clouds are rare and not ubiquitous, and that a main cloud layer made either mainly of NH_4SH or of pure or coated tholins is an optimal solution. As of today, only two works claim to have detected pure ammonia ice clouds [5,6] and in both cases, these detections seem to be connected to transitory events.

In this work, we investigate the presence of spectrally identifiable ammonia clouds (SIACs) by analyzing the infrared spectral data of the first perijove passage (JM0002 and JM0003) from the JIRAM image-spectrometer (range 2-5 microns) on board the NASA Juno mission.

Methods: To find the presence of SIACs we used three independent spectral parameters. The first one, following [6], is the ratio of the signal at 4 microns to that at 2.97 microns. These two wavelengths are characterized by similar transmission weighting function and therefore we should probe the same pressure level; however at 2.97 microns ammonia clouds are expected to absorb strongly. The second one is the ratio of the mean of the signal in the spectral ranges 2.98-3.01 micron and 2.94-2.98 micron. Lastly, we also performed a combined PCA-GMM (Principal Component Analysis + Gaussian Mixtures Models) clustering analysis using the scikit-learn python package.

By cross-referencing JIRAM data with JunoCam mosaics (courtesy of G. Eichstadt), we found that the first two indicators showed higher values in the proximity of a high-latitude Nautilus shaped cloud system (see Fig.1). Also the PCA-GMM analysis identified the spectra in this region as belonging to a specific cluster, different from the surroundings.

We first fitted all the spectra of this region (both inside and outside the Nautilus) with a toy model. We used the pressure-temperature profile from [7], constant mixing ratio profiles for H_2, He, and CH_4, a parameterized NH_3 profile (varying deep mixing ratio and relative humidity), a slab-like parameterized pure reflecting tropospheric haze (from [8]) and a Gaussian shaped parameterized tholin main cloud layer. To compute the optical properties of the tholin cloud layer we used Mie theory and considered a log-normal distribution. A Heyney-Greeinstein approximation for the scattering phase function has been adopted, and the optical constants from [9] were used. This model is capable to reproduce reliably JIRAM data at mid-latitudes in the solar region as already shown by [3] and [4]. It is worth stressing that Titan's like tholins must not be intended as a realistic candidate for Jupiter's aerosol clouds but as an approximation of the real amorphous unknown material that exhibits an evident N-H-bond-like absorption.

We performed the retrievals using the NASA Planetary Spectrum Generator (PSG) [10] and the PyOE [11] python package. PSG is a powerful and hybrid radiative transfer suite used to model spectra of planets, exoplanets, and also moons, and satellites [12, 13]. As of the author's knowledge, this is the first work regarding Jupiter for which PSG has been used.

In the retrieval, we considered only the 2.5-3.1 micron spectral range, because this interval contains most of the information content and encompasses eventual spectral features of ammonia ice clouds, thought to be present near in the 3 micron region.

We found that the described simplified model is well fitting the majority of the spectra outside the Nautilus, whereas the spectra near and inside the Nautilus require relaxing assumptions on cloud compositions.

These spectra have been re-modeled trying a different cloud composition. To do that we generated the optical properties for pure ammonia ice particles starting from the optical constants from [14] and the same methods described above. We also considered the possibility of having coated particles (tholin core and ammonia coating), for which the optical properties have been computed using the py-mie python package [15] and validated with the BART code [16].

Results: A total of 20 spectra are best fitted by a pure ammonia ice cloud model and so have been identified as SIACs. This is the first spectral evidence of possible pure ammonia clouds obtained thanks to the analysis of Juno data.

The SIACs are located at the center of the Nautilus-shaped cloud and in correspondence with the nearby swirls. In most cases, the SIACs are surrounded by

spectra best fitted by a cloud deck composed of tholins particles coated with ammonia.
In conclusion, our results in correspondence with the Nautilus are suggesting: (I) higher altitude hazes and clouds, (II) higher values of ammonia relative humidity that also reach super-saturation conditions, (III) smaller effective radii for the haze particles. Such results are compatible with the presence of pure ammonia ice clouds, formed at these latitudes as a consequence of an uplifting event from the lower troposphere that brought a large fraction of fresh ammonia up to reach super-saturation conditions, triggering condensation and/or coating of mixed particles. Both these processes, combined with global circulation, may explain the Nautilus-like white cloud that is visible from JunoCam images.

References:

[1] Atreya S. K. et al. (1999) *P&SS, 47,* 10-11, 1243-1262. [2] Irwin P. G. J. et al. (2001) *Icarus, 149, 2*, 397-415. [3] Grassi D. et al. (2021) *MNRAS, 503, 4*, 4892-4907. [4] Sindoni G. et al. (2017) *GRL, 44, 10,* 4660-4668. [5] Baines K. H. et al. (2002) *Icarus, 159, 1*, 74-94. [6] Sromovsky L.A. & Fry P. M. (2018) *Icarus, 307,* 347-370. [7] Braude A. S. et al. (2020) *Icarus, 338,* article id. 113589. [8] Sromovsky L. A. & Fry P. M. (2010) *Icarus, 210, 1*, 230-257. [9] Khare B. N. et al. (1984) *Icarus, 60, 1*, 127-137. [10] Villanueva G. L. et al. (2018) *JQSRT, 217,* 86-104. [11] Maahn M. et al. (2020) BAMS, *101, 9*, E1512-E1523. [12] Villanueva G. L. et al. (2023) *NatAs, 7, 1056*-1062. [13] Yang J. et al. (2023) *NatAs, 7, 1070*-1080. [14] Hudson R. L. et al. (2022) *ApJ, 925, 2*, id.156. [15] https://github.com/darothen/py-mie. [16] https://www.ugr.es/~aquiran/ciencia/codigos/bart.f

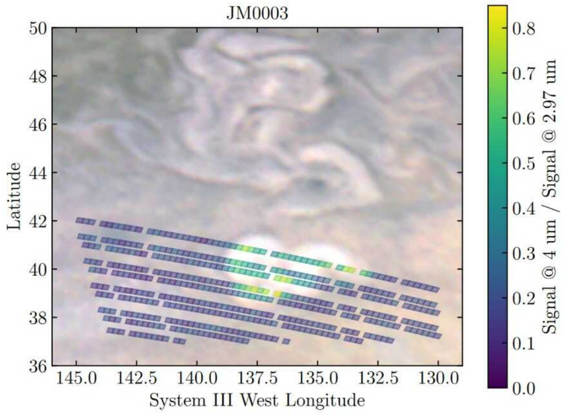

Fig. 1 *Ratio of the signal at 4 microns to the signal at 2.7 microns for a collection of PJ1 JIRAM spectra super-imposed to a JunoCam visible image*

TRACING THE UNIVERSAL EVOLUTION'S OPERATOR IN PREBIOTIC CHEMISTRY AND ORIGINS OF LIFE.

R. Saladino and B. M. Bizzarri Department of Ecological and biological Sciences, University of Tuscia, 01100 Viterbo (Italy). saladino@unitus.it

Introduction: It is generally recognized that Darwinian evolution provided at molecular level the chemical complexity for the emergence of self-organized systems, which are treated as dissipative structures in the context of the thermodynamics of irreversible processes theory [1]. This model also predicts the breaking of temporal symmetry (arrow of time), since the distribution of probability of the system is expected to change during the molecular evolution process, in agreement with the arrow of time which is characteristic of living organisms. Is it possible to design experiments able to identify the Universal evolution's operator in prebiotic chemistry? As we well known, prebiotic processes can produce different distribution of probability of organic molecules (each of which with its own structural individuality) depending on the specific geochemical and geophysical scenarios. The probability distribution function ρ associated with these events is theoretically described by the Liouville-von Neumann equation [2]:

$i\ \delta\rho/dt = L\rho$ where L indicates the Poisson operator, capable, when applied, to describe the eigenvalues of realize a pioneering study based on the superposition of specific perturbation events in a representative prebiotic system, in order to translate the theoretical eigenvalues of ρ. The formal resolution of the Liouville-von Neumann equation (that is the probability distribution function ρ at a given time t) is represented by the following equations:

$\rho(t)=e^{-iLt}\ \rho(0)$ and $\rho(t)= U\ \rho(0)$ where U is defined as the Universal evolution operator of the system.

This equation suggests, in the case of molecular Darwinian evolution, that the probability distribution function of organic molecules produced during a defined prebiotic process at a given time t is the result of the application of the evolution operator U to the probability distribution function $\rho(0)$ at the initial time t0. Since the same network of relationships between the molecules (Van der Walls interaction, hydrogen bonding networks, dipole-dipole interactions etc) has a very low probability to reproduce itself during the time (from the future to the past or vice versa), the application of U to ρ can break the temporal symmetry, introducing the arrow of time into the system, and producing dissipative structures. Exactly, what U should represent is "the appearance of a second time not linked to individual molecules, but to the relationships between molecules", as Prigogine said [3]. It follows that the demonstration of the breaking of temporal symmetry in prebiotic chemistry necessarily requires the translation of the operator U into an experimental (measurable) variable. The temporal and spatial scales of this "second time" are typically orders of magnitude larger than those of the constitutive parts. It follows that the demonstration of the break of temporal symmetry in prebiotic chemistry and Origins of Life necessarily requires the translation of the operator U into an experimental (measurable) variable. Oscillatory chemical behaviors, such as the Belousov−Zhabotinsky and chlorite/iodide/malonic acid reactions [4], have been suggested as possible example of dissipative systems mimicking the biological oscillations, but these oscillatory systems are totally deprived of the combinatorial explosion required for the emergence of complex and functional living organisms. Thus, to date, the "missing ring" between the continuous increase in chemical complexity and the formation of dissipative structures is still to be defined in terms of prebiotic chemistry measurable variables.

In this presentation preliminary data based on the revisitation of the pivotal Miller-Urey experiments [5] will be described in order to describe the use of specific perturbation events as a translation code for the definition of the general properties of ρ and of the universal evolution operator U.

Briefly, the prebiotic model selected for the experiments was referred to the prebiotic chemistry of formamide [6] associated to Miller-Urey electric discharge, while the perturbation of the system represented by the catalytic effect played by terrestrial and extra-terrestrial minerals in the reaction system, mimicking the pristine prebiotic scenarios [7-9]. In this framework, the mineral itself represents the operator U, that is the evolutionary effect played by the mineral on the composition of ρ at time t. The experimental scheme takes into account the existence of a probability distribution $\rho(t0)$ at time t0, deriving from the intrinsic reactivity of formamide and representig the contrast between chemomimesis and Darwinian molecular evolution [10]. The repetion of the prebiotic process more and more time (i.e. successive generation of the perturbation) starting from the panel of reaction products identified in $\rho(t1)$, in the presence of the same energy source and of the same perturbation, worked as an experimental tool to obtain information on the breaking of temporal symmetry, identifying the minimal distribution of organic molecules associated to the appearance of dissipative structures at the molecular level. Thus, RNA-peptides chimeras [11] were identified for the first time as co-evolving with canonical RNA molecules as recently predicted by the Carrel model [12], and proteins co-factors which are essential ingredients in present-day metabolisms were detected in the prebiotic mixture associated to the one-pot formation of long peptides. In addition, polycyclic aromatic hydrocarbons and melanin derivatives resembling insoluble organic matter in meteorites (IOM) [13] emerged in the late generations of prebiotic events. Unified mechanisms involving neutral and radical species can account for the formation of the reported products, and HCN oligomers have been identified as key intermediates in the reaction pathway. Overall these results describes for the first time the molecular evolutionary effect of geochemical and geophysical scenarios in the increase of chemical complexity, suggesting the possibility of alternative Life moving from the proto-planetary disk to habitable planets.

References:

[1] a) Prigogine I. and Defay R. (1950/1954), in Chemical Thermodynamics, Longmans, Green & Co, London, page 1; b) Prigogine I. (1955/1961/1967) in Introduction to Thermodynamics of Irreversible Processes, 3rd edition, Wiley Interscience, New York; c) Lebon G. (2008) in Understanding Non-equilibrium Thermodynamics: Foundations, Applications, Frontiers., Springer-Verlag, Berlin, e-ISBN 978-3-540-74252-4.

[2] Schwabl F. (2002) in Statistical mechanics, Springer, p. 16, ISBN 978-3-540-43163-3.

[3] Prigogine I. (1993) in The Laws of Change, Laterza ed. ISBN 88-420-4116-5.

[4] Lee K. J. and McCormick W. D. (1993), *Science* 261, 192.

[5] Criado-Reyes J., Bizzarri B.M., García-Ruiz J.M., Saladino R., Di Mauro E. (2021) *Scientific Reports* 11(1), 21009.

[6] Saladino R., Botta G., Pino S., Costanzo G., Di Mauro E. (2012), *Chem. Soc. Rev*., 41(16), 5526-5565.

[7] Bizzarri B. M., Botta L., Pérez-Valverde M. I., Saladino R., Di Mauro E., García-Ruiz J. M. (2018), *Chem. Eur. J.* 24(32), 8126-8132.

[8] Saladino R., Botta G., Delfino M., Kapralov M., Timoshenko G. N., Rozanov A., Krasavin E., Di Mauro E. (2015), *Proc. Natl. Acad. Sci. USA*, 112, E2746–E2755.

[9] Rotelli L., Trigo-Rodriguez J. P., Moyano-Cambero C. E., Saladino R. (2017), *Scientific Reports*, 6, 38888.

[10] Saladino R., Šponer J.E., Šponer, J., Pino S., Costanzo G., Di Mauro, E. (2018) Life, 8(2), 24.

[11] Gilbert W. (1986) Origin of life: the RNA world. *Nature* 319, 618.

[12] Müller F., Escobar L., Xu F., Carell. T. (2022) *Nature* 605, 279.

[13] Bizzarri B. M., Manini P., Lino V., Saladino R. (2020) *Chem. Eur. J*., 26(65),14919-14928.

DIFFERENTIAL COMPOSITION AND METABOLIC PROFILES OF SOILS AND ROCKS MICROBIAL COMMUNITIES IN ANTARCTIC DESERTS AS A MODEL FOR MARS EXPLORATIONS.

F. Canini[1], L. Borruso[2], L. Zucconi[1,3], [1]University of Tuscia, Department of Ecological and Biological Sciences, Viterbo, Italy (largo dell'Università s.n.c., canini.fabiana@unitus.it, zucconi@unitus.it), [2]Faculty of Agricultural, Environmental and Food Sciences, Free University of Bozen – Bolzano, Bozen-Bolzano, Italy (Universität Platz 5, luigimaria.borruso@unibz.it), [3]Institute of Polar Sciences, National Research Council of Italy (ISP-CNR), Messina, Italy.

Introduction: The peculiar conditions of ice-free environments of continental Antarctica, including very limited organic nutrients, extremely low moisture, low temperatures, frequent freeze-thaw and wet-dry cycles, fluctuating UV radiation regimes, strong desiccating winds, and locally high salinity [1], make them one of the closest analogues of the Martian environment [2].

In such limiting conditions, rocks and soils are the only substrates supporting microbial life, which is restricted to a few highly adapted and often endemic species. Both substrates are subjected to strong environmental pressures with, for example, higher water availability and lower desiccation and physical disturbance in rocks than in soil [3], [4]. The potential filtering effects imposed by rocks and soil on microbial communities have only been marginally investigated in Antarctic deserts despite the differences in microclimatic conditions between the two ecosystems [5], [6]. Furthermore, whether microbial propagules may be exchanged between rocks and soils is unknown. This may occur because rocks break frequently due to the subsurface growth of lichens and to freeze-thaw cycles that they often experience, and rock fragments are dispersed by the high winds characterizing this environment [7], [8]. On the other hand, the same wind can be responsible for propagules transports from soils to rocks. To provide suitable targets for exploratory missions on planets with camparable environmental characteristics to Antarctica, a clear characterization of the communities that differentiate these two substrates and the potential taxa under selective pressure in the rocks and soils is of particular interest.

Materials and Methods: To characterize the differential selective pressure of the two substrata, samples were collected in three different localities of Victoria Land, namely Battleship Promontory, Trio Nunatak, and Richard Nunatak, during the austral summer 2019/2020. Samples were collected near microclimatic stations that continuously monitor air, rock, and soil temperatures. In particular, soil samples were collected as close as possible to a sandstone outcrop (0 meters) showing evident endolithic colonization and at increasing distances of 50 and 100 meters. Samples of the corresponding rock outcrop have been collected as well. All samples were collected in triplicate.

Bacterial and fungal diversity have been studied through a DNA metabarcoding approaches, to finely define the distribution of microbial taxa in the two substrates.

Additionally, to control for the possible effect of extracellular DNA, which may be preserved for a long period in such cold environments, samples have been treated with propidium mono-azide (PMA), which binds to DNA not covered by membranes upon exposure to light. The bacterial diversity has been compared between treated and untreated samples.

The potential functionality of samples from Battleship Promontory, selected for their higher biomass content, has been investigated through a shotgun metagenomics approach. The metabolomic profiles were instead studied through NMR.

Results: During the austral summer, we observed higher temperatures in soils and rocks than in air for all three localities. Additionally, rocks reach higher temperatures during the warmest hours of the day and lower values during the coldest part of the day, while soils have more stable thermal regimes.

Regarding the microbial communities inhabiting the two substrates, higher fungal and bacterial diversity were observed in soils than in rocks. Additionally, the composition of the communities was well differentiated between the two substrates. For both rocks and soils, we observed a high proportion of sequences unique to the two substrates and a very small proportion of generalist taxa. In particular, several bacterial and fungal genera were differentially enriched in the two substrates, with rocks showing a significantly higher abundance of lichen-forming fungi, while soils were mainly dominated by yeasts.

The depletion of extracellular DNA did not change significantly the total bacterial diversity observed in the two substrates and had only a marginal effect on the taxonomic composition. However, the depletion of extracellular DNA through PMA resulted in a higher number of significant correlations with environmental variables observed for the diversity and the composition of the soil communities.

The shotgun metagenomic sequencing resulted in the assembly of several genomes, which were differentially distributed between rocks and soils, with the first substratum being characterized by the presence of Lecanoromycetes and algae, which were almost lacking in soils. Soils were instead dominated by bacteria of the phyla Actinobacteria, Chloroflexi, Verrucomicrobia, and Bacteroidetes. Also when clustering the samples on the basis of the KEGG orthologues that have been identified, we obtained a strong differentiation of rocks and soil samples, with a high number of genes that were differentially abundant in the two substrates.

Finally, the NMR profiles were strongly differentiated between the two habitats however, their analyses are still in progress to identify the metabolites that are differentially selected.

Discussion: Given the possibility that terrestrial-like life forms may have originated in the early geological history of Mars, it is reasonable to assume that they adopted the same strategies as terrestrial microorganisms to adapt to inhospitable environmental conditions, such as those found in Antarctic deserts [9].

In this work, we observed that rocks and soils represent two independent environments where life should be searched targeting different potential signatures. The differential selective pressure of the two substrata may be mainly linked to the different microclimatic conditions, including the different thermal regimes described above. In particular, the higher abundance of lichenized fungi in rocks was already documented, linked to higher water availability combined to lower desiccation [3]. As a consequence, cryptoendolithic communities are considered the major sources of organic matter in this environment. On the opposite, photosynthetic primary production seems to be impaired in soils. However, in Antarctic soils of the most remote regions, alternative pathways for carbon fixation have been documented, based on the scavenging of atmospheric traces of H_2 and CO [10], [11]. Therefore, these specific pathways could represent good markers of specific soil adaptations.

References:

[1] Cowan D. A. and Tow L. A. (2004). *Annu. Rev. Microbiol., 58,* 649–690. [2] Tamppari L. K. et al. (2012). *Antarct. Sci., 24,* 211–228. [3] Cowan D. A. et al. (2014). *Front. Microbiol., 5*, 154. [4] Wei S. T. et al. (2016). *Front. Microbiol., 7*, 1642. [5] Van Goethem M.W. et al. (2016). *FEMS Microbiol. Ecol., 92*, fiw051. [6] Rego A. et al. (2019). *Front. Microbiol., 10,* 1018.[7] Friedmann E. I. (1982). *Science, 215,* 1045–1053. [8] Campbell I. B. and Claridge G. G. C. (1987). Elsevier, Amsterdam. [9] Cockell C. S. (2014). *Philos. Trans. Royal Soc. A., 372*, 20130082. [10] Ji M. et al. (2017). *Nature, 552,* 400–403. [11] Ortiz M. et al. (2021). *PNAS 118,* e2025322118.

EXTREME ENVIRONMENTS: CRYOCONITE HOLES.

F. Pittino[1], R. Ambrosini[2], G. Diolaiuti[2], K. Zawierucha[3], E. Poniecka[4], R. S. Azzoni[5] and A. Franzetti[2],
[1]Department of Earth and Environmental Sciences (DISAT), University of Milano-Bicocca, Milano, Italy.
[2]Department of Environmental Science and Policy (ESP), University of Milan, Milano, Italy
[3]Department of Animal Taxonomy and Ecology, Faculty of Biology, Adam Mickiewicz University, Poznan, Poland
[4]Department of Environmental Microbiology and Biotechnology, Faculty of Biology, University of Warsaw, Warsaw, Poland
[5]Department of Earth Science "Ardito Desio," University of Milan, Milano, Italy

Introduction: Glaciers and ice sheets are known for their extreme conditions. High UV radiation, cold temperatures, freeze-thaw cycles low liquid water availability and oligotrophy are the main challenges organisms must face to survive in such environments. The study of the main survival strategies in these conditions may pave the way to understanding which are the most likely inhabited worlds. Indeed, cryospheric environments are present not only on the Earth but also on Mars, Europa and some Saturnian moons [1]. On Earth, they were recognized as a biome only in 2012 [2], but little information about their biota is currently available. Most of the published data focus on the supraglacial environment which has more interaction with the surrounding environments and is more homogeneous and of easier access than the englacial and subglacial ones (i.e., those within the ice mass and below it at the glacier-substrate interface). However, the very little information available indicates that life is present also in the other environments, where the logistics are more challenging [3], [4]. Furthermore, recent studies showed that microorganisms can proliferate not only at low temperatures but also at higher pressures than the one present in our atmosphere [5], which is one of the major challenges for life in the englacial environment. In the supraglacial environment, most of the studies focus on cryoconite holes: small ponds full of melting water with an airborne fine-grained material on the bottom (i.e. the cryoconite) (Fig. 1).

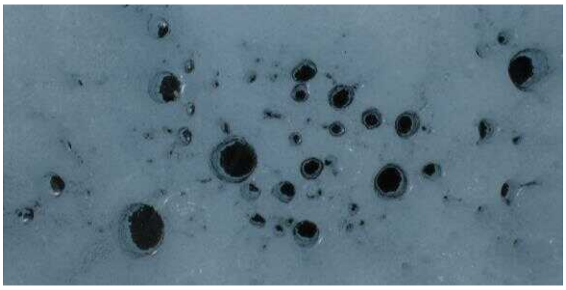

Fig. 1 Cryoconite holes of Forni Glacier.

In these structures, liquid water protects from desiccation, high UV radiation, and very low temperatures (below the freezing point). Furthermore, even when temperatures get very cold, instead of completely freezing, an ice lid forms on the surface, while the dark sediment keeps absorbing the solar heat below, keeping water liquid [6]. Thanks to these characteristics, cryoconite holes are hotspots of biodiversity on glaciers. They can host biological particles such as viruses and living organisms such as bacteria, fungi, algae, protists, annelids, arthropods, rotifers, and tardigrades, and all these taxa form a peculiar trophic net [7]. The cryoconite sediment presents aerobic conditions at its water-sediment interface, but it turns into a completely anaerobic substrate just a few micrometers below [8]. The bacterial communities within cryoconite holes colonize the whole sediment and have been described worldwide mostly by snapshot studies, but evidence exists indicating that they show seasonal trends [9]. This aspect is extremely important to understand how bacterial communities develop in such extreme conditions, as the taxa in the later stages of these temporal successions are likely those more suitable to survive.

So far, our data has allowed us to provide new insights into the bacterial communities of the Forni Glacier (Italian Alps), which may pave the way to future studies of the supraglacial environment.

Materials and Methods: Cryoconite samples have been collected on Forni Glacier (46° 24′ 00″ N, 10° 35′ 30″ E) for eight years (2012, 2013 and 2015—2020). In four years (2013, 2016, 2018, 2019) we collected samples along the ablation season approximately every second week to obtain data about their seasonal variation, while in the other years, samples were collected only once in July. To better investigate the daily activity variation of different bacterial populations in the community, on the 20th of July 2018 we also collected multiple samples from four cryoconite holes at four different times (4:30 am, 7:30 am, 1:30 pm, and 7:30 pm). DNA was extracted from the cryoconite samples to investigate their year and seasonal variation and RNA was extracted from samples collected to obtain the description of their diel temporal trend. The V5-V6 hypervariable regions of the 16S rDNA were sequenced through Illumina sequencing, as for 16S rRNA on samples collected on the 20th of July 2018 only. Metatranscriptomic was performed on one single cryoconite hole sampled more times along the day. The obtained ASVs [10] were classified with the SILVA database [11] and multivariate analyses were performed to investigate the temporal trends.

Results and Discussion: Results showed that the bacterial communities in Forni cryoconite differed significantly over the years. In addition, they also showed seasonal trends during the ablation seasons, with a prevalence of autotrophic cyanobacteria in early phases and of heterotrophic taxa in later ones.

Only a minor fraction of the whole bacterial community was active, however (Fig. 3).

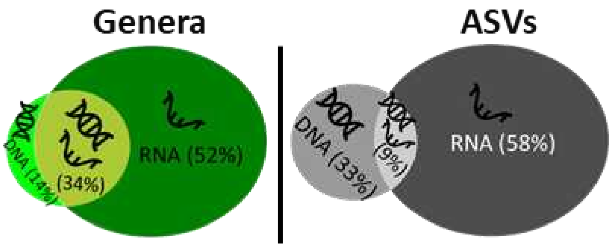

Fig. 2 Venn diagram on bacterial genera and ASVs

This is confirmed also by the observation that the active bacterial community is mainly anaerobic (as most of the cryoconite sediment), while the total community is mainly composed of aerobic taxa (Fig 4).

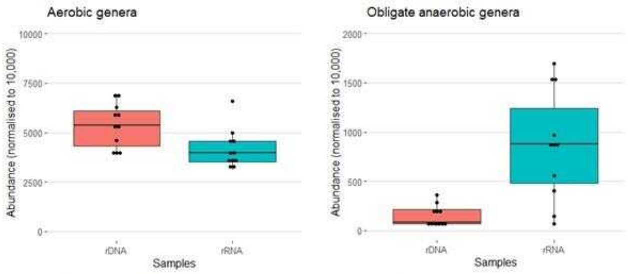

Fig. 3 Boxplot of the relative abundance of the aerobic and anaerobic bacterial genera in rDNA and rRNA.

Results from the metatranscriptome analysis showed clear differences in the metabolic profile of the community along the day (Fig. 5).

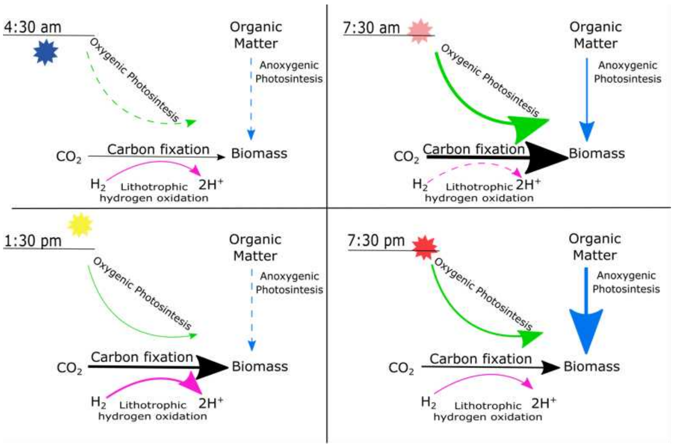

Fig. 4 Proposed model of a temporal trend of the main energy and carbon metabolisms. Thicker arrows mean higher presence of that metabolism.

Interestingly, carbon fixation and photosynthesis do not follow the same trend. Indeed, photoinhibition seems to occur when the solar radiation is higher, but no decrease in carbon fixation is observed. The increase in hydrogen oxidation observed at 1:30 pm (close to the solar noon) suggests that this metabolism can provide the reducing power necessary to produce organic matter when photoinhibition occurs.

Altogether, these results show that bacterial communities of cryoconite holes are active and their composition or metabolic profile change according to the time and environmental conditions (i.e. solar radiation). The active part is only a minor fraction, and the differences we see between different years are more related to the total community as they are the result of DNA sequencing. The atmospheric input is the most important source of the cryoconite biota, especially at the beginning of the ablation season. Therefore, the importance of this atmospheric input and how much it affects the active part of the community is still unclear, because the latter may be composed mainly of preexisting taxa (which can survive under the snow cover during winter). Further studies are necessary to better understand the dynamics of bacterial communities in such extreme environments, how they can face such harsh conditions and how they interact with the other organisms inhabiting glaciers. The change in the metabolic profile and the high dynamicity of the community structure may be key points to understanding how bacteria can live in cryospheric environments.

References:

[1] Laybourn-Parry J. et al. (2017) *Ed. Oxford University Press*, *58*, 211, 1021–1022. [2] Anesio A. M. and Laybourn-Parry J. (2012) *Trends Ecol. Evol.*, *27*, 4, 219–225, doi: 10.1016/j.tree.2011.09.012. [3] Martinez-Alonso E. et al. (2019) *Sci. Rep.*, *9*, 12158, 1–14, 2019, doi: 10.1038/s41598-019-47994-9. [4] Perini L. et al. *Sci. Rep.*, *9*, 20230, 1–15, 2019, doi: 10.1038/s41598-019-56290-5. [5] Miller K. M. et al. (2016) *Astrobiology*, *23*, 1, 94–104, doi: 10.1089/ast.2022.0043. [6] Cook J. et al. (2016) *Prog. Phys. Geogr.*, *40*, 1, 66–111, doi: 10.1177/0309133315616574. [7] Zawierucha K. et al. (2015) *J. Zool.*, *295*, 3, 159–169, doi: 10.1111/jzo.12195. [8] Poniecka E. A. et al. (2018) *Arctic, Antarct. Alp. Res.*, *50*, 1, doi: 10.1080/15230430.2017.1420859. [9] Franzetti A. et al. (2017) *Environ. Microbiol. Rep.*, *9*, 2, 71–78, doi: 10.1111/1758-2229.12499. [10] Callahan B. J. et al. (2016) *Nat. Methods*, *13*, 7, 581–583, doi: 10.1038/nmeth.3869. [11] Quast C. et al., (2013) *Nucleic Acids Res.*, *41*, D1, 590–596, doi: 10.1093/nar/gks1219.

Acknowledgements: We thank Stelvio National Park (Italy) for logistic assistance. Bioinformatics analyses were run on the MARCONI server (CINECA, Bologna, Italy). This work was partially funded by the Italian Ministry of Research (PRIN grant “Cold Case: structure and functioning of the disappearing glacier biodiversity” to RA)

ETHANOLAMINE ICES IN SIMULATED SPACE CONDITIONS

S. Biancalani[1,2] and J. R. Brucato[2],
[1]University of Trento/Italian Space Agency-University of Florence-Florence, Italy (sole.biancalani@unitn.it),
[2]INAF – Astrophysical Observatory of Arcetri, Largo E. Fermi 5, 50125 Florence, Italy (john.brucato@inaf.it)

Aims: Laboratory experiments on the interactions between complex organic molecules, interstellar dust and UV radiation are crucial to understand the physico-chemical mechanisms that lead to the synthesis of the already observed iCOMs and to search for new molecular species not yet observed in the gas phase in the ISM. Ethanolamine ($NH_2CH_2CH_2OH$) is an organic molecule of great astrobiological interest, proposed as a precursor of phospholipids [1], the main constituents of cell membranes, and of glycine, the simplest amino acid [2]. This molecule, already detected in the Almahata Sitta meteorite [3], has recently been observed in the interstellar medium in the giant molecular cloud Sagittarius B2 [1]. Its presence in the gas phase suggests that ethanolamine could also be adsorbed on dust grains, and thus participate in solid-state chemistry on their surface. The aim of this work was to study in the laboratory the physico-chemical properties of ethanolamine in simulated astrophysical condition, in order to understand its role in surface chemistry in the ISM.

Methods: At INAF-Arcetri Astrobiology Laboratory, we used an ultra-high vacuum chamber equipped with a cryostat capable of reaching cryogenic temperatures of 10 K in order to study ices of ethanolamine, both pure and mixed with water (mixing ratio 1:1). We irradiated the icy sample in situ with the UV-enhanced Xenon lamp, simulating the radiation of solar-type stars but also the secondary UV emission due to cosmic rays present inside dense molecular clouds [4]. In addition, we performed the same analyses by adsorbing the molecules directly onto the dust grains, in order to study their catalytic role in the presence or absence of UV radiation. To simulate the interstellar dust, we used nanometric fluffy grains of amorphous olivine produced in the laboratory by laser ablation [5].

Results: We analyzed the mass spectra of molecular species released in the gas phase during temperature-programmed desorption (TPD) processes. Ethanolamine was found to be quite stable when absorbed directly on the nichel-coated cold finger, even in the presence of water, when irradiated with UV light. The presence of amorphous olivine grains strongly modified the profile of the TPD curves, trapping the molecule up to higher temperatures than the clean cold finger. We then identified a series of products formed when the molecule was irradiated onto the dust substrate.

Conclusions: We were able to constrain the desorption temperature and energy for ethanolamine and its 1:1 mixture with water, and study the effect of dust and UV irradiation on the sample. The proven interaction of molecules with dust grains is crucial for the chemistry of the protoplanetary disks, because the precursors of some biological molecules could be retained on the surface of grains and planetesimals up to higher temperatute than expected, even in the innermost parts of the disk, where rocky planets like the Earth are formed. Of particular interest is the detection in our instrument of some high m/z molecular species that desorbed between 200 K and 300 K, which have not yet been detected in space. Our results provide support for understanding existing observational data and indicate possible targets for future observations; furthermore, they improve our knowledge of the role of the grain surface in the enrichment of chemistry in space.

References: [1] Rivilla V. M. et al. (2021) *PNAS 118 (22).* [2] Zhang X. et al. (2017), *Orig. Life Evol. Biosph., 47,* 413–425. [3] Glavin D. P. et al. (2010), *Meteoritics Planet Sci., 45,* 1695–1709. [4] Prasad S. S., Tarafdar S. P.(1983), *ApJ, 267,* 603–609. [5] Rotundi A. et al. (2002), *Meteoritics Planet Sci., 37,* 1623–1635

THE REACTION OF SULFUR ATOMS ON THE SURFACE OF WATER ICE

G. Di Genova[1], J. Perrero[2], N. Balucani[1], C. Ceccarelli[3], M. Rosi[4], A. Rimola[2].
[1]Dipartimento di Chimica, Biologia e Biotecnologie, Università degli Studi di Perugia, Via Elce di Sotto 8, 06123, Perugia, Italy (gabriella.digenova@studenti.unipg.it, nadia.balucani@unipg.it)
[2]Departament de Química, Universitat Autònoma de Barcelona, 08193, Catalonia, Spain (Jessica.Perrero@uab.cat, Albert.Rimola@uab.cat)
[3]Univ. Grenoble Alpes, CNRS, Institut de Planétologie et d'Astrophysique de Grenoble (IPAG), F-38100 Grenoble, France (cecilia.ceccarelli@univ-grenoble-alpes.fr)
[4]Dipartimento di Ingegneria Civile ed Ambientale, Università degli Studi di Perugia, Via G. Duranti 93, 06125, Perugia, Italy (marzio.rosi@unipg.it)

Introduction: Astrochemistry is a multidisciplinary subject that allows us to investigate the formation and destruction routes of molecules found in extraterrestrial environments, such as planets and moons, comets or the interstellar medium (ISM) [1].
To date, there is still a relevant lack of knowledge concerning the chemistry of minor species such as those including sulfur. For instance, an important aspect in ISM chemistry is the S-depletion problem [2]. Interestingly, many sulfur species (H_2S, OCS, SO, S_2, SO_2 and CS_2) have been identified in the coma of the comet 67P/Churyumov-Grasimenko [3] and some have been proposed as the main carriers of S, such as H_2S and OCS, condensed in the icy mantles of interstellar dust grains. Other more complex sulfur compounds have been suggested, even though their exact chemical structures remain elusive [4]. H_2S has also been detected in the plume of Enceladus by the Cassini INMS [5].
In this contribution, we present a theoretical investigation of the reactions involving atomic sulphur, in its first electronically excited state ^{1}D, with water ice. S(^{1}D) is produced by UV-induced photodissociation of precursor molecules, such as OCS [6] and CS_2 [7], which are relatively abundant in extraterrestrial environments. In. particular, OCS is among the few molecules for which a secure identification in interstellar ice has been provided [8-9]. In addition to that, also the photodissociation of H_2S can lead directly to the formation of S(^{1}D) [10].
Previous work in our research group focused on the reaction of S(^{1}D) with saturated and unsaturated hydrocarbons [11,12] in the gas phase. As expected, S(^{1}D) resulted to be much more reactive than sulphur in the ground ^{3}P state. In all cases, new molecular products holding a novel C-S bond were observed. In addition, the capability of S(^{1}D) of inserting into sigma bonds (already observed for the isovalent species O(^{1}D)) was confirmed [11,12].

S(^{1}D) + H_2O: S(^{1}D) precursors, like OCS and H_2S, have been identified in interstellar ice or in the Enceladus plume. Therefore, if formed on the ice surface by their photodissociation, as soon as it is formed S(^{1}D) will be able to react with water. According to our calculations, the reaction proceeds either by S(^{1}D) addition to one of the lone pairs of O or via insertion into one of the two O-H bonds. Two different intermediates can be formed: H_2OS and HOSH.

Theoretical method: We first characterized the gas-phase potential energy surface (PES) of the reaction S(^{1}D) + H_2O. We used the GAUSSIAN09 program package [13] to optimize all stationary points of the PES at the DFT level of theory, using the ma-TZVP [14] basis set. Frequencies analysis were carried out in order to determine the nature of the stationary points. Subsequently, we performed single-point calculations at the CCSD(T) level of theory [15] in order to refine the energy of each stationary point. We corrected all energies with the zero-point energies computed at the DFT level of theory.
We then optimized the geometry of an 18-H_2O cluster ice surface at DFT level of theory. We identified several surface binding sites on the grain, based on the amount of available hydrogen bonds that engage the sulfur atom with the surface. For each identified site, we then computed the binding energies of the sulfur atom in order to select the best configuration with which to investigate the catalytic effect of water molecules.
After each DFT geometry optimization, we employed the ORCA software [16] to refine all energies of the 18-H_2O + S(^{1}D) structures by using the DLPNO-CCSD(T) method [17].

Results: We computed the potential energy surface of the reaction S(^{1}D) + H_2O in gas phase and subsequently compared these results with the same reaction taking place on an 18-H_2O cluster ice surface model. As shown in Fig.1, when compared to gas-phase, the energetic profile of the same reaction on ice proves how water molecules act as catalysts by actively participating in the H transfer process (which is the one responsible, for example, of the conversion of H_2OS to HSOH), lowering the energy barriers.

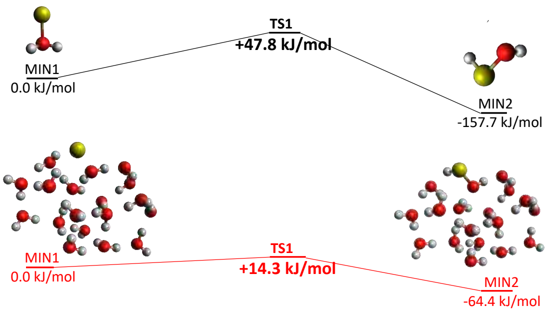

Fig.1: In black: gas phase energy profile of the isomerization process of H_2OS to HOSH. In red: the same process on the 18-H_2O cluster ice surface model.

Conclusions: In this contribution, we have shown the catalytic effect of the water ice: surrounding water molecules actively participate to the H-transfer process, reducing the energy barriers compared to the analogous gas phase steps for the isomerization toward the most stable isomer of gross formula SOH_2. According to our results, when $S(^1D)$ is formed by the dissociation of its precursors on the surface of water ice, it is immediately converted into H_2OS, H_2SO and HOSH. The chemistry of this excited species closely resembles that of $O(^1D)$, recently investigated in interstellar ice analogues [18].

Aknowledgments: This work has received funding from the Italian MUR (PRIN 2020, “Astrochemistry beyond the second period elements”, Prot. 2020AFB3FX).

References:

[1] Caselli P. and Ceccarelli C. (2012) *Astron. Astrophys. Rev.,* 56, 20

[2] Vidal T. H. G. and Wakelam V. (2018) *Mon. Not. R. Astron. Soc.*, 5575–5587, 474

[3] Calmonte U. et al., (2016) *Mon. Not. R. Astron. Soc.* 253-273, 462

[4] Hänni N. et al., (2022) *Nat. Commun.,* 3639, 13

[5] Waite Jr. J. H. et al., (2009) *Nat., 487-490, 460*

[6] Kim, M. H. et al., (2004) Can. J. Chem. 880-884, 82

[7] Black, G. and Jusinski, L.E. (1986) Chem. Phys. Lett., 90–92, 124

[8] Gibb E. L., et al., (2000) Astrophys. J., 347, 536

[9] Gibb E. L., et al., (2004) Astrophys. J. S. S., 35, 151

[10] Zhao Y. et al., (2021) *Nat. Commun., 4459, 12.1*

[11] Leonori F. et al., (2009) *J. Phys. Chem. A,* 15328–1534, 113

[12] Berteloite C. (2011) *Phys. Chem. Chem. Phys.*, 8485–8501, 13

[13] Frish M. J. et al., (2013) *Gaussian 09;* Gaussian Inc.: Wallingford CT

[14] Zheng J. et al., (2011) *Theor. Chem. Acc.,* 295-305, 128

[15] Purvis C. D., (1982) *J. Chem. Phys*., 1910, 76

[16] Neese F. et al., (2020) *JChPh,* 152, 224108

[17] Guo Y. et al., (2018) *J. Chem. Phys.,* 148.1

[18] Bergner J. B. et al., (2017) *Astrophys. J.* 845 (1), 29

ANTHELIA - ANalysis of illumination and THermal Environment of Lunar pIts and lavA tubes.

P. Cambianica[1], G. Cremonese[1], E. Simioni[1], E. Martellato[1], R. Pozzobon[2], M. Massironi[2], A. Lucchetti[1], M. Pajola[1]. [1]INAF Astronomical observatory of Padova, Vicolo dell'Osservatorio 5, 35122 Padova, Italy; [2]UNIPD, Department of Geosciences, Via G. Gradenigo, Padova, Italy. (email: pamela.cambianica@inaf.it).

Introduction: Planned space exploration shows that a human return to the Moon is pivotal to improve our knowledge about the geological processes that operate on the rocky bodies of the Solar System, including volcanism responsible for the deformation of the Moon's crust. Several lunar surface features are evidence of the past volcanic activity, including lava tubes. A lava tube is a natural conduit formed by lava, which flows out from a volcanic vent and moves beneath the surficial crust resulting from the hardening of the lava itself once it gets in contact with the low temperatures of the external environment. Once the lava diminishes, the tube drains, leaving an empty tube. Lunar lava tubes are considered candidates for future human exploration. Indeed, if accessible the interior of a vacant lava tube could provide astronauts shelter against possible meteorite impacts, cosmic radiation, as well as extreme temperature variations. In fact, the surface of an airless body is constantly affected by space weathering. The solar radiation is the major source of energy that significantly contribute to surface and subsurface degradation due to the repeated cooling and heating of the surface over daily cycles. This can result in the failure of the material to adapt to temperature changes through the combined action of differential dilation and thermal gradients. For these reasons, estimation of illumination conditions and surface radiative intensity on airless bodies becomes essential. The possibility to accommodate astronauts in subsurface lunar bases needs to be investigated in terms of temperature variations, in order to verify which are the best conditions (e.g., size, latitude, and depth of the lava tube) that could offer a thermally stable lunar base, since constant temperatures offer favorable environmental conditions both for human and industrial operations [1]. Different space missions (e.g., LRO, Kaguya) imaged the surface of the Moon looking for lava tubes evidence, allowing the identification of some lunar pits as possible lava tube skylight candidates [2,3]. The surface of the Moon is characterized by the presence of more than 200 collapse pit features, which represent a direct window into the lunar subsurface [3]. As evidenced by the Gravity Recovery and Interior Laboratory [4] and SELENE/Kaguya [5] missions, these collapse features provide direct access to subsurface voids of unknown lateral extent. Skylight candidates formed after the collapse of the roof of a potential lava tube, due to gravitational instabilities, such as seismic events or meteoroid impacts [6], and therefore represent natural gateways to lava tubes or caves. The images acquired by the Lunar Reconnaissance Orbiter (LRO, [7]) have shown that some of these steep walls expose a vertical cross-section of stratified lunar crust [2]. The stratification records fundamental hints of the Moon's formation and evolution, and the analysis of these layers would provide new knowledge on the volcanic history of the Moon[1]. Due to the complex illumination and thermal conditions, these collapsed pit features could trap volatiles and even solar wind particles that were trapped in the lunar surface during the formation stages. Ground-level exploration of lunar pits could then increase or modify our understanding of the Moon's formation and reveal the presence of entrances to caves or lava tube networks.

Objectives: In this research project, we will characterize the complex illumination and thermal conditions within lunar pits and lava tubes, in order to:

- support future lunar missions;
- improve our understanding of lunar cave thermal behavior;
- investigate the link between their size, morphology, and latitude with the thermal behavior;
- study the thermal stress they undergo as a result of temperature changes;
- investigate the extent of any temperature changes to identify what the depth of a tunnel might be to ensure a thermally stable environment;
- constrain theories about lunar vulcanism and lava-flow thermodynamics.

Skylights could also provide potential access to subsurface resources including volatiles [8]. The presence of volatiles on airless bodies are linked to the surface and subsurface thermal environment.

Thermal conductivity is often low and, in the absence of a significant atmospheric heat flow, volatiles can remain stable especially in polar regions. In particular, we also aim to study the possible presence of water ice by investigating the influence of temperature, geometry, and latitude on its stability. The reason is that this type of volatile represents an essential resource that enables an astronaut outpost.

Method: To obtain the surface and subsurface temperature distribution, we applied a ray-tracing illumination and thermal model we developed to study the self-heating effect on the surface of airless bodies [9]. An accurate thermophysical model requires detailed and realistic physical conditions such as topography, surface roughness, while the thermophysical parameters themselves depend on the direct illumination (with the consequent formation of shadows and penumbra), the back-scattering, and the reradiation cases. The model we developed takes as input a 3D Digital Terrain Model (DTM) of an entire surface or of a specific surface feature, e.g., pits. The model steps through time updating the orbital position and orientation (supplied by the NAIF SPICE toolkit) of the selected airless surface with respect to the Sun, which can be modelled as a point source (in the case of the Moon) or as a disk (in the case of Mercury). The 3D mesh is then the input of the 3D thermal model and the model is given an initial temperature based on its latitude. We run the 3D thermal model until it has equilibrated and execute the main modeling task during which the model outputs the surface temperatures on each facet of the 3D mesh at each timestep. The 3D thermal model output is then the input of the volatile transport model, which outputs volatile loss rates from the given pit geometry and latitude.

Preliminary results: In this work we present the preliminary surface and subsurface temperatures throughout a lunar day for different synthetic 3D pits and cave geometries (in Fig.1 some examples of geometries are shown.). We aim to investigate the link between morphology, size, and latitude with the thermal environment, and select the best geometry for sheltering both human explorer and lunar outposts. The TRANQUILLITATIS pit (8.335°N, 33.222°E, diam: 84-99 m) located in Mare Tranquillitatis was selected as test case. We highlight that from the computation, this pit is currently returning a thermal stability around 17°C (Fig.1).

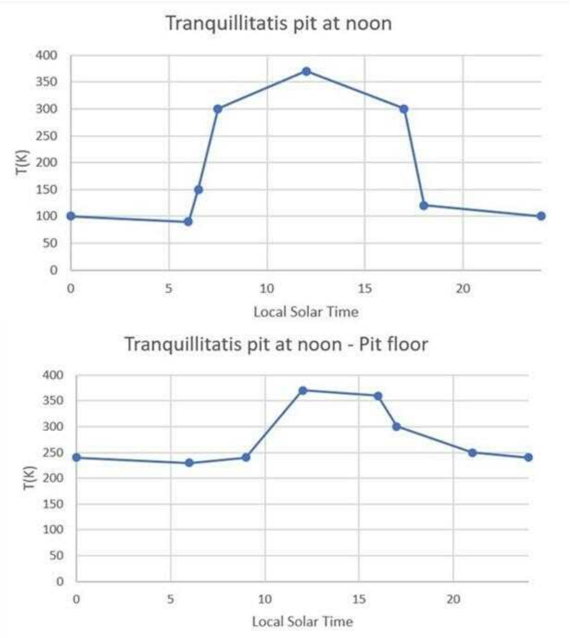

Fig. 1. Noon-time Tranquillitatis pit surface and floor temperatures, in line with Horvath et al. 2022

Acknowledgments: we gratefully acknowledge funding from the Istituto Nazionale di Astrofisica (INAF), decreto 5/22.

References: [1] Rossi, Angelo Pio, et al. DAEDALUS-Descent And Exploration in Deep Autonomy of Lava Underground Structures: Open Space Innovation Platform (OSIP) Lunar Caves-System Study. 2021. [2] Robinson, M. S., et al., PSS 69.1 (2012): 18-27. [3] Haruyama, J., et al. *Geophysical Research Letters* 36.21 (2009). [4] Zuber, M. T., et al., Science 339.6120 (2013): 668-671. [5] Kato, M., et al., Space science reviews 154.1 (2010): 3-19. [6] Martellato, E. et al. *Planetary and Space Science* 86 (2013): 33-44. [7] Chin, G., et al., Space Science Reviews 129.4 (2007): 391-419. [8] Blamont, J. Advances in Space Research 54.10 (2014): 2140-2149. [9] Cambianica, P., et al.,"Thermal impact of self-heating effect on airless surfaces. The case of Mercury. " in prep.

Moon multisEnsor and LabOratory Data analysis (MELODY): PRELIMINARY RESULTS.

F. Tosi[1], E. Pettinelli[2], C. Carli[1], J.-Ph. Combe[3], S. Fonte[1], L. Giacomini[1], M. Massironi[4], R. Pozzobon[4], G. Rinaldi[1], G. Salari[1], G. Tognon[4], F. Zambon[1], B. Cosciotti[2], C.H. Martella[2], E. Mattei[2], R. Orosei[5], R. Avanzinelli[7], E. Bruschini[1], M. Casalini[6], T. Cuppone[6], G. Pratesi[6]. [1]Istituto Nazionale di AstroFisica – Istituto di Astrofisica e Planetologia Spaziali (INAF-IAPS), Roma, Italy, federico.tosi@inaf.it. [2]Università degli Studi Roma Tre – Dipartimento di Matematica e Fisica, Roma, Italy. [3]Planetary Science Institute, Tucson, AZ, USA. [4]Università di Padova – Dipartimento di Geoscienze, Padova, Italy. [5]Istituto Nazionale di AstroFisica – Istituto di RadioAstronomia (INAF-IRA), Bologna, Italy. [6]Università degli Studi di Firenze – Dipartimento di Scienze della Terra, Firenze, Italy.

Introduction: The PRIN INAF research project "*Moon multisEnsor and LabOratory Data analYsis (MELODY)*" aims at a broader understanding of our Moon by means of a thorough analysis of a few specific regions of interest using several datasets gathered by previous exploration, combined with laboratory analyses of lunar regolith simulants and with laboratory measurements of lunar meteorite samples.

This ambitious goal is pursued by integrating the expertise found at Italy's National Institute for Astrophysics (INAF) and other Italian and foreign institutions. Here, we summarize the main results.

Analysis of specific Regions of Interest (ROI): *ROI #1: Mare Ingenii and Thomson crater.* Located within the outer edge of the South Pole-Aitken basin, Mare Ingenii is one of the few basaltic plains on the farside of the Moon. It includes two large craters, Thomson and Thomson M, and a prominent *swirl*, i.e. a high-albedo sinuous feature whose origin is still debated. Based on panchromatic imagery combined with elevation data, we first produced a detailed geological map of the Ingenii basin integrated with compositional information derived from the multispectral Clementine color data (**Fig. 1**). We then selected several Regions of Interest (ROIs) (**Fig. 2**) and used hyperspectral data returned by the Moon Mineralogy Mapper (M^3) instrument aboard the Chandrayaan-1 mission [1] to investigate the mineralogy of Mare Ingenii based on selected spectral parameters (visible reflectance, position and depth of the pyroxene bands at 1 and 2 µm, spectral slopes, band area ratio, FeO and TiO_2 abundance, and "Clementine" colors [2]). Compositional variability is revealed in terms of high-Ca, low-Ca or Ca-free pyroxenes, suggesting a mafic signature throughout the surface [3]. More details about this analysis are provided in [3, 4].

ROI #2: Tsiolkovskiy crater. Also on the lunar farside, Tsiolkovskiy is a large impact crater located in the southern hemisphere. Here, we too carried out mineralogical mapping based on M^3-derived Spectral Units (SUs), to highlight different mineralogical phases (e.g. plagioclase, olivine, pyroxene, opaques).

An updated geo-stratigraphic map for Tsiolkovskiy was then produced by integrating a morpho-stratigraphic map of the basin [5] with the spectral units. While most SUs show no unique geologic correlation, the basaltic mare is associated with three specific spectral units (i.e. SU1, SU2 and SU3), confirming the succession of three effusive events displaying a distinct composition and age [6, 7].

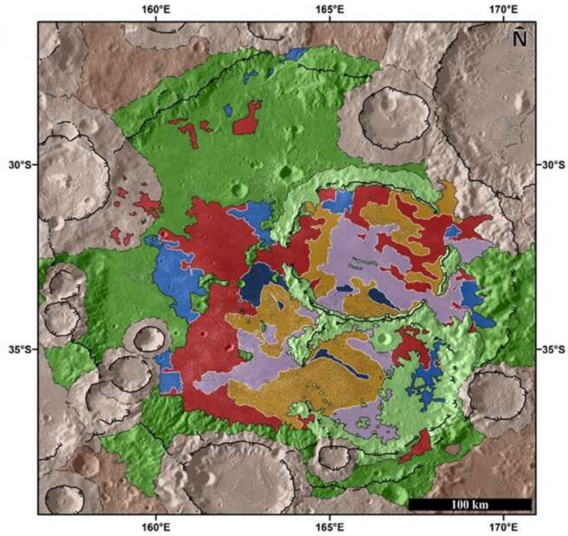

Fig. 1. Detailed geological map of the Ingenii basin region (33°15.0′ S, 164°49.5″ E) visualized on top of a DEM-derived hillshade basemap.

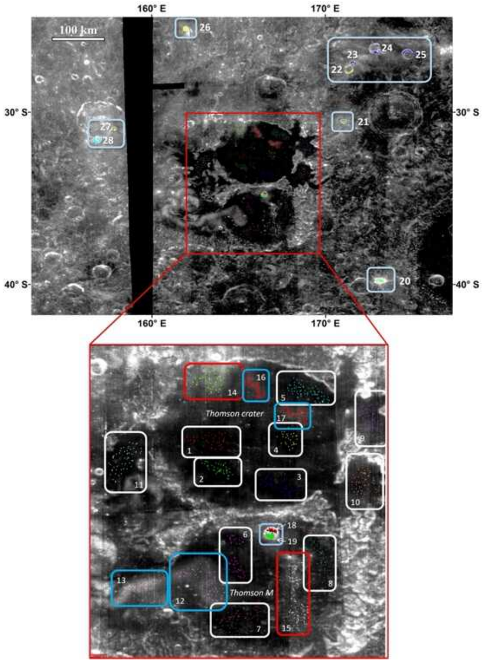

Fig. 2. Regions of interest considered in the Mare Ingenii area for our mineralogical analysis. These regions have been selected to be representative of different materials as inferred from the analysis of the optical images and of the geological map shown in Fig. 1.

Dielectric spectroscopy of lunar regolith simulants: Ground Penetrating Radar (GPR) might be a useful technique to detect water ice and volatiles in the lunar polar regions. In the framework of the MELODY project, we measured several lunar regolith simulants, produced by different commercial US suppliers, with a LCR meter over the frequency range 20 Hz–1 MHz and in the temperature range 200–350 K, to investigate the dependence of the lunar regolith dielectric properties (i.e., dielectric permittivity) as a function of temperature (**Fig. 3**). To properly constrain the mineralogical composition, not necessarily matching the one declared by the supplier, for each simulant we directly measured it each simulant in bins of grain size.

This laboratory analysis is also useful for constraining new analyses of past, ongoing and future lunar missions carrying a radar onboard.

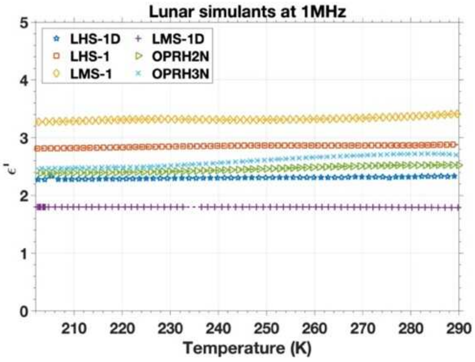

Fig. 3. Real part of dielectric permittivity for several regolith simulants representative of lunar highlands and maria, measured with the LCR meter setup in the temperature range 200–290 K. Uncertainties are less than few percent.

Mineralogical and spectral analysis of lunar meteorite samples: We purchased 6 lunar meteorite samples, selected to be representative of different lithologies (breccias, basalt, and troctolite). Using bidirectional VNIR reflectance spectroscopy provided by a FieldSpec Pro®, we first investigated a slab of the lunar feldspathic breccia NWA13859. The spectra obtained in the 0.35–2.5 µm range suggest a mineralogy dominated by mafic minerals: whitish clasts display spectral features (band I center and average reflectance) attributable to a mixture of orthopyroxenes and plagioclase, while the dark matrix is consistent with Fe-bearing glasses, olivine, and opaque materials (likely ilmenite) (**Fig. 4**, top and middle panels) [8].

Using the SEM and EMPA at the University of Florence, three small fragments of this meteorite slab were analysed, allowing us to discriminate the various clasts in therm of their affinity (ferroan anorthosite or FAN, Mg-rich, intermediate, and glass/matrix) (**Fig. 4**, bottom panel). LA-ICP-MS performed at the University of Pavia on plagioclase, olivine, pyroxene and matrix glasses showed that only matrix glasses reflect the contribution of exogenous material, whilst the single clasts may preserve the composition of the original lunar crust.

Finally, on three lunar meteorite samples (breccia NWA 13859, lunar basalt NWA 14188, and troctolite NWA 8687), hyperspectral images in the 0.4–2.5 µm were acquired using a new setup available at the University of Padua. This technique quickly allows identification of spectral endmembers on the whole surface of the slab.

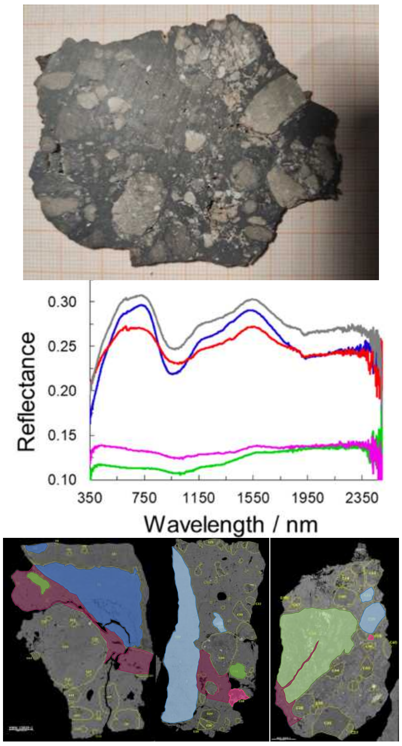

Fig. 4. **Top:** Slab of the meteorite NWA13859 (thickness ~2 mm). **Middle:** Representative reflectance spectra acquired along a transect of the slab. **Bottom:** Maps of the three slab fragments investigated by electron microprobe analysis. The red and green colors identify the Mg-rich and FAN units, respectively. The blue color refers to an intermediate mineralogy.

Acknowledgements: We acknowledge support from the research project: "*Moon multisEnsor and LabOratory Data analYsis (MELODY)*" (PI: Dr. Federico Tosi), selected and funded in November 2020 in the framework of the PRIN INAF (RIC) 2019 call.

References:

[1] Pieters, C.M., et al. (2009) *Current Science, 96* (4), 500-505. [2] Tompkins, S. & Pieters, C.M. (1999) *Meteor. & Plan. Sc.*, *34*, 25–41. [3] Salari, G., et al. (2023) *JGR Planets*, in press. [4] Salari, G., et al. (2023) XIX CNSP, *this conference*. [5] Tognon, G., et al. (2021) *Remote Sensing*, *13* (18), 3619. [6] Tognon, G., et al. (2024) *Earth Space Sci.*, submitted. [7] Tognon, G., et al. (2024) XIX CNSP, *this conference*. [8] Bruschini, E., et al. (2023) *Minerals*, *13* (8), 1000.

3200 PHAETHON, AN ACTIVE ASTEROID: SURFACE ALTERATIONS AND EXPECTATIONS FOR DESTINY+ SPACE MISSION

M. Angrisani[1-2] , E. Palomba[1], E. Rognini[3],G. Pratesi[4] , F. Dirri[1] , A. Longobardo[1], C. Gisellu[1], A. Migliorni[1] ,E. D'Aversa[1] , T. Arai[5], [1]INAF-IAPS Rome, Italy, Via Fosso del Cavaliere, 100 Rome, (marianna.angrisani@inaf.it); [2]Sapienza University of Rome,Italy; [3]ASI Space Science Data Center, Italy, [4]University of Florence, Italy; [4]Planetary Exploration Research Center (PERC), Chiba Institute of Technology, Chiba, Japan

(3200) Phaethon in a nutshell: (3200) Phaethon asteroid is the flyby target of 'DESTINY+' (Demonstration and Experiment of Space Technology for INterplanetary voYage, Phaethon fLyby and dUst Science), a JAXA/ISAS mission with a planned launch on 2024.

3200 Phaethon is supposed to be the parent body of Geminids meteor shower [1]. The top-shaped Phaethon has an effective diameter estimated to be in the range of 5–6 km with a rotation period of ≈ 3.6 h [2,3]. (3200) Phaethon is actually classified as a B-type asteroid [4]. B-type asteroids are commonly linked to dehydrated CI/CM chondrites. The spectral features of CI/CM chondrites are chemically altered from hydrated C-type to B-type by thermal metamorphism [5,6]. Thus, the surfaces of B-type asteroids are considered to be subjected to surface alteration due to thermal metamorphism.

What happens to 3200 Phaethon when it is at perihelion? It is on a 1.434 yr period, highly eccentric (e = 0.889990) orbit that brings it within 0.14 AU of the Sun during the perihelion passage. [7,8,9,10] It has been reported an anomalous brightening and a tail formation around its perihelion in 2009, 2012, 2016, likely due to the ejection of µm-sized dust. By using the observations from 2008 to 2022 by COR2 cameras onboard STEREO and colour imaging by the Solar and Heliospheric Observatory (SOHO) Large Angle Spectrometric Coronagraph (LASCO) during the 2022 May apparition, [11] and [12] concluded that the Phaethon's perihelion activity is not caused by the ejection of dust, but probably associated to gas emission, possibly Fe and/or Na.

However, the non-detection of a 3-µm hydration feature [13] rules out the possibility that Phaethon has hydrated minerals like comets.

A Thermal Model for Phaethon: In order to understand if the thermal processing due to the proximity to the Sun, induced some sort of compositional transformation, triggering material ejection (dust and/or gas), the temperature of Phaethon surface at perihelion have been estimated.

In the case of Near-Earth Asteroids (NEA) a thermal model has been developed and proven to be the most reliable (NEATM; [14]). However, NEATM assumes zero thermal emission on the night side of an asteroid. In order to better understand the thermal cycle on the Phaethon surface, a new thermal model has been developed: the temperature has been calculated by solving the 1D heat equation, by assuming Hanus' spin state solution and shape model as well, by considering the surface thermal inertia, Γ = 600 Jm^{-2} $s^{-0.5}$ K^{-1} and a rotation period, P =3.6 hr [3].

Ground-based observations: From 2007 to 2017 six campaigns have been performed in order to observe Phaethon from Earth at different times and telescopes in the VIS-NIR range [15,16,17,18,19]. All of them have observed it at different phase angles but no relevant spectral features have been found (only one "*weak*" absorption band around 0.43 µm has been reported by [19]). Moreover, some visible spectra showed a positive slope (i.e. *red* slope), whereas other spectra have been characterized by a negative one (i.e. *blue* slope). In order to understand if the observed spectral variability can be associated to the real asteroid surface heterogeneities, the surface portion effectively probed by each observation has been investigated with the shape model by [3]. Then, a complete Phaethon spectral (VIS-NIR range) database including all previous telescopic observations was drew up. Thus, for each observation the geometry, i.e., the observed asteroid portion, has been obtained by using the Phaethon shape model [3].

Results: By the new developed thermal model, it is possible to state that Phaeton can reach a sufficient high temperature for surface dehydration and decomposition due to solar radiation with maximum global temperatures found at the day side equatorial latitudes. Near perihelion passages, Phaethon's south pole is shadowed before the perihelion passage and becomes illuminated during and after the passage reaching temperature such as ≈1050 K (Fig.1).

Furthermore, the spectral phase reddening in the in the ∼0.55-0.7 µm range covering a phase angle range of 20°-80° has been computed and a photometric correction [20] has been applied to avoid misinterpretation of compositional information along the surface.

The phase reddening coefficient is of (5.0±1.7) ×10-3 μm^{-1} deg^{-1}. Later on, a photometric correction at 30° to all the observations has been performed and a slight difference in the photometric corrected spectral slope has been revealed, maybe reflecting a heterogeneity of its surface along the latitude. Moreover, same Phaethon surface's regions are observed under the same instrument, with a different percentage of illumination and don't share the same photometric corrected spectral slope, supports the hypothesis that the portion of illuminated surface can contribute to blueing/reddering Phaethon's spectra.

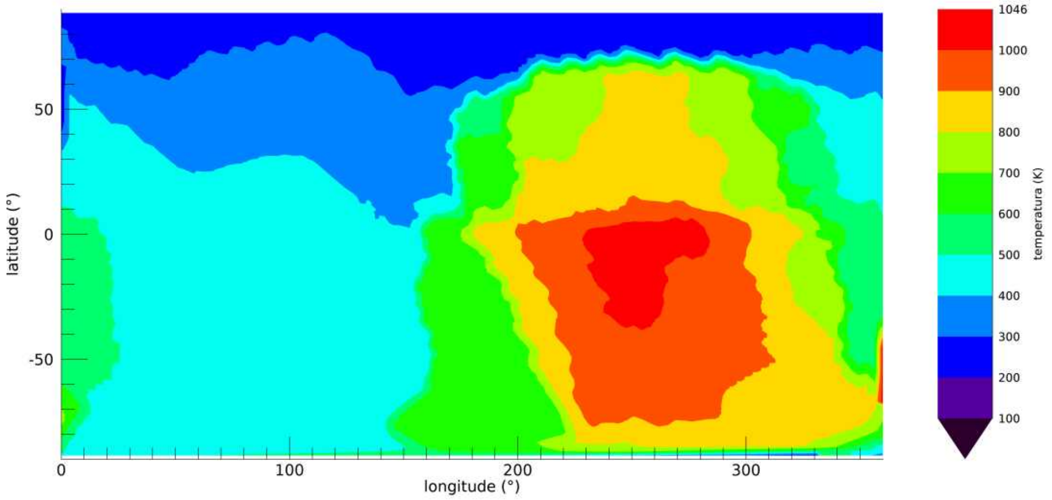

Fig.1: Phaethon surface temperature at the perihelion considering the surface thermal inertia, Γ = 600 Jm^{-2} s$^{-0.5}$ K^{-1} and a rotation period, P =3.6 hr

Acknowledgements: This research is supported by PRIN-INAF-2019. The team thanks Teddy Kareta, Myung-Jin Kim, Javier Licandro and Monica Lazzarin for sharing Phaethon telescopic data.

References:[1]Whipple,1983IAUCirc.,No.3881; [2]Taylor et al., (2019), P&SS, Vol. 167; [3]Hanuš et al. (2018) A&A;[4] De Meo et al. (2009),Icarus 202,160–180;[5]Hiroi et al. 1993, Sci., Vol. 261, Issue 5124, pp. 1016-1018; [6] Hiroi et al 1996, Meteorit. Planet. Sci., Vol. 31 ; [7] Jewitt & Li (2010), Astron. J., Vol. 140, Issue 5, pp. 1519-1527; [8] Jewitt et al. (2013), ApJL, Vol. 771, Issue 2, article id. L36, 5 pp.; [9] Li & Jewitt (2013), Astron. J., Vol.145, Issue 6, article id. 154, 9 pp; [10] Hui & Li (2017) Astron. J., Vol. 153, Issue 1, article id. 23, 7 pp.;[11] Hui et al (2023) Astron. J., Vol. 165, Issue 3, id.94, 13 pp.; [12] Zhang et al.,(2023) Planet. Sci. J., Vol. 4, Issue 4, id.70, 23 pp.; [13] Takir et al. (2020) Nat. C.; [14] Harris(1998),Icarus,131 ; [15] Licandro et al.,(2007), A&A, Vol 461; [16] Kareta et al.,(2018) , AJ, 156:287 (9pp); [17] Lee et al.,(2019)P&SS 165,296–302; [18] Palomba et al.,(2018) 42ndCOSPAR;[19] Lazzarin al., (2019), P&SS, Vol65; [20] Longobardo et al. (2020) MNRSAS, Vol. 496, Issue 1, pp.125-137

Spectral and photometric characterization of (98943) 2001 CC21, fly-by target of Hayabusa2#

J. Bourdelle de Micas[1], D. Perna[1], M.A Barucci[2], I. Belskaya[2,3], E. Dotto[1], S. Fornasier[2,4], S. Hasegawa[5], S. Ieva[1], R. Inasaridze[6], M. Ishiguro[7], K. Kitazato[8], Y. Krugly[3], D. Kuroda[9], E. Mazzotta Epifani[1], E. Palomba[10], and M. Yoshikawa[5], [1]INAF – Osservatorio Astronomico di Roma, via Frascati 33, Monte Porzio Catone, Italy, jules.bourdelledemicas@inaf.it, [2]LESIA, Observatoire de Paris, Université Paris Cité, Université PSL, CNRS, Sorbonne Université, Paris, France, [3]V.N Karazin Kharkiv National University, Ukraine, [4]Institut Universitaire de France, Paris, France, [5]ISAS-JAXA, Japan, [6]E. Kharadze Georgian National Astrophysical Observatory, Abastumani, Georgia, [7]Seoul National University, South Korea, [8]Aizu University, Japan, [9]Kyoto University, Japan, [10]INAF – Istituto di Astrofisica e Planetologia Spaziali, Roma, Italy.

Introduction: Following a successful sample-return mission, the JAXA Hayabusa2 mission has been extended to study two additionnal NEOs. The first target is the asteroid (98943) 2001 CC21. Little is known about this object: its diameter is estimated to be between 420-560m, with an absolute magnitude value of 18.6 [1] and a taxonomic type identified as S-complex [2,3] or L-type [4]. In late 2022 and early 2023, 2001 CC21 became visible for observation through ground-based telescopes.

Objectives: To prepare the upcoming fly-by of 2001 CC21 on July 2026, we decided to analyze this object spectroscopically and with multi-filter photometry. Our goal is to provide more information about its mineral composition, physical characteristics and probable origin.

Methods: Thanks to the European NEOROCKS project, we could obtain spectrophotometric data using the 1.2m telescope located at the Haute-Provence observatory in France, on November 2022. In addition, between January and March 2023, we conducted multiple observations using the 2.6m Nordic Optical Telescope (NOT), based at La Palma, Spain. Through these observations, we obtained spectroscopic data in the visile range (between 0.45 and 1.00 µm) and photometric data with several filters, covering the visible and the near-infrared range at different rotational phase. On January 22, 2023, we observed 2001 CC21 in R band and covered the whole rotational period. The CCD observations were carried out using the 0.70m telescope at the Abastumani Astrophysical Observatory, Georgia.

Results: The lightcurve study reveals an amplitude of 0.75 mag and rotational period of around 5.03 hours. The measurement of 2001 CC21's color indicates that this object is likely an Sq- or Sr-type asteroid, as expected. Examining the spectra, after reduction and combining it with near-infrared data from literature [1], we confirm that classification. Consequently, we do not support the L-type classification [4], as the 1-µm band is clearly present. Preliminary findings indicate that 2001 CC21 has a surface mineralogy close to the ordinary chondrite, specially L or LL types, with a metamorphic grade 6. Consequently, we should not find any traces of hydratation. Being a S-complex, 2001 CC21 may be a collisional fragment from one of the S-type families present in the inner main belt. Further study will be conducted to provide clues about its membership in one of these families.

Acknowledgments: This work received financial support from the Italian Space Agency (ASI) under contract No. 2022-12-HH.0

References: [1] Geem et al. (2023), *MNRAS*, 525:L17. [2] Lazzarin et al. (2005), *MNRAS*, 359:1575, [3] DeMeo et al. (2009), *Icarus*, 202:160, [4] Binzel et al. (2004), *M&PS*, 39:351.

LICIACube: THE LIGHT ITALIAN CUBESAT FOR IMAGING OF ASTEROIDS IN SUPPORT TO THE NASA MISSION DART

E. Dotto[1], M. Amoroso[2], I. Bertini[3,4], J.R. Brucato[5], A. Capannolo[6], S. Caporali[5], M. Ceresoli[6], G. Cremonese[7], M. Dall'Ora[8], V. Della Corte[8], J.D.P. Deshapriya[1], I. Gai[9], L. Gomez Casajus[9], E. Gramigna[9], P. Hasselmann[1], S. Ieva[1], G. Impresario[2], S.L. Ivanovski[10], R. Lasagni Manghi[9], M. Lavagna[6], M. Lombardo[9], A. Lucchetti[7], E. Mazzotta Epifani[1], D. Modenini[9], M. Pajola[7], P. Palumbo[4], D. Perna[1], S. Pirrotta[2], G. Poggiali[5], A. Rossi[11], P. Tortora[9], F. Tusberti[7], M. Zannoni[9], G. Zanotti[6], A. Zinzi[12,2].
[1]INAF Osservatorio Astronomico di Roma, via Frascati 33, 00078 Monte Porzio Catone (Roma), Italy, elisabetta.dotto@ inaf.it , [2]Agenzia Spaziale Italiana, Roma, Italy, [3]Università degli Studi di Napoli "Parthenope", Napoli, Italy, [4]INAF Istituto di Astrofisica e Planetologia Spaziali, Roma, Italy, [5]INAF Osservatorio Astrofisico di Arcetri, Firenze, Italy, [6]Politecnico di Milano, Italy, [7]INAF Osservatorio Astronomico di Padova, Italy, [8]INAF Osservatorio Astronomico di Capodimonte, Napoli, Italy, [9]Università di Bologna, Bologna, Italy, [10]INAF Osservatorio Astronomico di Trieste, Italy, [11]CNR Istituto di Fisica Applicata "Nello Carrara", Sesto Fiorentino (Firenze), Italy, [12]Space Science Data Center-ASI, Roma, Italy.

Introduction: The Light Italian Cubesat for Imaging of Asteroids (LICIACube) [1] is a 6U CubeSat developed for the Italian Space Agency (ASI). LICIACube was carried by NASA's Double Asteroid Redirection Test (DART) spacecraft and was deployed 15 days in advance of DART's impact with the asteroid Dimorphos [2] to acquire images of the event and its effects. During its post-impact flyby, LICIACube achieved a minimum distance of approximately 58 km from Dimorphos and returned more than 400 scientific images, obtaining a unique view of the event [3].

The DART/LICIACube mission: The Double Asteroid Redirection Test (DART was launched on 24 November 2021 to perform the first test of a planetary defence mitigation technology, redirecting the asteroid Dimorphos, the small satellite of the binary Near Earth Asteroid (NEA) (65803) Didymos [4], via a kinetic impact. During the 9.5-month cruise, LICIACube was hosted on the DART spacecraft. On 11 September 2022, fifteen days before DART's kinetic impact, LICIACube was released and autonomously continued its track toward the binary asteroid system. LICIACube is equipped with two different cameras, LICIACube Explorer Imaging for Asteroid (LEIA) and LICIACube Unit Key Explorer (LUKE) [1]. The science phase started 71 seconds before the nominal impact time, when LICIACube was about 1400 km from Dimorphos. The science phase of LUKE started 29 seconds after the impact, acquiring triplets of images with different exposure times. LICIACube followed the target and the evolution of the system up to 320 seconds after the impact. The spacecraft's Closest Approach (CA) occurred 167 s after the impact.

The LICIACube images: LEIA images testified the DART impact by an increase in the luminosity of the target, while LUKE images reveal that the DART impact into Dimorphos generated a cone of ejected material with a large aperture angle [3]. In the LICIACube viewing geometry, the produced effects were clearly seen in both pre-CA and post-CA LUKE images (Fig. 1). The ejecta plume shows a complex and inhomogeneous structure, characterised by filaments, dust grains, and single or clustered boulders, providing insights into the properties of the ejecta, as well as the nature of Dimorphos. Measurements from the LICIACube images constrain the asteroid shape [5], and the 3D shape of the cone plume [6]. Moreover, they inform the calculations of the momentum transferred to Dimorphos by DART's kinetic impact [7]. The accomplishments of LICIACube demonstrated the compelling potential for future deep-space CubeSats.

Figure 1. *Images obtained by LUKE pre-CA and post-CA.*

Acknowledgments: The LICIACube team acknowledges financial support from Agenzia Spaziale

Italiana (ASI, contract No. 2019-31-HH.0 CUP F84I190012600).

References: [1] Dotto E., et al. (2021) PSS 199, id. 105185. [2] Daly R.T., et al. (2023) Nature 616(7957), 443. [3] Dotto E., et al. (2023) Nature, in press. [4] Rivkin A.S., et al. (2021) PSJ 2(5), id.173. [5] Zinzi A., et al. (2023) PSJ in press. [6] Deshapriya J.D.P., et al. (2023) PSJ 4 id.231. [7] Cheng A.F., et al. (2023) Nature, 616(7957), 457.

SPECTROSCOPIC INVESTIGATION OF A POTENTIAL MARS ANALOG SITE: LAKE BAGNO DELL' ACQUA, PANTELLERIA, ITALY.

E. Bruschini[1], M. Ferrari[1], C. Mazzoni[2,3], S. Fazi[2,3], F. L. Chiocci[4,5], I. Mazzini[5], G. Costanzo[6], S. De Angelis[1], M. C. De Sanctis[1], F. Altieri[1], J. Brossier[1], E. Ammannito[7], [1]Institute for Space Astrophysics and Planetology INAF, Rome, Italy (enrico.bruschini@inaf.it), [2]Department of Biology and Biotechnology "Charles Darwin" Sapienza University of Rome, Rome, Italy, [3]Water Research Institute, National Research Council of Italy IRSA CNR, Montelibretti, Rome, Italy, [4]Department of the Earth Sciences Sapienza University of Rome, Rome, Italy, [5]Institute of Environmental Geology and Geoengineering National Research Council IGAG CNR, Montelibretti, Rome, Italy, [6]Institute of Molecular Biology and Pathology National Research Council IBPM CNR , Rome, Italy, [7]Italian Space Agency ASI , Rome, Italy

Introduction: Analog sites on Earth are places characterized by one or more features similar to those observed or inferred on planetary surfaces (e.g. [1]). So far, many sites have been identified and studied, but many other potential analog sites still need to be characterized. Concerning Martian analog sites, one interesting area is Lake Bagno dell'Acqua, which is an endorheic (closed) alkaline ($pH \geq 9$) lake located in the island of Pantelleria in Sicily, Italy. The lake was proposed to be a Martian analog site [2] but while there are a few mineralogical investigations of the lake sediments [3-4], so far, a comprehensive characterization of the lake is lacking. We report here the combined Visible to Near Infra–Red (VNIR) reflectance and Raman Spectroscopy investigation of a suite of nineteen samples from the studied area. The organic fraction of the samples was also investigated (DNA sequencing and fluorescent microscopy) to describe its composition and the spatial distribution of microbial communities. Our investigation will improve the comprehension of sediments derived by alkaline aqueous alteration and highlights the complex interplay between organic matter and inorganic matrix.

Materials and Methods: The samples were collected as push cores inside the lake and as loose sediments taken along the eastern and southeastern lake's shore. The samples underwent three thermal cycles (343 K for 24 hours, hereafter LT treatment, 383 K for 24 hours, MT treatment, and 473 K for 48 hours hereafter HT treatment) to remove excess water and organic matter. The VNIR reflectance spectra (350–2500 nm) were measured on each powdered (< 50 µm) sample after each thermal cycle to check the variation in the spectral features as a function of thermal treatment. The confocal Raman microscopy (µ-Raman) measurements were carried out on the fraction of the sediments heated after the LT treatment to characterize both the organic and inorganic components of the sediments. DNA sequencing allowed us to identify the main bacteria phyla and their abundance. A Confocal Laser Scanning Microscope (CLSM) was used to visualize the structure of the microbial community after staining the sediments with appropriate reagents (DAPI solution and Calcofluor-White)

Results and Discussions:

VNIR spectroscopy.

The spectral region between 350 and 1200 nm is characterized by complex absorptions in the LT and MT spectra which disappear after the HT treatment (Fig. 1A). The most prominent feature is a narrow and symmetric absorption at about 670 nm associated with other absorptions at 615, 410, 550 and 950 nm. At longer wavelengths the samples are characterized by complex absorption features roughly centered at 1400 nm (Fig. 1B), 1900 nm (Fig. 1C), 2310 and 2385 nm (Fig. 1D).

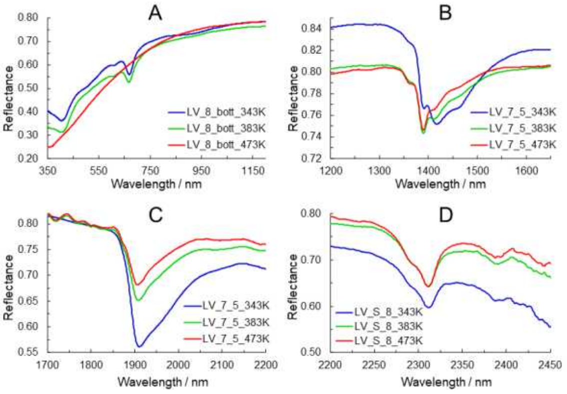

Figure 1. Reflectance spectra of representative spectra collected after LT (blue lines), MT (green lines), and HT (red lines) thermal treatments. Panel (A) shows a typical spectrum between 350 and 1200 nm. Panel (B) and panel (C) show the 1.4 µm and 1.9 µm bands for a representative sample. Panel D shows the absorptions between about 2310 nm and about 2390 nm characterizing most of the samples.

The VNIR spectral features indicate a very low amount of transition elements (i.e., iron) in the samples indeed the red line of HT spectra in Fig. 1 shows no absorption features between 350 and 1200 nm while in the same spectral range, the spectral features of the LT and MT spectra (blue and green lines in Fig. 1) suggest the presence of organic materials.

µ-Raman spectroscopy.

The samples were characterized by confocal µ-Raman spectroscopy to identify both inorganic and organic phases (Fig. 2). Mineralogical content of the push cores shows very little heterogeneity. Conversely the sediments collected on the shores are characterized by a higher mineralogical heterogeneity including mafic minerals which are however minor phases in the sediments.

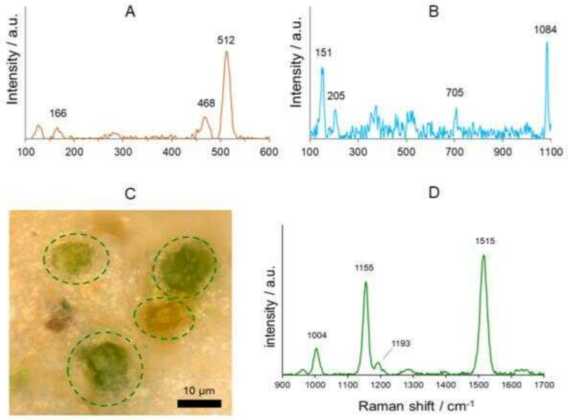

Figure 2. Representative Raman spectra for the investigated samples. Panel A and B show inorganic phases of the push cores while panel C shows the microphotograph of carotenoids founds in the sediments whose spectrum is showed in panel D.

The Raman spectra of the vast majority of the samples display a characteristic peak between 512-515 cm^{-1} (Fig 2A) which often is the only peak that is possible to distinguish due to intense fluorescence signal. Another Raman peak observed in many of the samples is centered at about 1083-1084 cm^{-1} (Fig 2B).

Microbial community characterization.

The microbial communities living in the sediments of Lake Bagno dell'Acqua are characterized by a rich diversity. The phylum Chloroflexi, present in all samples, is one of the large phyla containing bacteria with various metabolic features. Among these, there is also a phototrophic group, called filamentous anoxygenic phototrophic bacteria, capable of synthesizing carotenoids. These molecules are also synthesized by Proteobacteria and Cyanobacteria. All these microorganisms are present in the analyzed sediments and are embedded in a thick layer of Extracellular Polymeric Substance (EPS; Fig. 3).

Mineralogy and microbiology of Lake Bagno dell'Acqua.

The most represented minerals in the discussed samples are Mg-smectites detected through VNIR reflectance and carbonates (aragonite) identified via Raman spectroscopy (most intense peak at 1083 cm^{-1}). Clays are difficult to analyze with Raman spectroscopy due to intrinsic fluorescence phenomena [5], however the fact that we could not detect any clay spectrum in the samples using Raman spectroscopy but instead we detected the signal from K-feldspar (strongest peak at 512-515 cm^{-1}) in almost any sample could imply an incipient transformation: K-feldspar to Mg-smectite. The detected clay is likely characterized by a quite disordered structure or low crystallinity. Carbonate precipitation is also induced by the microorganisms which act like nucleation centers.

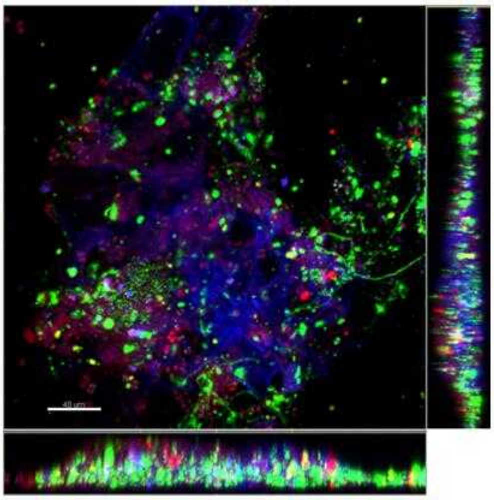

Figure 3. The superficial layer of sediments in LV_S_8: CLSM combined images showing the spatial distribution (X−Y, X−Z, and Y−Z planes) of DAPI stained cells and EPS stained by Calcofluor-White (blue), bacterial cells identified by CARD-FISH (green), autofluorescent Cyanobacteria (red). Bar length: 40 µm.

The carotenoids observed and detected with µ-Raman spectroscopy are very well explained by the high abundance of Bacterial Phila that can synthesize these molecules while the other detected phase can be attributed to EPS.

Conclusions: The physico-chemical features of the lake's water allow the formation of sediments enriched in Mg-smectite and carbonates. The association of these mineral phases was identified on Mars. The lake is also characterized by a rich microbial activity which influences the precipitation of carbonates. All these characteristics suggest that Lake Bagno dell'Acqua can be considered a very interesting Martian analog field site and its in-depth mineralogical, chemical, and biological characterization would indubitably help to shed light on the alkaline aqueous alteration processes occurred on Mars in its early history. The characterization of alkaline aqueous system is particularly useful if compared with more common acidic systems.

References:

[1] Farr T. G. (2004) *PSS, 52(1-3),* 3–10. [2] Baliva A., Marinangeli L., Piluso E., Ori G. G., and Ruscito V. *BAAS., 31,* 1145, id 47.04. [3] Cangemi M., Madonia P., & Speziale S. (2018) J. Limnol. 77(2), 220, 23. [4] Azzaro E., Badalamenti F., Dongarrà G. & Hauser S. (1983) Chem. Geol. 40(1-2), 149-165. [5] Demaret L., Lerman H. N., McHugh M., Hutchinson I. B., Fagel N., Eppe G., & Malherbe C. (2023) J. Raman Spectrosc 54(8), 823-835.

TRACE ELEMENT AVAILABILITY AND THE EVOLUTION OF BIOGEOCHEMISTRY: A PLANETARY PERSPECTIVE. D. Giovannelli[1,2,3,4,5], M. Selci[1,5], A. Bastianoni[1], A. Ricciardelli[1], D. Corso[1], S. Castaldi[1], D. Bastoni[1], B. Barosa[1], M. Cascone[1], F. Montemagno[1], M. Correggia[1], L. Tonietti[1,6], F. Migliaccio[1], F. Oliva[1], N. Nappi[1], M. Licata[1], A. Pelicciari Silva[1], J. Brusca[1], S. Diana[1], A. Longo[1], G. Climent Gargallo[1], M. Esposito[1], G. Gallo[1], R. Iacono[1], L. Di Iorio[1], A. Rotundi[6], M. Moracci[1], A. Pollio[1], R. Isticato[1], G. Covone[7], A. Cordone[1], [1]Department of Biology, University of Naples Federico II, Monte Sant'Angelo, Ed. 7, 80122, Naples – Italy, [2]Institute for Marine Biological Resources and Biotechnologies, National Research Council (CNR-IRBIM), Ancona – Italy, [3]Earth-Life Science Institute, Tokyo Institute of Technology, Ookayama, Tokyo – Japan, [4]Marine Chemistry & Geochemistry Department, Woods Hole Oceanographic Institution, Woods Hole, MA – USA, [5]Department of Marine and Coastal Science, Rutgers University, New Brunswick, NJ – USA, 6Department of Science and Technology, University of Naples Parthenope, Naples, Italy, [7]Dipartimento di Fisica, University of Naples Federico II, Monte Sant'Angelo, 80122, Naples

Introduction: Earth's geosphere and biosphere have coevolved for the last ~4 billion years keeping the planet habitable and enabling the development of complex life. Among the numerous events that controlled the life-planet coevolution, like the onset of plate tectonics and the formation of the moon among others, the change in planetary surface redox conditions arguably had the greatest impact, influencing mineralogy, geochemistry and biology alike and contributing to the evolution of biogeochemistry.

Extant biogeochemistry is controlled by a small set of microbial-encoded proteins containing redox-sensitive transition metals as their core catalytic centre includes, among others, Fe, Mo, W, Zn, Cu, V, Mn, Mg, Ni and Co [1]. The distribution and availability of these essential trace metals is controlled by geological and geochemical processes, including tectonics, volcanism, rock weathering and local redox conditions, and thus change over time [2] (Figure 1). These changes have influenced the diversity of redox couples available for energetic metabolisms and the available trace elements that could be used to access them, creating a complex network of geo-bio interactions.

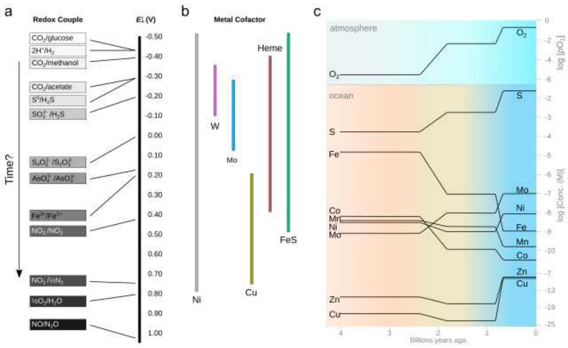

Fig. 1. Relationship between redox metabolic couples mid point potential (a) with a possible embedded time axis (marked with a?), metal cofactors used in metalloproteins and the extension of their midpoint potential (b), and changes in biologically relevant metal concentrations through time as a consequence of planetary surface redox alterations (c). Changing surface redox conditions mutated both the availability of redox couples and the availability of transition metals used to access them.

Yet, despite these geosphere-biosphere connections, fundamental knowledge regarding the distribution and availability of transition metals in controlling microbial functional diversity, even in extant ecosystems, is scarce. Past and ongoing research indicate a strong connection between the environmental availability of trace metals and their utilization as cofactors influencing microbial functional diversity.

Here, we will discuss combined data from astronomy, geochemistry, microbial ecology and microbial physiology of diverse laboratory models to show that the availability of trace metals can impose a strong control on the taxonomic and functional diversity of microorganisms, and that it can be used as a powerful explanatory tool to investigate the emergence and evolution of biogeochemistry on this planet [2] and the search for life elsewhere [3]. Understanding the roles of trace metal environmental distribution and availability in controlling microbial taxonomic and functional diversity holds the key to understanding the co-evolution of life and the planet and has the potential to contribute new tools required to understand and manipulate microbial metabolism in diverse ecosystems.

References: [1]. Hay Mele B. et al. (2023) *Essays in Biochemistry* **67**, 1–18 (2023). [2] Giovannelli D. (2023) *Nat Rev Earth Environ*, 1–2 (2023). [3] Covone G. and Giovannelli D. (2022) *arXiv,* 2207.03748.

Acknowledgments: This work was supported by funding from the European Research Council (ERC) under the European Union's Horizon 2020 research and innovation program Grant Agreement No. 948972—COEVOLVE—ERC-2020-STG.

A MULTIDISCIPLINARY APPROACH TO EXPLORE HOW LIFE MIGHT ORIGIN AND PERPETUATE ON MARS USING PLANETARY FIELD ANALOGUES: A COMPARISON BETWEEN THREE PROJECTS.

M. Pedone[1*], M.E.M Gangi[1], C. Pacelli[1], M. Bellucci[1], S. Pezzilli[1], D. Billi[2], L. Selbmann[3], B. Cavalazzi[4], B. Negri[1]
[1]Agenzia Spaziale Italiana, ASI, via del Politecnico snc, 00133 Rome, Italy
([*]corresponding author mail address: maria.pedone@asi.it)
[2]University of Rome Tor Vergata, Department of Biology, Via della Ricerca Scientifica snc, 00113 Rome, Italy
[3]Dept of Ecological and Biological Sciences, University of Tuscia, Via Santa Maria in Gradi 4, 01100 Viterbo, Italy
[4]UNIBO-Centro Interdipartimentale di Ricerca Industriale – Ciri Aerospaziale, Via Baldassarre Carnaccini 12, 47121 Forlì, Italy.

Introduction: The Italian Space Agency (ASI) has promoted the definition of a national long-term Astrobiology Roadmap [1], a common platform for the scientific communities working on different topics with the aim to create synergies and identify future opportunities for joint activities. This far-seeing initiative is strengthened by the need to optimize the Italian contribution to the international activities and programs in the next decade of research, exploration and discoveries in the field of Astrobiology. In preparing this long-standing strategy for scientific activities, the Roadmap identifies specific areas of interest for the community: analogue environments and extremophiles; the development of more effective proxies for life detection (biosignatures); macromolecule synthesis, stability, and function in the context of plausible prebiotic conditions and environments; development of activities, including space missions, scientific experiments and theoretical modelling, devoted to the detection of life as well as to the determination of habitable conditions within worlds beyond Earth.

Among the identified areas of interest for ASI, the Planetary Field Analogues (PFA) are considered hot topic since they help our understanding of where and how life (as we know it) may exist and evolve, how we can search life beyond Earth and prepare future exploration missions [2-5]. Among the seven projects funded by ASI in the Announcement of Opportunity for the support of scientific experimentation/project in the field of Astrobiology (2022), three projects, ASTERIA, CRYPTOMARS, and HELENA, share the study of the origin of life, evolution and habitability in PFA by combining approach of planetary science, geology and microbiology.

The projects will be carried out for three years and they will investigate microbial communities living in extreme environments considered terrestrial analogues of the Martian environment, the potential for preserving life itself in such extreme environments, as well as investigating the implications regarding the origin of life which could have started its history from a similar habitat, according to recent hypotheses. In this context, CRYPTOMARS project aims to identify which genetic and functional characteristics would allow a microbial community to resist, adapt, spread and perpetuate itself on Mars or on Mars-like planets. To this purpose, a comparative analysis of microbial communities, known as cryptoendolithic, living in ice-free cold areas in continental Antarctica (e.g., the McMurdo Dry Valleys), will be conducted. Given the analogy of the geological history of the planet Mars with these areas, in fact, these ecosystems are optimal models for studying the characteristics and adaptations that may allow life settlement. During the project, a wide range of selected rocks samples (cryptoendolithic communities) will be exposed to different physical and climatic stresses simulating past and present Martian environments, such as UV and ionizing agents, dehydration and extreme temperatures. After exposure to stress, the survival responses of these microbial communities will be investigated, by using a metabolomic and lipidomic approach. These results will be then integrated with the genomic data previously collected to better understand the genetic and metabolic specific pathways involved in the resistance and survival of the cryptoendolithic communities. A study with such a multidisciplinary approach, where biological, chemical and physical skills interact synergistically, will allow identifying and characterizing the diversity and metabolic characteristics that a community, *in toto*, potentially capable of colonizing the Martian environment should have.

The ASTERIA project will investigate the adaptive potential of cyanobacteria to stellar ultraviolet radiation (UVR) through a multidisciplinary approach based on laboratory simulations and theoretical models. Cyanobacteria isolated from environments with low light conditions enriched in far-red/infrared, such as communities colonizing rocks in hot and cold deserts, will be used as a model system. Their growth and survival limits will be analysed after exposure to UVR, while the adaptability of the most resistant isolates will be tested through laboratory simulations of paleo-planetary environmental conditions. Additionally, their photosynthetic activity will be monitored in real time during exposure to simulated solar and M-star spectra, in the presence of UVR, while cellular survival will be tracked using miniaturized experiment units. Omics techniques, including transcriptomics and comparative genomics, will be employed to identify resistance mechanisms under simulated conditions, particularly photoprotection mechanisms such as UV-protective pigments and DNA repair systems. The results of this project will contribute to a better understanding of the only type of life known to us, providing valuable insights into the past habitability conditions of Mars and the possibility of oxygenic photosynthesis on planets orbiting stars different from the Sun.

Finally, the HELENA project aims at characterizing the extreme and polyextreme habitats of Lake Bagno dell'Acqua (LBA), in the Pantelleria Island National Park in Sicily. This study will be carried out in an astrobiological perspective through a combined approach for the comprehensive characterization of the site chosen as a "terrestrial analogue" (PFA) and laboratory analogue (LA), in order to be used for the preparation (of concepts and simulations) of future Mars exploration missions. The project involves the integration of astrobiology skills with those of planetary sciences with a particular focus on the analysis of potentially inherited structures in the fossil record and on the presence of accumulations of phosphate, considered a biogenic element of extreme importance in astrobiology and for the origin of life, on the sediments and surfaces of the lake.

Besides the common thematic of PFA study, the three projects could benefit from synergies and sharing of methods and results. In ASTERIA and CRYPTOMARS, the growth, resistance and adaptability of the microorganisms, which are isolated in extreme habitats, will be studied in a dedicated chamber simulating the conditions (past and present) on Mars-like environments. The operational parameters will be selected on the basis of modelling studies on planetary climate and atmosphere, while the genetic and metabolic response to stresses derived from UV radiation will be investigated by molecular tools.

While in CRYPTOMARS and ASTERIA one of the main objectives is to develop and validate a realistic model of the adaptability of microbes in environmental Mars-like conditions following laboratory and computational tests, in HELENA a model will be developed on the basis of the actual physico-chemical characteristics of the bedrock and water columns of the vulcanic Sicilian target.

The final models of the three projects will also describe the interactions between the microbial community structure and geochemical composition of substratum. As a matter of fact, a comparison of response to physical stresses as well as of substrate and habitat in terms of differences between cold arid deserts (CRYPTOMARS), hydrothermal vents (ASTERIA), volcanic lakes (HELENA) will be carried out in a synergy between researchers of prime and partners and the ASI staff of project managers, project scientists. In particular, by investigating the responses of Antarctic microbial communities and cyanobacteria to different kind of radiation, and by characterizing the microbiomes of Lake Bagno dell'Acqua, we aim at defining and expanding the boundary conditions under which life can thrive. Also, by studying the strategies adopted by microorganisms to resist simulated or real stressful conditions, we may identify an unexpected mechanism of resistance. This integrative approach, may outline the physical and chemical boundary conditions of Earth's environments and compare them to the conditions observed on other planetary bodies to discuss whether life could originate, evolve, or survive elsewhere in our Solar System.

In conclusion, we would promote the possibility to create a common platform for the scientific communities working on different topics in order to create synergies and identify future opportunities for joint activities, not only inside the projects described, but together to the ongoing research and the next.

Acknowledgements: The present abstract was concieved to promote and describe the contribution of the Italian Space Agency in the field of Astrobiology in support of the future space missions, human and robotic. The authors thank the ASI funding and the Directorate of Science and Research of ASI.

References: [1] Negri B. et al. (2022) Roadmap for Astrobiology – ASI. [2] Preston L. J., and Dartnell L. R. (2014) *International Journal of Astrobiology*, 13(1), 81-98. [3] Cassaro A., Pacelli C., Aureli L., Catanzaro I., Leo P., and Onofri S. (2021) *Extremophiles*, 1-22. [4] Foucher F., Hickman-Lewis K., Hutzler A., Joy K. H., Folco L., Bridges J. C., ... and Westall F. (2021) *Planetary and Space Science*, 197, 105162. [5] Merino N., Aronson H. S., Bojanova D. P., Feyhl-Buska J., Wong M. L., Zhang S., and Giovannelli D. (2019). *Frontiers in microbiology*, 10, 780.

ORGANIC OR NOT ORGANIC? UPDATES FROM THE NASA MARS 2020 MISSION. T. Fornaro[1] and J. R. Brucato[1], [1] INAF-Osservatorio Astrofisico di Arcetri, Largo E. Fermi 5, 50125 Firenze, Italia, teresa.fornaro@inaf.it

Introduction: The Perseverance rover of the NASA Mars 2020 mission is currently operating on Mars at the Jezero crater, a site of an ancient lake in the past, to look for biosignatures in rocks characterized by high preservation potential, select and cache astrobiologically relevant samples to be returned to Earth by the subsequent NASA-ESA Mars Sample Return (MSR) Campaign to perform detailed analyses with the most advanced instrumentations available in terrestrial labs. The main criterion to assess the astrobiological relevance of a Martian sample is the presence of minerals characterized by high biosignature preservation potential and organic matter. The primary instrument onboard the Perseverance rover capable of detecting organic matter is SHERLOC, a deep UV resonance Raman and fluorescence spectrometer designed to map the distribution of organic molecules and minerals on rock surfaces at a resolution of 100 µm, utilizing a 248.6-nm DUV laser <100 micron spot size. Additional evidence can be provided by the SuperCam instrument, which combines Time Resolved Raman (532 nm) and Luminescence, visible and Near InfraRed (400–900 nm, 1.3–2.6 µm) reflectance spectroscopy. Both SuperCam and SHERLOC instruments are based on non-destructive spectroscopy techniques, which should not alter the organic matter possibly contained in the samples, nor any clues to their biogenicity/abiogenicity, facilitating identification of non-refractory organic compounds such as potential biomarkers of extant life.

Results: SHERLOC has observed various different fluorescence features that might be consistent with the presence of organic compounds both in the igneous rocks of the Jezero Crater Floor and the sedimentary rocks of the Jezero Delta Front. In the igneous rocks of the crater floor, the general spatial correlation between these detections and minerals that have undergone substantial aqueous processing, such as sulfates and carbonates, suggests that organic molecules may have been abiotically aqueously deposited or synthesized within these altered volcanic materials within the Crater Floor [1]. These results indicate that a complex organic geochemical cycle may have existed as evidenced by several distinct pools of possible organics. Also in the sedimentary rocks at the Delta Front, deposited under habitable conditions as mud and fine sand settled in an evaporating saltwater lake, SHERLOC's analysis indicates the presence of possible organic molecules spatially correlated with sulfate minerals.

However, it is very challenging to confirm the organic origin of the SHERLOC fluorescence observations and specifically identify these molecules with the Mars 2020 payload because they are present at relatively low concentrations and therefore difficult to detect by Raman, while the more sensitive fluorescence technique cannot return very specific information about the molecular structure.

It is important to highlight that luminescence can be caused by non-organic sources as well as organic. The SHERLOC excitation in the deep UV has been chosen to resonantly enhance the Raman scattering of one- and two-ring aromatics and at the same time avoid most of the interfering luminescence responses from rare earth elements (REEs), which in most cases have emissions at wavelengths higher than the SHERLOC spectral range (more than 360 nm) [2]. The only REE that can generate emissions within certain minerals in the detection range of SHERLOC is cerium. For example, Ce^{3+} in phosphates has been reported to emit roughly 340 nm luminescence [3] that resembles some fluorescence detections by SHERLOC, and it is difficult to discern if both organic and inorganic sources, or inorganic sources alone, contribute to these signals, as REE-bearing phosphates and organics preserved in phosphates have both been reported within martian meteorites [4][5]. Phosphates crystallized from magma always contain ~10-1000 ppm cerium in martian meteorites and in most Earth rocks. Moreover, in the literature double peaked emissions in the SHERLOC wavelength range, at 319/339 and 322/339 nm, have been reported for Ce^{3+} in pentahydrated sulfates and anhydrous sulfate, respectively, and at 304/327 nm for synthetic heat-treated anhydrite doped with Ce^{3+} [6], which is the closest to one of the most widespread SHERLOC observations both at the Crater Floor and Delta Front.

In this contribution, we will review the most recent results from Perseverance, and we will present our current laboratory efforts that might help discern between organic vs inorganic origin of the SHERLOC observations.

References:

[1] Sharma S. et al. (2023) *Nature*, *619*, 724–732.
[2] Gaft M. and Panczer G. (2013) *Mineralogy and Petrology*, *107*, 363–372. [3] Shkolyar S. et al. (2021) *Icarus*, *354*, 114093. [4] Liu Y. et al. (2016) *Earth and Planetary Science Letters*, *451*, 251-262.
[5] Agee C. B. et al. (2013) *Science*, *339*, 780-785.
[6] Baumer A. et al. (1997) *Chemical Geology*, *138*(1–2), 73-80.

THE PANTELLERIA *BAGNO DELL'ACQUA* LAKE: A NEW MARS-LIKE ENVIROMENT AS A REACTOR FOR PREBIOTIC CHEMISTRY

G. Costanzo[1], C. Mazzoni[2], A. Cirigliano[1], E. Bruschini[3], M. Ferrari[3], M. C. De Sanctis[3], F. Altieri[3], J. Brossier[3], E. Ammannito[4], [1]Institute of Molecular Biology and Pathology National Research Council IBPM CNR, Rome, Italy (giovannamaria.costanzo@cnr.it), [2]Department of Biology and Biotechnology "Charles Darwin" Sapienza University of Rome, Rome, Italy, [3]Institute for Space Astrophysics and Planetology INAF, Rome, Italy, [4]Italian Space Agency ASI , Rome, Italy

Introduction: The ongoing exploration of planets such as Mars is producing a wealth of data which is being used to shape a better understanding of potentially habitable environments beyond the Earth. On Mars, the relatively recent identification of minerals that indicate the presence of neutral/alkaline aqueous activity has increased the number of potentially habitable environments that require characterization and exploration. The study of terrestrial analogue environments enables us to develop a better understanding of where life can exist, what types of organisms can exist and what evidence of that life may be preserved. Recently, a new site has been identified in Italy and its characterization has begun: the *Bagno dell'Acqua* Lake, located on the island of Pantelleria in Sicily, Italy. The possibility that cyclic ribonucleotides could polymerize abiotically *in situ* opens up the possibility of investigating the origin of life in interesting extraterrestrial analogues.

Materials: 3',5'cGMP (hereafter abbreviated as cGMP), was obtained from BioLog LSI (Bremen) in acid form (3',5' cGMP, H^+) as 1 mM solution in water, pH 3.4. The compound was custom made and specially purified in order to guarantee the maximal possible purity relative to the absence of adducts-forming cations (mostly Na^+), and the absence of evaporation or precipitation steps in the course of the whole process.

Methods: Polymerization of the cyclic nucleotides was performed as described in [1]. Typically 150 μL of 1 mM cyclic nucleotide solution ($1.5x10^{-7}$ mol, Na^+-free, H^+ form) was concentrated from the initial 1 mM concentration in Super Purity unbuffered water by evaporation in Savant SpeedVac Concentrator in Eppendorf plastic tubes and cooling mode till the desired dryness was achieved. Dried samples were resuspended *in situ* with 150 μL of lake water (filtered with 0.22μ MF-Millipore membrane filters) or with Romil-SpS Super Purity water as control and incubated as described in the Results section. After incubation, samples were precipitated by the addition of 3 μL of glycogen (Thermo Scientific 20 μg/μL in water), 0.3 M (final volume) of sodium acetate pH 7.5 and 3 volumes of 96 %. Once in the laboratory, the samples were centrifuged, washed once with a 70 % ethanol/water mixture, dehydrated, terminal labeled with [γ-^{32}P]ATP, suspended in 100 % formamide and separated on 18% polyacrylamide gels (19:1 ratio acrylamide:N,N'-methylene-bis-acrylamide) containing 7 M urea, in 1 × TBE buffer. **HPLC:** The samples were analysed by a 1260 Infinity HPLC (Agilent, Ca, USA) equipped with Diode Array Detector (DAD) and automatic sampler. The injected volumes ranged from 2 to 20 µl. A Phenomenex (Ca, USA) column Clarity® oligo-RP (150x4.6mm, 3µm) was used as the stationary phase. The mobile phase was constituted by solution A: 10mM TPCA, and solution B: methanol. The analyses were carried out at 40°C according to the following scheme: T0 TPCA 80% methanol 20%, T30 min TPCA 50% methanol 50%, hold until T45 min. Flow rate was 0.8 ml/min and spectra were collected at 255 nm.

Results and Discussions:

Since the definition of the problems concerning the first steps of the origin of the RNA world [2] numerous scenarios have been proposed. Favored scenarios consist of syntheses of long RNAs in icy environments or on mineral surfaces and usually involve the use of highly activated phosphoimidazolide precursors. Verlander and Orgel reported in 1973 that mildly activated 2',3' cyclic nucleotides may also serve as plausible precursors for the synthesis of short RNA-sequences [3] . More than three decades later, using the more sensitive autoradiographic detection technique, some of us reported that 3',5' cyclic nucleotides also oligomerize and that especially the free acid form of 3',5' cyclic GMP, due to its unique stacking properties, could play a dominant role in the abiotic generation of the first oligonucleotide sequences [1]. Polymerization of cGMP, a chemical process that could lead to the very first biopolymers on the early Earth, was revisited in dry form as well as in aqueous solution [4]. For the first time, here we show cGMP polymerization experiments outside the laboratory conditions and in a potentially analogous Martian environment. Analog sites on Earth are places characterized by one or more features similar to those observed or inferred on planetary surfaces (e.g. [5]). So far, many sites have been identified and studied, but many other potential analog sites still need to be characterized. Concerning Martian analog sites, one interesting area is Lake *Bagno dell'Acqua*, which is an endorheic (closed) alkaline (pH ≥ 9) lake located on the island of Pantelleria in Sicily, Italy. The lake was proposed to be a Martian analog site [6] but while there are a few mineralogical investigations of the lake sediments [7-8], so far, a comprehensive characterization of the lake is lacking. Table 1 shows the water chemical composition of the lake as reported in [9].

Date	T	pH	Na	K	Ca	Mg	Cl	Br	SO4	Alk	TDS (g/l)
1881			173	5.29		4.03	159		7.1	58	10.2
1963			264.2	9.87	0.5	5.6	197.5		14.4	37.8	14.2
1966			210	5.91	0.2	6.91	160		7.1	72.8	11.2
June 1980	21.4	9.1	272	8.6	0.3	9.3	227.5		13.8	62.1	15.5
Sept. 1980	26.2	9	281	10.2	0.3	10.3	232.9	0.43	14.9	63.2	16.0
Dec. 1980	15.3	9	278	14.6	0.2	9.7	229.2		20.3	63.4	16.2
June 1987		9.1	310	10.3	0.1	10.8	255	0.36	17.9	61.5	17.6
April 1989	23.5	9.1	357	10.6	0.3	12.9	301		19.9	67.2	20.4
May 1990	24.5	9.2	313	13.7	0.5	12.1	260		22.9	58.7	18.2
1990	26	9	384.8	20.5	0.5	7.98	340		20.6	79.8	22.8
Jan. 1994			325.5	10	0.54	13.1	271.3	0.53	18.4	59.9	18.6
Oct. 1994			280	5.17	14.2	7.6	238.5	0.4	16.3	48.9	16.0
Sept. 1995			358	14.2	17.9	9.95	327		20.8	54.2	21.6
May 1996	19.7	9.25	273, 3	9. 40	1	10.3	234.7		15.1	52.6	15.9
May 2008	26, 2	9. 3	324.3	9.2	0.5	12.7	286.7		17.0		19.0
Dec. 2008	14, 5	9. 1	323.2	9.2	0.5	12.8	313.9		16.9		19.9
July 2014	27.2	8.97	351.86	11.56	1.3	15.99	297	0.43	25.22	57	20.6

Table 1. Water chemical composition of the lake (meq/l). Total Dissolved Solids (TDS) is expressed in gram per liter. The table has been modified from the Reference [9].

Figure 1 shows the PAGE (**P**olyacryl**A**mide **G**el **E**lectrophoresis analysis) of the oligomers formed as a function of time. Polymerization of cGMP (three independent series of samples for each condition were analyzed) is strongly stimulated by the salts dissolved in the *Bagno dell' Acqua* lake water with a double effect:

1) enhance the total amounts of polymers produced,

2) favours the formation of long polymers (up to 15 bases in length)

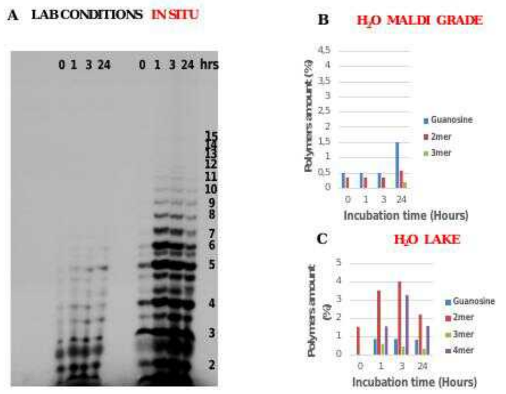

Figure 1. Panel A. Time-dependence (0 to 24 hours) of the oligomerization of 3’,5’ cGMP in liquid form at 50 °C (temperature of the lake spot) in laboratory conditions (left panel) and *in situ* (right panel). Each sample was prepared by lyophilizing 150 µL of 1 mM 3’,5’ cGMP, subsequently resuspended in 150 µL of MALDI grade water or lake water and incubated independently at 50 °C for the indicated time. Panel B. HPLC analysis of the same samples of Panel A (left). Panel C. HPLC analysis of the same samples of Panel A (right).

The HPLC analysis confirms the PAGE results and shows the presence of trimers (green bar in Figure 1) starting from 1 hour (instead of 24 hours) and a greater amount of dimers (red bar in Figure 1) up to 11,4 times more at three hours, comparing the MALDI grade Super Purity water and the lake water, while the formation of tetramers (purple bar in Figure 1) is observed in lake water only. Furthermore, the amount of guanosine (blue bar in Figure 1), produced by oligomers degradation, increases at 24 hours in MALDI grade Super Purity water (up to 1,5% of the total cGMP amount), while remains constant at around 0.8 % of the total cGMP amount in the lake water, suggesting a protective role for the salts dissolved.

Further investigations are needed to understand the role of the salts contained in the Lake Bagno dell' Acqua water. The increased efficiency of the cGMP polymerization reaction in the enviromental compared to laboratory conditions, even at the same temperature, could suggest a photoactivated mechanism.

Acknowledgements:

This work was supported by the Italian Space Agency (ASI) project N° 2023-3-HH.0 "Attività scientifica di preparazione all' esplorazione marziana" and by PRIN 202082CE3T-PE4 *“ARES: A Road from Earth to the Stars*”.

References:

[1] Costanzo G. et al. (2009) *J. Biol. Chem.*, *284*, 33206–33216. [2] Gilbert, W. (1986) *Nature*, *319*, 618. [3] Verlander M. S. R. et al. (1973) *J. Mol. Evol.* *2*, 303–316. [4] Costanzo G. et al. (2020) *ChemSystemsChem*, https://doi.org/10.1002/syst.202000011.[5] Farr T. G. (2004) *PSS*, *52(1-3)*, 3–10. [6] Baliva et al. *BAAS.*, *31*, 1145, id 47.04. [7] Cangemi M. et al. (2018) *J. Limnol. 77(2*), 220, 23. [8] Azzaro E. et al. (1983) *Chem. Geol. 40(1-2),* 149-165. [9] Paz M.P.J. et al. (2016) *Bull Volcanol 78*, 29, https://doi.org/10.1007/s00445-016-1023-6

Hyperspectral imaging in the VNIR of NWA13367 Martian Shergottite. S. De Angelis[1], F. Altieri[1], E. La Francesca[1], M.C. De Sanctis[1], M. Ferrari[1], E. Ammannito[2], J. Brossier[1], E. Bruschini[1], M. Formisano[1], A. Frigeri[1]. [1]National Institute of Astrophysics, INAF-IAPS, via Fosso del Cavaliere, 100, 00133, Rome (Italy) (simone.deangelis@inaf.it); [2]Italian Space Agency – ASI-Rome.

Introduction: Studying Martian Meteorites in the laboratory provides fundamental clues about the surface composition as well as the evolution of Mars. Spectroscopic and geochemical investigations furnish valuable insight both regarding the planet composition and information related to secondary processes (i.e. aqueous alteration) [1,2] SNCs meteorites have compositions that are mafic to ultramafic [1,2] essentially basalts or basaltic cumulates. Spectroscopic investigations in the VIS-NIR moreover provide important laboratory data for comparison with rover missions that currently are exploring the Martian surface with *in situ* spectrometers at even higher spatial resolutions with respect to past instruments.

Here we present reflectance spectroscopic measurements on a large sample of Martian Shergottite, North West Africa (NWA) 13367, by using the VIS-IR hyperspectral imaging technique

The sample has been investigated in the range of 0.35-5.1 µm by means of the SPIM setup at IAPS-CLab [5,6].

Setup and sample description: the meteorite slab has been investigated with the Spectral Imager (SPIM) instrument in use at C-Lab laboratory at INAF-IAPS. The facility consists in an imaging spectrometer operative in the 0.35-5.1 µm-range [5,6], and contains the laboratory spare of VIR spectrometer onboard the Dawn mission [7]. The setup includes two bidimensional focal planes, a CCD (0.35-1 µm) and an HgCdTe (1-5.1 µm) detectors both hosted, together with the spectrometer, inside a liquid N_2 cooled Thermal Vacuum Chamber. The entry slit is 9x0.038 mm corresponding to a single acquired image on the sample of 256 px, with spatial resolution of 38 µm/px on the target. The sample to analyze is placed outside the TVC on a 3-axis motorized stage: by moving the target at 38 µm-steps and acquiring consecutive frames it is possible to construct a hyperspectral cube of 876 spectral bands and the desired number of lines.

The analyzed sample is a slab of about 5x5 cm. According to the Meteoritical Bulletin, this sample is constituted mainly of olivine (50%), pyroxene (40%), and 5-10% maskelynite, and is characterized by ophitic/poikilitic texture. Pyroxenes range from a low Ca/Fe-rich pigeonite to a Ca-rich augite. Other phases include Fe-Ti oxides, sulfides, and merrillite (Ca-rich phosphate containing Na and Mg).

Measurements and Results: Two scans covering each an area of about 9x6 mm**2** have been acquired on the same meteorite face. Each image has been constructed by acquiring 150 consecutive frames at 38-µm steps (dimension along the vertical axis). Here we focus on the first of the two scans. In order to get a first preliminary and explorative global view of the spectral data, several band parameters maps have been retrieved. In particular, here we show the map of (i) band depth at 1 µm [Fig.1], (ii) band depth at 4 µm [Fig.2], and (iii) band depth at 0.65 µm [Fig.3]. The first map is related to the distribution of iron silicates (pyroxenes and olivine), and as can be seen, these phases cover the almost totality of the distribution map (Fig.1). Nevertheless most of the spectra resemble at first glance those of pyroxenes, characterized by the occurrence of the two Fe^{2+} bands at 1 and 2 µm (as shown in fig.4), with the second band shifted towards 2.3 µm, indicative of clinopyroxene. Very few pure spectra of olivine are immediately observable indicating that olivine is mixed with pyroxenes and/or dark phases at the sub-pixel level. In other cases olivine grains could be characterized by large grain size. A search for the VIS peak and also mapping the width and area at 1 µm would help in identifying zones containing olivine.

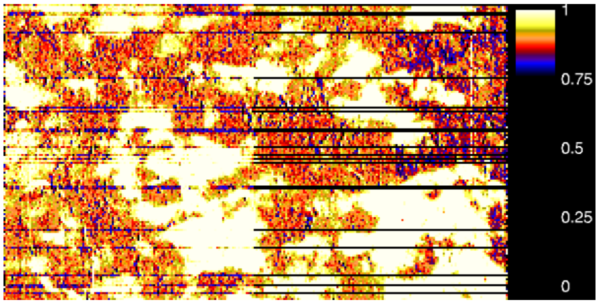

Fig.1. Map of band depth at 1 µm for NWA 13367 cube, indicative of pyroxene/olivine distribution. This map and the following ones have dimensions of 9 mm x 5.7 mm.

The map of band depth at 4 µm provides clear evidence of the distribution of carbonates (Fig.2), likely of terrestrial origin. These seem to be somewhat distributed in correspondence with the zones with higher pyroxene abundance.

Finally, in Fig.3 the distribution map of 0.65 µm band depth is shown. Although this absorption band could be consistent with spin-forbidden transition in Ti^{3+} in augite as reported in [8], here it appears, when present, quite large and intense. Moreover, it seems to correlate with the 1-µm band more shifted towards longer wavelengths, pointing to a more Fe-rich composition (Fig.4). However it is evident how this phase forms outer rims (yellowish in this map) around core pyroxene grains with different composition (zonation) (Fig.3).

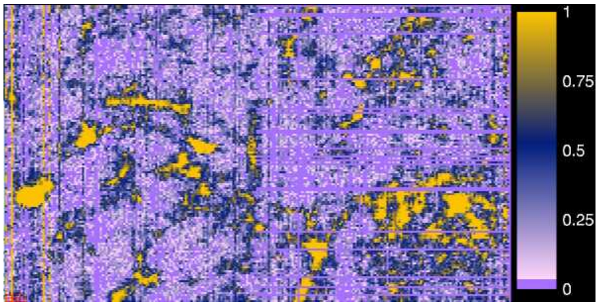

Fig.2. Map of band depth at 4 µm for NWA 13367 cube, indicating the carbonate distribution.

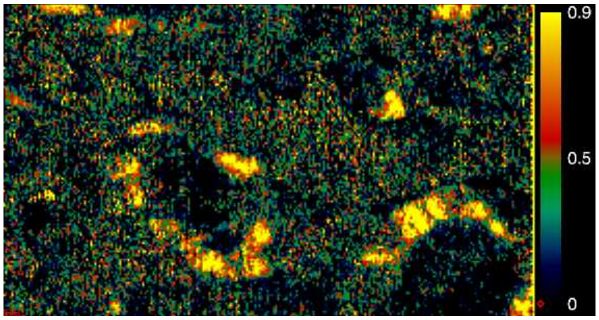

Fig.3. Map of band depth at 0.65 µm for NWA 13367 cube. This feature is related to Fe and/or Ti present in clinopyroxene.

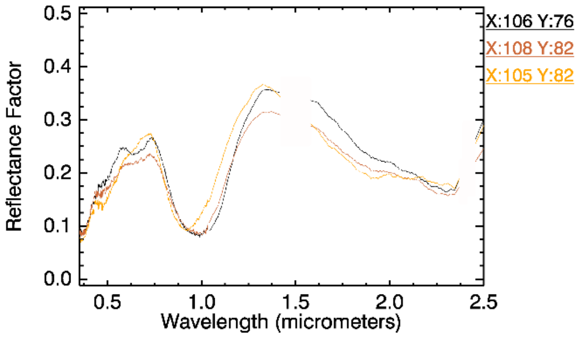

Fig.4. Spectra showing the 1 and 2 µm absorption of pyroxene. The 0.65 µm absorption band seems to occur in correspondence of the 1-µm band more shifted towards longer wavelengths.

Conclusions and Future Work:

We started to investigate by means of VIS-IR imaging spectroscopy a Martian Shergottite (NWA 13367) at the spatial resolution of 38 µm. As preliminary spectral analysis, we retrieved several maps, for example at 1 µm (Fe silicates), 4 µm (carbonates, likely from terrestrial alteration), and 0.65 µm (Ti or Fe-rich clinopyroxene). In particular, in some zones, the pyroxenes show zonation, with a likely Fe-rich outer rim. The correlation of 0.65-µm band depth with 1-µm band position will be further investigated. The 38-µm spatial resolution will allow to investigate in detail both the mineralogy of this sample and also at least some aspects related to the texture at the sub-mm scale. Moreover, additional analyses will be performed on a portion of this sample by means of coupled FTIR spectroscopy and mass spectrometry.

References: [1] Udry A. et al. JGR Planets 125 2020. [2] Treiman A H et al PSS, 48 1213 1230 2000 [3] Hicks L.J. et al. Geoc. Et Coscmoc. Acta, 136 194 210 2014. [4] Bishop J. L. et al. 80th Met. Soc. 6115 2017. [5] Coradini A. et al., Vol. 6, EPSC-DPS2011-1043, 2011. [6] De Angelis S. et al., Rev.Sci.Instr. 86, 093101, 2015. [7] De Sanctis M.C. et al., Space Sc. Rev., 163:329–369, 2011. [8] Klima R.L., et al., M&PS, 42, n.2, 235-253, 2007.

Acknowledgements: Scientific activities with SPIM are funded within the ExoMars program by the Italian Space Agency (ASI) grant ASI-INAF n.2023-3-HH.0.

SPECTRAL SURVEY ON CLAY DEPOSITS & POSSIBLE CARBONATES ALONG THE MARTIAN CRUSTAL DICHOTOMY, IN CONTEXT WITH THE EXOMARS ROVER MISSION.

J. Brossier[1], F. Altieri[1], M.C. De Sanctis[1], A. Frigeri[1], M. Ferrari[1], S. De Angelis[1], E. Bruschini[1], and A. Apuzzo[2], [1]Istituto di Astrofisica e Planetologia (IAPS), Istituto Nazionale di Astrofisica (INAF), Via del Fosso del Cavaliere 100, 00133 Roma, Italy (jeremy.brossier@inaf.it), [2]Dipartimento di Scienze, Universitá Roma Tre, Roma, Italy.

Introduction – On Mars, the crustal dichotomy marks the boundary between the old cratered highlands and the northern lowlands (i.e., planitiae). Infrared datasets display several sites therein with extensive clay-bearing outcrops, further testifying for widespread aqueous conditions on early Mars [1]. Here, we investigate clay deposits identified in notable regions along this boundary, and compare them with other deposits found in circum-Chryse Planitia (Figure 1) [2–4]. Clay-bearing outcrops are valuable targets to seek traces of life on the planet, as clay minerals are known to accumulate and preserve organic compounds [5]. Knowing the exact positions of absorption band centers is crucial to determine possible species present in these outcrops, and search for changes in clay mineralogies linked to differences in formation and weathering conditions. Here we examine hyperspectral infrared data to characterize in detail the near-infrared signatures of clay deposits, where we concentrate particularly on the key absorptions centered in the 1.1–2.6 µm range.

Data & Methods – Spectral signatures of the clay deposits are obtained from data gathered by the CRISM instrument [6], with spatial resolutions ranging from 20 to 40 m.px^{-1} and a spectral resolution of 6.6 nm. We used over hundred CRISM cubes acquired in the infrared range (1–4 µm), targeting the selected regions (Figure 1). They were first preprocessed with the CAT ENVI toolkit for atmospheric and photometric corrections. Corrected cubes were then denoised to reduce noise and residual atmospheric contributions, and to finally emphasize mineralogical absorptions in the "*ratioed*" spectrum. Once the cubes are corrected and denoised, we defined our regions of interest (ROIs) to outline the clays. For doing that, we calculated band depths at 1.9 and 2.3 µm [7] to select pixels with strong absorptions and map the ROIs for each cube.

Results – We retrieved the band centers for all pixels composing the ROIs within the three absorptions of interest (1.4, 2.3 and 2.4 µm), after continuum removal to emphasize the absorptions. Band centers vary a little from a region to another, with average values being 1.410, 2.305 and 2.397 µm, respectively (e.g., Oxia Planum [2,8]). Some exceptions are observed, notably in Mawrth Vallis, Oxia's catchment area, and McLaughlin crater, where absorptions are slightly shifted to 1.42, 2.29 and 2.40 µm.

Diverse Clay Mineralogies? – CRISM cubes reveal several absorptions in the 1.1–2.6 µm range. Paired absorptions near 1.4 and 1.9 µm are common to hydrated minerals, while an absorption near 2.3 µm indicates a (Fe,Mg)-OH vibration. Clay deposits in our ROIs are consistent with Fe,Mg-rich clays, combining absorptions at approximately 1.4, 1.9, 2.3 µm and weaker overtones near 2.4 µm. Martian Fe,Mg-rich clays generally show spectral variability in these absorptions, from Fe-rich (nontronites) to Mg-rich (saponites) compositional species. For instance, nontronites display typical absorptions near 1.42, 2.29 and at 2.40 µm, while saponites have absorptions near 1.38, 2.31 and at 2.38 µm [9]. Nevertheless, intermediate band centers obtained for most of clay deposits rather correlate with Fe-rich saponites (ferrosaponites) or vermiculites, notably in Oxia Planum [2,8]. Band centers within these absorptions may vary depending on the regions. Exact positions therein depend on the relative abundance of iron and magnesium in the clay structure, and also the oxidation state of iron [10].

Overall, these "*intermediate*" clays correspond to Fe-rich species, particularly ferrous smectites with a trioctahedral composition. Conversely, nontronites commonly found in Mawrth Vallis, Oxia's catchment area, and some outcrops in McLaughlin crater, are rather ferric smectites with a dioctahedral composition. Interestingly, ferric smectites are thought to form from oxidation of the ferrous smectites. Indeed, the reducing atmosphere of early Mars would favor the formation of ferrous smectites, while their subsequent oxidation would explain the presence of ferric smectites nowadays [11,12].

Possible Ubiquity of Carbonates? – All CRISM cubes studied here exhibit an additional, shallow absorption centered near 2.5 µm. It appears to correlate well with strong absorptions near 1.9 and 2.3 µm, and is therefore detected across the clay-bearing outcrops. Such an absorption in the 2.5 µm range indicates the presence of carbonates or other smectites together with the clays [2,8,13]. Carbonates are usually best identified by paired absorptions at 2.3 and 2.5 µm, although these features are hidden by the clays. An absorption near 2.53 µm would be consistent with Fe,Ca-rich carbonates (siderites, calcites), whereas an absorption at shorter wavelengths is often associated with Mg-rich carbonates (magnesites or even dolomites) [14].

To complement this detection, we search for a specific pattern in the 3–4 µm range, where a broad peak near 3.6–3.7 µm is expected by deep absorptions (x-CO_3^{2-} vibrations) at 3.4–3.5 µm and 3.8–3.9 µm. A clear absorption near 3.4–3.5 µm is usually missing in our spectra, likely due to the deep water absorption near 3 µm induced by the clays, masking the carbonate absorption. This prevents a definitive identification and characterization of the carbonates. Nonetheless, coprecipitation of clays and carbonates throughout the studied outcrops further strengthens the exobiological potential of the regions, where biosignatures might still be preserved. Presence of carbonates is confidently suggested in some regions, like Nili Fossae and surrounding areas [e.g., 14].

Conclusions – In this study, we follow-up and complements recent investigations [2–4,8]. We report a detailed analysis of clay deposits found in key regions located along the martian crustal dichotomy, to compare them with carefully selected terrestrial analogs [2–4]. By doing that, we retrieved the exact positions of the 1.4, 2.3 and 2.4 µm absorption bands, and searched for possible variations in these band centers. Variations observed between the targeted clay deposits imply subtle changes in iron and magnesium content [10]. Mineralogical similarities observed in most regions suggest that clay deposits (i.e., ferrosaponites, vermiculites) may share a common weathering history. Conversely, nontronites extensively detected near Mawrth Vallis and surrounding areas indicate a different formation and alteration setting. Nonetheless, the region may have shared a common aqueous history with the other deposits found elsewhere on the planet, and then diverged to form more leached or oxidized clays with Al,Fe-rich compositions [e.g., 15]

Presence of additional absorption near 2.5 µm characteristic of carbonates, may indicate their co-occurrence with clay deposits. This testifies for a widespread distribution of carbonates on Mars, more ubiquitous than originally thought.

This work is in context with the ExoMars rover mission, expected to deliver the "*Rosalind Franklin*" rover to explore Oxia Planum. ExoMars rover will investigate clay deposits in surface and subsurface to search for signs of past or present life on the planet, as biosignatures might be preserved therein [5].

Acknowledgments – This work is funded and supported by the Italian Space Agency (ASI) [Grant ASI-INAF n. 2017–48–H.0]. We are greatly thankful to the European Space Agency (ESA) for the ExoMars "*Rosalind Franklin*" project.

References – [1] Carter et al. (2013) *JGR Pl.*, [2] Brossier et al. (2022) *Icarus*, [3] Brossier et al. (2023) *PSJ*, [4] Brossier et al. (under review) *PSS*, [5] Vago et al. (2017) *Astrobiology*, [6] Murchie et al. (2007) *JGR Pl.*, [7] Viviano-Beck et al. (2014) *JGR Pl.*, [8] Mandon et al. (2021) *Astrobiology*, [9] Bishop et al. (2013) *JGR Pl.*, [10] Michalski et al. (2015) *EPSL*, [11] Chemtob et al. (2015) *JGR Pl.*, [12] Chemtob et al. (2017) *JGR Pl.*, [13] Bultel et al. (2019) *JGR Pl.*, [14] Ehlmann et al. (2008) *Science*, [15] Carter et al. (2015) *LPSC Abs.*

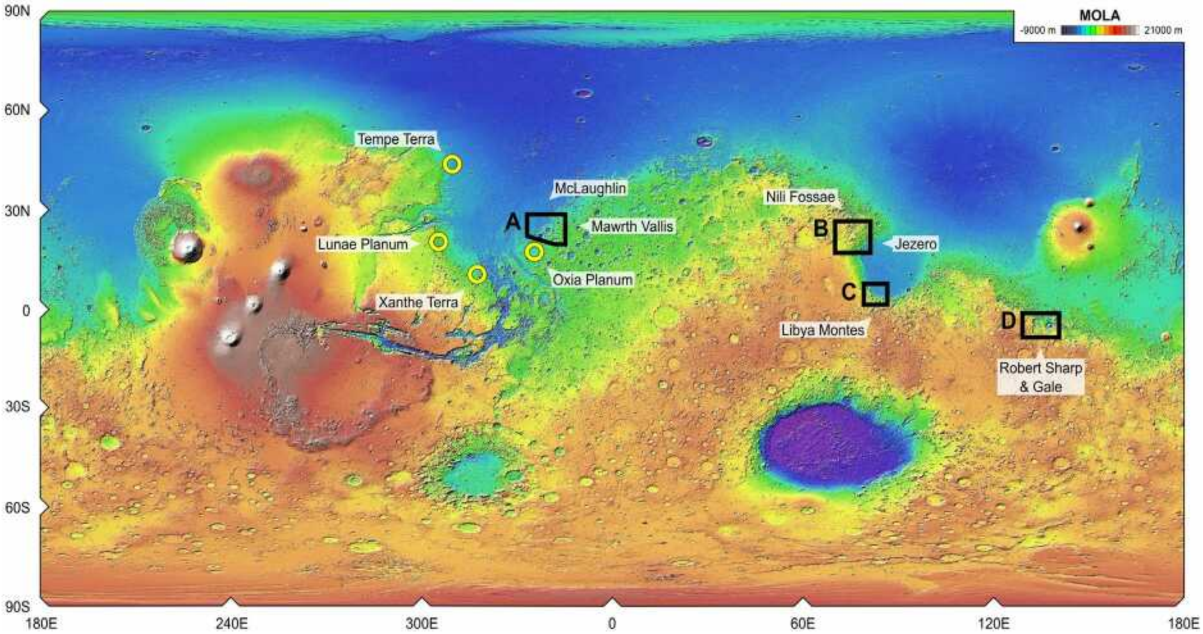

Figure 1 – Mars with colorized topography (MOLA), with key regions included in our spectral survey. Yellow circles: Oxia Planum, Xanthe Terra, Lunae Planum and Tempe Terra were already investigated in our previous studies [2–4], and they are now compared with other regions along the crustal dichotomy. Black frames: (A) Mawrth Vallis and McLaughlin crater, (B) Nili Fossae and Jezero crater, (C) Libya Montes, and finally (D) Robert Sharp and Gale craters.

Analysis of the OMEGA 0.4-2.5 µm spectra of the Martian satellite Phobos

J. Beccarelli[1,2 x], M. Pajola[2], G. Munaretto[2], A. Lucchetti[2], G. Poggiali[3,4], E. Simioni[2], F. Tusberti[2], John Robert Brucato[4]

[1] Centro di Ateneo di Studi e Attività Spaziali – Giuseppe Colombo (CISAS), Padova, via Venezia 15, 35131 Padova, Italy (joel.beccarelli@studenti.phd.it); [2] Istituto Nazionale di Astrofisica (INAF) – Osservatorio Astronomico di Padova (OAPd), Vicolo dell'Osservatorio n.3, Padova, Italy; [3] LESIA Observatoire de Paris, Universiteé PSL, CNRS, Universiteé Paris Citeé, Sorbonne Université, 5 place Jules Janssen, F-92190 Meudon, France; [4] INAF Osservatorio Astronomico di Arcetri, largo E. Fermi n.5, I-50125 Firenze, Italy

Introduction

Context. The origin of the Martian satellite Phobos is still an open question. There are a few proposed main theories, such as [i] asteroidal capture due to migration of Phobos toward the inner region of Solar System **[1, 2]** and [ii] the in situ reaccretion of Martian material **[3-6]**. So far none of them has been ruled out, hence future investigations are needed. For instance, compositional studies provide useful information about the mineralogy of Phobos, giving additional benchmarks for establishing the most appropriate formation theory. A future mission exploration with Phobos as main target, i.e., the JAXA Martian Moon eXploration (MMX) **[7],** will clarify better its mineralogy and will provide the possibility to study samples of Phobos surface on Earth, thanks to its sample return program. In this work, we analyze spectral data of Phobos to find laboratory analogues that indicate the possible minerals present on the surface of the Martian moon.

Work Overview and Dataset. In this work we present a compositional study based on the analysis of four spectral data-cubes acquired by OMEGA (Observatoire pour la Minéralogie, l'Eau, les Glaces et l'Activitè) **[8],** instrument on board Mars Express spacecraft. In particular, we have analyzed the orbits 0756, 5851, 7926, 8477, in the wavelength region 0.4-2.5 µm (see Table 1). A representation of the swaths of the four datasets is shown in Fig. 1. The main goal of this analysis is to find an asteroidal and meteoric analogue for Phobos, that would shed light to its mineralogical composition and formation scenario. Phobos surface can be divided in two main units: the blue and the red one **[10]**. While the blue one seems to be associated to the biggest crater on the surface (*Stickney Crater*, 9 km in size), the red unit occupies the rest of the surface. In addition, the blue unit's spectrum has a higher reflectance in the visible wavelength range with respect to the red unit's spectrum, and a shallower trend in the infrared. Another unit can be found in the region between the blue and the red unit, indicating a possible mix between the two **[11-13]**.

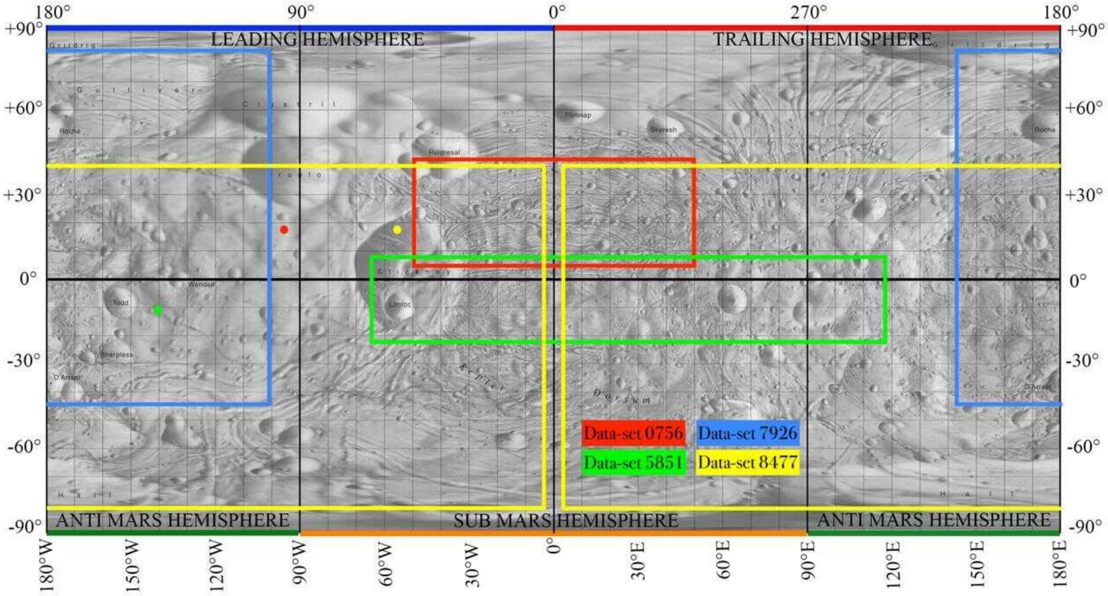

Figure 1. Representation of the swaths of the analyzed data-cubes on the surface of Phobos. The points indicate the sub-solar point (i.e., where the light perpendicularly hits the surface of the moon (the blue and the green dots are superimposed). For a matter of visualization, the point has been made with the same color of the respective taken swath.

	Acquisition Date	Start Time (UT)	Stop Time (UT)	Distance (km)	Spatial Scale (m/px)	Phase Angle (°)	Hemisphere Observed
Orbit 0756	22 Aug 2004	12^h:00^m:30.060^s	12^h:12^m:20.045^s	151.91	171.9	63	sub-Mars
Orbit 5851	23 Jul 2008	04^h:47^m:47.011^s	04^h:52^m:26.076^s	88.17	101.0	101	Both
Orbit 7926	10 Mar 2010	05^h:55^m:06.010^s	06^h:02^m:45.034^s	285.92	328.8	37	anti-Mars
Orbit 8477	17 Aug 2010	15^h:35^m:58.020^s	15^h:40^m:50.050^s	845.08	971.1	70	Both

Table 1. Main characteristics of the acquisitions that have been analyzed in this work **[9]**.

Results

Spectra Extraction. A set of both blue and red unit's spectra have been extracted. The bluer unit is the region nearby the Stickney crater, consistent with previous works **[10]**. The transition from bluer to redder unit has been found to be gradual and not sharp. This feature may be linked to the nature of the blue unit, being made with ejected material produced by the impact that formed *Stickney*. This would be compatible with the gradual transition observed passing from the bluer to the redder unit and with the transitional unit between the two. In addition, the blue unit shows a possible feature located in the range 0.95 μm - 1.05 μm, which could be linked to the presence of pyroxene, olivine or a mixture of the two. This feature has been found only in the blue unit *Region of Interest (ROI)* of 0756 dataset. However, its nature should be verified with higher resolution data due to the low band depth measured (few %), which is a possible effect of the space weathering, Moreover, the presence of gaps in the OMEGA data add more uncertainties in the evaluation of the band minimum.

Spectra Comparison. Many spectral comparisons have been attempted with asteroids and meteorites spectra, finding that the most primitive and carbonaceous objects are the best match for Phobos blue and red units. In particular, Kaidun and the Murchison fusion crust fit well for the bluer unit, while Tagish Lake (TL) is a good fit for the red unit. TL and Kaidun mixtures can reproduce well the whole range between the blue and red unit but not the possible 1 μm band. This may be an indication that a second unknown component could be present on Phobos. In addition, the comparisons made with asteroids show a clear correlation with the most carbonaceous objects, D-types for the red unit and T-type **[14]** for the blue one. The blue unit of the Orbit 0756 is the bluest spectrum of the region ever observed of Phobos.

Future Works. Future investigation on additional OMEGA datasets will be performed to provide a better mineralogical context to the forthcoming MMX mission, and in particular the observation of MIRS instrument on board the spacecraft, which will be pivotal to finally understand the composition and origin of Phobos.

References:

[1] Tsiganis et al. (2005), *Science, 435, 459-461;* **[2]** Walsh et al. (2011), *Science, 475, 206-209;* **[3]** Craddock et al. (2011), *Icarus, 211, 1150-1160;* **[4]** Rosenblatt et al. (2012), *Astron. Astrophy. Rev., 19, 44;* **[5]** Rosenblatt and Charnoz (2012), *Icarus, 221, 806-815;* **[6]** Hyodo et al. (2017), *APJ, 845, 125-132;* **[7]** Kawakatsu, Y. et al. (2020), *IAC, Vol. 2020, IAF;* **[8]** Bibring et al. (2004), *ESP, Vol. 1240, 37-49;* **[9]** Witesse et al. (2014), *Planet Sp. Sci., 102, 18-34;* **[10]** Murchie and Erad (1996), *Icarus, 123, 63-86;* **[11]** Pajola et al. (2012), MNRAS, 427, 3230-3243*;* **[12]** Pajola et al. (2013), *APJ, 777, 127-132;* **[13]** Pajola et al. (2018), *Planet. Sp. Sci., 154, 63-71;* **[14]** Bus and Binzel (2002), *Icarus, 158, 106-145*

Investigating the origin and formation mechanisms of Martian Recurring Slope Lineae (RSL) from TGO/CaSSIS 4-band spectrophotometry

Munaretto, G. (1), Doutè, S. (2), Tornabene, L. (3), Silvestro, S. (4), Pajola, M. (1), Lucchetti, A. (1), Cremonese, G. (1), Bertoli, S. (1,5), Tusberti, F. (1), Rossi, C. (1), Beccarelli, J (1), Thomas, N. (6)

(1) INAF-Osservatorio Astronomico di Padova (giovanni.munaretto@inaf.it) (2) Institut de Planetologie et d’Astrophysique de Grenoble (IPAG) (3) Inst. Space & Earth Exploration, Dept. Earth Sci., Western University, London, Canada (4) INAF, Osservatorio Astronomico di Capodimonte, Napoli, Italy (5) Center of Studies and Activities for Space "G. Colombo" (CISAS), Padova (6) Physikalisches Institut Universitat Bern, Switzerland

Introduction: Recurring Slope Lineae (RSL) are narrow dark streaks that incrementally lengthen down Martian warm steep slopes [1]. Early RSL observations [1-3] highlighted that their activity occurred during warm seasons and that RSL completely disappeared during winter and recurred annually, suggesting that RSL could be related to flows of liquid water or brines [4] or from the deliquescence of hygroscopic salts [4,5]. However, subsequent extensive RSL monitoring detected observational evidence incompatible with a water or brine-related origin. Correlations between RSL activity and surface sand/dust, RSL length and surface slope and contemporary RSL lengthening and fading, led authors to interpret RSL as dry granular flows [6], possibly related to aeolian processes [6,7]. In particular, [8, 9] investigate RSL as aeolian sandy flows. In this study, we combine three independent analyses to investigate whether RSL are better explained as sandy flows or they are dust removed features.

Methodology

Nearest Neighbour Analysis : We performed a nearest eighbour analysis using the most updated RSL database [9] together with the global digital dune database (MGD^3) from [10]. In particular, for each RSL site we computed the great circle distance of its nearest sand deposit. We also repeated this procedure using a random distribution of points as a control sample. We then computed the nearest-neighbour distance distribution of RSL and sand dunes and compared it with RSL and random points.

4-band photometry : We analyzed a set of RSL sites in Valles Mariners, located at (-13.106 N, 294.771°E). This locations is interesting because it hosts RSL, sand sheets and dunes, and dust devil tracks (DDTs). They were observed by the Colour and Surface Science Imaging System (CaSSIS, [11]) in 4 filters (BLU 499.0 nm, PAN 675.0 nm, RED XXX.0 nm, NIR XXX.0 nm) at 4.65 m/px resolution. Extensive HiRISE [12] imagery at 0.25 m/px and DTMs at 1.0 m/px are also available at this site. We define Regions of Interest (ROIs) inside the RSL, DDTs and sand deposits, and for each of them we also define a background ROI nearby (called (BK_RSL, BK_DDT, BK_SAND, respectively), having similar slope and aspect and without either RSL, sand or dust-devil tracks on it. We extract the reflected flux from all these ROIs, corrected with standard atmospheric corrections [13]. We then computed the NIR/RED and PAN/BLU band ratios, indicative of the spectral slopes in the near-UV and near-IR wavelength range. We also extracted spectra of relevant minerals for this locations from the CRISM spectral library, convolved them into the CaSSIS photometric system [11,14] and calculated the RED/NIR and PAN/BLU band ratios. We considered Fe/Mg-Olivines, and High (HCP) and Low Calcium pyroxenes (LPC). The RED/NIR vs PAN/BLU spectral slopes are then compared for all the ROIs and selected minerals

Morphology and temporal evolution : We use existing HiRISE imagery and DTMs to characterize the RSL and sand deposits morphology and their temporal evolution. In particular, we analyze the ripples evolution with time and compare it with the RSL temporal evolution.

Results: The global distribution of RSL and sand deposits and a set of random points projected on the surface of Mars are displayed in Fig. (1A), while the corresponding nearest-neighbour distance distributions are in Fig. (1B). We find that RSL are spatially associated with sand deposits, since their nearest neighbour distance is statistically lower than the distance from an uncorrelated, random sets of points. In particular, we find that most RSL are within 100 km of their nearest neighbour dune field, consistent with the typical scale of aeolian sediment transports on Mars [10]. We report in Fig. (2) the RED/NIR and PAN/BLU band ratios of RSL, sand deposits, DDTs and their background ROIs. We also report these band ratios for Martian dust [15], for Fe/Mg Olivines, HCP and LCP. We find that RSL and Sand dunes have similar band ratios as Mg-Olivines, consistent with their detection in Martian dunes [15].

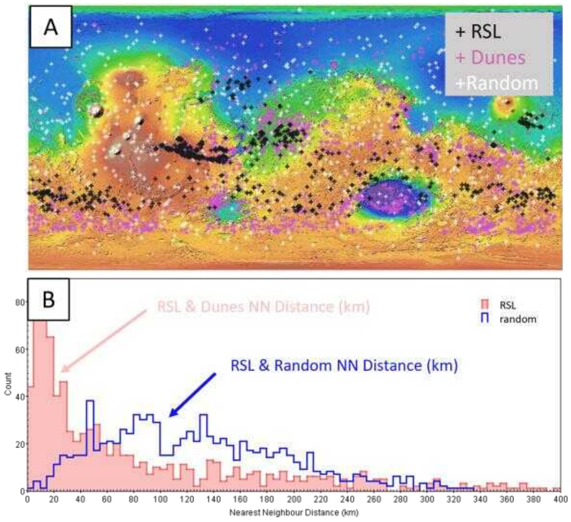

Figure 1. A) Spatial distribution of RSL, Sand Dunes and a random control sample overlain on the MOLA colorized elevation map. B) Nearest Neighbour distance distrubutions between RSL and Dunes (pink) and RSL and the control sample (blue).

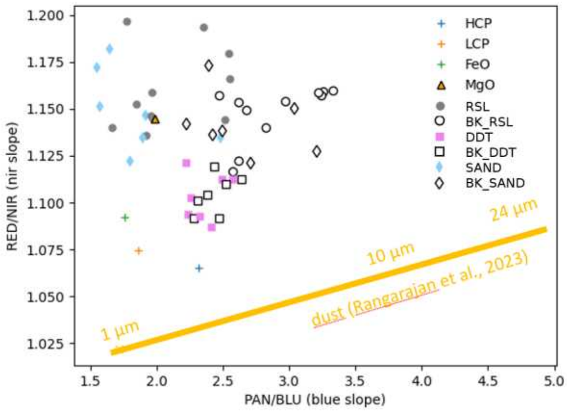

Figure 2. CaSSIS band ratios for RSL, Sand, DDTs and their background ROIS (BK_RSL, BK_SAND, BK_DDT), for LCP, HCP and MG/Fe-Olivines and for dust deposits of variable grain size (yellow).

Discussion: Preliminary results suggest that RSL are spatially associated to sand dunes on Mars, as demonstrated by our nearest neighbour analysis. We also find that RSL and nearby sand deposits have similar spectrophotometric properties, i.e. band ratios, thereby suggesting a common sandy origin. In particular, we find that RSL and sand band ratios are consistent with the Mg-Olivine band ratio. Since Olivines are commonly detected on Martian Dunes [15], this also provide further evidence that RSL have a sandy origin. In contrast, there results are difficult to interpret with dust removal. The full multidisciplinary analysis, including also the morphological and temporal evolution of ripples and their correlation with RSLs, will be presented at the conference

Acknowledgements: This study has been supported by the Italian Space Agency (ASI) through the ASI-INAF agreement no. 2020-17-HH.0

References: [1] A. S. McEwen et al. (2011), Science (6043), 740–743 [2] Levy, J et al. (2012), Icarus, 219, (1), 1-4 [3] McEwen et al. (2014), Nat. Geosci. 7 (1), 53–58 [4] Stilllman et al. (2016), Icarus 265, 125–138. [5] Wang et al. (2020), Icarus 333, 464–480 [5] Dundas et al. (2017), Nat. Geosci. 10 (12), 903–907 [6] Vincendon et al. (2019), Icarus 325, 115–127 [7] Dundas et al. (2020), Icarus 343, 2020, 113681 [8] Dundas et al. (2020) Icarus, 343, 113681.[9] Stillman et al. (2021), Icarus 369, 114648 [10] Fenton et al., (2019), Icarus, 330, 15, 189-203 [11] Thomas et al. (2017) Space Sci. Rev. 212 (3–4), 1897–1944 [12] McEwen et al., (2007), JGR, 112 [13] Munaretto et al., (2020), PSS, 187, 10497 [14] Munaretto et al., (2022),PSS, 214, 105443 [15] Lane et al., 2013, GRL, 40, 14,3517-3521.

TGO/NOMAD UVIS AND LNO CHANNELS COMBINED NADIR DATASETS' ANALYSIS: MARTIAN DUST CHARACTERIZATION.

F. Oliva[1,*], E. D'Aversa[1], G. Bellucci[1], F.G. Carrozzo[1], L. Ruiz Lozano[6,7], O. Karatekin[6], F. Altieri[1], F. Daerden[2], I.R. Thomas[2], B. Ristic[2], M.R. Patel[3], J. Mason[3], Y. Willame[2], C. Depiesse[2], J.-J. Lopez-Moreno[4], A.C. Vandaele[2] and G. Sindoni[5]
[1]*Istituto di Astrofisica e Planetologia Spaziali* (IAPS/INAF), Rome, Italy; [2]*Royal Belgian Institute for Space Aeronomy* (IASB-BIRA), Brussels, Belgium; [3]*School of Physical Sciences, The Open University*, Milton Keynes, U.K; [4]*Instituto de Astrofisica de Andalucia* (IAA), Consejo Superior de Investigaciones Científicas (CSIC), Granada, Spain; [5]*Agenzia Spaziale Italiana* (ASI), Rome, Italy; [6]*Royal Observatory of Belgium*, Brussels, Belgium; [7]*Université Catholique de Louvain-la-Neuve* (UCLouvain), Louvain-la-Neuve, Belgium; ***Correspondence: fabrizio.oliva@inaf.it**

Abstract

In this work we update the analysis presented in [15], focused on the characterization of Martian dust microphysical properties through the combined investigation of the TGO/NOMAD [1] UVIS and LNO channels' nadir data. We aim at applying the MITRA radiative transfer (RT) tool [2,3,4,16] to spatially and temporally coincident observations of the two datasets, covering ultraviolet-visible and near-infrared wavelengths respectively. The exploitation of the extended range enables constraining the dust grains' densities and, in particular, their radii. Indeed, the study of sizes requires information on how the observed spectra bend between visual and infrared wavelengths. We plan to apply the presented method to the whole NOMAD nadir dataset registered by the two channels.

1. Introduction

Martian dust is one of the main drivers of the Red Planet's thermal structure and climate [6]. It affects the distribution and circulation of atmospheric gases and has a role in triggering water ice clouds formation [5,17]. Airborne dust heats the lower atmosphere by absorbing in the VIS-NIR spectral range [7] and radiates heat to space through IR emission [7,8,9,10]. The efficiency of these mechanisms depends on the dust composition, but also on its microphysical properties and abundance. For these reasons, in order to fully comprehend the planet's atmospheric processes, Martian dust properties need to be efficiently characterized.

2. Instrument and observations

NOMAD is a suit of three spectrometers observing with different pointing geometries in the ultraviolet-visible and near-infrared spectral ranges. While the SO channel is dedicated to solar occultation measurements in the near-infrared (2.3 – 4.3 µm), both the UVIS and the LNO channels (0.2 – 0.65 µm and 2.2 – 3.8 µm) can observe in nadir, limb and solar occultation geometries. In this work, in order to retrieve Martian dust microphysical properties, we select the nadir data of UVIS and LNO channels, probing the full atmospheric column down to the surface, registered from the end of March 2018 (beginning of NOMAD scientific phase) up to October 2023. Such an extended dataset encompasses different Mars Years (MY, from the second half of MY34 to the first half of MY37) hence allowing to study the dust properties evolution both globally and seasonally.

3. Method

The method, described in [15], is briefly summarized here along with the implemented updates. UVIS data are exploited down to 0.36 µm, which is the lowest wavelength available in MEx/OMEGA-derived surface albedo spectra. These are obtained through an approach based on the SAS method [14], capable of removing the atmospheric contribution from OMEGA reflectance factors that are spatially coincident to NOMAD data. We adopt LNO spectral orders from 168 to 202, also covering the wavelength range 2.20 - 2.55 µm. This interval is approximately devoid of strong absorption lines and is therefore suitable for a reliable estimation of the spectral continuum. While the investigation can of course be extended to the retrieval of ice clouds properties, we here focus on dust only, in order to speed up the computational time. To this extent, observations potentially containing ice are filtered out by adopting 1) the conditions by [18] on the reflectance factor in the ultraviolet and 2) by studying the presence of the eventual ice absorption at 2.6 μm, probed by LNO orders less than 175. Moreover, we refine the criterion to determine the data spatial coincidence by considering the smearing of both UVIS and LNO observations during their integration time. Finally, the retrieval of dust grains effective radii and densities is performed through the MITRA RT tool, taking advantage of temperature-pressure profiles derived from the Mars Climate Database (MCD, [11]) and of the dust optical constants from [12,13] (a benchmarking with the recently derived optical constants from [19] is also planned).

4. Summary

The presented method is focused on the exploitation of the NOMAD UVIS and LNO observations for the construction of a dataset that allows deriving the microphysical properties of Martian dust integrated column. The use of the two combined datasets is mandatory for constraining, in particular, the dust grains' sizes, whose spectral information is scattered on wavelengths pertaining to both channels. The framework behind the retrieval is updated, with respect to the analysis presented in [15], in order to better select spatially and temporally coincident data. Moreover, at this stage we filter out observations possibly containing ice, whose properties' retrieval is postponed for future work. The analysis is planned for all spatially and temporally coincident UVIS and LNO observations. This will allow to track down the evolution of dust in different MYs and to compare with the properties retrieved at high altitude by exploiting NOMAD SO channel's data [20].

Acknowledgements

Acknowledgments: ExoMars is a space mission of the European Space Agency (ESA) and Roscosmos. The NOMAD experiment is led by the Royal Belgian Institute for Space Aeronomy (IASB- BIRA), assisted by Co-PI teams from Spain (IAA-CSIC), Italy (INAF-IAPS), and the United Kingdom (Open University). This project acknowledges funding by the Belgian Science Policy Office (BELSPO), with the financial and contractual coordination by the ESA Prodex Office (PEA 4000103401, 4000121493), by the Spanish MICINN through its Plan Nacional and by European funds under grants PGC2018-101836-B-100 and ESP2017-87143-R (MINECO/FEDER), as well as by UK Space Agency through grants ST/V002295/1, ST/V005332/1, ST/Y000234/1 and ST/X006549/1 and Italian Space Agency through grant 2018-2-HH.0. The IAA/CSIC team acknowledges financial support from the State Agency for Research of the Spanish MCIU through the 'Center of Excellence Severo Ochoa' award for the Instituto de Astrofísica de Andalucía (SEV-2017-0709). This work was supported by the Belgian Fonds de la Recherche Scientifique – FNRS under grant numbers 30442502 (ET_HOME) and T.0171.16 (CRAMIC) and BELSPO BrainBe SCOOP Project. US investigators were supported by the National Aeronautics and Space Administration. Canadian investigators were supported by the Canada Space Agency.

References

[1] Neefs, E., et al, 2015. Appl. Opt. 54, 28, 8494-8520.
[2] Oliva, F., et al, 2016. Icarus 278, 215-237.
[3] Sindoni, G., et al, 2013. EPSC2013.
[4] Oliva, F., et al, 2018. Icarus 300, 1-11.
[5] Vandaele, A.C., et al, 2019. Nature 568, 521-525.
[6] Kahre, M.A., et al, 2008. Icarus 195, 576-597.
[7] Korablev, O. ,et al, 2005. Adv. Space Res. 35, 21–30.
[8] Gierasch, P.G., Goody, R.M., 1972. J. Atmos. Sci. 29, 400–402.
[9] Pollack, J.,et al, 1979. J. Geophys. Res. 84, 2929–2945.
[10] Määttänen, A., et al, 2009. Icarus 201, 504-516.
[11] Millour, E., et al., 2019. EPSC-DPS 2019
[12] Wolff, M.J., et al, 2009. J. Geophys. Res., 114, E9.
[13] Wolff, M.J., et al, 2010. Icarus, 208.
[14] Geminale, A., et al, 2015. Icarus 253, 51-65.[16]Aoki, S., et al. 2019. J. Geophys. Res.: Planets,124, 3482-3497.
[15] Oliva, F., et al., 2021. 15th EPSC, EPSC2021-501.
[16] D'Aversa, E., Oliva, et al., 2022. Icarus, 371, 114702.
[17] Aoki, S., et al. 2019. JGR: Planets,124, 3482-3497.
[18] Wolff, M. et al., 2019. Icarus, 332, 24-29.
[19] Martinkainen, J., et al., 2023. APJ Suppl.Ser. 268:47
[20] Stolzenbach, A., et al., 2023. JGR Planets, 128

A BAYESIAN INFERENCE FRAMEWORK TO DETERMINE THE INTERNAL STRUCTURE OF TERRESTRIAL PLANETS AND ICY MOONS.

Antonio Genova[1], Flavio Petricca[1] and Anna Maria Gargiulo[1], [1]Dipartimento di Ingegneria Meccanica e Aerospaziale, Sapienza University of Rome. Via Eudossiana 18, Roma, 00184, Italy (antonio.genova@uniroma1.it).

Introduction: The characterization of the internal structure of icy moons and planets is a fundamental objective of future missions to better understand the formation and evolution of the solar system. A multidisciplinary approach is required to jointly process measurements acquired by instruments onboard interplanetary spacecraft. By mainly focusing on geophysical data, including gravity, magnetic field and topography, we present a Bayesian inference framework based on the Markov Chain Monte Carlo (MCMC) method.

Data and Methods: Key measurements of the interior of a celestial body are its shape and mass that are determined by using images/altimetry and gravity, respectively. To enhance our knowledge of its degree of internal differentiation, accurate measurements of the degree-2 gravity field and orientation parameters, including pole obliquity and precession rate, enable the determination the Moment of Inertia (MoI) of the body. Further constraints on its internal structure are provided by the tidal responses of the body arising from an external perturbation. These effects can be measured by gravity, altimetry and imaging by estimating the Love numbers k_2, h_2, and l_2, respectively. Internal magnetic dynamo or induction data provide complementary constraints on the deep interior of terrestrial planets and the hydrosphere of icy moons.

To combine these interdisciplinary measurements in the interior model inversion, we implement a multi-layer structure of the body by using a Bayesian approach. The multi-dimensional parameter space, including the density and size of the internal layers, is sampled through the Metropolis-Hastings algorithm implemented in our MCMC method [1]. This approach allows us to determine the posterior probability distributions of the parameters of interest. By using gravity, magnetic and topography data as observations, we explore the multi-dimensional parameter space through the generation of multiple chains and the use of random walkers. After the convergence of the chains, we compute the probability distribution for each parameter to determine the likely internal structure of the investigated body that match the statistical distribution of the observations.

Terrestrial Planets: The MCMC method was used to determine the internal structure of Mercury by using the gravity measurements acquired by the Mercury Surface, Space ENvironment, GEochemestry, and Ranging (MESSENGER) mission [2]. The accurate estimate of the pole obliquity led to the determination of Mercury's polar MoI that was used as observation in the MCMC.

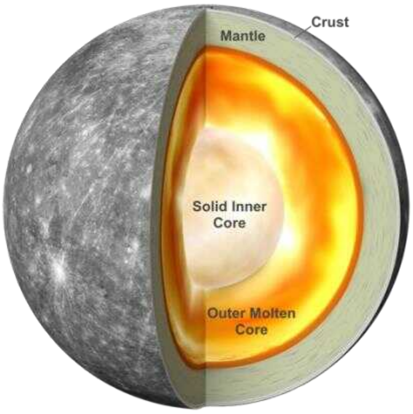

Figure 1 Four-layer modeling of Mercury's internal structure.

Four-layer (Fig. 1) and multi-layer models of the internal structure were adopted to provide new insights into the core structure of the planet. An additional constraint was provided by the measurements of the amplitude of the physical librations that led to an estimate of the moment of inertia of the outer layers (crust and mantle). The joint analysis of Mercury's mass and MoIs in the interior model inversion allowed us to provide constraints on the radius of the inner core as shown in Fig. 2.

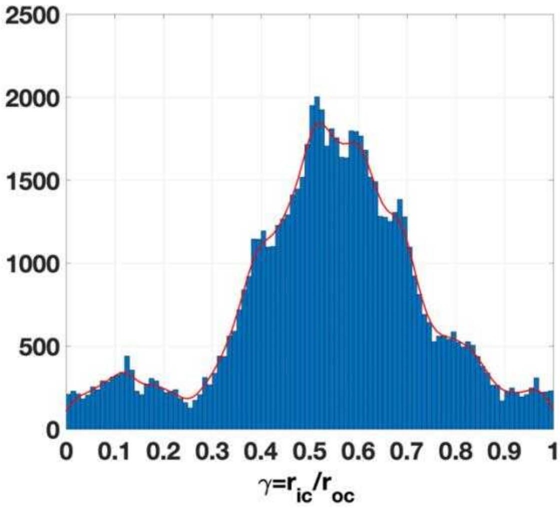

Figure 2 Histograms of the ratio between inner (r_{ic}) and outer core (r_{oc}) for the samples of four-shell MCMC solutions.

Further analyses of Mercury's interior structure were carried out by including the Love number k_2 measured by MESSENGER as observation of the MCMC [3], confirming the presence of the solid inner core. The geophysical data of the BepiColombo mission will provide refined measurements of Mercury's pole obliquity, amplitude of the physical librations and Love number k_2, enabling significant enhancements in the characterization of the core and mantle properties.

The MCMC method based on the multi-layer modeling accounts for the the Equation of State of realistic geochemical compositions of the rocky mantle and the metallic core providing pressure and temperature profile. This technique is also well-suited to investigate Venus' interior, by including as observations the geophysical measurements that will be acquired by the EnVision mission (*e.g.*, [4]).

Icy Moons: The interior model inversion for icy moons is based on the MCMC approach with a modeling of the internal layers that accounts for a metallic core, a rocky mantle and a hydrosphere, which models the subsurface ocean and the outer ice shell. First results were obtained for the Jovian moon, Europa, since the NASA mission Europa Clipper will conduct thorough investigations of its interior structure and composition. Europa Clipper Magnetometer (ECM) and gravity/radio science (G/RS) investigation will provide key measurements on the ocean and ice shell.

Europa Clipper L2 measurement that will be obtained through G/RS data is the Love number k_2, which will enable further evidence of the existence of a subsurface ocean and constraints on the hydrosphere thickness. To include this measurement in our interior model inversion, we included the software ALMA3 [5] that provides predictions of the Love numbers. Gravity measurements also constrain Europa's MoI that is a fundamental geophysical quantity to better understand the internal mass distribution. These measurements will thus be used to carry out the inversion of the interior structure of Europa, enabling an accurate inference of the properties of the deep interior and the hydrosphere.

To better characterize the properties of the ice shell and subsurface ocean, ECM will collect data to measure the magnetic field induced at Europa by Jupiter's primary field. The magnetic induction was revealed through the analysis of Galileo measurements, suggesting a conducting salty water ocean beneath the outer ice shell.

By using our MCMC method with Europa's mass, MoI [6-7] and magnetic induction data (*e.g.*, [8]) from Galileo as observations, we first inverted Europa's internal structure to better constrain the properties of Europa's hydrosphere [9]. While inversions based solely on gravity or magnetic field measurements yield degenerate solutions, our joint analysis of these two datasets yields the estimation of both ocean and ice shell thicknesses (Fig. 3). By using the latest estimate of Europa's MoI, our MCMC solutions also show that the metallic core is smaller than previously thought.

This methodology can be applied to combine the measurements that will be acquired by Europa Clipper G/RS and ECM to provide highly accurate constraints on Europa's interior.

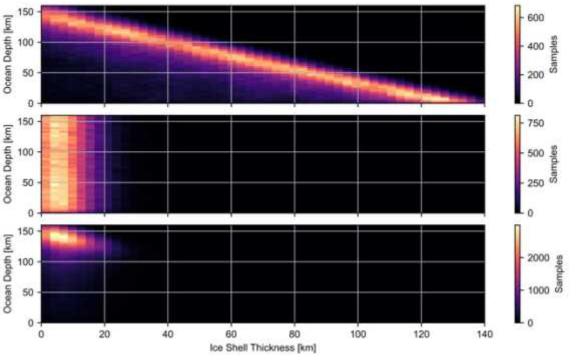

Figure 3 Histograms for ocean and ice shell thicknesses obtained through (top) inversion of gravity data only [7], (middle) inversion of magnetic induction data only [8], (c) joint inversion of gravity and magnetic induction data.

Summary: A thorough determination of the internal properties of terrestrial planets and icy moons is a key objective of planned space missions to Mercury, Venus, and the Jovian system, and mission concepts to the icy moons of Saturn and Uranus. The global inversion proposed in this study would allow to significantly enhance the scientific return of those missions.

References: [1] Mosegaard K. and Tarantola A. (1995) *JGR: Solid Earth*, *100*, 12431–12447. [2] Genova A. et al. (2019) *GRL*, *46*, 3625–3633 [3] Goossens S. et al. (2022) *PSJ*, *3(2)*, 37. [4] Rosenblatt P. et al. (2021) *Remote Sens.*, *13*, 1624. [5] Melini D. et al. (2022) *Geophys. J. Intern.*, *231*, 1502–1517. [6] Anderson J.D. et al. (1998) *Science*, *281*, 2019–2022. [7] Casajus L. G. et al. (2021) *Icarus*, *358*, 114187. [8] Schilling N. et al. (2004) *JGR: Planets*, *109*, E5. [9] Petricca et al. (2023) *GRL*, *50*, e2023GL104016.

Ongoing investigation of ice analogs of the Solar System icy moons using laboratory facilities.

A. Migliorini[1], Z. Kanuchova[2], S. Ioppolo[3], G. Strazzulla[4], [1]Institute for Space Astrophysics and Planetology, INAF, Italy, [2]Astronomical Institute, Slovakia, [3]Aarhus University, Denmark, [4]Catania Observatory, INAF, Italy

Introduction: Spectroscopy in the visible and near-infrared allows investigating surface composition, thanks to the several diagnostic features due to H_2O, CO_2, nitrogen-rich organics and nitriles, as an example. Minor species can also be identified, as atomic and molecular oxygen, the latter observed in the icy form on the surfaces of Ganymede, Europa and Callisto with telescopic observations. In particular, ground-based observations revealed two features centered at 577.3 and 627.5 nm that were attributed to solid O_2 in Ganymede's trailing hemisphere [1]. The same molecule was identified through the absorption feature at 577.3 nm on Europa and Callisto during subsequent campaings [2], and recently reobserved in Europa and Ganymede with a higher contrast, able to identify the two bands also in Europa (Spencer J., personal comm.). The observed features are recognized to be the result of a double electronic transition of two adjacent O_2 molecules [3, 4], although the presence and mantaince of molecular oxygen in icy surfaces like those of the Galilean satellites are still debated. If primordial, some mechanisms should occur to efficiently trap O_2 in the water ice layers. On the other hand O_2 in its solid phase must be constantly replenished through radiolysis to compensate for its depletion due to desorption. Despite these hypotheses, it is still debated how O_2 can be trapped and sustained on the surfaces of the icy satellites of the outer solar system planets. Laboratory experiments on ice analogs to the surfaces of the icy moons of Jupiter and Saturn can help address this open question. The same data would be of interest to study the surface composition of icy moons of Saturn, Uranus and Neptune, properly scaled to the thermal and ionospheric environments at these solar distances.

Method: Our purpose is to provide new insight on the properties of molecular oxygen and mixtures with H_2O, CO_2, N_2, CH_3OH, CH_4, exploring temperatures from 8 K to 80 K to further constrain the nature of the observed features on the Galilean satellites. Experiments have been performed in the vis range using the AU-UV beam line of the ISA ASTRID2 ring storage, at the University of Aarhus.

In this work we summarize measurements obtained in three runs in 2019, 2022 [5] and 2023 and a comparison with the Ganymede and Europa observations. In particular, we show that oxygen mixed with CH_3OH allowed to heat the sample up to 80 K with the two O_2 bands still visible, thus providing an icy sample at temperatures closer to those on the surface of the Galilean moons.

These laboratory measurements allow building a background for the future interepretation of data acquired with the MAJIS instrument [6] on board the ESA JUICE mission.

References:

[1] Spencer et al. 1995, J. Geophys. Res. 100 (E9), 19049-19056.

[2] Spencer and Calvin, 2002, ApJ 124 (6), 3400-3403.

[3] Landau et al. 1962, Astrochim. Acta 18 (1), 1-19.

[4] Mason et al. 2006, Faraday Discuss. 133, 311-329.

[5] Migliorini et al. 2022, Icarus 383, 115074.

[6] Piccioni et al. 2019, IEEE 5th International Workshop on Metrology for AeroSpace (MetroAeroSpace).

INFRARED ANALYSIS OF THE SURFACE OF JUPITER'S GALILEAN FROZEN MOONS WITH JUNO/JIRAM DATA.

E. Di Mico[1,2], A. Mura[2], G. Piccioni[2], F. Tosi[2], F. Biagiotti[2,3] and the whole JIRAM Team. [1]University of Rome Tor Vergata, Department of Physics, [2]INAF-IAPS, Via del Fosso del Cavaliere 100, Rome, [3]University of Rome La Sapienza, Department of Physics.

Introduction: Jupiter's frozen satellites - Europa, Ganymede and Callisto - became one of the main targets of the astrophysical interest in the Solar System in the last decades, since it was first hypothesized the presence of liquid water underneath their icy surface [1]. We have been able to confirm the presence of these subsurface liquid oceans on Ganymede [2] and Europa [3], while on Callisto this scenario has not been determined with certainty yet, because of the more static geology of this moon [4]. The study of the surface is of fundamental importance in order to understand the composition and history of the moons, but also to comprehend the mechanisms at work in their interiors and also in their atmospheres and exospheres. Analyzing the surface spectra of these icy moons we have found - other than ice in both crystalline and amorphous form - also peculiar elements like CO_2 and SO_2, and we hypothesize the presence of hydrated salts of sodium, magnesium, sulfur, nitrogen [5][6]. Their precise characterization and localization on the surface may be the key in understanding the nature and history of the moons and so this could give a hint in the knowledge of the origin and evolution of the whole Solar System.

Surface Characteristics: The infrared spectra of the frozen satellites of Jupiter share some characteristics. In all of them we can observe specific absorption features of water-ice (in the range $\sim [1-3]\mu m$) and some asymmetric features that have been attributed to hydrated materials: compounds (like salts or silicates) in which some molecules are associated to one or more water molecules, distorting the absorption lines of pure ice. The exact composition of these compounds is still unknown, as well as the nature of the so-called "darkening agent", a spectrally flat component that have been observed mostly on the surface of Callisto [7] but also on Ganymede [8]. Some of these material may come from the subsurface oceans of these moons: when tides stress the surface ice too much, the icy crust cracks and the internal materials break through the ice [9]. We can then obtain information about their internal structure. We know also that many compounds on the surface form because of the interaction of the ice of the crust with the flux of energetic particles ejected by Io's volcanic activity, that reach the Jovian magnetosphere and then precipitate onto the surface of the moons. Here they react with the water-ice through radiolysis and this may lead to the formation of compounds like carbon dioxide, methanol and carbonic acid, which could be very important for biological reactions [10].

Spectral Analysis: For our study we used the data collected by the instrument JIRAM (Jupiter InfraRed Auroral Mapper) on board NASA's satellite Juno, which is orbiting in the Jovian system since 2016. We used both the imager and the spectrometer data, which observed the satellites in the infrared range $(2-5)\mu m$. We used these to create spectral absorption maps in which we represented the I/F radiance factor, which is defined as "the reflectance relative to a perfect Lambertian surface perpendicularly illuminated" [11], with respect to the observed wavelength. The I/F factor is calculated taking into account the approximate distance of the Galilean Moons from the Sun ($\sim 5\ AU$) and scaled with the radiation spectra of the Sun [12]. From the so-obtained spectra we selected the absorption band of the features of interest for our study, like those associated with water-ice and with compounds like the carbon dioxide, other carbon and sulfur bearing compounds and possible hydrated salts [13]. Then we calculated their band depth, given by the formula:

$$BD(\lambda) = 1 - \frac{I/F(\lambda)}{I/F_C(\lambda)}$$

where we have the ratio between the radiance factor I/F at a certain wavelength and the radiance factor of the continuum spectrum at the same λ. As a last step we located the spectra with longitude and latitude coordinates on the surface of the moon, exploiting the geological maps and pictures taken by Galileo and JunoCam, the visible-light camera/telescope on board Juno.

References:

[1] S.W. Squyres, *Advances in Space Research*, 9, 79-85 (1989). [2] A. Mura et al., *Journal of Geophysical Research: Planets,* 125 (2020). [3] C. Zimmer and K. Khurana, *Icarus,* 147, 329-347 (2000). [4] C. A. Hibbitts et al., *Journal of Geophysical Research,* 105, 22541-22557 (2000). [5] F. Tosi et al., *Nature Astronomy* (2023). [6] M. E. Brown and K. P. Hand, *The American Astronomical Society*, 4, 110,

145 (2013). [7] A. L. Lane and D. L. Domingue, Geophysical Research Letters, 24, 9, 1143-1146 (1997). [8] N. Ligier et al., *Icarus*, 333, 496-515 (2019). [9] K. P. Hand et al., *Europa* (2009). [10] R. Pappalardo, Astronomy, 32, 7, 34-41 (2004). [11] B. Hapke, *Cambridge University Press* (1993) [12] R. L. Kurucz, Laboratory and Astronomical High Resolution Spectra, 81, 17 (1995). [13] T. B. McCord et al., *Journal of Geophysical Research*, 103, 8603-8626 (1998).

MID-SIZED SATURNIAN ICY SATELLITES INVESTIGATION BY SPECTRAL MODELING (MISSIS): THE CASE OF RHEA.

M. Ciarniello[1], G. Filacchione[1], A. Raponi[1], V. Galluzzi[1], E. D'Aversa[1], B. Gorga[1,2]. [1]INAF-IAPS, via del Fosso del Cavaliere, 100, 00133, Rome, IT (mauro.ciarniello@inaf.it). [2]Sapienza Università di Roma, Piazzale Aldo Moro, 5, 00185 Rome, IT.

Introduction: The Cassini mission orbited in the Saturnian System for thirteen years (2004-2017) providing an outstanding wealth of data that allowed the characterization of Saturn, its rings, and the moons. A primary scientific goal of the mission was the study of the physical and compositional properties of Saturn's icy moons, aimed at understanding the interplay among the endogenic and exogenic processes affecting their surfaces. The Visual and Infrared Mapping Spectrometer (VIMS, [1]) onboard the Cassini orbiter extensively characterized the spectrophotometric properties of the Mid-sized Saturnian icy Satellites (MISS, hereafter), namely Mimas, Enceladus, Tethys, Dione, and Rhea, in the 0.35-5.1 µm spectral range, revealing surfaces dominated by crystalline water ice (as evidenced by the diagnostic absorption bands at 1.5, 2, 3 µm) with the occurrence of contaminants, of debated nature (iron-bearing materials vs organics), inducing color (e. g. spectral reddening in the 0.35-0.55 µm interval) and albedo variations within and among the moons (Fig. 1).

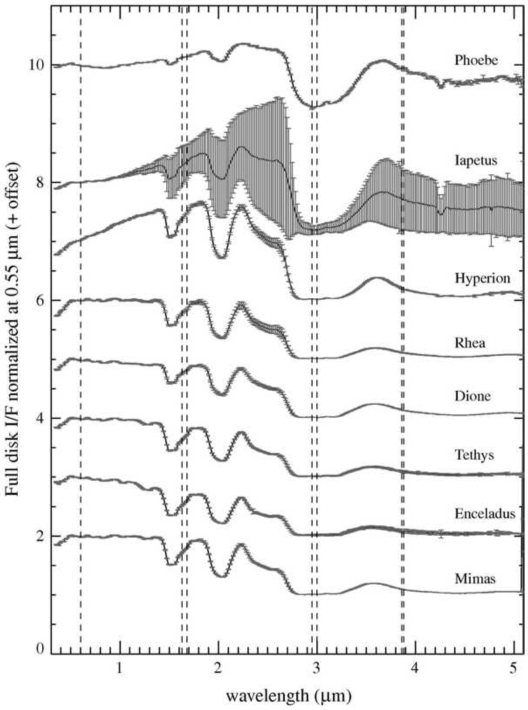

Figure 1. VIMS spectrum of a selection of Saturn's icy moons. Note the characteristic water ice absorption features at 1.5, 2. and 3 µm. Variations of the VIS-NIR spectral slope (e.g. the sharp UV downturn at 0.35-0.55 µm) and albedo are due to presence of non-icy contaminants. From ref. [2].

Several studies investigated MISS' spectral variability by defining suited spectral indicators (e.g. spectral slopes in selected wavelength ranges and band depths of water ice features) linked to water ice/contaminant abundances and regolith grain size. This approach allowed defining qualitative trends of the surface properties at full-disk [2,3] and hemispherical [4] scales, along with disk-resolved mapping [5-7], but could not provide a fully quantitative characterization of the compositional/physical properties, as this information remains at least partially entangled in the spectral indicators.

A more quantitative investigation of the compositional and physical properties of the surface of MISS has been attempted by comparing the VIMS hyperspectral data with solutions of the radiative transfer equations in particulate surfaces [e.g. Hapke theory, 8] applied to appropriate mixtures of selected compositional endmembers for which optical constants are available. By means of such physically based models, the spectra of the mixtures can be computed as a function of endmember abundances, mixing modalities, and grains size distributions, thus allowing to unravel the spectral contribution of the different compositional/physical properties on the observed spectral shape (spectral modeling). Given the inherently greater complexity of the spectral modeling approach, similar efforts have been conducted in a limited number of cases, to constrain the composition of characteristic terrains for selected targets (see [9] for Dione), or to infer the full-disk compositional properties of the MISS [10, 2], while a systematic application of this methodology to disk-resolved observations of MISS is still missing.

Within the MISSIS project we aim to go a step further, and by taking advantage of VIMS photometrically corrected disk-resolved data of MISS [7], we propose a systematic spectral modeling of their surfaces. This will allow us to characterize the non-icy components and their mixing modality with water ice on MISS, and to map quantitatively the distribution of water ice and contaminants across the surface, along with the regolith grain size.

Here we present the preliminary results of this effort applied to Saturn's moon Rhea, while a companion paper [12] is devoted to the study of Dione.

Method: for this investigation we take advantage of the photometrically corrected spectral maps of Rhea from VIMS observations, adapting the approach described by [7] (Figure 2, top panel). The spectral map is produced by sampling the surface with a regular longitude-latitude grid with 0.5°x0.5°

bins, by averaging photometrically corrected VIMS observations falling in each bin. The result is a hyperspectral cube with a spectrum associated to each position of the map.

We perform a systematic spectral modeling for each pixel of the spectral map by applying Hapke theory. Following from previous modeling attempts [11], we describe the surface as a mixture of water ice, a macromolecular organic compound (tholin, inducing the UV absorption) and amorphous carbon grains (as a darkening contaminant.)

Preliminary results: in Figure 2 (middle panel) we show a preliminary compositional map of Rhea. The results of the spectral modeling effort point to a surface composition dichotomy, with the leading hemisphere (longitudes 0°-180°) hosting larger amounts of water ice with respect to the trailing one (longitudes 180°-360°), where non-icy materials (tholin and carbon) are present in greater amounts. This distribution of the different endmembers reflects the albedo and color dichotomy of the surface (figure 2 bottom panel), with a redder/darker trailing side compared to a bluer/brighter leading hemisphere of the satellite.

We will discuss the inferred endmember spatial variability in the context of the exogenous processes (bombardment from E-ring grains, charged particles, and exogenic darkening material, and photolysis; [13]) altering the composition, taking into account their longitudinal dependence, along with cratering and endogenous processes which shaped the surface of Rhea.

Acknowledgements: this work is supported by the INAF data analysis grant "Mid-sized Saturnian icy Satellites Investigation by Spectral modeling" (MISSIS).

References: [1] Brown et al., 2004. SSRv 115, 111–168. [2] Filacchione et al., 2012. Icarus 220, 1064–1096. [3] Filacchione et al., 2013. ApJ 766. [4] Hendrix, et al., 2018. Icarus 300, 103–114. [5] Stephan et al., 2016. Icarus 274, 1–22. [6] Scipioni et al., 2017. Icarus 290, 183–200. [7] Filacchione et al., 2022. Icarus 375. [8] Hapke, B., 2012. Theory of reflectance and emittance spectroscopy (Cambridge Univ. Press). [9] Clark et al., 2008. Icarus 193, 372–386. [10] Ciarniello et al., 2011. Icarus 214, 541–555. [11] Ciarniello et al., 2019. Icarus 317, 242–265. [12] Gorga et al., this conference. [13] Hendrix et al., 2018. Icarus 300, 103-114.

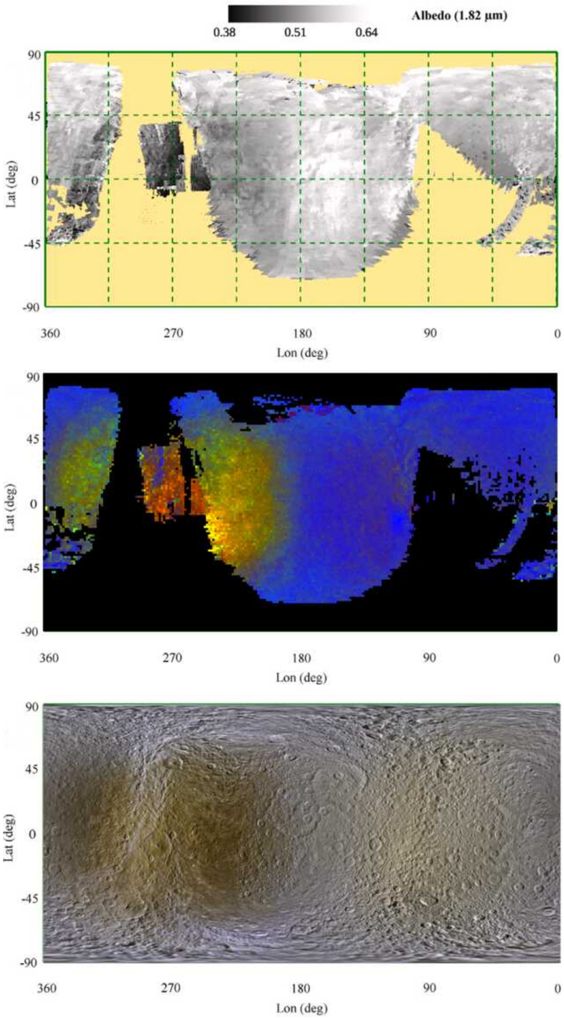

Figure 2. Top panel: 1.82-µm equigonal albedo map of Rhea in cylindrical projection [7]. Middle panel: RGB compositional map of Rhea (red: tholin abundance; green: carbon abundance; blue: water ice abundance). Bottom panel: Cassini Imaging Science Subsystem global color (IR, Green, UV) map (PIA18438, image credit P. Schenck, NASA/JPL-Caltech/Space Science Institute/Lunar and Planetary Institute).

THE ROLE OF GRAPHITE IN THRUST FAULTS FORMATION ON MERCURY.

N. A. Vergara Sassarini[1] and M. Massironi[2], L. Giacomini[3], A. Bistacchi[4]. [1] CISAS, Università degli Studi di Padova, 35131 Padova, Italy, amanda.vergara@unipd.it [2] Dipartimento di Geoscienze, Università degli Studi di Padova, 35131 Padova, Italy [3] INAF- IAPS, Via delFosso del Cavaliere 100, 00133 Rome, Italy [4] Dipartimento di Scienze dell'Ambiente e della Terra, Università degli Studi di Milano, Milan, Italy

Introduction:

Globally, the most widespread contractional landforms on Mercury are lobate scarps. Lobate scarps are linear or curvilinear topographic features interpreted as the surface expression of thrust faults, formed as a consequence of planetary cooling and contraction. These features have been studied extensively, from the initial images captured by Mariner-10 to the more recent data acquired by MESSENGER's Mercury Dual Imaging System (MDIS). However, a comprehensive interpretation of fault geometry and their mechanical behavior on a global scale remains unconstrained. Here, we show that the formation and growth of large-scale lobate scarps is facilitated by the presence of a graphite-rich layer(s), acting as fault lubricant.

Data and Methods:

We studied thrust faults from seven different Mercury quadrangles and derived their geometric characteristics (relief height, amount of shortening, detachment depth) considering a fault-propagation geometry for a range of possible dip angles on isolated thrusts. Using a critical taper theory-based model (iterative mechanical model) we then estimated the basal (i.e., décollement) friction coefficient (μ_b) for thrust-belts located in the same quadrangles.

Figure 1. shows the workflow for the geometric and mechanic analysis of thrust faults on Mercury. The dataset (in purple) includes the global DEM (665 m/px) provided by USGS and published surface traces of contractional features[1 2 3]. The methods (in blue) begin with target selection across Mercury's surface, with each target comprising a thrust belt zone along with an isolated thrust with the same vergence. The geometric model, implemented in Matlab, is based on a fault-propagation-folding geometry, and is utilized to calculate the décollement (i.e., detachment horizont) depth (T), serving as an input parameter for the Mechanic Iterative Model (MIM) based on the critical taper theory, developed in Matlab. The MIM determines the best fitting basal friction coefficient (μ_b) for the observed topography through iterative adjustments of several fault parameters (e.g., dip angle β, T). The output (in green) consists of the predicted μ_b values for the different targets.

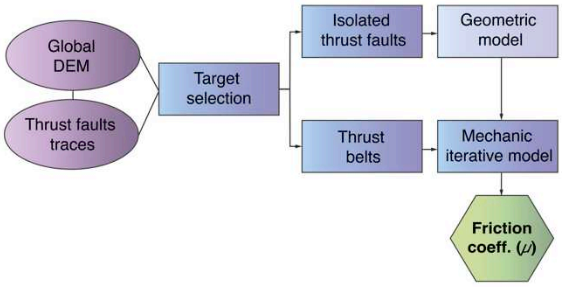

Figure 1 Workflow

Results and discussions:

Graphite is often enriched within fault zones on Earth as a result of mechanical or chemical processes. An important distinction between Earth and Mercury's graphite lies in their composition. On Earth, discussions predominantly focus on fluid-deposited carbon/graphite induced, for instance, through processes like pressure solution and metamorphic graphite originating in situ from organic matter [4]. It is well-established that carbon arranges its crystalline structure in response to pressure and temperature, creating layered structures thus facilitating fault slip. On Earth, achieving this effect typically involves transforming carbon from a carbon source into a more organized structure (graphite) through frictional heating. Conversely, on Mercury, it is plausible that a layer comprising pure graphite exists, which may have formed the primary buoyant crust of graphite[5]. Considering this, we expect to find an optimal material that facilitates thrust fault nucleation and propagation on Mercury.

The low friction coefficients (average μ_b <0.45 for dip angles between 15° and 20°) obtained under three different crustal initial conditions (i.e., highly fractured crust, mildly fractured crust, and a combination of both) suggest the presence of a weakening mineral along the slip surface, which is fundamental to allow ubiquitous deformation of Mercury's surface.

We propose that such low μb values may be attributed to the presence of graphite since: (1) there is evidence suggesting the possible presence of graphite in LRM deposits, where it may act as the darkening material[6]; (2) previous research has established the role of graphite as a lubricating agent in fault zones on Earth[7 8]; (3) the lower-end μ_b values (~ 0.1) observed in our study are in agreement with values obtained from friction experiments involving synthetic gouges containing graphite as the weakening agent [9].

Our results demonstrate the crucial role that graphite possibly plays in shaping Mercury's surface, providing new understanding on thrust faults nucleation and growth and establishing a possible connection between surface deformational processes and Mercury's early crust composition.

References:

[1] Giacomini, L., Massironi, M., Galluzzi, V., Ferrari S., Palumbo, P. (2020). Dating long thrust systems on Mercury: New clues on the thermal evolution of the planet. Geoscience Frontiers, 11(3), 855-870. https://doi.org/10.1016/j.gsf.2019.09.005

[2] Byrne, P. K., Klimczak, C., Celâl Şengör, A. M., Solomon, S. C., Watters, T. R., & Hauck, II, S. A. (2014). Mercury's global contraction much greater than earlier estimates. Nature Geoscience, 7(4), 301-307. https://doi.org/10.1038/ngeo2097

[3] Man, B., Rothery, D. A., Balme, M. R., Conway, S. J., & Wright, J. (2023). Widespread small grabens consistent with recent tectonism on Mercury. Nature Geoscience, 1-7. https://doi.org/10.1038/s41561-023-01281-5

[4] Cao, S., & Neubauer, F. (2019). Graphitic material in fault zones: Implications for fault strength and carbon cycle. Earth-Science Reviews, 194, 109-124. https://doi.org/10.1016/j.earscirev.2019.05.008

[5] Peplowski, P. N., Klima, R. L., Lawrence, D. J., Ernst, C. M., Denevi, B. W., Frank, E. A., Goldsten, J. O., Murchie, S. L., Nittler, L. R. & Solomon, S. C. (2016). Remote sensing evidence for an ancient carbon-bearing crust on Mercury. Nature Geoscience, 9(4), 273-276. https://doi.org/10.1038/ngeo2669

[6] Klima, R. L., Denevi, B. W., Ernst, C. M., Murchie, S. L., & Peplowski, P. N. (2018). Global distribution and spectral properties of low□reflectance material on Mercury. Geophysical Research Letters, 45(7), 2945-2953. https://doi.org/10.1002/2018GL077544

[7] Oohashi, K., Hirose, T., Kobayashi, K., & Shimamoto, T. (2012). The occurrence of graphite-bearing fault rocks in the Atotsugawa fault system, Japan: Origins and implications for fault creep. Journal of Structural Geology, 38, 39-5. https://doi.org/10.1016/j.jsg.2011.10.011

[8] Kuo, L. W., Li, H., Smith, S. A., Di Toro, G., Suppe, J., Song, S. R., ... & Si, J. (2014). Gouge graphitization and dynamic fault weakening during the 2008 Mw 7.9 Wenchuan earthquake. Geology, 42(1), 47-50. https://doi.org/10.1130/G34862.1

[9] Oohashi, K., Hirose, T., & Shimamoto, T. (2013). Graphite as a lubricating agent in fault zones: An insight from low□to high□velocity friction experiments on a mixed graphite□quartz gouge. Journal of Geophysical Research: Solid Earth, 118(5), 2067-2084. https://doi.org/10.1002/jgrb.50175

MERCURY'S CRUSTAL STRUCTURE MODELING

S. Buoninfante[1,2], M. Milano[1], B. Negri[3], C. Plainaki[3], G. Sindoni[3], M. Fedi[1].
[1]Department of Earth, Environment and Resources Sciences (DiSTAR), University of Naples Federico II, Naples, Italy (salvatore.buoninfante@inaf.it), [2]Istituto di Astrofisica e Planetologia Spaziali (IAPS), INAF, Rome,Italy, [3]Agenzia Spaziale Italiana (ASI), Rome, Italy

Introduction: The study of the internal structure of Mercury is fundamental for understanding the formation and evolution of the planet and of the entire Solar System. Mercury is constituted by a very large iron-rich core with a radius of ~2000 km, a ~400 km thick mantle made of iron-poor and magnesium-rich silicates, and a silicate crust with an average thickness of ~35 km. The main purpose of this work was the analysis of the NASA MESSENGER MESS160A gravity field [1] to generate the map of the isostatic gravity anomalies of Mercury, representative of the intra-crustal sources. We first estimated a 30 km mean elastic lithosphere thickness and calculated the flexural response function of the lithosphere. Assuming a flexural compensation model, we modeled the lithospheric flexure regardless of the gravity field (e.g., [2]) and calculated the isostatic gravity anomalies by subtracting the gravity effect caused by compensating roots to Bouguer anomalies. In this way, we proved that considerable lateral density variations occur within the Mercury crust. We, then, also estimated the curst-mante interface depth, varying from 19 to 42 km.

Methods and results: Following [3], we searched for the average elastic lithosphere thickness as the one giving the best fit between observed and calculated free-air anomalies along a series of 1-dimensional profiles. In Fig. 1 we show the results obtained along a NW-SE profile. The L2 misfit between the observed and calculated data reaches its minimum at the elastic thickness of 30 km. By also evaluating the results obtained for other chosen profiles, we may assume T_e= 30 ± 10 km as representative of the mean elastic lithosphere thickness.

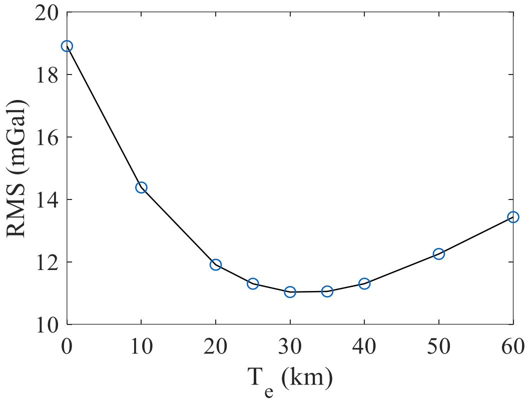

Figure 1. Plot of the root mean square difference (RMS) between observed and calculated free-air gravity anomalies vs T_e, for the NW-SE profile.

The flexural response function (Fig. 2) represents the flexural response of the lithosphere to loading and allows understanding what type of isostatic model should be considered for a given spherical harmonic degrees range. The lithosphere of Mercury flexes for spherical harmonic degrees of the topography in the range $5<l<80$, i.e., for topography wavelengths ranging $190<\lambda<2800$ km. For spherical harmonics up to degree 5 and wavelengths longer than 2800 km, the flexural rigidity $D \to 0$, and we may assume the Airy compensation model. For surface features with wavelengths shorter than 190 km, $D \to \infty$ so that no lithospheric flexure occurs since the rigidity of the lithosphere is such to resist the topographic load.

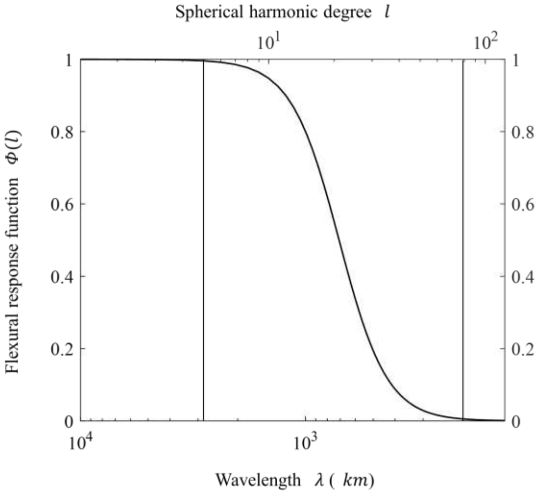

Figure 2. Flexural response function $\Phi(l)$ as a function of spherical harmonic degree and of topography wavelength, for the elastic thickness 30 km.

In Figure 3 we show the isostatic gravity anomalies obtained by subtracting the topographic and the isostatic gravity effects from the free-air anomalies and constrained by the MESS160A degree strength map [1], which shows the local resolution of the gravity field.

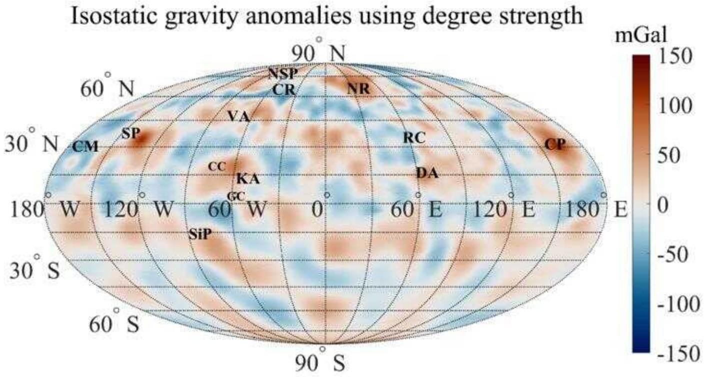

Figure 3. Isostatic gravity anomalies constrained with the MESS160A degree strength. Major features indicated are: **CM** = Caloris Montes; **CP** = Caloris Planitia; **CR** = Carneige Rupes; **DA** = Derain anomaly; **KA** = Kuiper anomaly; **NR** = Northern Rise; **NSP** = Northern Smooth Plains; **RC** = Rachmaninoff Crater; **SiP** = Sihtu Planitia; **SP** = Sobkou Planitia; **VA** = Victoria Anomaly; **CC** = Catullus Crater; **GC** = Giotto Crater. Maps are in Mollweide projection.

After calculating the lithospheric deflection coefficients we also modeled the crust-mantle interface (Figure 4) by means of a spherical harmonic expansion. We considered the previously estimated mean elastic thickness of 30 km and assumed densities for crust and mantle of 2800 kg/m3 and 3200 kg/m3, respectively [4].

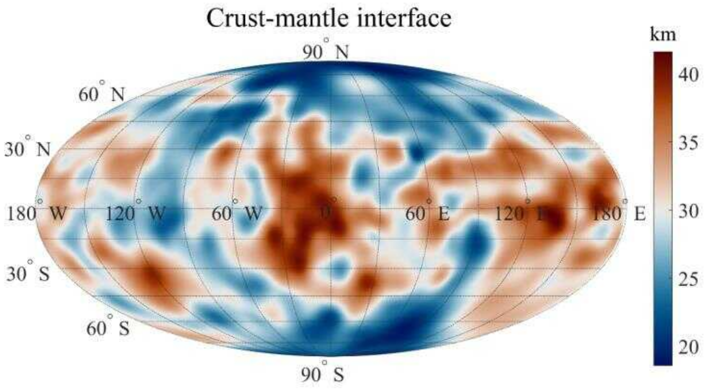

Figure 4. Map of crust-mantle interface of Mercury, expressed as depth (km), in a Mollweide projection.

Conclusions: The isostatic gravity anomalies provide a useful tool for the geological interpretation of Mercury. The estimated mean elastic lithosphere thickness is 30 ± 10 km. The crust-mantle interface is 19 to 42 km deep. The larger crust-mantle interface depths (down to ~42 km) are reached in the equatorial regions, the smaller in the polar regions (down to ~19 km). The crustal roots thickening due to larger topographic loads is responsible for these depths. Isostatic gravity highs are mostly interpreted with intra-crustal magmatic intrusions and isostatic gravity lows as the effect of a heavily fractured crust. BepiColombo mission will provide better data resolution on the Southern hemisphere of Mercury, leading to an improved gravity field model and a more detailed isostatic gravity anomaly map.

Acknowledgements: We gratefully acknowledge funding from the Italian Space Agency (ASI) under ASI-INAF agreement 2017-47-H.0.

References:

[1] Konopliv, A. S. et al. (2020). *Icarus*, 335.
[2] Turcotte, D. L. et al. (1981). *J. Geophys. Res.*, 86.
[3] Watts, A. B. (2010). *Treatise on Geophysics*, 6.
[4] Genova, A. et al. (2019) *Geophys. Res. Lett.*, 46.

LAVA LAKES ON IO

A. Mura[1], F. Tosi[1], F. Zambon[1], R. Sordini[1], A. Adriani[1], A. Altieri[1], C. Castagnoli[1], M. Ciarniello[1], A. Cicchetti[1], E. Di Mico[1], G. Filacchione[1], D. Grassi[1], A. Migliorini[1], A. Moirano[1], R. Noschese[1], G. Piccioni[1], C. Plainaki[2], G. Sindoni[2], S. Stefani[1], D. Turrini[1]

[1]Istituto Nazionale di Astrofisica – Istituto di Astrofisica e Planetologia Spaziali (INAF – IAPS), Rome, Italy; alessandro.mura@inaf.it
[2]Agenzia Spaziale Italiana (ASI), Rome, Italy

Introduction: Recent infrared observations of Io, acquired from the JIRAM instrument [1] on board the NASA mission Juno during its latest orbits recorded high-resolution images of previously unexplored regions of Io's surface.

Numerous paterae have been identified to be lava lakes, with a surprising prevalence of a "lava rings" morphology, despite the apparent absence of visible evidence for an island within most of the paterae.

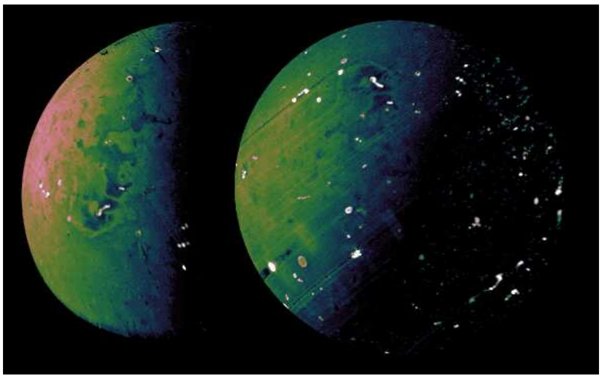

Figure 1:L band (left) and M-band (right) images of Io captured during the 51st orbit of Juno

Methods:

JIRAM has been proven to be well suited for the investigations of Galilean moons, and in particular of Io [2, 3, 4, 5]- The analysis of the thickness of the hot regions and their relative positions with respect to the viewing geometry provides valuable insights, and suggests that the hottest region lies at the edge of the lava lake, supporting the hypothesis of crust break-up near the shoreline. This could also indicate vertical movement of the lava within the lake, resulting in the observed ring-like shapes.

Surprisingly, the infrared imaging does not reveal significant high-temperature regions away from the patera walls. This phenomenon could imply one of two possibilities: either the lava lake crust in the central area is too thick to break up, or the margin deformation primarily arises from the vertical movement of lava within the lake.

These findings offer a fresh perspective on the dynamic nature of Io's volcanic activity and provide essential clues to the underlying mechanisms shaping the geological features of the moon.

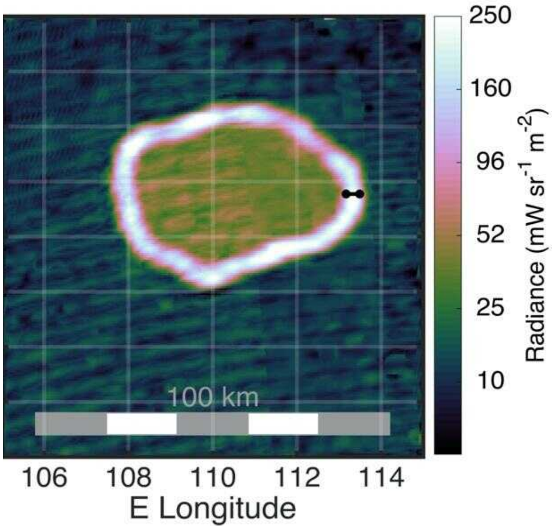

Figure 2: M-band IR image (Oct. 2023, resolution: 3 km) of Chors patera. The new observations constraint the annular width to less than 30 m.

References:

[1] Adriani, A., et al. (2014). *Space Sci. Rev., doi: 10.1007/s11214-014-0094-y.*
[2] Mura A., et al.(2020) *Icarus, 341, doi: 10.1016/j.icarus.2019.113607*
[3] Tosi F., et al.(2020) *JGR Planets, 125,11*, doi: 10.1029/2020JE006522
[4] Mura A., et al.(2020) *JGR Planets, 125,11, doi: 10.1029/2020JE006508*
[5] Zambon F., et al.(2023) *GRL, 50,1, doi: 10.1029/2022GL100597*

Acknowledgments

We thank Agenzia Spaziale Italiana (ASI) for the support of the JIRAM contribution to the Juno mission; this work is supported by the ASI–INAF Addendum n. 2016-23-H.3-2023 to grant 2016-23-H.0.

Tematica: Pianeti e Satelliti;
Focus: Tettonica, Vulcanesimo e Fratturazione nel Sistema Solare

PRELIMINARY RESULTS FROM LABORATORY INVESTIGATIONS INTO ELECTROMAGNETIC PROPERTIES OF GANYMEDE ICY CRUST ANALOGUES

Alessandro Brin[1], *Sebastian Emanuel Lauro*[1], *Barbara Cosciotti*[1], *Elisabetta Mattei*[1], *Gabriele Turchetti*[1], *Elena Pettinelli*[1]
[1]Mathematics and Physics Dept., Roma Tre University

Introduction: Ganymede, Jupiter's largest moon, presents a compelling target for Solar System exploration due to its unique characteristics and potential insights into planetary evolution. The moon is in fact an example of water world, due to the presence of a subsurface ocean beneath an icy crust. Moreover, Ganymede's surface exhibits a distinctive dichotomy between bright and dark terrains, unlike the other Jupiter icy moons: the brighter regions are younger, grooved and ice-rich, while the darker regions are older, heavily cratered and dominated by a darkening agent. Through the spectral analysis of Galileo Near Infrared Mapping Spectrometer (NIMS) measurements [1] and the ground-based VLT/SPHERE (Very Large Telescope/ Spectro-Polarimetric High-contrast Exoplanet REsearch) observations [2] it was inferred the composition of the dark terrains on the moon: a mixture of water ice, hydrated salts, and a hydrated carbonaceous material compatible with the spectra of carbonaceous chondrites. In addition to that, models for the composition and structure of the satellite point out that the geochemical parameters of its rock-iron constituent are similar to the material of L/LL chondrites [3]. Ganymede will be the main target of the space mission JUICE (Jupiter icy Moons Explorer [4]), that mounts on board a radar, RIME [5], since the radio echo sounding is becoming a fundamental method for examining the subsurface geology and geophysics of planets and other solar system bodies and for detecting the presence of subsurface water [6-8]. Nevertheless, radar signal penetration and subsurface layer imaging performances are dependent on the dielectric permittivity and magnetic permeability of the materials that compose the crust of such objects. For this reason, we have studied the electromagnetic properties of Ganymede icy crust analogues in the frequency range of interest for RIME, considering the composition suggested by measurements and models and given the absence of comparable measurements in the literature.

Methodology and samples characterization: *Measurement technique.* We used the coaxial transmission line approach to measure the complex dielectric permittivity (ε) and the complex magnetic permeability (μ) of our analogues in the frequency range of 1MHz-1GHz. The measuring cell consists in a transmission line filled with the sample; its scattering parameters were measured by means of a two port Vector Network Analyzer. The probe-line used in this study was connected to an Agilent E5071C VNA via two 50 Ω coaxial cables terminating with N-type connectors. Using an adapted Nicolson-Ross-Weir (NRW) algorithm [9], the complex dielectric permittivity and magnetic permeability were estimated from the scattering parameters, by means of the following equations:

$$\sqrt{\frac{\varepsilon}{\mu}}F_g = \frac{1-\Gamma}{1+\Gamma} \tag{1}$$

$$\sqrt{\varepsilon\mu}\,l = \frac{ic}{2\pi\nu}\ln(\Psi) \tag{2}$$

where F_g is the geometrical factor related to the impedance mismatch between the coaxial cable and the transmission line, Γ is the reflection coefficient, $l = 10$ *cm* is the length of the transmission line, c is the velocity of the light in vacuum and Ψ is the transmission coefficient.

Samples' characterization. For this work we used two different samples: 1) a crushed L5 ordinary chondrite (see [10-11] for details), and 2) a CI carbonaceous chondrite simulant produced by CLASS Exolith Lab [12]. We measured the electromagnetic properties of the two samples, both anhydrous and saturated with double-distilled water and saline solutions. With the saturated samples we intend to reproduce the frozen soils present on the satellite, since ice porosity should rapidly drop to zero at a depth of few hundred meters because of the expected pressure [13].

Experimental procedure. For the anhydrous measurements the granular samples underwent controlled heating in a vacuum environment using the SalvisLab Vacucenter VC20 oven, reaching a temperature of 378 K at approximately 20 mbar for a duration of twelve hours, precluding the presence of residual moisture. After that, the measuring cell was transferred inside the NEXUS H Angelantoni Life Science ultra-freezer and left there for a day prior to the measurement. Eventually the cell filled with the sample was taken out of the ultra-freezer and connected to the VNA for the electromagnetic measurement, while a pt100 temperature sensor put inside the sample constantly monitored its temperature. A similar procedure was employed for the saturated samples, after having saturated them with double-distilled water and saline solutions.

Results: Measurements of the anhydrous samples were performed at a fixed porosity and in the temperature range 205 – 290 K. We report the frequency spectra of the dielectric permittivity of the anhydrous L5 ordinary chondrite sample at different temperatures in Fig. 1.

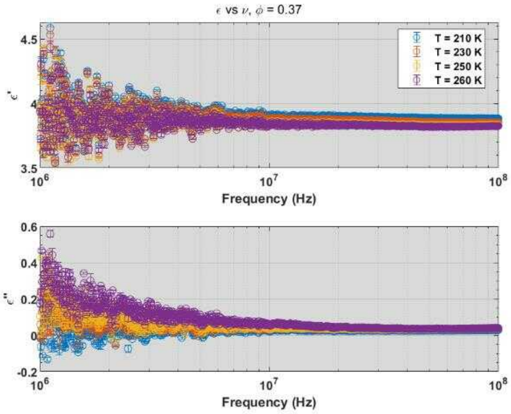

Fig. 1. Frequency spectra of complex permittivity of the anhydrous ordinary chondrite at a porosity $\boldsymbol{\phi = 0.37}$ and at four different temperatures, ranging from 210 K to 260 K.

Fig. 2 shows the dependence of the complex permittivity of the granular chondrite on temperature: there is a very slight variation of the electrical parameter as the temperature rises.

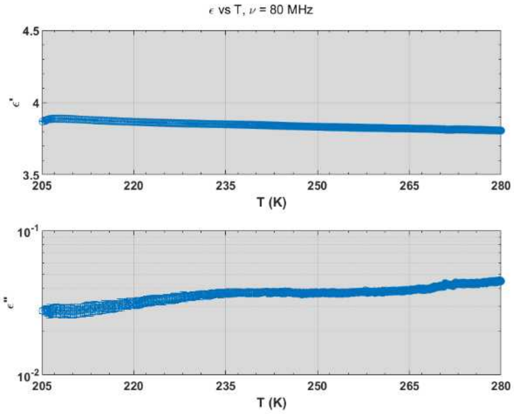

Fig. 2. Complex permittivity of the anhydrous L5 ordinary chondrite as a function of temperature in the range 205-280 K at the frequency of 80 MHz.

Moreover, it's important to note that the granular chondrite has non-negligible magnetic properties to take into account when calculating the attenuation of the radar signal [11].

In Fig. 3 we show the trend of complex permittivity as function of frequency at five different temperatures for the saturated ordinary chondrite.

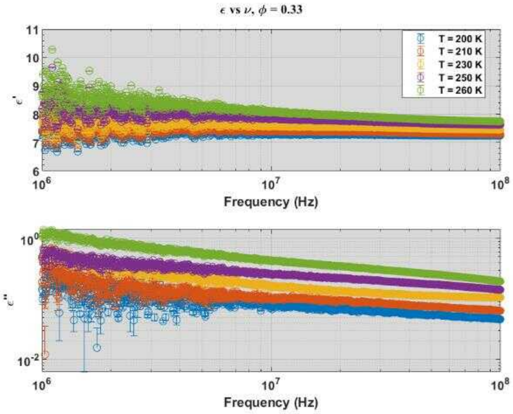

Fig. 3. Frequency spectra of complex permittivity of the saturated ordinary chondrite at a porosity $\boldsymbol{\phi = 0.33}$ at five different temperatures, ranging from 200 K to 260 K.

The same measurement has been repeated for the CI carbonaceous chondrite simulant, both anhydrous and saturated with double-distilled water and a NaCl solution. Our results highlight the importance of such experiments, that will be essential for constraining the geophysical properties of materials detected through RIME during the JUICE mission.

References: [1] Hibbitts, C. A. (2023). Icarus, 394, 115400. [2] King, O., & Fletcher, L. N. (2022). Journal of Geophysical Research: Planets, 127(12), e2022JE007323. [3] Kronrod, V. A. & Kuskov, O. L. (2006). Geochemistry International, 44, 529-546. [4] Grasset, O. et al. (2013). Planetary and Space Science, 78, 1-21. [5] Bruzzone, L. et al., (2013). In 2013 IEEE international geoscience and remote sensing symposium-IGARSS (pp. 3907-3910). IEEE. [6] Plaut, J. J., et al. (2007), Science, 316(5821), 92–95. [7] Kofman, W. et al., (2015), Science 349, aab0639 1-6. [8] Orosei, R. et al. (2018). Science, 361(6401), 490-493. [9] Mattei, E. et al., (2013), IEEE transactions on instrumentation and measurement 62.11, 2938–2942. [10] Cosciotti, B. et al. (2021). Icarus, 362, 114426. [11] Brin, A. et al. (2022). Icarus, 374, 114800. [12] Britt, D. T. et al. (2019). Meteoritics & Planetary Science, 54(9), 2067-2082. [13] - Byrne, P. K., et al. 49th Annual Lunar and Planetary Science Conference. No. 2083. 2018.

EXPERIMENTAL RESULTS ON THE H_2-H_2 AND H_2-HE COLLISIONAL-INDUCED ABSORPTION COEFFICIENTS AT TYPICAL JUPITER'S UPPER TROPOSPHERIC CONDITIONS.

F. Vitali[1,2], S. Stefani[1], G. Piccioni[1], D. Grassi[1] and M. Snels[3]. [1]IAPS-INAF, Via del fosso del cavaliere 100, 00133 Rome, Italy, Università degli studi di Roma "Tor Vergata", Via Cracovia 50, 00133, Rome, Italy, [3]ISAC-CNR Via del fosso del cavaliere 100, 00133, Rome, Italy
francesca.vitali@inaf.it

Introduction: Jupiter's atmosphere is primarily composed of molecular hydrogen and helium.

Since the atmosphere of this gaseous giant represents a high-density environment, the H_2-H_2 and H_2-He Collision Induced Absorption (CIA) bands represent its main source of opacity in the infrared part of the spectrum, particularly between 1 and 5 μm, which is a spectral range widely used by remote sensing instruments.

For this reason, it is important to have experimental data on the CIA absorption and to compare them with the theoretical models present in the literature, in order to have an as much as accurate possible estimation of Jupiter's atmospheric opacity.

Consequently, measurements of the hydrogen CIA fundamental band have been performed at temperature and pressure conditions typical of the Jovian upper-tropospheric profile, using an H_2-He mixture with 13.8 % of helium (typical of Jupiter's atmosphere).

In this work, we report the measurements performed for this study, while more data in the not-yet.explored temperature range will be presented at the conference (work in progress).

Experimental setup: To perform these measurements an experimental setup called PASSxS has been used. It allows to record spectra in the spectral range from 1 to 6 μm.

It comprises two stainless steel concentric vessels, as shown in Figure 1. The inner one contains the gas or mixture of gases under investigation, while the external can be evacuated to ensure thermal insulation of the sample chamber from the external environment.

Moreover, the inner vessel contains a Multi-Pass cell, characterized by an optical path of about 3.2 m, coupled with a FT-IR spectrometer. The range of spectral resolutions achievable with the present FT-IR goes from 0.06 to 10 cm^{-1}. For a more detailed description of the experimental setup refer to [1].

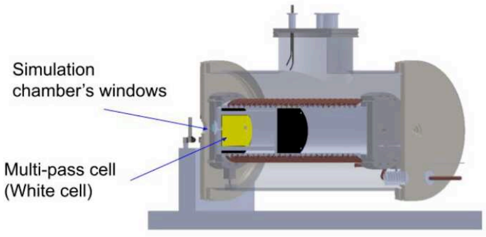

Figure 1: graphical sketch of the PASSxS.

Results and discussion: First of all we demonstrated that, for a specific temperature, the binary absorption coefficients (which are the absorption coefficients normalized for the density squared) don't depend on pressure.

Figure 2 shows the binary absorption coefficients for three measurements taken at 300 K for three different pressures. As one can see the three curves overlap.

By demonstrating this, we were able to perform measurements at a specific temperature at high pressure, calculate the binary absorption coefficients, and then re-calculate the absorption coefficients for the pressure desired, obtaining a high-signal-to-noise measurement.

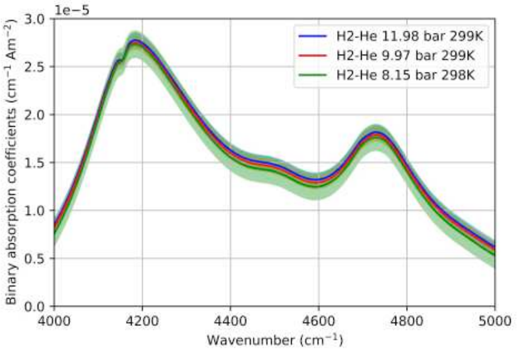

Figure 2: Binary absorption coefficients at 300 K for a H_2-He mixture.

In Figure 3 the Jovian atmospheric profile is shown [2]. The three dots superimposed on the curves represent the pressure and temperature set points at which the measurements have been performed.

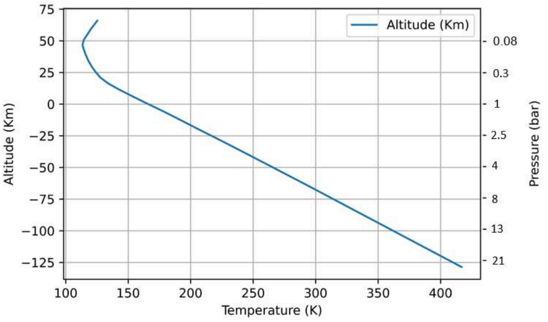

Figure 3: Jovian atmospheric profile [2].

Figure 4 shows the experimental absorption coefficients (blue curve) acquired for an H_2-He mixture for

typical Jovian concentrations at 402 K and a pressure of 19.2 bar.
The band shows a maximum absorption around 4200 cm^{-1} where the absorption coefficients reach a value of almost 5.8 10^{-4} cm^{-1}.
Furthermore, the experimental data have been compared with Abel's theoretical model [3] shown as the red curve. As one can see, there are some discrepancies between the data and the model, which have to be further investigated.
Despite those discrepancies, it is important to say that this has been the first attempt to study the CIA fundamental band of H_2 at these high temperatures from an experimental point of view.

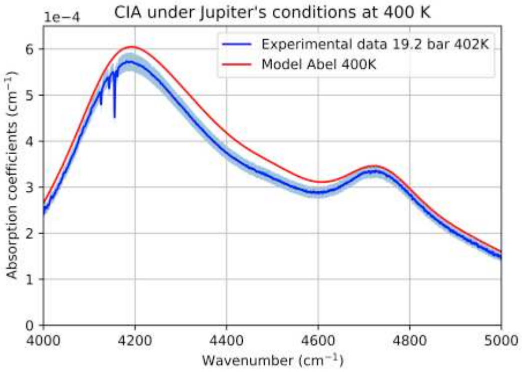

Figure 4: Experimental absorption coefficients (blue curve) at typical Jupiter's upper-tropospheric conditions.
The red curve represents Abel's theoretical model [3].

Looking at the left side of the main peak of the band shown in Figure 4, it is easy to notice the presence of some tiny features called interference dips [4].
They have been studied by acquiring some high-resolution spectra, shown in Figure 5, for a pure H_2 gas at three different pressure set points for a temperature of 296 K.

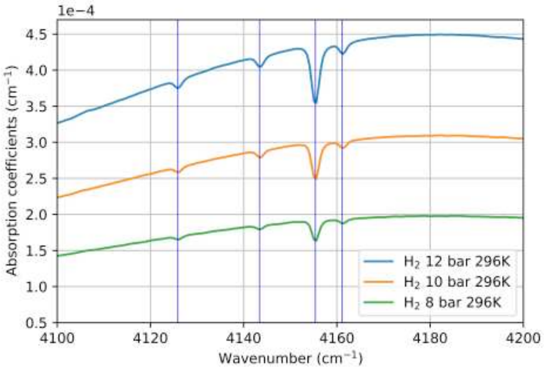

Figure 5: Blow up of the main peak of the CIA fundamental band acquired at three different pressures for a temperature of 300 K. The interference dips [4], superimposed on the band, can be easily observed.

The interference dips represent a lack of absorption at specific wavelengths.
It is of primary importance to have some experimental data around these frequencies since the theoretical models are not able to reproduce them.
Thanks to the high resolution reached, we were able, for the first time, to resolve all four interference dips.
The next step (work in progress) will be to acquire data at higher temperatures, to add valuable information on the CIA fundamental band in a not yet explored range of physical conditions, along with some low-temperature data.

Conclusions: The CIA fundamental band of H_2-H_2 and H_2-He has been investigated for typical Jovian upper-tropospheric conditions and mixing ratio.
With the present work, we have been able to investigate the CIA of H_2-H_2 and H_2-He in a wide temperature and pressure range, obtaining for the first time experimental data at a temperature equal to or exceeding 400 K.
The CIA absorption coefficients acquired at the lowest (experimental feasible) altitude along Jupiter's tropospheric profile, as shown in Figure 3, present a value of almost 5.8 10^{-4} cm^{-1} around 4200 cm^{-1}.
Moreover, our measurements have also been compared with a theoretical model [2], showing some discrepancies, especially in the data acquired at the highest temperature which have to be further investigated.
Furthermore, thanks to the high resolution reached with the present experimental setup, we were able to resolve all four interference dips, superimposed on the left side of the main peak of the hydrogen CIA fundamental band.
Finally, the next step will be to acquire data at lower temperatures, around 100 K, but most importantly to acquire data at higher temperatures, in order to investigate a temperature range not yet studied experimentally (work in progress).

Acknowledgments: This work has been developed under the ASI-INAF agreement n. 2023-6-HH.0.

References:

[1] M. Snels and al. (2021), AMT 14, 7187–7197, https://doi.org/10.5194/amt-14-7187-2021.
[2] A. Seiff (1997), Science Vol 276, pp.102-104,https://www.science.org/doi/10.1126/science.276.5309.102.
[3] M. Abel et al., (2012), The Journal of Chemical Physics, 136,https://doi.org/10.1063/1.3676405
[4] J. Van Kranendonk (1968), Canadian Journal of Physics Vol. 46, N. 10, https://doi.org/10.1139/p68-150.

SPACE-WEATHERING ON PRIMITIVE BODIES: A MULTI-SCALE LABORATORY STUDY ON WEATHERED GRAINS. Stefano Rubino[1], Ernesto Palomba[1], Marianna Angrisani[1-5], Fabrizio Dirri[1], Andrea Longobardo1, Giuseppe Massa[1-5], Giovanni Pratesi[2], Xhonatan Shehaj[2], Maria Elisabetta Palumbo[3], Giuseppe Baratta[3], Daniele Fulvio[3], Carlotta Scire` Scappuzzo[3], Riccardo Giovanni Urso[3], Mariangela Cestelli Guidi[4], Martina Romani[4], and Marco Angelucci[4]. [1]INAF-Istituto di Astrofisica e Planetologia Spaziali (INAF-IAPS), Rome, Italy; stefano.rubino@inaf.it; [2]Dipartimento di Scienze della Terra, Università degli Studi di Firenze, Florence, Italy; [3]INAF-Osservatorio Astrofisico di Catania (INAF-OACT), Catania, Italy; [4]INFN-Laboratori Nazionali di Frascati – Frascati, Italy; [5] University of Rome 'La Sapienza'.

Studying small bodies in our Solar System is fundamental for understanding its origin and evolution. These small "primitive" bodies are undifferentiated: their components did not separate according to their density, irreversibly modifying their mineralogy. They have evolved very little since their formation, yielding a composition relatively close to that of the primordial proto-planetary disk [1]. However, other processes such as thermal alteration, aqueous alteration, shocks, or space weathering (SpWe) can affect these bodies' surfaces. In particular, the spectral changes induced by surface weathering can bias and complicate compositional studies led by remote sensing. Therefore, it is paramount to understand how these processes can affect the surface of primitive asteroids. These bodies can be studied remotely by acquiring spectroscopic data, but it is also possible to conduct laboratory investigations on analogous samples such as certain classes of meteorites (carbonaceous chondrites, CCs [2]), terrestrial analogs (hydrated silicates - which dominate the mineral composition of "primitive" bodies [3]), or directly on returned materials brought back by sample return missions (such as the Hayabusa2 (JAXA) and OSIRIS-REx (NASA) missions [4–6]).

In this work, we emulate the effects of solar particles on the surface of primitive asteroids in a laboratory environment by conducting ion-implantation experiments (INAF-OACT). We use a 400 keV Ar^+ flux to weather a mm-sized grain from the carbonaceous chondrite C2-ung Tagish Lake meteorite. The Tagish Lake meteorite has been chosen since its properties, such as density and H abundance, are compatible with those of the surface of the B-type asteroid Bennu, the target of the OSIRIS-Rex mission (NASA - [8, 9])

The sample has been characterized using micro-FTIR spectroscopy in reflection mode (both imaging and mapping) and micro-Raman spectroscopy at the DAΦNE-Light synchrotron radiation laboratory (INFN-LNF) to assess changes in the mineralogy, hydration, and state of the endogenous organic matter upon ion implantation. The sample was also studied using scanning electron microscopy (SEM) and x-ray photoelectron spectroscopy (XPS) at the Università di Firenze to probe morphological and elemental changes induced by weathering.

This work will directly support the data acquisition, analysis, and interpretation of two mm-size grains from Ryugu allocated to our group during the second AO for Hayabusa2 samples (Primitive Asteroid Weathering: New Studies - "PRAWNS" proposal, Ernesto Palomba), which will follow the same analytical pipeline of the Tagish Lake grain.

This work is funded by the Istituto Nazionale di Astrofisica (INAF) Large Grant PRESTIGE (Pristine Returned Sample Testing InvestiGation and Examination, F.O.:1.05.12.01.05).

References:

[1] E.R.D Scott et al. (2018) Astrophys J. 854. [2] R.C. Greenwood et al. (2020) Geochim Cosmochim Acta.;277: 377–406. [3] F. Usui et al. (2018) Publ Astron Soc Jpn Nihon Tenmon Gakkai. 71. [4] T. Yokoyama et al. (2022) Science 379. [6] T. Noguchi et al. (2022) Nature Astronomy 1–12. [7]. S-I Watanabe S-I et al. (2017) Space Sci Rev 208: 3–16. [8] VE Hamilton et al. (2019) Nat Astron. 3: 332–340. [9] A. Praet et al. (2021) Icarus. 363: 114427.

CONSTRAINING THE LIFETIME OF ORGANICS ON PLANETARY SURFACES

R. G. Urso[1], G.A. Baratta[1], G. L. Dalla Pria[1, 2], D. Fulvio[1], M. Germanà[1,3], C. Scirè[1], M. E. Palumbo[1]
[1]INAF-Osservatorio Astrofisico di Catania, via Santa Sofia 78, 95123 Catania, Italy, [2] Luleå University of Technology, Campus, Porsön, Luleå, 97187, Sweden [3]Università degli Studi di Catania, Dipartimento di Fisica e Astronomia, via Santa Sofia 64, 95123 Catania, Italy
email presenting author: *riccardo.urso@inaf.it*

Introduction: Organic materials were revealed in a variety of extraterrestrial samples, such as carbonaceous chondrites [1] interplanetary dust particles [2], cometary dust [3], and asteroid grains [4]. Lunar samples collected during the Apollo 17 mission also contain organic materials [5].

Unveiling the chemical composition and physical properties of organic matter in small bodies and satellites can provide information on the conditions at the dawn of the Solar System. However, a variety of processes could have altered organics on atmosphere-less planetary surfaces. Among such processes, the bombardment by cosmic rays and solar particles can significantly alter organics [6, 7], determining their alteration or destruction. It is thus fundamental to shed light on the effects of ion irradiation to get correct information on the organics origins and survival.

Methods: We performed experimental activities to shed light on the effects of energetic ions on a variety of samples containing carbon-bearing compounds, also in presence of minerals [8, 9]. Ion irradiation was performed on carbon-bearing ices deposited at low temperature ($\leq$17 K) and on organic refractory materials that simulate complex organics possibly present on the surface of the Moon and other atmosphere-less bodies. Laboratory experiments were performed with the facilities available at the Laboratory for Experimental Astrophysics (LASp) at the INAF-Astrophysical Observatory of Catania (Italy), where ices and refractory organics were placed in a high vacuum chamber ($P\leq10^{-8}$ mbar) connected to a 200 kV ion accelerator. Before, during, and after irradiation, samples were analysed in-situ by means of infrared spectroscopy in transmittance. Further analysis were performed ex-situ by means of reflectance infrared spectroscopy. The analysis of infrared spectra allowed us to look for changes in the samples' physical and chemical properties and to relate them to the irradiation dose experienced by the processed samples.

We also modeled the irradiation conditions at the surface of the Moon and of other atmosphere-less bodies by cosmic-rays and solar particles.

Results: We analysed experimental data to follow the evolution of infrared features attributed to organic compounds with increasing irradiation dose. In particular, we analysed the changes in the C-H stretching mode bands at 3.4 μm, in the C-H bending mode at 7.2 μm and in the C-N stretching band at 7.5 μm. Experimental data showed a decrease in the intensity of the spectral features attributed to organics that testify the destruction of the organic compounds.

We combined the data from laboratory experiments with the modeling of cosmic-rays and solar particles propagation in the Solar System and we estimated the lifetime of organics on the Moon and on other small bodies. Our estimations also take into account the role of resurfacing events, such as impact gardening, that expose fresh materials buried in the sub-surface and thus compete with the alteration induced by energetic particle irradiation, determining an increase in the organics lifetime detection.

References: [1] Schmitt-Kopplin, P., Gabelica, Z., Gougeon, R. D., et al. 2010, Proc. Natl. Acad. Sci., 107, 2763; [2] Chan, Q. H. S., Franchi, I. A., Zhao, X., et al. 2020, Meteor. Planet. Sci., 55, 1320; [3] Sandford, S. A., Aléon, J., Alexander, C. M., et al. 2006, Science, 314(5806) :1720-4; [4] Pilorget, C., Okada, T., Hamm, V., et al. 2021, Nat. Astron., 6, 221 ; [5] Thomas-Keprta, K., Clemett, S., Messenger, S., et al. 2014, Geochimica et Cosmochimica Acta 134, 1-15 ; [6] Rothard, H., Domaracka, A., Boduch, P., et al. 2017, J. Phys. B, 50, 062011; [7] Urso, R. G., Hénault, E., Brunetto, R., et al. 2022, A&A, 668, A169; [8] Dalla Pria, G., Scirè, C., Urso, R. G. et al., in prep.; [9] De Sanctis, C., Baratta, G. A., Brucato, J. R. et al., in prep.

Reconstruction of the 3D ejecta structure of the DART impact on Dimorphos

Deshapriya J.D.P.(1), Hasselmann P.H.(1), Gai I. (2), Dotto E.(1), Rossi A.(3), Ivanovski, S. L. (4), Della Corte V. (5), Bertini I. (6,7), Ieva S.(1), Mazzotta Epifani E.(1), Perna D.(1), Dall'Ora M.(8), Hirabayashi M.(9), Farnham T.(10), Amoroso M.(11), Brucato J. R.(12), Capannolo A.(13), Caporali S.(12) , Ceresoli M.(13), Cremonese G.(14), Gomez Casajus L. (2), Gramigna E.(2) , Impresario G.(11), Lasagni Manghi R.(2), Lavagna M.(13) , Lombardo M.(2) , Lucchetti A. (14), Modenini D. (8), Pajola M. (14), Palumbo P.(7) , Pirrotta, S.(11) , Poggiali G. (12,15), Tortora P. (2), Tusberti F.(14), Zannoni M. (2) , Zanotti G. (13), Zinzi A.(11), Sanchez P.(16)

(1) INAF Osservatorio Astronomico di Roma, Italy, prasanna.deshapriya@inaf.it
(2) Università di Bologna, Bologna, Italy
(3) CNR Istituto di Fisica Applicata "Nello Carrara", Sesto Fiorentino (Firenze),
(4) INAF Osservatorio Astronomico di Trieste, Italy
(5) IAPS-INAF, Roma
(6) Università degli Studi di Napoli "Parthenope", Napoli, Italy
(7) INAF Istituto di Astrofisica e Planetologia Spaziali, Roma, Italy
(8) INAF Osservatorio Astronomico di Capodimonte, Napoli, Italy
(9) Auburn University, AL-USA
(10) University of Maryland, Department of Astronomy, MD-USA
(11) Agenzia Spaziale Italiana, Roma, Italy
(12) INAF Osservatorio Astrofisico di Arcetri, Firenze, Italy
(13) Politecnico di Milano, Italy
(14) INAF Osservatorio Astronomico di Padova, Italy
(15) Observatory of Paris, France
(16) Colorado Center for Astrodynamics Research, University of Colorado
Corresponding e-mail: prasanna.deshapriya@inaf.it

Introduction: The Italian cubesat LICIACube and NASA's Double Asteroid Redirection Test (DART) spacecraft were jointly launched on November 24th, 2021, bound for the Didymos binary asteroid system, consisting of Didymos and Dimorphos. Ahead of DART's planned impact on Dimorphos, LICIACube was released from the DART spacecraft on September 11th, 2022 [1,2]. It autonomously navigated towards the Didymos system to observe DART's impact, which aimed to test the feasibility of altering the orbit of the asteroid Dimorphos around Didymos. LICIACube successfully documented the impact event, capturing images of the impact and the resulting ejecta cone.

Through an analysis of the LICIACube images obtained by the LUKE instrument, we characterized the axis and the aperture angle of the observed ejecta cone. Utilizing a series of LUKE images where the ejecta cone was observable in a projected side-on profile and using the geometric relationship between a cone and its projection onto a plane, we initially determined an upper limit for the aperture angle of the cone. Subsequently, we developed a system of non-linear equations for numerical solution to recover the axis and the aperture angle of the ejecta cone. Following this, we generated synthetic images with the solved ejecta cone at the same original LUKE observing geometries to validate or discard the solutions obtained by solving the system of non-linear equations. Then we further sophisticated the model to allow rotated cones with elliptical bases to capture all the possible orientation and projected observed conditions. Following our simulations, we were able to closely reproduce the LUKE observations as can be seen in Fig. 1 excerpt from our recent work [3].

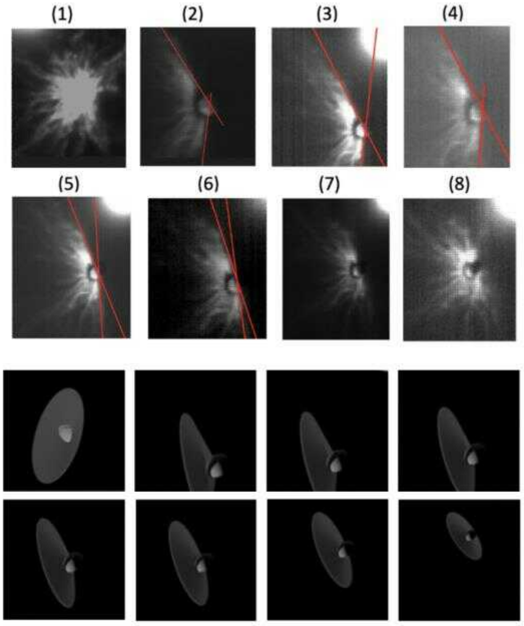

Fig.1 Observations of LUKE and simulations at same observation geometries and illumination conditions.

Following this work, we are now extending this ejecta cone solution to recover the ejecta morphology in 3D by means of a method that involves coregistering the different ejecta features to a model centred at the apex of the ejecta cone solution. The methods and current status of the work at the time of the congress will be presented and discussed.

Acknowledgements: The LICIACube team acknowledges financial support from Agenzia Spaziale Italiana (ASI, contract No. 2019-31-HH.0 CUP F84I190012600). This work was supported by the DART mission, NASA Contract 80MSFC20D0004. Work by E.G.F. was carried out at the Jet Propulsion Laboratory, California Institute of Technology, under a contract with the National Aeronautics and Space Administration (#80NM0018D0004)

References: [1] Dotto et al., (2021). [2] Dotto et al., (2023) [3] Deshapriya et al., (2023), in press

THE DYNAMICS OF THE EJECTA PLUME FOLLOWING THE DART IMPACT.

A. Rossi[1], F. Marzari[2], K. Langner[1,2], G. Zanotti[3], D.P. Deshapriya[4], P.H. Hasselmann[4], E. Dotto[4], E. Mazzotta Epifani[4], A. Zinzi[5], F. Ferrari[3], S. Raducan[6], M. Amoroso[7], J. Beccarelli[8], I. Bertini[9], J.R. Brucato[10], A. Capannolo[3,11], S. Caporali[10], M. Ceresoli[3], G. Cremonese[8], M. Dall'Ora[12], V. Della Corte[12], I. Gai[13], S. Ieva[4], G. Impresario[7], S.L. Ivanovski[14], R. Lasagni-Manghi[13], M., Lavagna[3], A. Lucchetti[8], D. Modenini[13], M. Pajola[8], P. Palumbo[15], D. Perna[4], S. Pirrotta[7], G. Poggiali[10,16], P. Tortora[13], M. Zannoni[13], E.G. Fahnestock[17], M. Hirabayashi[18] , and Li, Y.-J.[19]

1-*IFAC-CNR, Sesto Fiorentino, Italy. 2-Università di Padova, Padova, Italy 3-Politecnico di Milano, Dip. di Scienze e Tecnologie Aerospaziali, Milano, Italy. 4-INAF-Osservatorio Astronomico di Roma, Monte Porzio Catone, Italy.* 5-*Space Science Data Center, ASI, Rome, Italy. 6-Space Research and Planetary Sciences, University of Bern. 7-Agenzia Spaziale Italiana, Rome, Italy. 8-INAF- Osservatorio Astronomico di Padova, Padova, Italy. 9-Università degli Studi di Napoli "Parthenope", Naples, Italy. 10-INAF-Osservatorio Astrofisico di Arcetri, Florence, Italy.* 11-*ISAE-SUPAERO, Université de Toulouse, Toulouse, France.* 12-*INAF-Osservatorio Astronomico di Capodimonte, Naples, Italy.* 13-*Alma Mater Studiorum - Universita di Bologna, Dipartimento di Ingegneria Industriale, Forlì, Italy.* 14-*INAF-Osservatorio Astronomico di Trieste, Trieste, Italy. 15-INAF - Istituto di Astrofisica e Planetologia Spaziali 16-LESIA, Observatoire de Paris-Meudon, Meudon, France. 17-Jet Propulsion Laboratory, California Institute of Technology, Pasadena, CA, USA.. 18. Auburn University, Auburn, AL, USA. 19- Planetary Science Institute, Tucson, AZ, USA.* ***Corresponding e-mail: a.rossi@ifac.cnr.it***

Introduction: On September 26, 2022, the impact of the DART probe against the asteroid Dimorphos, the small moon of the binary 65803 Didymos asteroid system [1], generated a large ejecta plume. The images taken by the small LICIACube cubesat [2], released by DART 15 days before the impact, revealed a complex plume with a cone-like structure, crammed with dust, clumps of objects, filaments and larger boulders [3][4]. The event and the resulting ejecta were also observed by several space and ground based observatories which allowed the characterization of the plume evolution and, in particular, the formation of a long lasting tail of debris, pushed by the solar radiation pressure, stretching for thousands of km [5]. The complex mechanisms responsible for the shape of the observed tail, its temporary "double" nature and its continuous presence after several months are related to the interaction of the ejecta particles with the binary system gravity and to secondary collision events of larger ejecta against the two asteroids [6][7][8].

The model: The LICEI (LICIACube Ejecta Integrator) model is used to study the dynamical evolution of the debris after its ejection from Dimorphos [8]. The model accounts for the irregular gravity field of both Dimorphos and Didymos and include the effects of radiation pressure and solar tide. The ejecta particle are treated as rotating ellipsoids with variable dimensions. The numerical integration of the fragments' orbits is performed in the IAU_DIMORPHOS rotating reference frame as given by NASA SPICE kernels. The accurate heliocentric orbit of the Didymos system and the binary orbital dynamics is derived from the SPICE kernels too, allowing an accurate matching with the LICIACube data. The model allows the integration of a large number of ejecta particles thus providing a global view of the plume evolution (e.g., see Fig. 1).

The study: The aim of this study is to characterize the first phases of the fragments evolution after the ejection from the crater. The full dynamics of the system is modelled up to several months after the impact to try to reproduce the LICIACube images details and to further study the tail evolution. In particular its relation with the re-impacting mechanisms able to generate further tail-feeding particles is investigated.

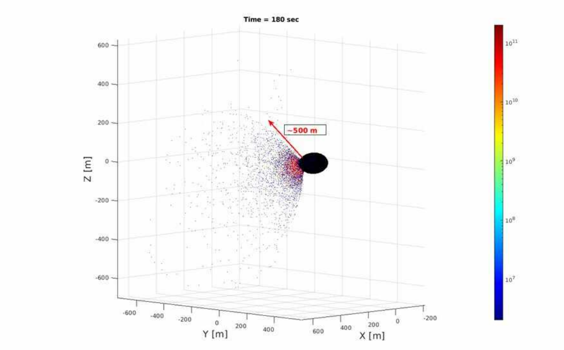

Figure 1: example of a simulation of the initial phases of the plume evolution with LICEI.

Different initial populations stemming from the DART impact, related to different possible physical properties of the Dimorphos asteroid [9], are generated [10] in order to find the best match with the LICIACube images. Moreover, as pointed out in [4], the actual observed cone is not circular (i.e., its base is elliptic and oriented roughly along the North-South direction on the surface of Dimorphos). The effect of different orientations of the non-circular cone on the initial evolution of the eject plume is explored considering also different cone aperture angles around the "nominal" one described in [3]. The relevance of these cone features for "immediate" re-impact of particles against Didymos is explored as well [11]. Finally, the effects of the ejecta particles complex evolution and of the simulated cone properties on the computation of the momentum enhancement factor, β, is analyzed.

Acknowledgments: This work was supported by the Italian Space Agency (ASI) within the LICIACube project (ASI-INAF agreement AC n. 2019-31-HH.0).

References:

[1] Cheng, A. F., Agrusa, H. F., Barbee, B. W., et al. (2023) *Nature*, 616, 457. [2] Dotto, E., Della Corte, V., Amoroso, M., et al. (2021) *Planetary and Space Science*, 199, 105185. [3] Dotto, E. & al. (2023) *Nature*, in press. [4] Deshapriya, J. D. P. & al. (2023) *Planetary Science J.*, in press. [5] Li, J.-Y., Hirabayashi, M., Farnham, T. L., et al. (2023) Nature, 616, 452 [6] Moreno, F., A. Campo Bagatin, G. Tancredi, Li, J.-Y., A. Rossi et al., (2023) *The Planetary Science Journal*, 4:138. [7] Ferrari F. et al. (2023) *submitted*, 2023. [8] Rossi, A., Marzari, F., Brucato, J. R., et al. (2022) *The Planetary Science Journal*, 3, 118. [9] Raducan et al. (2023), *Nature Astr.*, in press. [10] Zanotti, G. & Lavagna, M. (2020) in *71st International Astronautical Congress* (IAC 2020), 1–15 [11] Mazzota Epifani E. et al., (2023) ACM 2023.

FRACTURING BY THERMAL FATIGUE ON DIMORPHOS

A. Lucchetti[1], S. Cambioni[2], R. Nakano[3,7], O.S. Barnouin[4], M. Pajola[1], F. Tusberti[1], K.T. Ramesh[5], E. Dotto[6], C.M. Ernst[4], R.T. Daly[4], E. Mazzotta Epifani[6], M. Hirabayashi[3,7], L. Parro[8,9,10], G. Poggiali[11,12], A. Campo Bagatin[8,13], R.-L. Ballouz[4], L. Penasa[1], N. L. Chabot[4], P. Michel[14,15], N. Murdoch[16], J.B. Vincent[17], Ö. Karatekin[18], A.S. Rivkin[4], J.M. Sunshine[19], T. Kohout[20], J.D.P. Deshapriya[6], P.H.A. Hasselmann[6], S. Ieva[6], J. Beccarelli[1], S.L. Ivanovski[21], A. Rossi[22], F. Ferrari[23], S. D. Raducan[24], J. Steckloff[25], S. Schwartz[25], J.R. Brucato[11], M. Dall'Ora[26], A. Zinzi[27], A. F. Cheng[4], M. Amoroso[28], I. Bertini[29], A. Capannolo[16], S. Caporali[11], M. Ceresoli[23], G. Cremonese[1], V. Della Corte[26], I. Gai[30], L. Gomez Casajus[30], E. Gramigna[30], G. Impresario[28], R. Lasagni Manghi[30], M. Lavagna[23], M. Lombardo[30], D. Modenini[30], P. Palumbo[31], D. Perna[6], S. Pirrotta[28], P. Tortora[30], M. Zannoni[30], G. Zanotti[23].

[1]INAF-Astronomical Observatory of Padova, Vic. Osservatorio 5, 35122 Padova, Italy (alice.lucchetti@inaf.it); [2]Department of Earth, Atmospheric and Planetary Sciences, Massachusetts Institute of Technology, Cambridge, MA-USA; [3]Daniel Guggenheim School of Aerospace Engineering, Georgia Institute of Technology, Atlanta, GA 30332, USA. [4]Johns Hopkins University Applied Physics Laboratory, Laurel, MD 20723, USA; [5]Johns Hopkins University, Baltimore, MD, USA; [6]INAF-Osservatorio Astronomico di Roma, Monte Porzio Catone, Roma, Italy; [7]Department of Aerospace Engineering, Auburn University, AL 36849, USA; [8]IUFACyT. Universidad de Alicante, Alicante, Spain; [9]University of Arizona. (Tucson, AZ. USA); [10]Universidad Complutense. Madrid (Spain); [11]INAF-Osservatorio Astrofisico di Arcetri, Firenze, Italy; [12]LESIA-Observatorie de Paris PSL, Paris, France; [13]Departamento de Física, Ingeniería de Sistemas y Teoría de la Señal, Universidad de Alicante, Alicante, Spain; [14]Université Côte d'Azur, Observatoire de la Côte d'Azur, CNRS, Laboratoire Lagrange, Nice, France; [15]The University of Tokyo, Department of Systems Innovation, School of Engineering, Tokyo, Japan; [16]Institut Supérieur de l'Aéronautique et de l'Espace (ISAE-SUPAERO), Université de Toulouse, France;[17]DLR Institute of Planetary Research, Berlin, Germany; [18]Royal Observatory of Belgium, Belgium; [19]University of Maryland, Departments of Astronomy and Geology, College Park, MD-USA; [20]University of Helsinki, Helsinki Finland; [21]INAF-Osservatorio Astronomico di Trieste, Trieste, Italy; [22]IFAC-CNR, Sesto Fiorentino, Firenze, Italy; [23]Politecnico di Milano - Bovisa Campus, Dipartimento di Scienze e Tecnologie Aerospaziali, Milano, Italy; [24]Space Research and Planetary Sciences, Physikalisches Institut, University of Bern, Bern, Switzerland;[25]Planetary Science Institute, Tucson, AZ, USA; [26]INAF-Osservatorio Astronomico di Capodimonte, Napoli, Italy; [27]Space Science Data Center – ASI, Roma Italy; [28]Agenzia Spaziale Italiana, Roma, Italy; [29]Università degli Studi di Napoli "Parthenope", Dipartimento di Scienze & Tecnologie, Centro Direzionale, Napoli, Italy; [30]Alma Mater Studiorum - Università di Bologna, Dipartimento di Ingegneria Industriale, Forlì, Italy. [31]INAF-Istituto di Astrofisica e Planetologia Spaziali, Roma, Italy.

Introduction: On 26 September 2022, the Double Asteroid Redirection Test (DART) spacecraft impacted the surface of Dimorphos, the ~150 m-size moonlet of the binary system (65803) Didymos (~780 m-size, [1]), allowing detailed surface characterization. Both DART and the Light Italian Cubesat for Imaging of Asteroids (LICIACube, [2]) provided direct observations of geological features, including lineaments, rocks' fractures and/or cracks, boulders, craters and signs of mass movements. Here, we study Dimorphos boulders' fractures to constrain their formation processes. In particular, we analyse Dimorphos' fracture length distribution and direction to test the hypothesis that these fractures propagate via thermal fatigue.

Dataset: DRACO, the scientific camera onboard DART [3], imaged the surface of Dimorphos with a spatial resolution from few meters to a maximum of 5.5 cm. Here, we use the DRACO image taken 1 s before impact with a resolution of 5.5 cm to analyze Dimorphos boulders cracks, as shown in Fig. 1.

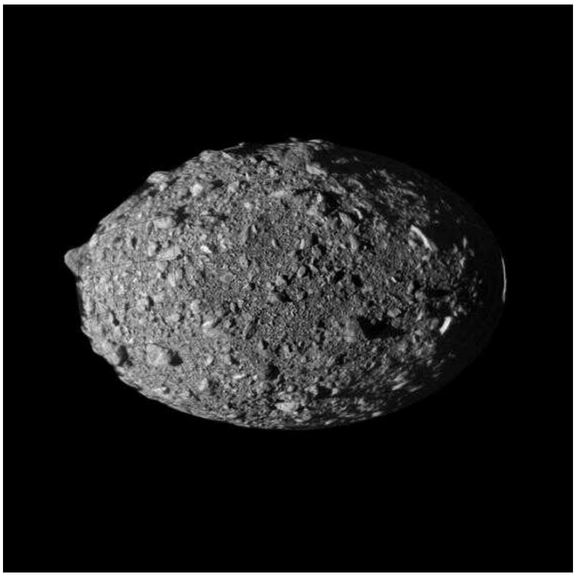

Figure 1. Dimorphos high resolution mosaic created with the final 10 DRACO images from 11.447 s to 0.856 s before the impact (pixel scale ranging between 34.9 cm/px and 2.6 cm/px).

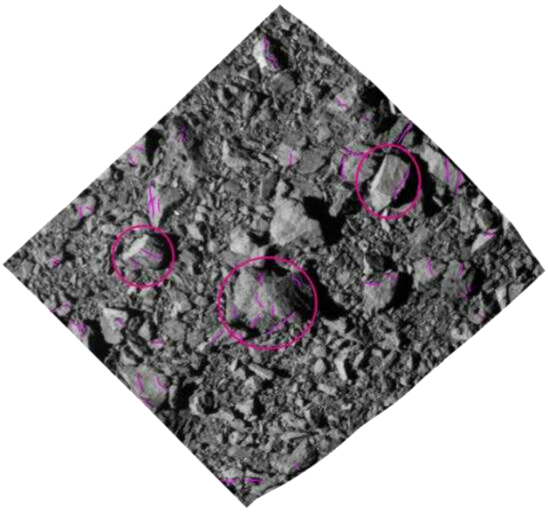

Figure 2. Close up of the image (dart_0401930049_43695_01_iof) acquired 1.818 s before the impact with a pixel scale of 5.5 cm where boulders' fractures are mapped. The pink boxes indicate the three boulders on which the thermophisycal and thermal fatigue modelling has been applied.

Boulders cracks mapping and analysis: We mapped approximately 50 fractures with a length ranging from 1 to 10 m, investigating their length size distribution and orientation. We derived a rose diagram showing an E-W preferred orientation, which may point to a thermal mechanism formation for the boulder cracks [4]. Indeed, on other asteroids, as Bennu and Ryugu, the evidence of preferential meridional orientation of boulders' fractures is consistent with cracking induced by diurnal thermal cycling supporting the hypothesis that thermal fracturing plays an important role on asteroid surfaces in general [4, 5]. The fractures' length distribution is well-fitted by an exponential law for lengths larger than 0.77 m, which is indicative of the important role of thermal stress in fracture propagation.

Thermophysical and thermal fatigue modelling: To assess the thermal fatigue hypothesis, we applied a Finite Element Method (FEM) thermophysical model [6] on three different boulders (Atabaque hosting 6 fractures and other two boulders hosting one and two fractures, respectively, Fig. 1). We then derived the diurnal and seasonal temperature evolution profiles finding a similar trend for all the three boulders. We input the solution from the thermophysical model into established thermal fatigue models to model the propagation of fractures in boulders in the direction towards the center of the asteroid (normal depth direction z) and in the direction of preferential propagation of fracture (horizontal fractures in direction x). In particular, thermal stresses generate the propagation of fractures faster in the horizontal direction with respect to the vertical one, constraining their development on Dimorphos' boulders between 10-100 kyr.

Hence, we propose that the fractures observed on Dimorphos' boulders are shallow and that the vertical propagation mode is not the dominant mode of fracture propagation. Indeed, the propagation of fractures along the boulder surface on Dimorphos may occur one to two orders of magnitude faster than in vertical direction (Myr).

Acknowledgments: *This work was supported by the Italian Space Agency (ASI) within the LICIACube project (ASI-INAF agreement n. 2019-31-HH.0) and HERA project (ASI-INAF agreement n. 2022-8-HH.0). S.C. acknowledges funding from the Crosby Distinguished Postdoctoral Fellowship Program of the Department of Earth, Atmospheric and Planetary Science, Massachusetts Institute of Technology. R.N. acknowledges support from NASA/FINESST, United States (NNH20ZDA001N/80NSSC21K1527). R.N. also would like to thank Joseph Ivarson for assistance in conducting the thermophysical simulation. This work was supported by the DART mission, NASA Contract 80MSFC20D0004. SDR acknowledges support from the Swiss National Science Foundation (project number 200021_207359). P.M. acknowledges funding support from the French space agency CNES, ESA and The University of Tokyo. L.P. contribution was supported by the Margarita Salas postdoctoral grant funded by the Spanish Ministry of Universities – NextGenerationEU and CIAPOS/2022/066 postdoctoral grant (European Social Fund). OK acknowledges funding support from the PRODEX program managed by the European Space Agency (ESA) with help of the Belgian Science Policy Office (BELSPO)*

.

References: *[1] Rivkin, A.S., et al. 2021. PSJ, 2, 173; [2] Dotto, E. et al. 2021, PSS, 199, 105185; [3] Fletcher, Z. J., et al. 2018. SPIE 10698; [4] Delbo, M. et al., 2022, Nature Geoscience, 15, 453–457; [5] Delbo M. et al., 2014, Nature, 508(7495), 233-236.* [6] *Ryota and Nakano,*

The Didymos and Dimorphos global boulder size-frequency distributions: implications on their mutual origin

M. Pajola[1], F. Tusberti[1], A. Lucchetti[1], O. Barnouin[2], S. Cambioni[3], C.M. Ernst[2], E. Dotto[4], R.T. Daly[2], G. Poggiali[5,6], M. Hirabayashi[7,8], R. Nakano[7,8], E. Mazzotta Epifani[4], N.L. Chabot[2], V. Della Corte[9], A. Rivkin[2], H. Agrusa[10,11], Y. Zhang[12], L. Penasa[1], R.-L. Ballouz[2], S. Ivanovski[13], N. Murdoch[14], A. Rossi[15], C. Robin[14], S. Ieva[4], J.B. Vincent[16], F. Ferrari[17], S.D. Raducan[18], A. Campo-Bagatin[19], L. Parro[19,20], P. Benavidez[19], G. Tancredi[21], Ö. Karatekin[22], J.M. Trigo-Rodriguez[23], J. Sunshine[10], T. Farnham[10], E. Asphaug[24], J.D.P. Deshapriya[4], P.H.A. Hasselmann[4], J. Beccarelli[1], S.R. Schwartz[24], P. Abell[25], P. Michel[11,26], A. Cheng[2], J.R. Brucato[5], A. Zinzi[27,28], M. Amoroso[27], S. Pirrotta[27], G. Impresario[27], I. Bertini[29], A. Capannolo[14], S. Caporali[5], M. Ceresoli[17], G. Cremonese[1], M. Dall'Ora[9], I. Gai[30], L. Gomez Casajus[30], E. Gramigna[30], R. Lasagni Manghi[30], M. Lavagna[17], M. Lombardo[30], D. Modenini[30], P. Palumbo[31], D. Perna[4], P. Tortora[30], M. Zannoni[26], G. Zanotti[17].

[1]INAF-Astronomical Observatory of Padova, Vic. Osservatorio 5, 35122 Padova, Italy (maurizio.pajola@inaf.it); [2]Johns Hopkins University Applied Physics Laboratory, Laurel, MD 20723, USA; [3]Dept. of Earth, Atmospheric and Planetary Sciences, Massachussets Institute of Technology, Cambridge, MA-USA; [4]INAF-Osservatorio Astronomico di Roma, Monte Porzio Catone, Roma, Italy; [5]INAF-Osservatorio Astrofisico di Arcetri, Firenze, Italy; [6]LESIA-Observatorie de Paris PSL, Paris, France; [7]Daniel Guggenheim School of Aerospace Engineering, Georgia Institute of Technology, Atlanta, GA 30332, USA; [8]Department of Aerospace Engineering, Auburn University, AL 36849, USA; [9]INAF-Osservatorio Astronomico di Capodimonte, Napoli, Italy; [10]University of Maryland, Department of Astronomy, MD-USA; [11]Université Côte d'Azur, Observatoire de la Côte d'Azur, CNRS, Laboratoire Lagrange, Nice, France; [12]Climate & Space Sciences and Engineering, University of Michigan, MI-USA; [13]INAF-Osservatorio Astronomico di Trieste, Trieste, Italy; [14]Institut Supérieur de l'Aéronautique et de l'Espace (ISAE-SUPAERO), Université de Toulouse, France; [15]IFAC-CNR, Sesto Fiorentino, Firenze, Italy; [16]DLR Berlin, Germany; [17]Politecnico di Milano - Bovisa Campus, Dipartimento di Scienze e Tecnologie Aerospaziali, Milano, Italy; [18]Space Research and Planetary Sciences, Physikalisches Institut, University of Bern, Bern, Switzerland; [19]Universidad de Alicante, Spain; [20]University of Arizona, AZ-USA; [21]Dpto. Astronomia, Facultad Ciencias Igua 4225, Montevideo, Uruguay; [22]Royal Observatory of Belgium, Belgium; [23]Institute of Space Sciences (ICE, CSIC) and Institut d'Estudis Espacials de Catalunya (IEEC), Spain; [24]Planetary Science Institute; University of Arizona, AZ-USA; [25]NASA Johnson Space Center, Houston, TX-USA; [26]The University of Tokyo, Department of Systems Innovation, School of Engineering, Tokyo, Japan; [27]Agenzia Spaziale Italiana, Roma, Italy; [28]Space Science Data Center – ASI, Roma Italy; [29]Università degli Studi di Napoli "Parthenope", Dipartimento di Scienze & Tecnologie, Centro Direzionale, Napoli, Italy; [30]Alma Mater Studiorum - Università di Bologna, Dipartimento di Ingegneria Industriale, Forlì, Italy; Alma Mater Studiorum - Università di Bologna, Centro Interdipartimentale di Ricerca Industriale Aerospaziale, Forlì, Italy. [31]INAF-Istituto di Astrofisica e Planetologia Spaziali, Roma, Italy.

Introduction: On 26 September 2022, the Double Asteroid Redirection Test (DART) spacecraft impacted the surface of Dimorphos [1], the ~150 m satellite of the binary near-Earth asteroid (65803) Didymos (~730 m diameter). Boulders on small asteroids represent fragments of their parent-body disruptions followed by evolutionary processes (cratering, thermal breakdown, size-sorting, and migration of granular materials [2]). Hence, the observed morphological properties and size-frequency distribution (SFD) of boulders are powerful tools for understanding formation and evolution processes [3].

During the last minutes of DART, the DRACO scientific camera obtained multiple images of Didymos and Dimorphos with pixel scales ranging from a few meters (on parts of Didymos' surface) to centimeters (for Dimorphos impact site, [1]). To identify and manually count all boulders located in the illuminated areas of both asteroids we use 1) four DRACO images, with a Didymos spatial scale ranging from 4.90 to 3.26 m, and 2) two DRACO images with a spatial scale on Dimorphos ranging from 0.26 to 0.20 m. For the Didymos case, all boulders larger than 10-15 m can be detected, while for Dimorphos all features larger than 0.6-0.8 m can be identified. Using the Small Body Mapping Tool (SBMT) we directly project the DRACO images onto the Didymos and Dimorphos shape models and count boulders as ellipses.

Dimorphos: On Dimorphos, we identified a study area of 0.0132 km^2, outside of which all surface features appear distorted and stretched due to high emission angles. Within this area we counted 4734 boulders, finding a maximum size of 16 m (Fig. 1A). The mode, median and mean of the boulder distribution are 0.7 m, 1.1 m and 1.4 m, respectively. To be conservative on the boulder counts, we decided to increase the three-pixel sampling rule to five-pixels, i.e. setting a lower size limit of a boulder that is 1.0 m in size to our data. The cumulative number of boulders per km^2 versus size is in Fig. 1B. The number density/km^2 of boulders $\geq$ 1.0 m is ~203000, for blocks $\geq$ 5.0 m is 6300, while it is 833 for boulders larger than 10.0 m. To evaluate if the resulting SFD can be fit by a power-law curve or not, we made use of the [4] methodology. We derived that our distribution is well fit by a power-law curve (p-value of 0.19) when a completeness limit x_{min} of 5.0 ± 1.2 m is identified, returning a scaling parameter α of -3.4 ± 1.3. Nevertheless, even if the -3.4 index represents the Dimorphos ≥ 5 m SFD, it is clear (Fig. 1B) that at smaller sizes (1 – 5 m), a departure from the power-law curve is real and not a resolution effect. For the widest possible boulder size range (1-16 m), we find that the best fitting curve to the data is the Weibull function.

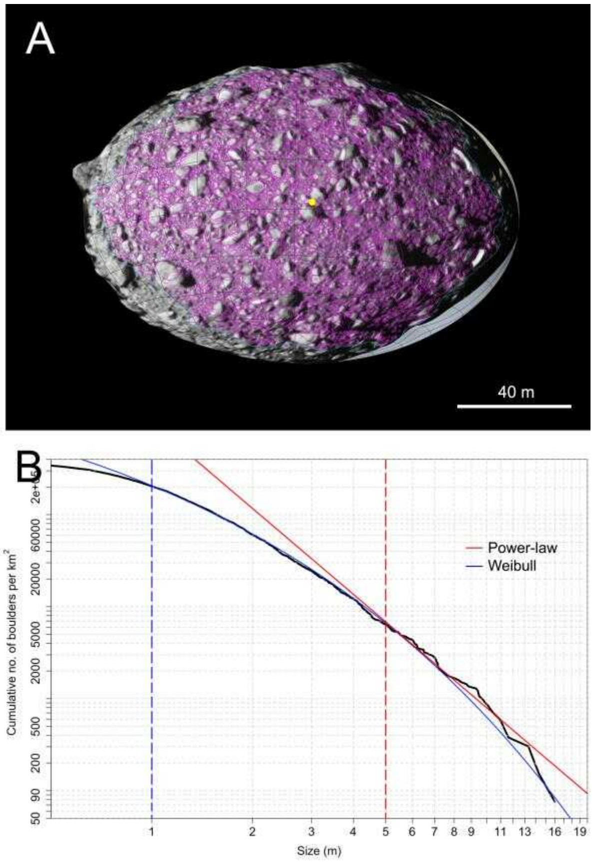

Figure 1. A) The 4734 boulders identified on the study area of Dimorphos. B) The Dimorphos cumulative number of boulders per km^2. The derived power-law fitting curve in red, is obtained for boulders ≥ 5.0 m. The Weibull curve, highlighted in blue, is obtained for boulders ≥ 1.0 m.

Didymos: On Didymos, we identified a study area that is 0.3660 km^2 wide. We identified a total number of 169 boulders, getting a maximum size of 93 m. The mode, median and mean of the boulder distribution are 13.9 m, 21.8 m and 23.7 m, respectively. As for Dimorphos, we decided to increase the three-pixel sampling rule to five-pixels, i.e. setting a lower size limit of a boulder that is ~16.5 m in size to our data. The number density/km^2 is 353 for ≥ 16.5-m boulders, 273 for ≥ 20.0-m boulders, 74 for ≥ 30.0-m boulders, 30 for ≥ 40.0-m boulders and 14 for ≥ 50.0-m boulders. Using the Clauset et al. (2009) methodology we derived that the cumulative number of boulders per km^2 is well fit by a power-law curve with α = -3.6 ± 0.7 and x_{min} = 22.8 ± 2.3 m. The p-value derived from 2500 Kolmogorov-Smirnoff statistical tests is 0.6, i.e. well above the 0.1 significance level.

Discussion: Boulders on all stony NEAs previously visited by spacecrafts—Itokawa, Eros and Toutatis—are characterized by power-law fitting curves with indices steeper than -3.0, obtained from size ranges larger than 5 m, 10 m and 20 m, respectively [5-7]. The Dimorphos and Didymos power-law indices confirm the generally steeper stony boulder SFD when compared to the one obtained for carbonaceous asteroids [8], as well as they indicate an impact-related origin for the identified boulders [6]. This evidence, coupled with the maximum identified boulder dimensions that both exceed 1/10 the NEAs' diameters, imply that such asteroids are rubble piles formed after the catastrophic disruption of a parent body [3]. In addition, the fact that both the primary and the secondary power-law fits reasonably overlap within error bars suggests that Dimorphos' surface has directly inherited part of Didymos' boulders. This result supports the findings of dynamical studies [9] which show that Dimorphos could have formed as the result of a mass shedding event from Didymos.

A detailed description of the global boulder properties for both asteroids (size versus latitude, longitude, slope, acceleration, potential energy and heliocentric average insolation) will be presented at the time of the conference.

Acknowledgments: This research was supported by the Italian Space Agency within the LICIACube project (ASI-INAF agreement AC n. 2019-31-HH.0, & n. 2022-8-HH.0) and the DART mission, NASA Contract No. NNN06AA01C to JHU/APL.

References: [1] Daly, R.T., et al (2023). *Nature* 616, 443-447. [2] Schröder, S. E. et al. (2020). *Earth Space Sci.* 8, e00941. [3] Pajola, M. et al. (2022). *Planet. Sci. J.* 3, 210. [4] Clauset, A., et al. (2009). *SIAM Rev.* 51, 661-703. [5] Thomas, P. C., et al. (2001). *Nature* 413, 394-396. [6] Michikami, T. et al. (2008). *Earth Planets and Space*. 60, 13-20. [7] Jiang, Y. et al. (2016). *Proceedings of IAU Symposium* 10, 153-155. [8] Burke, K. N. et al. (2021). *Remote Sens.* 13, 1315. [9] Agrusa, H. F. et al. *Planets. Sci. J., Submitted.*

The Unusual Brightness Phase Curve of Didymos.

P. H. Hasselmann[1], V. Della Corte[2], P. Pravec[3], S. Ieva[1], I. Gai[4], D. Perna[1], J. D. P. Deshapriya[1], E. Mazzotta-Epifani[1], E. Dotto[1], A. Zinzi[5,6], G. Poggiali[7,8], I. Bertini[9], A. Lucchetti[10], M. Pajola[10], J. Beccarelli[10], M. Dall'Ora[2], J.-Y. Li[11], S. L. Ivanovski[12], A. Rossi[13], J. R. Brucato[7], C. A. Thomas[14], O. Barnouin[15], J. Sunshine[16], A. S. Rivkin[17], M. Amoroso[5], A. Capannolo[18,19], S. Caporali[7], M. Ceresoli[19], G. Cremonese[10], R. T. Daly[20], G. Impresario[5], R. Lasagni-Manghi[4], M., Lavagna[19], D., Modenini[4], E. E. Palmer[21], P. Palumbo[9], S. Pirrotta[5], P. Tortora[4], M. Zannoni[4], and G. Zanotti[19]. 1-*INAF-Osservatorio Astronomico di Roma, Monte Porzio Catone, Italy.* 2-*INAF-Osservatorio Astronomico di Capodimonte, Naples, Italy.* 3-*Astronomical Institute, Academy of Sciences of the Czech Republic, Ondrejov, Czech Republic.* 4-*Alma Mater Studiorum - Universita di Bologna, Dipartimento di Ingegneria Industriale, Forlì, Italy.* 5-*Agenzia Spaziale Italiana, Via del Politecnico, 00133, Rome, Italy.* 6-*Space Science Data Center, ASI, Rome, Italy.* 7-*INAF-Osservatorio Astrofisico di Arcetri, Florence, Italy.* 8-*LESIA, Observatoire de Paris-Meudon, Meudon, Île-de-France, France.* 9-*Università degli Studi di Napoli "Parthenope", Naples, Italy.* 10-*INAF- Osservatorio Astronomico di Padova, Padova, Italy.* 11-*Planetary Science Institute, Tucson, AZ-USA.* 12*INAF-Osservatorio Astronomico di Trieste, Trieste, Italy.* 13-*IFAC-CNR, Sesto Fiorentino, Firenze, Italy.* 14-*Department of Physics and Astronomy, Northern Arizona University, Flagstaff, AZ-USA.* 15-*Johns Hopkins University Applied Physics Laboratory, Laurel, MD-USA.* 16-*University of Maryland, Department of Astronomy and Department of Geology, College Park, MD-USA.* 17-*University of Maryland, Department of Astronomy, MD-USA.* 18-*ISAE-SUPAERO, Université de Toulouse, Toulouse, France.* 19-*Politecnico di Milano, Dip. di Scienze e Tecnologie Aerospaziali, Milano, Italy.* 20-*Center for Research and Exploration in Space Science and Technology, NASA/GSFC, Greenbelt, MD-USA.* 21-*11. Planetary Science Institute, Tucson, AZ-USA.* ***Corresponding e-mail: pedro.hasselmann@inaf.it***

Introduction: On the 2022 September 26*th*, NASA Double Asteroid Redirection Test (DART) successfully hit Dimorphos, the smaller companion being of the binary system formed with the asteroid (65803) Didymos. Both the binary system and the impact event were imaged by The Light Italian Cubesat for Imaging of Asteroids (LICIACube), detached from DART 15 days before the impact [1,2]. Images from the on-board LUKE RGB camera together with ground-based observations [3] enabled the reconstruction of Didymos brightness phase curve, with phase angles ranging from 2.35° to 107°.

Observations: In the present study, the disk-integrated phase curve of Didymos is composed from previously published R-Cousins and SDSS r' ground-based observations [4,5,3] and new data from LUKE RGB Bayer pattern camera. Didymos remained observable during the LICIACube post-impact fly-by, while Dimorphos was highly obscured by the ejecta plume. Both data were converted to Cousins R-Cousins [7]. We derived the apparent albedo, removing topographic, emission features and aspect effects from LUKE images, to finally combined it to ground-based observations. The final phase curve spans from 2.35° to 107° phase angle, covering regimes from near Opposition Effect (OE) to surface macro-scale roughness and topographic effects.

Analysis: Phase Curve parameters are obtained through the standard HG and HG1G2 magnitude systems [8] and are compared to other cataloged parameters for asteroids of diverse spectral type. The opposition effect is also studied using Exponential-Linear equation [9], Shevchenko function [10,11] and linear-by-parts [12], then compared in similar fashion with their pre-analysed database. The central solutions are obtained using Ordinary Least Squares for the Linear-by-parts model, while we used MCMC with a NUTS sampler as solver for Linear-Exponential and Shevchenko functions. Tab. 1 shows the central solutions.

Tab. 1: The central solutions for the narrower angle observations (α<45°) with respect to the three models.

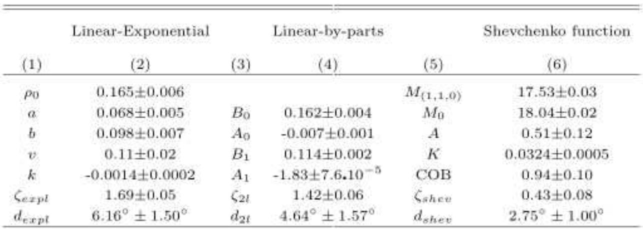

	Linear-Exponential		Linear-by-parts		Shevchenko function
(1)	(2)	(3)	(4)	(5)	(6)
ρ_0	0.165±0.006			$M_{(1,1,0)}$	17.53±0.03
a	0.068±0.005	B_0	0.162±0.004	M_0	18.04±0.02
b	0.098±0.007	A_0	-0.007±0.001	A	0.51±0.12
v	0.11±0.02	B_1	0.114±0.002	K	0.0324±0.0005
k	-0.0014±0.0002	A_1	$-1.83 \pm 7.6.10^{-5}$	COB	0.94±0.10
ζ_{expl}	1.69±0.05	ζ_{2l}	1.42±0.06	ζ_{shev}	0.43±0.08
d_{expl}	6.16° ± 1.50°	d_{2l}	4.64° ± 1.57°	d_{shev}	2.75° ± 1.00°

Discussion: The ground-based observations enable the study of the Opposition Effect regime under varied models. In hold of the full phase curve, we compared it to a large corpus of asteroid phase curve parameters. Besides the important intrinsic errors from both datasets, Didymos comes out as an unusual S-type asteroid. The OE parameters point to scattering properties in the outskirts of the habitual cluster of S-types, skewing closer to G/Cg-type asteroids, and situated among M-Types. One particular model, the linear-by-parts, enables a tentative comparison with meteorite samples and places Didymos well among L/LL Chondrites.

In Fig. 1, Didymos HG1G2 parameters are compared to other asteroid spectral types. Didymos' curve is confronted with the central parameters for S-, M-, C-, and D-types. Under 40° phase angle, Didymos could be well misinterpreted as C- or D-type, while 40° posits the asteroid among S- and D-types. Important to notice that Didymos does not display same sharpness in the Opposition Effect regime of brighter asteroids like S-types. Its inflection around 5° is not visually remarkable. Looking into the macro-group of spectral types associated with carbon-based compositions, the C-type G1G2 center is near with P-, B- and Ch- types (Malkhe et al., 2021). The ambiguities are broken with the addition of LUKE data for wider phase angles.

The Linear-exponential function and HG1G2 model yield geometric albedo ρv ranging from 0.14 to 0.16. Either way, these albedos are ∼ 30 − 45% smaller than the central tendency for asteroids of the S taxonomic complex (ρ0 = 0.26 ± 0.04). Kohout et al. [14] show that shock-darkening and impact melt may suppress by ∼70% the albedo of ordinary chondrite at 650 nm. To reduce the average S-type R-band albedo considering only these both darkening agents, Didymos may bear 30−40% of shock darkening or 40−50% of impact melt. Taxonomically, a silicatic asteroid can skews from Q as much as to C/Ch spectral type, through 1-μm band suppression, given that the original spectrum departs from a fresh non-weathered composition.

Didymos is possibly a representive of small S-type asteroid analogs to LL chondrite composition which until then are not sampled enough in the literature concerning phase curve of Near-Earth asteroids. For example, from the ATLAS catalog [13] we find 47 S-type asteroids with HG1G2 parameters similar to Didymos. Therefore, sampling more phase curves of NEAs could help detect more of such unusual compositional cases. In addition, this would also shed light to the question whether as we get further into smaller asteroids we depart from the usual and expected compositional trends.

This work is submitted to the Planetary Science Journal in the DART focus issue.

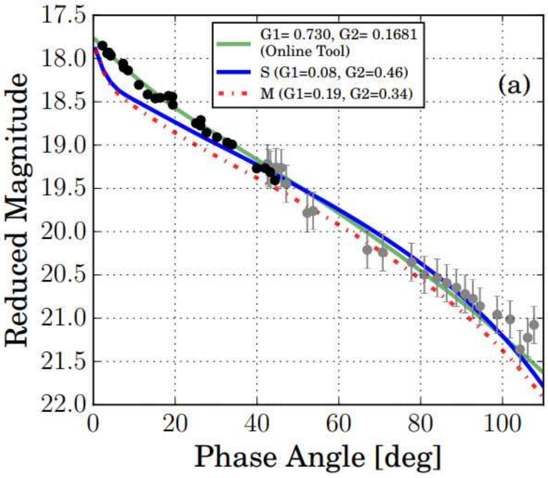

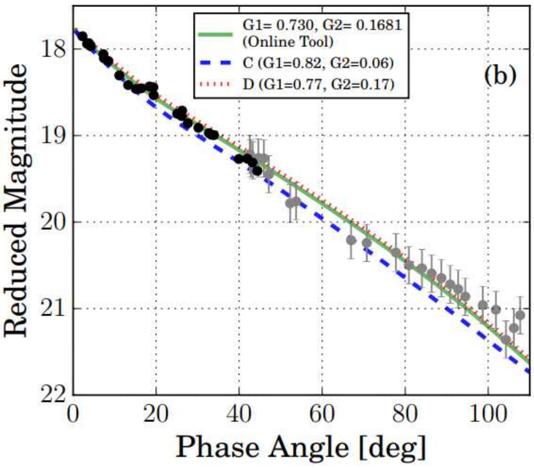

Fig. 1. Didymos' Cousins R phase curve compared to the median G1G2 parameters for S-, C-, M-, and D-type asteroid from Malkhe et al. [13].

Acknowledments: This research was supported by the Italian Space Agency (ASI) within the LICIACube project (ASI-INAF agreement AC No. 2019-31-HH.0 CUP 84I190012600). P.P. acknowledges support by the Grant Agency of the Czech Republic, grant 20-04431S. R.T.D, A.R., O.B. were supported by the DART mission, NASA Contract No. 80MSFC20D0004.

References: [1] Dotto et al., P&SS 199, 105185 (2021). [2] Dotto et al., Nature, in. pub (2023). [3] Pravec et al., PSJ 3, 175 (2022). [4] Kitazato et al., LPSC (2004). [5] Pravec et al., Icarus 181, 63 (2006). [7] Park et al., ASR 57, 509 (2016). [8] Minonen et al., Icarus 209, 542 (2010). [9] Minonen et al., MPS 44, 1937 (2009). [10] Shevchenko, LPSC 27, 1193 (1996). [11] Belskaya & Shevchenko, Icarus 147, 94 (2000). [12] Déau et al., Icarus 272, 149 (2016). [13] Mahlke et al., Icarus 354, 114094 (2021). [14] Kohout et al. PSJ 1, 37 (2020).

DUST CLUMPS DYNAMICS OF THE DIMORPHOS EJECTA PLUME

Ivanovski, S. L.(1), Hasselmann, P. H.(2), Zanotti, G. (3), Bertini, I.(4,5), Deshapriya J.D.P.(2), Ieva, S.(2), Lucchetti, A.(6), Pajola, M.(6), Perna, D.(2) , Poggiali G.(7,8), Dotto, E.(2), Della Corte, V.(9), Herreros, M. I. (10), Ormo, J. (10), Ferrari, F.(3), Li, J-Y.(11), Amoroso, M. (12), Pirrotta, S. (12), Zinzi, A.(12), Brucato, J.R. (7), Capannolo, A. (3), Caporali, S. (6), Ceresoli, M. (3), Cremonese, G. (6), Dall'Ora, M. (9), Gai, I. (13), Gomez Casajus, L.(13), Gramigna, E. (13), Impresario, G. (11), Lasagni Manghi, R. (13), Lavagna, M. (3), Lombardo, M. (13), Marzari, F. (14), Mazzotta Epifani, E. (2), Modenini, D. (13), Palumbo, P. (5), Rossi, A.(15), Tortora, P.(13), Tusberti, F. (6), Zannoni, M.(13), Fahnestock, E.G.(16), Farnham, T. L.(17), Fitzsimmons A.(18), Hirabayashi M.(19), Raducan S. D.(20), Soldini S.(21), and Luther R.(22)

(1) INAF Osservatorio Astronomico di Trieste, Italy (2) INAF Osservatorio Astronomico di Roma, Italy (3) Politecnico di Milano, Italy (4) Università degli Studi di Napoli "Parthenope", Napoli, Italy (5) INAF Istituto di Astrofisica e Planetologia Spaziali, Roma, Italy (6) INAF Osservatorio Astronomico di Padova, Italy (7) INAF Osservatorio Astrofisico di Arcetri, Firenze, Italy (8) Observatory of Paris, France; (9) INAF Osservatorio Astronomico di Capodimonte, Napoli, Italy; (10) Centro de Astrobiología (CAB), CSIC-INTA (11) Planetary Science Institute, Tucson, AZ, USA (12) Agenzia Spaziale Italiana, Roma, Italy; (13) Università di Bologna, Bologna, Italy (14) Università di Padova, Italy (15) CNR Istituto di Fisica Applicata "Nello Carrara" (16) Jet Propulsion Laboratory, California Institute of Technology, USA (17) University of Maryland, College Park, Maryland, USA (18) School of Mathematics and Physics, Queen's University Belfast, UK (19) Auburn University, Auburn, AL, USA (20) Space Research and Planetary Sciences, University of Bern (21) University of Liverpool, UK (22) Museum für Naturkunde - Leibniz Institute for Evolution and Biodiversity Science, Berlin, Germany

Corresponding author: stavro.ivanovski@inaf.it

Introduction: The NASA Double Asteroid Redirection Test (DART) impact [1], was the first space mission that successfully demonstrated the kinetic impactor technique for planetary defense. It was at the same instant, on 26th September 2022, when ASI/Light Italian Cubesat for Imaging of Asteroids (LICIACube) [2] was the first Cubesat to image the plume coming from Dimorphos, the smaller body of the binary asteroid (65803) Didymos. The DART impact into Dimorphos [3] caused ejecta plume propagation with high velocity and very filamentary structure, composed of dust particles from μm to cm sizes in size [4]. The large aperture and observed spikes did not prevent propagation of larger excavated material, namely, boulders up to ~2 m [5]. Far-field observations such as HST clearly showed dust tail formed from the low-speed ejecta dust due to solar radiation pressure (SRP) [4].

The scientific objectives: The estimation of the size distribution and velocity distribution of the plume in close vicinity to Dimorphos, captured in the LICIACube images is still an unanswered question. While the long-term monitoring of the tail can reveal the size distribution up to tens of cm in size, the impact simulations can constrain the initial velocity of the excavated material. Near and mid – field simulations considering different dynamical properties at local scale can address the complex collimated but inhomogeneous distribution of the dust within the plume. Here, we discuss some of the dynamical properties of the plume using the available observational DART and LICIACube data of the plume propagation. We try to constrain the particle sizes within the collimated plume structures.

The model: We apply the 3D+t model – LIMARDE [6,7] constrained with laboratory observations [8], impact simulations and near- and far- field observations such as the LICIACube [9] images and HST [2] dust observations, respectively. The model computes single particle trajectories, the dust rotational frequencies and velocity as well as the particle orientation at any time and distance. We compute the dust velocity distribution based on the physical properties (size, mass and shape) derived from the LICIACube observations. The results are useful to check what is the role of the fragmentation of the particles and to constrain the physical properties based on the dynamical properties of the ejected dust in the near- and mid- environment.

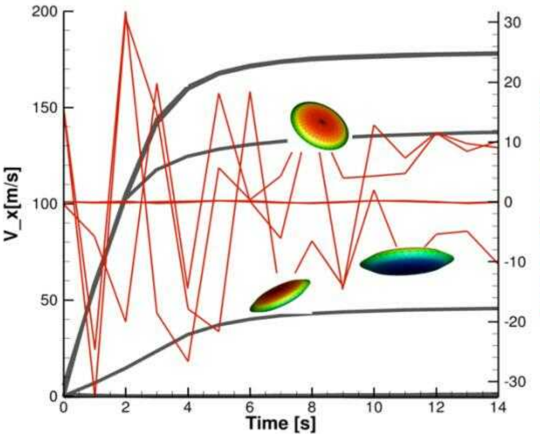

Fig. 1. The dust speed and rotation frequency of particles with different shapes as constitutes of the dust clumps shown in the observations of ASI/LICIACube/LUKE, 2022-09-26T23:17:04.

Discussion: The LICIACube observations suggest that we have the locations of accumulation of different particles along the collimated plume streamers. The latter may contain particles of the same density and shape but with different velocity and rotation due to the initial ejected position and form not-linear motion within the collimated filament – like structures. In Fig. 1 we show LIMARDE simulations with particles of different shapes that result with different velocities suggesting a scenario where the dusty clumps could occur at the same location due to motion of particles with different shapes. The study discusses what is the probability that these dust clumps are formed owing to fragmentation, or their location is a result of their motion history of the ejected particles.

Acknowledgements: This research was supported by the Italian Space Agency (ASI) within the LICIACube (ASI-INAF agreement AC n. 2019-31-HH.0).

References: [1] Rivkin, A.S. et al. 2021, PSJ, 2, 24pp; [2] Dotto, E. et al. 2021, PSS 199, [3] Daly, R.T. et al. (2023) Nature. [4] Li, J.-Y., et al. (2023) Nature. [5] Farnham et al. LPSC abs. [6] Ivanovski et al. 2023, u.rev.; [7] Fahnestock et al. 2022, PSJ; [8] Ormo et al. 2022, *E&PSL* [9] Dotto et al. 2023, Nature

COMPARING DIDYMOS AND DINKINESH ASTEROID BINARY SYSTEMS: COLLISIONAL HISTORY AND ORBITAL EVOLUTION.

A. Campo Bagatin[1], A. Dell'Oro[2], L. M. Parro[1], S. R. Schwartz[1]. [1]Universidad de Alicante (acb@ua.es), [2]Osservatorio Astrofisico di Arcetri – INAF (aldo.delloro@inaf.it).

Introduction: On the 26th of September, 2022, the near-Earth asteroid (NEA) binary system Didymos was visited by the DART (NASA) spacecraft and the LICIACube (ASI) cubesat [1, 2]. DART impacted Dimorphos, the secondary of the system, in the first-ever asteroid deflection experiment [3], while LICIACube flew by the system right after the impact [4].

One year later, on the 4th of November, 2023, the Lucy (NASA) spacecraft -on its way to the Jupiter Trojan asteroid region- flew by the inner asteroid belt binary system Dinkinesh.

The two systems share some similar characteristics -they both belong to the S taxonomic classification- but they also exhibit some differences.

The two primary bodies have essentially the same size (~800 m), Dinkinesh has a clear top-shape, while Didymos looks like a degraded one [5, 6]. It is interesting that none of the satellites had the expected prolate shape for an asteroid satellite. In fact, Dimorphos was inferred to have an oblate shape [7], while the Dinkinesh satellite images reveal what it seems to be a contact binary satellite.

The Didymos primary is spinning very fast, at 2.26 hr, on the edge of instability [8], and the orbital period of Dimorphos was 11.92 hr. Instead, the spin period of Dinkinesh is still not clear. An unambiguous former period of 52.67 +- 0.04 hr [8] was measured for the system (previous to the satellite discovery), and may now be revisited to disentangle the primary rotation and the satellite orbital motion.

Didymos is a NEA with an eccentric orbit, driving it well inside the inner asteroid belt, where it spends 1/3 of its orbital period, while Dinkinesh is an inner belter spending less than 30% of its orbit inside the limits of the asteroid belt ($q < 2.06$ au). On the other hand, Dinkinesh is not far away from a secular resonance that may dive it into the NEA region in the future.

Motivation: We recently studied the collisional history of the Didymos system in the frame of the interpretation of the surface features observed by the DART spacecraft, which may be relevant to the operations of the Hera (ESA) [9] space mission that will thoroughly study the system in 2026/27.

We now do the same exercise on Dinkinesh, and compare collisional probabilities and distributions of impact velocities, and we will try interpretations of the evolution of the two systems. Is Dinkinesh an early version of Didymos? Is it possible to relate orbital evolution of inner belt asteroids to their future evolution as NEAs? Is there a common formation pattern in the asteroid belt for km-size binary asteroids with top-shape-like primaries? Are collisional processes in the asteroid belt driving the formation of binary systems, as opposed to constant gentle spin up by YORP, eventually triggering fission or mass shedding?

With this study we try to contribute to the debate and find common processes that may have led Didymos and Dinkinesh to look like they currently are.

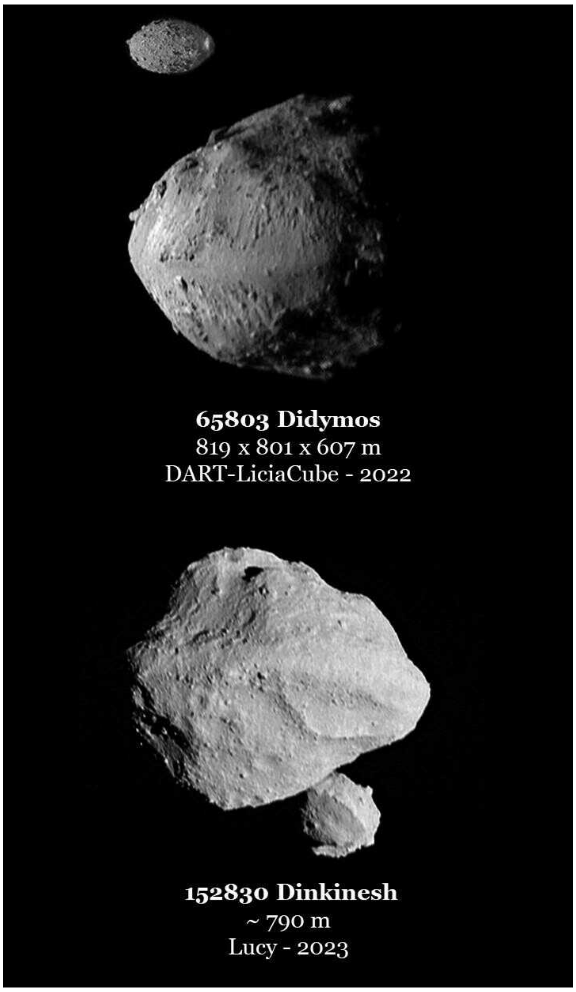

Fig. 1. Binary asteroids Didymos (top) and Dinkinesh (bottom) as imaged by the DART and Lucy spacecraft, respectively.

References:

[1] Rivkin A.S. et al. (2021) *PSJ*, *2,* 173. [2] Dotto E. et al. (2021) *PSS, 199*, 105185. [3] Cheng A.F. et al. (2023) *Nature*, *616,* 457-460. [4] Dotto E. et al. . (2023) *Nature. Submitted.* [5] Barnouin O.S. (2023) *Nature Comm. Submitted.* [6] Campo B. et al. (2023) *Nature Comm. Submitted.* [7] Daly R.T. et al. (2023) *Nature, 616,* 443-447. [8] Trògolo et al. (2023) *Icarus*, 397, 115521. [9] Mottola S. et al. (2023) *MNRAS Letters*, *524*, L1-L4.

Granular surface\artifact contact modeling in support of small bodies landing operations design

Davide Intra[1] Giovanni Zanotti[1], Michèle Lavagna[1], [1]*Politecnico di Milano, Via La Masa 34, 20156, Milano, Italia,*
davide.intra@mail.polimi.it, giovanni.zanotti@polimi.it, michelle.lavagna@polimi.it

Introduction: Small bodies in situ exploration represents an added value to remote data collection; however, among other challenges risen by the numerous uncertainties those targets present, landers bouncing prediction and containment is here considered. To model small bodies granular surfaces is the basis for a numerical campaign to drive the lander and operations design robust to the regolith features uncertainties. As a case study, the landing phase of the TASTE (Terrain Analyzer and Sample Tester Explorer) mission to Deimos, ASI financed [1], is considered. The TASTE mission aims at inspecting the small martian moon with both in-situ and remote science. By means of an accurate surface modelling, the aim is to characterize the landing dynamics, focusing on the touchdown effects onto the satellite structure, as well as onto the expected bouncing phase. A Soft-Sphere Discrete Element Method (SSDEM) is adopted to model Deimos superficial regolith, taking into account friction, and contact forces and the cohesion between the particles. As for the regolith properties, Phobos' data are preliminarily employed [2], assuming similarities between the two martian moons. Sensitivity analysis on material properties will run in the next study step.

Discrete Element Method: A Soft-Sphere Discrete Element Method is implemented, being the state-of-the-art approach for this kind of analysis. It models the regolith particles as deformable spheres, which are allowed to partially overlap. From the overlapping extent, both normal and tangential contact forces are retrieved through Flores' model [3]. For the sake of reliability of the approach and accuracy of the results, friction forces are considered. The static and dynamic frictions determine the static or slipping nature of the contacts. The twisting (spinning) friction resistance is computed whenever two particles in persistent contact show a different rotating velocity around the contact normal axis. Finally, the rolling friction resistance is included when two particles in contact exhibit a relative rotational velocity. Cohesion among the regolith grains is fundamental to reproduce a realistic model. The more cohesive the surface is, the more it behaves like a rocky material, thus leading to a shorter contact duration, higher contact forces and lower energy dissipation. Perko's cohesion model [4] is adopted, which links the cohesive effect among the particles to a cleanliness factor which is an indicator of the particles separation at molecular level. No adhesive model is implemented in this work, given the expected short duration of the contact, since the adhesion effect between the regolith and the spacecraft is considered negligible from the landing design point of view. The numerical environment asks to first create the superficial regolith layer by dropping a set of randomly displaced grains in a limited volume until a quasi-static condition is reached. The limited volume size is driven by the clashing criteria of containing the computational time and avoiding unrealistic borders effects on the post-contact dynamics. The trade-off leads to a regolith bed size 5x the lander's major dimension in width, and 2.5x its minor dimension in depth, in line with [5].

Regolith model: Due to the uncertainties regarding Deimos' regolith properties, and given its expected similarities to the bigger martian satellite, Phobos, the majority of the data employed in this work are retrieved from the MMX mission studies [2]. An exception is represented by the parameters influencing the cohesive force, namely the Hamaker's constant, the cleanliness factor and inter-particle distance, which are set equal to those of the lunar regolith, since the Moon is deemed to be a conservative environment for smaller celestial bodies. Table 1 reports Deimos regolith properties adopted for this study.

Table 1: Deimos regolith properties

Property	Particle-particle	Lander-particle
Particle radius [mm]	0.3 – 2	
Density [kg/m^3]	2600	
Young's modulus [GPa]	70	
COR	0.6	0.5
Static friction coefficient	0.6	0.45
Dynamic friction coefficient	0.6	0.45
Rolling friction coefficient	0.09	
Spinning friction coefficient	0.01	
Hamaker's constant [J]	$4.3 \cdot 10^{-20}$	-
Inter-particle distance [m]	$1.5 \cdot 10^{-10}$	-
Cleanliness factor	0.75 – 0.88	-

Given that both particle-particle and particle-lander contacts are expected, some properties exhibit two values. The properties for container-particle and lander-particle contacts are assumed equal. A grain size equal to the upper limit presented in Table 1 is adopted for simulations, to reduce the computational load in this tuning phase of the whole numerical tool.

Results: The results reported in this Section are produced by a simulation campaign carried out in *Chrono Project* [6] with a reduced-scale lander, in order to further decrease the simulation time. The parameters of interest are the effective Coefficient of Restitution (COR) (Figure 1), which is defined as the ratio between the velocity magnitude after and before the impact and indicates the energy dissipation, the outgoing velocity magnitude (Figure 2) and direction (Figure 3) and finally the overall contact force acting onto the spacecraft (Figure 4). The impacting velocity magnitude and direction with respect to the local normal to Deimos vary, as well the prismatic lander attitude: a short-edge impact and a most-likely long-edge impact.

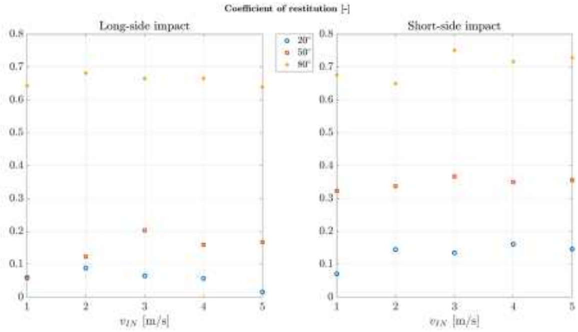

Figure 1: Coefficient of restitution

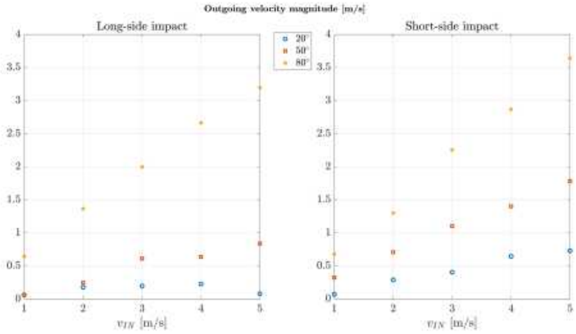

Figure 2: Outgoing velocity magnitude

The COR mainly depends on the impacting attitude, while the outgoing velocity magnitude almost linearly increases with the impacting speed magnitude. The lower the incident angles on surface, the lower outgoing directions are. Moreover, the contact force experienced by the lander depends on how energetic and steep the impact is. The steeper the impacting direction, the higher the penetration depth in the regolith layer is, thus leading to a longer contact duration and a greater energy dissipation. Finally, the lander post-impact velocity magnitude drives the entire bouncing dynamics, and allows checking the range and final velocity against the celestial body size and escape conditions.

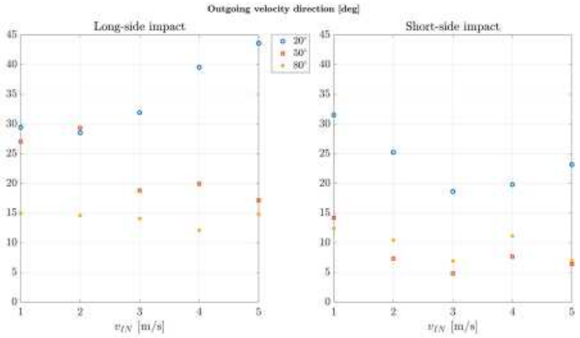

Figure 3: Outgoing velocity direction

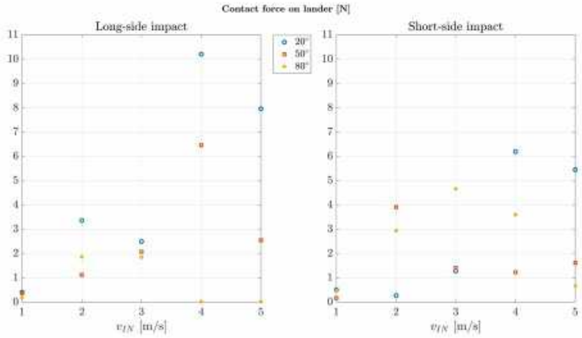

Figure 4: Contact force onto lander

Final remarks: The SSDEM is adopted to settle an accurate contact numerical model for landing on granular surfaces, and is giving preliminary promising results to drive lander release conditions to be robust to bounce and escape. By including the soil properties uncertainty, a database useful in operations can be produced: indeed the impact duration, coefficient of restitution and contact forces, could be exploited to quantify the energy dissipation during landing, which could be considered as a scientific experiment to assess the surface terrain properties.

Acknowledgement: the authors want to acknowledge the ASI ALCOR program team and the TASTE phase A consortium for the landing use case scenario data.

References: [1] Lavagna, M., et al. Taste Mission to Deimos: Terrain Analyzer and Sample Tester Explorer with Smallsat and Miniaturized Lander. In: *52nd Lunar and Planetary Science Conference*. 2021. p. 1991. [2] Sunday, C. *Landing, sinking, and rolling on small body surfaces*. 2022. PhD Thesis. Toulouse, ISAE. [3] Flores, P., et al. On the continuous contact force models for soft materials in multibody dynamics. *Multibody system dynamics*, 2011, 25: 357-375. [4] Perko, H. A.; Nelson, J. D.; Sadeh, W. Z. Surface cleanliness effect on lunar soil shear strength. *Journal of geotechnical and geoenvironmental engineering*, 2001, 127.4: 371-383. [5] Seguin, A.; Berho, Y.; Gondret, P., Influence of confinement on granular penetration by impact. *Physical Review E*, 2008, 78.1: 010301. [6] P. C. development team. Chrono: An Open Source Framework for the Physics-Based Simulation of Dynamic Systems. http://projectchrono.org. Accessed: May 2023.

THERMAL ANALYSIS OF THE COMET 67P

E. Rognini[1,2], F. Tosi[3], A. Zinzi[1,4], M. Giardino[1,4]
[1]ASI Space Science Data Center (SSDC), Via del Politecnico, 00133 Rome, Italy (edoardo.rognini@ssdc.asi.it)
[2]INAF-OAR Osservatorio Astronomico di Roma, Via Frascati 33, 00078, Monte Porzio Catone (RM), Italy
[3]INAF-IAPS Istituto di Astrofisica e Planetologia Spaziali, Via del Fosso del Cavaliere 100, 00133 Rome, Italy (federico.tosi@inaf.it)
[4]Agenzia Spaziale Italiana (ASI), Via del Politecnico snc, 00133, Rome, Italy

Introduction: The ESA mission Rosetta was the first to enter orbit around a comet, namely 67P/Churyumov-Gerasimenko, and to deploy a lander to its surface. In this work we aim at designing a database of thermal observations provided by the VIRTIS-M instrument onboard the Rosetta orbiter [1], with the goal of making it easier to analyze thermal data [2] and compare them with temperature values predicted by thermophysical models. This can ultimately disentangle diurnal and seasonal effects for various morphological regions.

Methods: We have loaded VIRTIS-derived temperature data on a SQL database. These data are accessible and processable through proper SQL queries, making it possible to perform a systematic analysis for any given location of the comet nucleus covered by VIRTIS data. The shape model (in SPICE format) is "CSHP_DV_130_01_LORES_OBJ.bds" [3], made up of 104k triangular plates ("facets"). To project each temperature model onto the observer's plane, we used a dedicated three-dimensional data visualization tool named MATISSE [4], which allows a proper characterization of both measured and modelled data on the bilobate nucleus of comet 67P.

Results and future work: From preliminary analysis, we found a first seasonal trend in which the temperature increases as the heliocentric distance decreases (Fig. 1). The comparison between observed and predicted temperature values in principle could constrain thermophysical models not only for a small portion of the surface [2] but also for much larger areas of the comet nucleus, allowing a link with morphological and geological processes. The use of a SQL database will allow a series of systematic comparisons that will prove crucial for future studies following up the work presented in [2].

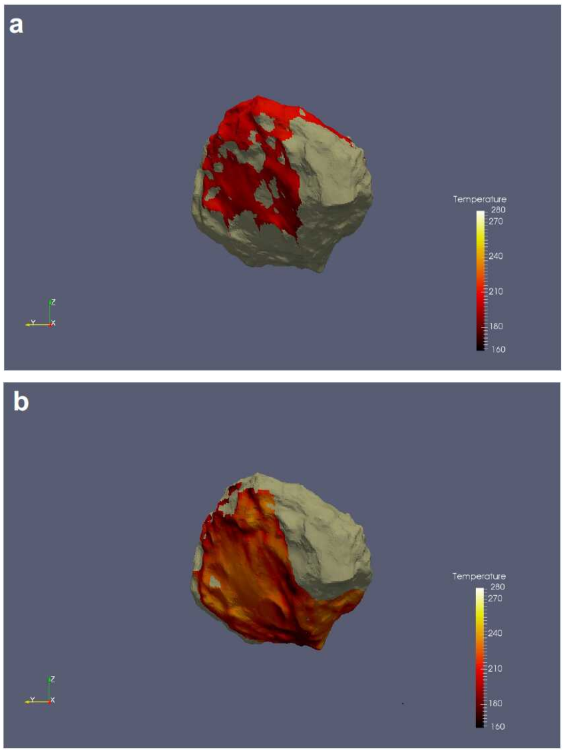

Figure 1. Snapshots of the comet nucleus obtained in a 30-minute period centered around local noon for the equatorial Imhotep region as observed by VIRTIS at 3.5 (a) and 1.9 (b) AU from the Sun.

References:

[1] Coradini, A., et al. (2007), *Space Science Reviews*, 128, 529-559

[2] Tosi, F., et al. (2019), *Nature Astronomy*, 3, 649–658

[3] Beth A., et al., (2017), in European Planetary Science Congress. pp EPSC2017–516, 634

[4] Zinzi, A., et al. (2016), *Astronomy and Computing*, 15, 16-28

The EU H2020 programme NEOROCKS.

E. Mazzotta Epifani[1], E. Dotto[1], E. Perozzi[2], on behalf of the NEOROCKS team*, [1]INAF – Osservatorio Astronomico di Roma, Via Frascati 33, 00040 Monte Porzio Catone (Roma), Italy; ASI – Agenzia Spaziale Italiana, Via del Politecnico snc, 00133 Roma. *Corresponding email: elena.mazzottaepifani@inaf.it.*

Introduction: In the last years the research about Near Earth Objects (NEOs) has been a major topic in planetary science, also in view of the potential hazard some of them pose to our civilization and, more in general, to life on our planet.

Moreover, the physical characterization of NEOs allows us to put constraints on the material in the protoplanetary nebula at different solar distances, and can give us insights into the early processes that governed the formation and the evolution of planets, including the delivery of water and organics to Earth.

The "NEOROCKS - The NEO Rapid Observation, Characterization and Key Simulations" Collaborative Research Project has been approved to address the topic c) "Improvement of our knowledge of the physical characteristics of the NEO population" of the call SU-SPACE-23-SEC-2019 from the Horizon 2020 - Work Programme 2018-2020 Leadership in Enabling and Industrial Technologies – Space.

It was developed by an international consortium in the timeframe 2020-2023, with the following main ambitions:

- Ambition 1: Networking large aperture telescopes;
- Ambition 2: Advancing NEO physical properties modelling and simulations, to understand their physical nature. In particular, focussing on small size objects is of uttermost importance for designing effective mitigation measures in space and on the ground;
- Ambition 3: Improving the orbit determination process, by developing and validating advanced mathematical methods and innovative algorithms for NEO orbit determination;
- Ambition 4: Addressing the imminent impactors monitoring;
- Ambition 5: Establishing a NEO physical properties data centre, to provide scenarios and roadmaps with the potential to scale-up at a global level the experience gained during the project;
- Ambition 6: Fostering international cooperation for follow-up observations;
- Ambition 7: Raise the public awareness on NEO and impact hazard, by appling and guaranteeing continuity of educational and public outreach activities needed to improve significantly public understanding and perception of the asteroid hazard, counteracting the spreading of fake news and unjustified alarms.

The NEOROCKS results: An overview of the activities we carried out and of the results we obtained [1] [2] [3] [4] [5] [6] [7] [8] [9] [10] [11] [12] [13] [14] will be briefly presented.

Moreover, the legacy that NEOROCKS leaves to the Planetary Defence community will be discussed.

References: [1] Deshapriya J.D.P. et al., 2023, A&A 674, A50. [2] Ieva S. et al., 2022, MNRAS 513, 3104. [3] Hromakina T. et al., 2021, A&A 656, A89. [4] Hromakina T. et al., 2023, MNRAS 520, 2, 3143. [5] Popescu M. et al. (2020). MNRAS 496, 3572. [6] Simion N.G. et al. (2021). MNRAS 508, 1128. [7] Reddy V. et al. 2022, PSJ 3, id.123. [8] Morate D. et al., 2023, MNRAS 519, 1677. [9] Licandro J. et al. 2022, MNRAS 521, 3784. [10] Popescu M. et al., 2023, A&A 676, A126. [11] Sergeyev A. & Carry B., 2021, A&A 652, A59. [12] Sergeyev A. et al., 2022, A&A 658, A109. [13] Licandro J. et al., 2023, MNRAS 521, 3, 3784. [14] Rozek A., et al., 2022, MNRAS 515, 3, 4551.

Additional Information:

*The NEOROCKS team is composed by: Istituto Nazionale di Astrofisica (I) – coordinating partner; Agenzia Spaziale Italiana (I); University of Padova (I); LESIA – Observatoire de Paris (F); Observatoire de la Cote d'Azur (F); University of Edimburgh (UK); Astronomicky Ustav AV CR (CZ); Instituto de Astrofisica de Canarias (S); Space Dynamics Services s.r.l. (I); DEIMOS Space s.l.u. (S); DEIMOS Space s.r.l. (RO); DEIMOS Castilla La Mancha sl (S); NEOSPACE Spolka z Ograniczona Odpowiedzialnoscia (PL); Resolvo s.r.l. (I).

The whole NEOROCKS team is composed by: S. Anghel, M. Banaszkiewicz, S. Banchi, M.A. Barucci, F. Bernardi, A. Bertolucci, M. Birlan F. Calderini, B. Carry, A. Cellino, F. Colas, J. De Leon, A. Del Vigna, A. Dell'Oro, A. Di Cecco, L. Dimare, I. Di Pietro, E. Dotto, P. Fatka, S. Fornasier, E. Frattin, P. Frosini, M. Fulchignoni, R. Gabryszewski, M. Giardino, A. Giunta, T. Hromakina, J. Huntingford, S. Ieva, J.P. Kotlarz, F. La Forgia, M. Lazzarin, J. Licandro, E. Mazzotta Epifani, H. Medeiros, A. Mediavilla, F. Merlin, J. Nomen Torres, D. Perna, E. Perozzi, V. Petropoulou, F. Pina, G. Polenta, M. Popescu, P. Pravec, A. Rozek, P. Scheirich, A. Sergeyev, C. Snodgrass, A. Sonka, C. Teodorescu, G.B. Valsecchi, P. Wajer, A. Zinzi.

MINERALOGICAL MAPPING OF CERES AS REVEALED BY THE 1 μm ABSORPTION

F. G. Carrozzo[1], Maria Cristina De Sanctis[1], Marco Ferrari[1], Andrea Raponi[1], Mauro Ciarniello[1], Eleonora Ammannito[2]
[1]INAF-IAPS (giacomo.carrozzo@inaf.it), [2]Agenzia Spaziale Italiana

Introduction: Various minerals have been detected on Ceres and their abundance and spatial distribution have been mapped in the near infrared spectral domain [i.e. 1, 2]. In this work, we study the 1 μm absorption to map Ceres mineralogy at a global scale. It is based on the determination of the whole 1 μm absorption from VIR spectra. VIR is the imaging spectrometer on board the NASA mission Dawn launched in September 2007. VIR is composed of two channels: the VIS channel working in the visible wavelengths between 0.26-1.07 μm and the NIR channel operating in the near infrared between 1.02-5.1 μm. The 1 μm absorption is, indeed, in between the instrument channels.

Method: To study the 1 μm spectral range, an automatic method to co-register the VIS and NIR channels, where they overlap, has been implemented, thus allowing the study of this band. After the spatial co-registration, a residual difference in the I/F at 1 μm between the two channels can remain due to the difference in the PSF's. To avoid this problem, each VIS spectrum is rescaled to the value of the I/F at ~1 μm of the corresponding NIR spectrum. The exact wavelength at which the two VIR channels are matched, inside the overlapping range between 0.92–1.8 μm, is selected for each spectrum based on the best match. The difference between the VIS and NIR reflectance at ~1 μm (ΔR) is usually 1-2% and only about 1% of data show a ΔR>10%. The spectra with the largest mismatch between the two channels are located along the walls of the craters and valleys where the influence of PSF differences is expected to be larger. In this study, the data with ΔR>10% are discarded. The maps have global longitudinal coverage, latitudinal coverage from 66°S to 66°N, and a spatial resolution of ~1.86 km/pixel at the equator.

Each spectrum of the surface is the result of an areal or intimate mixing of different minerals, and the resulting spectral reflectance properties are a complex combination of the spectra of each mineral end-member. Several studies have shown that it is possible to explore Ceres mineralogical diversity utilizing specific spectral parameters [1, 2].

In order to extract compositional information from the spectra, we have introduced some spectral indices and studied the correlations between them all over the VIR data set. Global maps of the 1 μm signature on Ceres have been derived from various spectral indices, such as band centers, depths, integrated areas, etc.

Results: A better understanding of the spatial distribution and the content of the different mineral phases can thus be obtained by investigating the spectral characteristics of the 1 μm band.

In general, the VIR spectrum of Ceres is dominated by a broad absorption at about 1.2 μm. It is mostly uniform across the surface, but some differences can be seen in the map of the band parameters, like the band depth. Variation in the band depth could be due to various factors, such as the relative abundance and grain size of the present minerals.

However, the spectral properties of the 1 μm band have been related to other spectral parameters in the NIR domain where mineralogy is known. For example, the attribution of the 3.1 μm band to ammonia-bearing species [1] show that this mineral phase is dominant where we see low values of 1 μm band. In fact, the spatial variability in the 1.0 μm band intensity is anticorrelated with respect to the 3.1 μm band.

Some terrains show a different behavior of the 1 μm band with respect to 3.1 band. This suggests the presence of a distinctive mineralogy.

This work, together with the results of other authors [1,2], completes the global mapping of the Ceres mineralogy.

Acknowledgments: The Visible and Infrared Mapping Spectrometer (VIR) was funded and coordinated by the Italian Space Agency (ASI), with the scientific leadership of the Institute for Space Astrophysics and Planetology, Italian National Institute for Astrophysics, Italy (IAPS-INAF).

References: [1] E. Ammannito et al. (2016) *Science, 353*, issue 6303. [2] Carrozzo et al. (2018), *Science Advances*, vol. 4, 3, e1701645.

The diversity of Neptune-sized Exoplanets

Luigi Mancini
Department of Physics University of Rome “Tor Vergata”, Via della Ricerca Scientifica 1, I-00133 Roma, I
E-mail: lmancini@roma2.infn.it

Abstract: Sub-Neptune and Neptune-sized Exoplanets exhibit a more and more surprising wide diversity of masses and bulk density. Determining their internal composition is, actually, a key parameter that can provide insights into whether these planets are predominantly composed of volatile materials or if they have significant amounts of denser substances such as water or rocky materials. Such information is, therefore, fundamental for understanding their formation and evolution, especially for those that lie in the hot-Neptune “desert” where the vicinity with their parent stars can induce atmospheric escape processes. The TESS space telescope is providing many transiting-planet candidates, orbiting bright stars, that are excellent targets for high-precision spectroscopic follow-up observations, which allow us to physically characterize these planets and explore their parameter space. In this context, we will present the results of a high-cadence RV monitoring of a list of Neptune-sized TOIs performed with the HARPS-N spectrograph at the Telescopio Nazionale Galileo [1].

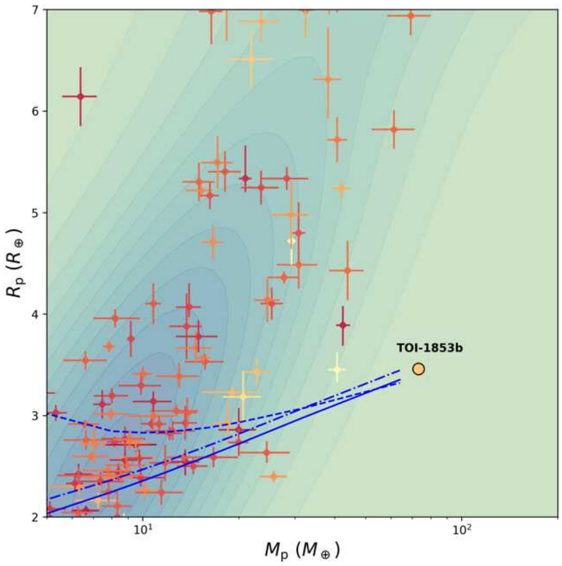

Fig.1: An example of composition degeneracy: the super-massive TOI-1853 [2] can be composed of 50% rock and 50% water (solid blue line), 50% water 49% rock and 1% hydrogen (dot-dashed blue line), or 99% rock and 1% hydrogen (dashed blue line).

In particular, we will highlight the recent discovery of TOI-1853 b [2], which has a mass of 73 Earth masses, almost twice that of any other Neptune-sized planet known so far, and a density of roughly 10 grams per cubic centimetre, that is six times that of Neptune. These remarkable properties place TOI-1853 b in the middle of the Neptunian desert and present a puzzle for conventional theories of planetary formation and evolution. Moreover, TOI-1853 b represents an emblematic case of composition degeneracy, since it can be composed of 50% rock and 50% water, or 99% rock and 1% hydrogen (see Fig. 1). Such an uncanny discovery tell us that the parameter space of Neptune-sized planets can still hide other exceptional surprises and needs to be systematically investigated.

References:

[1] Naponiello, Mancini et al., 2022, A&A 667, A8 https://www.aanda.org/articles/aa/full_html/2022/11/aa44079-22/aa44079-22.html

[2] Naponiello, Mancini et al., 2023, Nature 622, 255 https://www.nature.com/articles/s41586-023-06748-4

GLOBAL ARCHITECTURE OF PLANETARY SYSTEMS (GAPS): SEARCHING FOR AND CHARACTERIZING EXOPLANETS WITH TNG.

R. Claudi[1,2] and GAPS Collaboration [1]INAF – Astronomical Observatory of Padova (riccardo.claudi@inaf.it); [2] Dip di Matematica e Fisica dell'Università di Roma-tre

Global architecture of planetary systems (GAPS) project is an Italian collaboration started in the 2012 [1] and aimed to exploit the high resolution spectrographs (HARPS-N [2] in the visible and GIANO-B in the NIR) at the Telescopio Nazionale Galileo (TNG) to search for and characterize extrasolar planets. In its first phase (ended in 2017) the project has been aimed to search new planets in known planetary systems and around other peculiar stars (low metallic and M stars) by means of high precision radial velocity time series [3-4]. In the 2017 started the second phase of GAPS triggered by the implementation of the new TNG observing mode GIARPS [5] that allows the simultaneous use of HARPS-N and GIANO-B. In this second phase, GAPS is devoted to the studies of young planets and planetary atmospheres and is still on going [6-]. In its 12 years long history, the project produced more than 50 refereed papers and discovered about 30 new planets, revised and refined several planetary masses, and characterize a bunch of transiting system analyzing their Rossiter McLaughlin effects. Furthermore, in the last 5 years GAPS identified CH_4, NH_3, CO, C_2H_2,H_2O, HCN, CO_2 molecules in the atmospheres of different transiting planets.

REFERENCES: **[1]** Covino, E., Esposito, M., Barbieri, M., et al. 2013, A&A, 554, A28 ; **[2]** Cosentino, R., Lovis, C., Pepe, F., et al. 2012, Society of Photo-Optical Instrumentation Engineers (SPIE) Conference Series, Vol.8446, Harps-N: the new planet hunter at TNG, 84461V**;** **[3]** Affer L. et al., 2019, A&A, 662, A193; **[4]** Maldonado J., 2022, A&A, 663, A142**,** **[5]**Claudi, R., Benatti, S., Carleo, I., et al. 2017, European Physical Journal Plus, 132, 364 ; **[6]** Carleo, I., Benatti, S., Lanza, A. F., et al. 2018, A&A, 613, A50; **[7]** Carleo, I., Giacobbe, P., Guilluy, G., et al. 2022, AJ, 164, 101; **[8]** Carleo, I., Malavolta, L., Lanza, A. F., et al. 2020, A&A, 638, A5; **[9]** Guilluy, G., Andretta, V., Borsa, F., et al. 2020, A&A, 639, A49

ARE PLANETS WITH LARGE EARTH-SIMILARITY INDEX REALLY HABITABLE?

E. Bisesi [12], G. Murante [1234], J. von Hardenberg [56], J. A. Caballero [7], P. Simonetti [1], M. Maris [134] and L. Silva [13]

[1] INAF – Osservatorio Astronomico di Trieste, Italy; [2] CNR – Istituto di Geoscienze e Georisorse, Pisa, Italy; [3] Institute for the Fundamental Physics of the Universe – SISSA, Trieste, Italy; [4] ICSC – Centro Nazionale di Ricerca in HPC, Big Data e Quantum Computing; [5] DIATI, Politecnico di Torino, Italy; [6] CNR – Istituto di Scienze dell'Atmosfera e del Clima, Torino, Italy; [7] Centro de Astrobiología, CSIC-INTA, Madrid, Spain. Contact person: erica.bisesi@inaf.it

Background: The search for habitable worlds is one of the most exciting topics in Astrobiology. Since the discovery of the first exoplanet in 1995, thousands of them have been detected. Exoplanets may hugely differ by mass, radius, orbital parameters, and hosting star's spectral type. In recent years, a special attention has been devoted to planets orbiting around M-type stars: as smaller worlds, whose masses and radii are similar to the Earth's, they are easier to be observed. Conversely, giant and gaseous planets are not good candidates for hosting life. Our hunt for habitable planets therefore focuses on rocky or water worlds. Currently, about 20 Earth-like sized planets have been detected in the habitable zone (see, e.g., https://phl.upr.edu/projects/habitable-exoplanets-catalog). Almost all of them belong to M-type stellar systems.

Here, we define "habitability" as the presence of liquid water – a condition for the emergence and sustainability of complex life [1]. The temperatures of potentially habitable worlds range between the freezing point of water (for a given atmospheric pressure) and an upper limit of $T \approx 50°C$, which is required for the persistence of an active metabolism and for reproduction of multicellular poikilotherms (organisms whose body temperature and vital processes are very sensitive to the environmental temperature). As for habitability definition, we consider both the temperature ranges [273.15 – 323.15] K (h_{50}) and [273.15 – 373.15] K (h_{100}). Such habitability indices for complex life correspond to the mean orbital fractions of planetary surface that satisfie the indicated temperature limits.

According to this criterion, habitability can be quantified by using climate models to compute the surface temperature as a function of stellar, orbital and planetary parameters, among which atmospheric pressure and composition play a primary role. Second, one should estimate whether the pressure and the atmospheric composition of the planet are compatible with the presence of liquid water.

Such planets are very likely tidally-locked – i.e., they always face one side to the star, the other one being permanently dark. To deal with the climate of planets in such configurations, numerical models such as Earth System Models of Intermediate Complexity (EMICs) are especially needed.

Aims and Methods: We have adopted the intermediate complexity model PLASIM (PLAnet SIMulator, [2]) – an atmospheric model with a spectral dynamical core and simplified physics [3] that can be coupled to the fully three-dimensional Large Scale Geostrophic Ocean model (LSG; [4]). A first advantage of PLASIM is that, while being completely three-dimensional, it does not include all the details of a full Global Circulation Model (GCM) as those used for studying the evolution of the Earth's climate (e.g., a very detailed topography and complex physical parameterizations). As such, it is better suited for being applied to exoplanets, for which most of such information is and will be unknown in the near future. Second, PLASIM is very fast (a single modeled year can be run on a single core in a couple of minutes), which allows to perform large ensembles of runs to explore large parameter spaces. As for other EMICs, however, PLASIM was initially designed for the Earth. We then adapted the code to make the PLASIM-LSG combination applicable also to synchronously rotating terrestrial planets, to planets orbiting around stars with non-solar spectra, and to planets with non-Earth-like surface pressures. Our changes are akin to what obtained by similar efforts applied to PLASIM versions without LSG, such as [5].

PLASIM has been exploited to systematically classify and compare potential habitable exoplanets as a function of different parametric configurations (Bisesi et al., in preparation). Our analysis focuses on the 22 exoplanets with the highest Earth-Similarity Index (ESI) values in the Conservative Sample of Potentially Habitable Exoplanets (PHL @ UPL Arecibo, 2023; [6]). Sorted by ESI, they are: Teegarden's Star b, TOI-700 d, Kepler-1649 c, TRAPPIST-1 d, Proxima Cen b, K2-72 e, GJ 1002 b, GJ 1061 d, GJ 1061 c, Ross 128 b, GJ 273 b, Kepler 296 e, TRAPPIST-1 e, Kepler-442 b, GJ 667 C f, TRAPPIST-1 f, Teegarden's Star c, Kepler-1229 b, Kepler-186 f, GJ 667 C e, GJ 1002 c, and TRAPPIST-1 g. Each of such planetary system is characterized by homogeneous stellar and basic planet parameters and and some of them have already been observed with state-of-the-art instrumentation, such as the James Webb Space Telescope.

Our aim is to homogenously estimate, for the first time, the liquid water habitability of all the above-mentioned exoplanets as a function of a systematic exploration of the selected parametric space. Habitability values correspond to the planetary surface fraction where temperature is comprised in the above-defined ranges.

We generate two grids of models: (i) by focusing on the modern-Earth atmosphere, we adopt planetary configurations with aqua-planet topography, ocean treatment (mixed layer), zero obliquity and eccentricity, and different atmospheric pressures; (ii) by keeping all planetary parameters fixed and setting an aqua-planet topography, we generate a second grid of models in which each star-planet pair is associated to four different atmospheric compositions [7]: as the modern Earth, as the early Archean Earth, CO_2-dominated and Titan-like.

Preliminary Results: Planetary habitability is strongly affected by climate and atmospheric composition. By fixing the CO_2 fraction and increasing (decreasing) the surface pressure, surface temperature increases (decreases). As an example, a "cold" planet is more habitable at high pressure, while a "hot" planet does the opposite (Fig. 1).

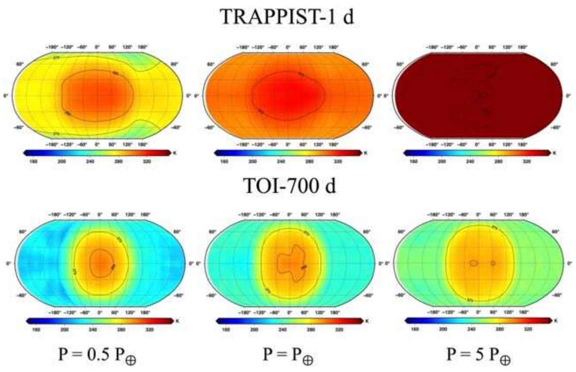

Fig. 1. Surface temperature and dependence on atmospheric pressure for two selected exoplanets: TRAPPIST-1 d (upper panels) and TOI-700 d (lower panels). Obliquities and eccentricities are set to zero, CO_2 fractions have all been fixed to 360 ppm, atmospheric chemistries are Earth-like, and atmospheric pressures are respectively 50%, 100% and 500% than on Earth (from left to right).

Fig. 2 illustrates the habitability of the ten exoplanets with highest ESI values in the Conservative Sample of Potentially Habitable Exoplanets as a function of their effective temperature, radius and rotation period. According to our definition, all such considered planets are habitable. Six out of them are hot, while the other four are quite cold. For the four hottest ones, h_{50} is significantly smaller than h_{100} – i.e., those planets may be subject to runaway greenhouse effect.

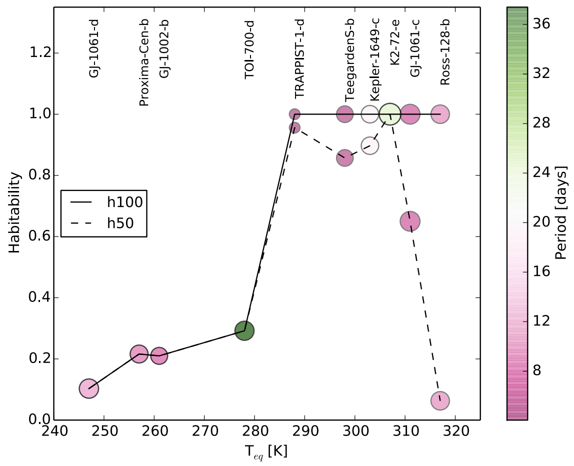

Fig. 2. Habitability of the ten exoplanets with highest ESI values as a function of their effective temperature (on the x axis), radius (rescaled as circle's size) and rotation period (indicated by colormap).

References: [1] Silva L., Vladilo G., Murante G. and Provenzale A. (2022), *MNRAS, 470,* 2270-2282. [2] Fraedrich K., Jansen H., Kirk E. et al. (2005), *Meteorol. Z., 14,* 299-304. [3] Lunkeit F., Borth H., Böttinger M. et al. (2011), *Planet simulator reference manual, version 16,* https://www.mi.uni-hamburg.de/en/arbeitsgruppen/theoretische-meteorologie/modelle/sources/psreferencemanual, Last Accessed 16 June 2022. [4] Maier-Reimer E., Mikolajewicz U. and Hasselmann K. (1993), *J. Phys. Oceanogr., 23,* 731-757. [5] Paradise A., Macdonald, E., Menou K. et al. (2022), *MNRAS, 511,* 3272-3303. [6] PHL @ UPL Arecibo (2023), https://phl.upr.edu/projects/habitable-exoplanets-catalog, Last Accessed 30 November 2023. [7] Simonetti P., Vladilo G., Silva L. et al. (2022), *ApJ, 925,* 105-122.

DYNAMICAL STABILITY OF HIGHLY INCLINED PLANETS IN BINARY STAR SYSTEMS.

F. Marzari[1] and K. Gozdziewski[2], [1] Dept. of Physics and Astronomy, University of Padova, Italy, (marzari@pd.infn.it) [2]ANicoulaus Kopernicus University, Torun (Poland), k.gozdziewski@umk.pl

Introduction: Exoplanets in circumprimary orbits in a binary star systems may have highly inclined orbits. Either the secondary star was born on an orbit tilted respect to the equator of the primary or dynamical mechanisms like planet-planet scattering or Kozai pumped up the inclination of putative planets. We intend to investigate the stability regions for highly inclined planets in close binary systems.

Numerical methods: We compute stability maps in semi-major axis and inclination by using MEGNO (the Mean Exponential Growth factor of Nearby Orbits [1], [2]) closely related to the maximum Lyapunov exponent. For strongly interacting systems, MEGNO converged to 2 indicates dynamical stability for the characteristic time scale of the interactions. We randomly choose the initial orbital elements of the planet(s) orbiting the primary star of the binary and integrate its orbit long enough to calculate MEGNO.

Results: Initially highly inclined orbits may lead to very high eccentricities during the anti-phased oscillations of these two orbital parameters according to the Kozai mechanism ([3], [4]). As a consequence, during the numerical integration performed to evaluate MEGNO we also compute the maximum eccentricity. If the pericenter becomes too small (smaller than the radius of the star or within a few star radii within which a strong tidal interaction is expected) we do not perform a stability analysis and we do not include that particular set of initial conditions in our stability map.

In Fig. 1 we show the stable orbits (MEGNO equal to 2) in a test system with two equal mass solar-like stars having an orbit with a_b = 50 au and e_b=0. The planet is a Jupiter-like planet with initial semi-major axis ranging from 0.05 to 35 au. The different colors give the value of the maximum eccentricity obtained during the Kozai cycle induced by the secondary star.

According to the stability map, highly inclined orbits need to be closer to the star to be stable and the critical semi-major axis reduces from about 25 au for low inclination orbits to about 15 au. Retrograde orbits appear more stable, as expected, and the critical semi-major axis extends out to about 30 au.

Mean motion resonances between the planet and the stars are clearly visible.

Future work: we are adding the effects of general relativity (GR) to the numerical integration. The forced pericenter precession induced by GR affects the Kozai cycles and it may fully inhibit them in particular for orbits where the pericenter comes very close to the star. We also plan to study multi.planet systems to test the effects of the planet mutual interactions on the long term stability.

References:

[1] Cincotta, P.~M. and Simo C. (2000), AAS 147, 205-228. [2] Gozdziewski et al (2001) A&A 378, 569-586- [3] Naoz S. (2016) ARAA 54, .441-489. [4] Lei H. (2022) AJ 163, id. 214, 15 pp.

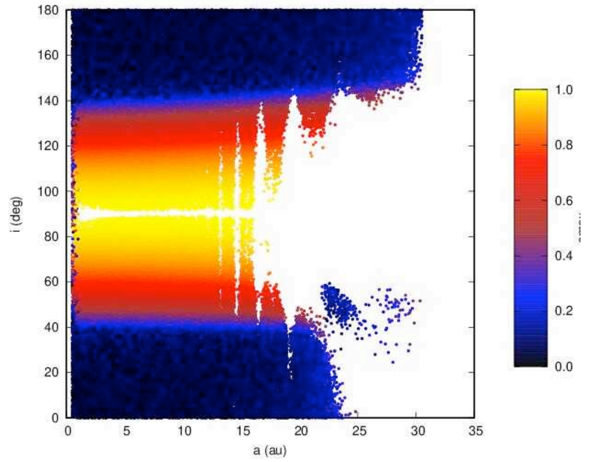

Fig. 1: stable orbits of exoplanets around the primary star. The color coding gives the maximum eccentricity reached due to the Kozai mechanism.

POTENTIAL CLIMATES ON Gl 514 b: A SUPER-EARTH EXOPLANET WITH HIGH ECCENTRICITY.

L. Biasiotti[1,2], P. M. Simonetti[2], G. Vladilo[2], S. L. Ivanovski[2], M. Damasso[3], S. Monai[2], A. Sozzetti[3], [1]University of Trieste (lorenzo.biasiotti@inaf.it), [2]INAF-OATs, [3]INAF-OATo.

Introduction: The recently discovered super-Earth planet Gl 514 b, orbiting the nearby (7.6 pc, [1]) M-dwarf, is an interesting case to explore the habitability of planets that radically differ from the Earth. Habitability studies often rely on the classic definition of the Habitable Zone (HZ), and in particular on the so-called Conservative Habitable Zone (CHZ, [2]). Due to the combination of its relatively large semi-major axis (a=0.42 AU) and eccentricity (e=0.45), Gl 514 b lies part of the time inside the CHZ (about 34% of the orbital period) and the rest of the time beyond the outer edge of the CHZ. This suggests the presence of strong seasonal variations that impact the actual habitability of the planet. Tracking the seasonal evolution of habitability is not possible using the HZ approach and requires the application of seasonal climate models tailored for specific stellar, orbital and planetary parameters.

Investigating the potential climates of planets that exhibit seasonal episodes of habitability is intriguing because it could provide insights into the dynamic nature of planetary systems and the potential for the support of life in exotic scenarios. In this sense, the study of the habitability of Gl 514 b can be generalized to all that cases in which there are strong instellation variations, thus helping to define a "Seasonal Habitable Zone".

The Model: In our study we use the climate model, EOS-ESTM [3,4] for exploring the habitability of Gl 514 b by calculating an index of surface habitability based on the surface temperature distribution. In practice, we explore the habitability as a function of climate factors currently unconstrained by the observations (e.g., Fig. 1), such as the ocean cover fraction, the obliquity, and the atmospheric composition. We consider three different types of atmospheres: (i) CO_2-dominated, (ii) CO_2 + 0.1% CH_4 and (iii) CO_2 + 1.0% CH_4.

Since transits of Gl 514 b have not been detected so far, we estimate the radius and the surface gravity from interior structure models (e.g. [5]) and from the measurements of the minimum mass (5.2 $M_\oplus$). The high eccentricity of Gl 514 b suggests that the system is dynamically young and that spin-orbit tidal synchronization may not have yet occurred (e.g. [6]). Assuming that the planet is not tidally locked, we test a set of climate models by adopting a rotation period of 1 day.

Results: In the present work, we show how the habitability of Gl 514b is impacted by different combinations of planetary, orbital and atmospheric parameters. The impact of the ocean cover fraction is significant due to the orbit of Gl 514 b. In fact, the large thermal capacity of even a 25-m shallow ocean provides sufficient thermal inertia to avoid freezing conditions near apoastron. Similarly, the obliquity plays a fundamental role in seasonal habitable events. The higher the obliquity of the planet, the greater the thermal excursion to the poles is. Nonetheless, we show that these effects are regulated by the total surface pressure and the content of methane in the atmosphere. We present preliminar results of the parameter space that allows conditions of continuous and transient habitability.

Further investigations will include the impact of the host star on the exoplanet environment, especially concerning the photochemical reactions in the atmosphere driven by the large UV flux of the parent star. Apart from the direct impact on habitability due to its ionizing effects, the radiation environment of Gl 514 b may be conductive to the presence of high-altitude organic hazes that directly affect the climate state of the planet.

Due to the proximity to Earth and the spectral class of the parent star, future observations of the emission and reflection spectra of Gl 514 b are expected to be possible with the E-ELT. These observations will allow us to test and constrain the models of planetary climate and habitability developed in our investigation.

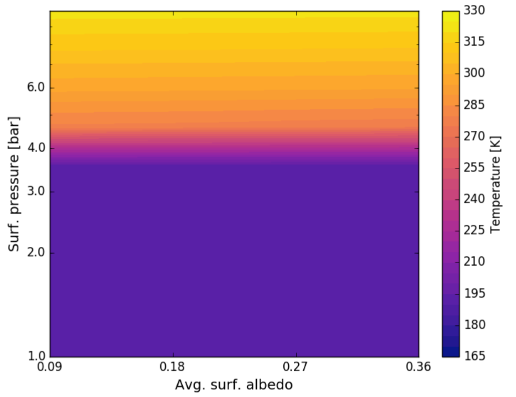

Figure 1. Variation of surface temperature as a function of surface albedo and surface pressure for an atmosphere composed of CO_2 and 1% CH_4.

References:

[1] Damasso M., et al., 2022, A&A, 666, A187.
[2] Kopparapu R. K., et al., 2013, ApJ, 765, 131.

[3] Simonetti P., Vladilo G., Silva L., Maris M., Ivanovski S. L., Biasiotti L., Malik M., von Hardenberg J., 2022, ApJ, 925, 105.
[4] Biasiotti L., et al., 2022, MNRAS, 514, 5105.
[5] Fortney J. J., Marley M. S., Barnes J. W., 2007, ApJ, 659, 1661.
[6] Barnes R., 2017, Celestial Mechanics and Dynamical Astronomy, 129, 509.

SEARCH FOR THERMAL EMISSION OF PROTOPLANETS WITH VLT/ERIS - INITIAL RESULTS

D. Fedele[1] , F. Maio[2,1], V. Roccatagliata[1], A. Garufi[1], A. Zurlo[3] and the ERIS GTO-Protoplanets team
[1]INAF - Osservatorio Astrofisico di Arcetri, L.go E. Fermi 5, 50125 Firenze, davide.fedele@inaf.it
[2]Università degli Studi di Pisa, Largo Bruno Pontecorvo 3, 56127 Pisa
[3]Núcleo de Astronomía, Facultad de Ingeniería y Ciencias, Universidad Diego Portales, Av. Ejercito 441, Santiago, Chile

In the last decade, the study of the planet formation process has grown enormously thanks to the outstanding capabilities of ALMA. Since the iconic image of the HL Tau system, ALMA has revealed sub-structures in the dust distribution of tens of protoplanetary disks, such as: inner dust cavities and rings (e.g., [1], [2], [3]), horseshoe-shaped rings (e.g., [4]), spirals (e.g., [5]). There is growing evidence that the observed dust sub-structures are due (in some cases) to the dynamical interaction between the disk and embedded protoplanets although a number of other processes can explain some of them such as magneto-rotational instability, condensation fronts, photoevaporation and stellar encounters (e.g., [6]).

The definitive confirmation of the existence of protoplanets comes from direct imaging at optical and infrared wavelengths, as shown in the PDS70 system, where two young protoplanets (PDS 70b and PDS 70c) have been detected inside the dust cavity [7]. The detection of PDS 70c in Hα using VLT/MUSE [8] and of dust continuum emission in correspondence with the two protoplanets [9] supports the hypothesis of on-going accretion from the circumstellar disk and of the presence of circumplanetary disks.

Beside PDS 70, a handful of protoplanets candidates have been detected in other disks via high contrast imaging observations but the nature of the point-like emission is often debated and requires further confirmation. Despite the growing evidence of planet-disk interaction, PDS 70 remains the only bona-fide direct detection of protoplanets so far, possibly because of local dust extinction, as large dust grains (observable with ALMA at mm wavelengths) are easily trapped in local pressure maxima while the micron-sized particles (that dominate the dust extinction in the optical and near-infrared) follow the gas kinematics and tend to diffuse inside the gap.

In May 2023 we started an observational campaign to search for thermal emission of protoplanets with ERIS, the new high contrast imager of the Very Large Telescope in Chile [10]. The great advantage of ERIS compared to previous high contrast instruments is the extension to longer wavelengths covering the L (3-4μm) and M (4-5μm) photometric bands. At these wavelengths, the contamination by local dust in the planet's surroundings is largely attenuated allowing us to observe deeper in the disk. Moreover, the planet-to-star flux contrast is more favorable in the thermal infrared (e.g., [11]). During the first night of observation in May 2023 we observed an initial sample of 7 protoplanetary disks with ERIS with the Apodized Phase Plate coronagraph (APP) using the NIX camera. The observations have been carried out with a narrow filter centered at the Brγ line at 3.95 μm. After a careful data reduction of the ERIS/NIX images we performed standard and new, ad-hoc, post-processing techniques (e.g., angular differential imaging, principal component analysis) to remove the residual of the stellar point spread function. During my talk I will briefly report the initial results of our survey, highlighting the main findings, and discussing the main challenges and future perspectives of our ongoing survey.

AS 209 stacking

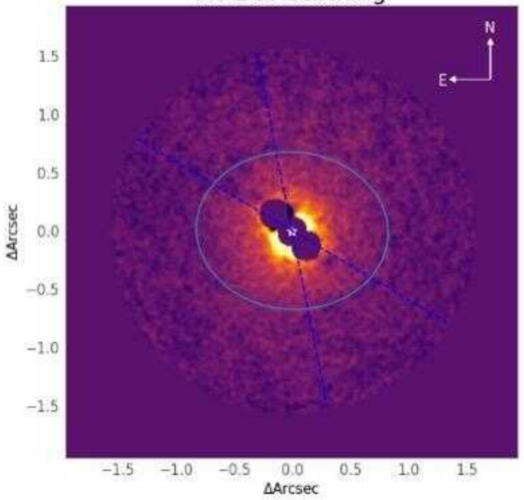

AS 209 cADI

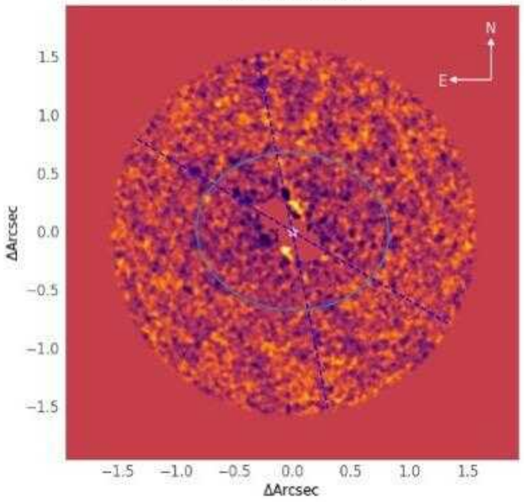

Figure 1: *ERIS/NIX-APP images of the disk AS 209 showing the disk (top) and a candidate protoplanet (bottom).*

References: [1] Fedele et al. 2017, A&A, 600, 72; [2] Fedele et al 2018, A&A, 610, 24; [3] Andrews et al 2018, ApJ, 869, 41; [4] Casassus et al 2013, Nature, 493, 191; [5] Benisty et al 2017, A&A, 597, 42; [6] Bae et al. 2022arXiv221013314B; [7] Keppler et al. 2018, A&a, 617, 44; [8] Haffert et al. 2019, Nat.As, 3, 749; [9] Isella et al. 2019, ApJ, 879, 25; [10] Davies et al. 2023 A&A, 674, 207; [11] Sanchis et al. 2020, MNRAS, 492, 3440;

REFRACTION IN TRANSITING HABITABLE EXOPLANETS.

M. Maris[1,2,3,*], L. Silva[1,2], E. Bisesi[1,4], G. Murante[1,2,3,4], P. M. Simonetti[1] . [1]INAF/Trieste Astronomical Observatory, Via G.B. Tiepolo 11, 34135 Trieste; [2]IFPU - Institute for Fundamental Physics of the Universe, Via Beirut 2, 34014 Trieste, Italy; [3]Fondazione ICSC - Centro Nazionale di Ricerca in HPC, Big Data and Quantum Computing, Casalecchio di Reno (BO), Italy; [4]CNR IGG – Institute of Geosciences and Georesources, Pisa, Italy; [*]michele,maris@inaf.it

Abstract:

The recent observation of WASP39b and K2-18b with the James Webb Space Telescope (JWST) [1, 2], the advancement of the Extremely Large Telescope (ELT) [3], and the approval of missions devoted to study exoplanets' atmospheres have opened the way to the search for biosignatures in the transit spectra of exoplanets in the habitable zone. One important effect affecting the spectroscopic study of the atmospheres of transiting rocky exoplanets is the refraction of transmitted light from the host star [4-12]. If the level of deflection induced by refraction is larger than the apparent angular diameter of the host star, as seen from transiting exoplanets, refraction could prevent the observation of a significant part of the exoplanet's troposphere weakening the signal of potential biosgniatures (see Fig.1). As in the case of transmission spectra, exoatmospheric refraction is a further index of the state of the exoatmosphere that can be linked to the surface temperature and pressure using climate models. As an example, refraction could modulate the time dependence of the transiting spectrum in a very specific way, disclosing the possibility to recover atmospheric scale heights and densities [4]. Here we analyze the predicted level of refraction for simulated atmospheres in the framework of the ARTECS archive of terrestrial-type climate simulations [13, 14]. The more than 20 thousand models in the archive are based on the the ESTM Energy Balance Model [15, 16]. Our target is to systematically explore the level of refraction in exoatmospheres of terrestrial planets in the habitable zones of their stars. One of the scopes is to determine the extent by which refraction could be considered a diagnostic to determine wether a planet on the outer border of the habitable zone is in a temperate or a snowball state.

References:

[1] A. D. Feinstein et al., Nature, 2023, in press; [2] Madhusudhan et al., 2023, arxiv/2309.05566; [3] R. Bowens et al., A&A, 2021, 653, A8; [4] O. Sidis and R. Sari, ApJ, 2010, 720, 904; [5] A. García Muñoz et al., ApJ, 2012, 755, 103; [6] Y. Bétrémieux and L. Kaltenegger, ApJL, 2013, 772, L31; [7] Y. Bétrémieux and L. Kaltenegger., ApJ, 2014, 791, 7; [8] Y. Bétrémieux and L. Kaltenegger, L., MNRAS, 2015, 451, 1268; [9] T. D. Robinson, ApJ, 2017, 836, 236; [10] Y. Bétrémieux and M. R. Swain, MNRAS, 2017, 467, 2834; [11] T. D. Robinson, J. J. Fortney and W. B. Hubbard, ApJ, 2017, 850, 128; [12] D. Alp and D. -O. Demory, A&A, 2018, 609, A90; [13] https://wwwuser.oats.inaf.it/exobio/climates; [14] G. Murante et al., MNRAS, 2020, 492, 2638; [15] G. Vladilo et al., ApJ, 2015, 804, 1; [16] L. Silva et al., IJAsB, 2017, 16, 3, 244

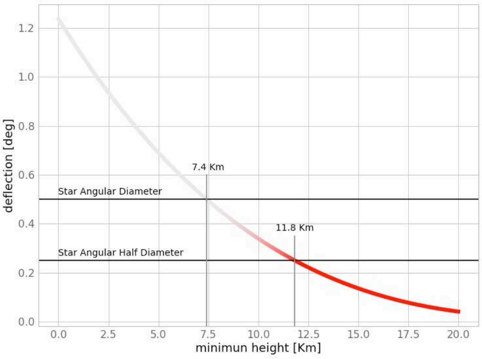

Fig.1 Deflection of the line of sight for an Earth analog as a function of its impact parameter. Altitudes below 7.4 km are not observable during the transit, while those above 11.8 km are observable throughout the entire transit. Intermediate altitudes are observable during a fraction of the transit.

THE IMPACT OF PLANETS AND FLYBYS ON THE EVOLUTION OF SOLAR SYSTEM ANALOGS, THE DEBRIS DISK SYSTEMS

V. Roccatagliata[1] and M. Kim[2]

[1]INAF - Osservatorio Astrofisico di Arcetri - veronica.roccatagliata@inaf.it
[2]Department of Physics, University of Warwick, UK - Minjae.K.Kim@warwick.ac.uk

Introduction: Debris disks represent the last phase of the evolution of protoplanetary disks. As a by-product of the planet formation process, debris disks might host planetesimal belts, dust, and gas. Dust detected in debris disks is thought to be removed by stellar radiation on a timescale that is shorter than their age, meaning that dust should be more likely continuously replenished during the ongoing collisions of bigger objects such as planetesimals. Thus, the presence of dust, planetesimals, and even planets in debris disks should be correlated. In particular, low-mass or substellar companions could have an impact on the planetesimal and dust grain dynamics due to their gravitational perturbation. For example, even earth-sized planets or close encounters would leave an imprint in the structure of a debris disk (e.g., Wyatt et al. 1999; Pearce et al. 2014). This implies that tracing planets or perturbers within debris disks, or characterizing the flybys events, can provide valuable constraints on the history of the evolution of these disks.

Planets in debris disks: After the first resolved image of the debris disk around beta Pictoris, various peculiar structures and features (e.g. Hughes 2018) have been found in the well-resolved disk systems across a wide range of wavelengths. For example, the sharp inner edges of many disks have been inferred to be indirect evidence of a planet. Furthermore, other asymmetric structures, such as eccentric disks (Picogna & Marzari 2014), clumps (Holland et al. 2017), spirals (Konishi et al. 2016), and non-axisymmetric structures (Kalas et al. 2015) in debris disks have also been interpreted as evidence for planet-sized substellar companions. The warp and puffy structures found in the debris disks around both, beta Pictoris (Roberge et al. 2012; Apai et al. 2015) and HD 106906 (Moore et al. 2023), may also be linked to a companion, such as a planet, with an inclined orbit in the system. The vertical structure of disks with scale heights of the order of a few percent have been interpreted to be resulting from stirring processes by embedded planetary bodies within or even near the disks as well (Daley et al. 2019).

Using N-body simulations (Ertel et al. 2012), SPH simulations (Picogna & Marzari 2014), and collisional evolution models of debris disk systems (Stuber et al. 2023), they demonstrated observable planet-disk configurations with large-scale signatures of the brightness distributions (e.g., spiral structures and/or two local azimuthal maxima) in both the face-on and the edge-on case. The imprint on the structure of debris disk is potentially detectable in the near-to mid-infrared wavelength range (e.g., H and K band; see Fig. 1; Picogna & Marzari 2014, Stuber et al. 2022).

Moreover, some exoplanets on extreme elliptical orbits and misaligned planets may indicate a violent dynamical past, where the planets and/or past flybys likely had unstable gravitational interactions with other planets or stars (e.g., Kennedy et al. 2013; Picogna & Marzari 2014). These types of interactions can eject planets from a system, while dramatically changing the orbits of the remaining planets.

Flybys in debris disks: To constrain the influence of encounters in the formation and evolution of debris disks, Bertini et al. (2023) reconstructed the flybys experienced by a statically significant sample of debris disks in the last 5 Myr and predicted for the next 2 Myr.

In this talk I will present the sample of 254 debris disks with ages between 2 Myr and 8 Gyr. The Gaia eDR3 position, proper motions and radial velocities have been used to reconstruct the relative linear motions between each debris disk and all possible perturbed in volume of the sky around it. We found that 90% of the analyzed systems have at least a close flyby, implying that the very high incidence of encounters (in particular, close encounters) experienced by the systems in the last 5 Myr. I will also discuss the debris disk systems with known planets, companions and/or flyby(s) (see Fig. 3). It is important to highlight that also our solar system itself experienced at least a close encounter (e.g. Mamajek et al. 2015, de la Fuente Marcos & de la Fuente Marcos 2018). This implies the fundamental impact of flybys in the evolution of debris disks. The confirmation of the statistical significance of flybys in debris disk systems can also be responsible for stirring of debris material.

I will finally present an ongoing work to resolve the spatial dust distribution and debris disk features which can be the physical imprint of an unseen substellar companion, or the interaction with possible perturbers during recent close flybys.

References:

[1] Apai et al. (2015) *ApJ, 800, 136A*

[2] Bertini L. Roccatagliata V. and Kim M. (2023) *A&A, 621,* 2.
[3] Daley et al. (2019) *ApJ, 875, 87*
[4] de la Fuente Marcos R. and de la Fuente Marcos C. (2018), *RNAAS, 2, 30*
[5] Holland et al. (2017), *MNRAS 470,3606H*
[6] Hughes et al. (2018) *ARA&A 56, 541H*
[7] Kalas et al. (2015) *ApJ, 814, 32K*
[8] Kennedy et al. (2013) *MNRAS, 436, 898K*
[9] Konishi et al. (2016) *ApJ, 818L, 23K*
[10] Mamajek E. E. et al. (2015) *ApJL, 800, L17*
[11] Moore et al. (2023) *ApJ, 943, 6M*
[12] Pearce et al. (2014) *MNRAS, 443, 2541P*
[13] Picogna, G. & Marzari, F. (2014), *A&A, 564, 28*
[14] Roberge et al. (2012) *PASP, 124, 799R*
[15] Wyatt et al. (1999) *ApJ, 527, 918W*

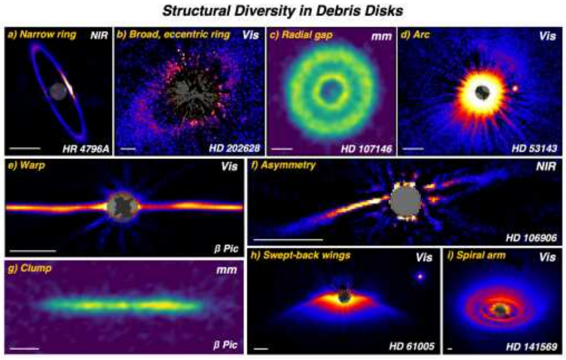

Figure 1: From *Hughes et al. (2018)*: Scattered light and millimeter thermal emission for eight systems illustrating the range of asymmetries observed in debris disks.

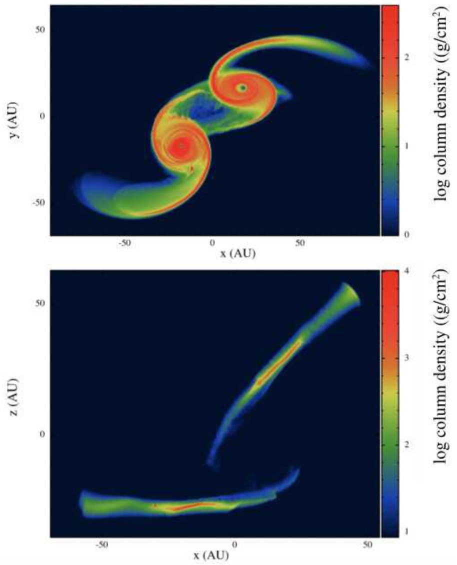

Figure 2: From *Picogna & Marzari (2014)*: SPH simulations of close encounters between equal-mass stars which led large spiral arms and warped disks.

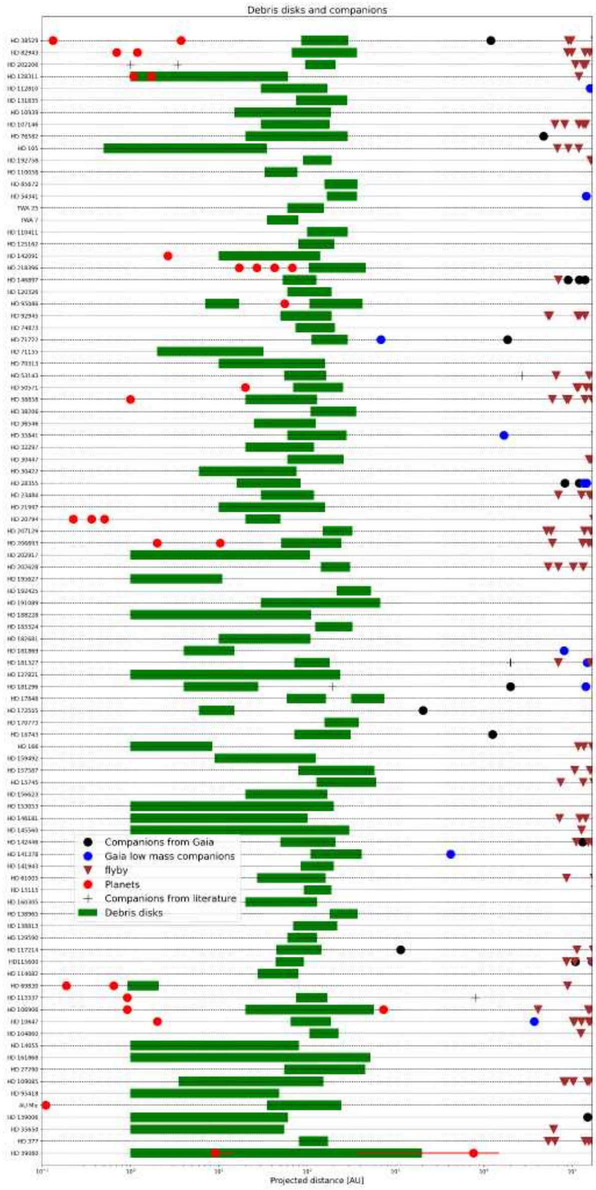

Figure 3: From *Bertini et al. (2023)*: Sizes of the resolved debris disk systems and the positions of planets, companions, and flybys from the central object. On the *x*-axis, the projected distance from the main star is given in AU. In the *y*-axis, all systems with resolved debris disks are listed. The panel overlaid in the figure explains the different symbols and colors.

COMMISSIONING AND FIRST SCIENTIFIC RESULTS OF LOCNES: A SPECIALIZED SMALL TELESCOPE DESIGNED FOR THE INVESTIGATION OF THE SUN-AS-A-STAR SPECTRA IN THE NEAR INFRARED.

L. Cabona[1], R. Claudi[2], A. Ghedina[3], S.J. Liu[4], M.Rainer[1], V. D'Orazi[2], E.Pace[5] and S. Stefani[4]. [1] INAF Osservatorio Astronomico di Brera, via Bianchi 46, 23807 Merate (LC), Italy lorenzo.cabona@inaf.it, [2] INAF Astronomical Observatory of Padova, vicolo Osservatorio, 5, Padova, Italy, [3] INAF – Fundacion Galileo Galilei, Rambla Jose Ana Fernandez Perez, 7, Brena Baja–TF, Spain, [4] INAF– IAPS, via del Fosso del Cavaliere, 100, Roma, Italy, and [5] Dep. of Physics and Astronomy, Università degli studi di Firenze, Firenze, Italy.

LOCNES, which stands for LOw-Cost NIR Extended Solar telescope, is a solar telescope installed at the TNG (Telescopio Nazionale Galileo). It feeds the Near-infrared spectrograph GIANO-B [1-2] with light from the Sun, through a 40-m patch of optical fiber. The design of LOCNES [3] is geared towards obtaining Sun as a star spectra with a high signal to noise ratio and precise wavelength calibration, achieved through the use of molecular-band cells. This novel approach opens up a new area of investigation that will provide timely results to improve the search for telluric planets. The NIR spectral region will sample different layers of the solar atmosphere down to the lowest accessible level at 1600 nm, where continuum opacity is at its minimum. Molecular features should correlate with sunspots passing across the solar disk, while the chromosphere would be monitored by the He I 1083 nm line. We will extract several disk integrated activity indicators and mean magnetic field measurements for the Sun in the NIR. Eventually, they will be correlated with both the RV of the Sun-as-a-star and the resolved images of the solar disc in visible and NIR. Such an approach will allow a better understanding of the origin of activity-induced RV variations and will help to improve the techniques for their correction, in order to minimise its impact on the detection and characterisation of exoplanets.

Within the LOCNES project, GIANO-B will be equipped with NIR absorbing cells in order to have an inertial inner reference for high precision RV measurements. The cells will be mounted on a revolver inside the preslit optics to be able to put the absorbing cell into the optical path towards the GIANO-B slit. In this way, the cell spectrum of methane, acetylenethe and ammonia gas mixture present into the absorbing cell [4-5], is over imposed to the stellar spectrum. By using these cells, the value of the Radial Velocity of the star is evaluated by fit of the composite spectrum by a synthetic reconstruction of it using the cell spectrum, the instrumental profile of GIANO-B and a high signal to noise spectrum of the star alone. The absorbing cell technique is described in Butler et al. (1996) [4].

Based on the VLT/CRIRES+ infra-red gas-absorption cell with short path length, an improved design has been developed specifically for the GIANO-B instrumental parameters. The tailored design for GIANO-B with optimized performance comes in two flavours: an H-band design that covers the 1.4-1.7 um range, and a K-band design for the 1.9-2.4 um. To minimize systematic errors the gas cell should be filled with gases at the lowest possible pressure, because the lines are intrinsically narrower and because the pressure-induced line-shift becomes much less important at lower pressures. This implies that, for a given mixture of gases, a long cell filled at low pressure should be always preferred to a shorter cell filled at higher pressures. For this reason we use the maximum space/length available within the volume of the GIANO-B pre-slit.

In this talk, I will outline the scientific drivers for the LOCNES project and its first commissioning and scientific results.

[1] Claudi, R., et al., "GIARPS@TNG: GIANO-B and HARPS-N together for a wider wavelength range spectroscopy", European Physical Journal Plus 132, 364 (Aug. 2017).
[2] Claudi, R., et al., "GIARPS: commissioning and first scientific results", in SPIE Conference Series 10702, 107020Z (July 2018).
[3] Claudi, R., et al., "LOCNES: A solar telescope to study the stellar activity in the near infrared", in SPIE Conference Series 11445, 114452S (Dec. 2020).
[4] Butler, R. P., et al., "Attaining Doppler Precision of 3 M s-1", Pub. Astron. Soc. Pacific 108, 500 (June 1996).
[5] Seemann, U., et al. "Wavelength calibration from 1-5 m for the CRIRES+ high-resolution spectrograph at the VLT" in SPIE Conference Series 9147, 91475G (Aug. 2014).

MARS AS A TERRESTRIAL EXOPLANET: INSIGHT FROM ATMOSPHERIC CO_2 MEASUREMENTS

E. Balbi[1] (evandro.balbi@edu.unige.it), P. Cianfarra[1], F. Borsa[2], A. Harutyunyan[3], S. Tosi[2, 4], and M. Rainer[2] [1] University of Genoa, Department of Earth, Environment and Life Sciences, Corso Europa, 26, 16132 Genova, Italy [2] INAF - Osservatorio Astronomico di Brera, Via E. Bianchi, 46, 23807 Merate (LC), Italy [3] INAF - Fundación Galileo Galilei, Rambla José Ana Fernandez Pérez 7, 38712 Breña Baja (TF), Spain [4] University of Genoa, Department of Physics, Via Dodecaneso 33, 16146, Genova, Italy

Introduction: The ever-improving knowledge in planetary sciences acquired in the last decades allowed considering our Solar System as a proxy to better frame the setting of other planetary systems. In particular, among the numerous major bodies that orbit the Sun, Mars represents a good analogue of terrestrial exoplanets and an optimal natural lab to explore their global-scale geologic properties. The surface of Mars is characterised by evidence of multiple global-scale geological processes. Numerous regional-scale fracture zones (e.g., Claritas Fossae, Noctis Labyrinthus, Cerberus Fossae) exist and affect the entire Martian crust. These crustal-scale fracture zones represent preferential pathways for fluid migration connecting the planetary interiors with its atmosphere. Recent missions and studies highlighted young/present-day, tectonic, volcanic, and even seismic activity associated to these regions (e.g., Hauber et al., 2011; Sita & van der Lee, 2022; Fernando et al., 2023; Pieterek et al., 2024). In this way, signatures of planetary geodynamic evolution might be hosted in the Martian atmosphere.

The aim of the present study is to detect possible temporal and spatial variations of the Martian CO2 atmospheric signal. We identified the CO_2 as a crucial molecule due to i) its high concentration in the Martian atmosphere, and ii) its possible linkage, such as on Earth, with multiple geologic processes (e.g., volcanic activity). We investigated Mars as if it was an exoplanet by applying astrophysical observational techniques and analytical strategies usually used for exoplanetary studies. To compare Mars with terrestrial exoplanets a methodological "downscaling" of the data has been necessary. In this way, the identified signatures will be sought in the atmospheric spectra of terrestrial exoplanets to look for geologic activity. This will be of particular interest on terrestrial exoplanets when the first data collected by the new generation telescopes (e.g., ANDES) will be available.

Methodology and data analysis:

We observed Mars in stare mode using the high-resolution near-infrared slit spectrograph GIANO-B (Claudi et al. 2018) at the Telescopio Nazionale Galileo (TNG). We planned six observations before, around and after the equinox and during a period close to the Martian opposition phase. Each visit consisted of six pointings spatially distributed at different latitudes of the northern and southern hemisphere (Figure 1). Each pointing was composed of five 10 seconds exposures that we then summed up to increase the signal-to-noise ratio. Only three visits were completed due to adverse weather conditions during autumn and winter 2022. The three conducted observations covered homogeneously the time interval before and near the equinox whereas they did not allowed monitoring any eventual seasonal CO_2 variation after the equinox.

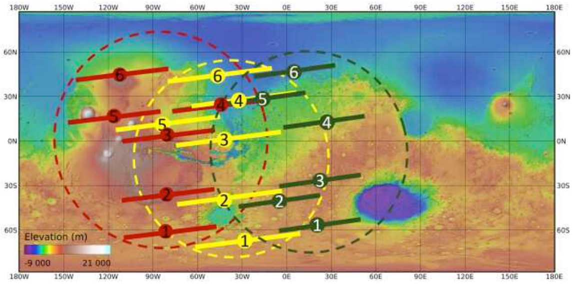

Figure 1. Positions of the slit during each pointing. Dashed circles indicate the observed portion of the Martian surface during the three conducted observations (yellow: 2022-10-09; green: 2022-11-17; red: 2022-12-16).

The obtained raw data were firstly processed through the online data reduction software (DRS) (Harutyunyan et al., 2018) at the telescope, and later re-reduced offline with the software Gofio (Rainer et al., 2018) to improve the wavelength calibration. Then, contamination of the telluric bands of CO_2 (i.e., signal related to the CO_2 content in Earth's atmosphere) was removed from the obtained spectra with a dedicated software (ESO software *molecfit2* - Smette et al., 2015; Kausch et al., 2015) (Figure 2).

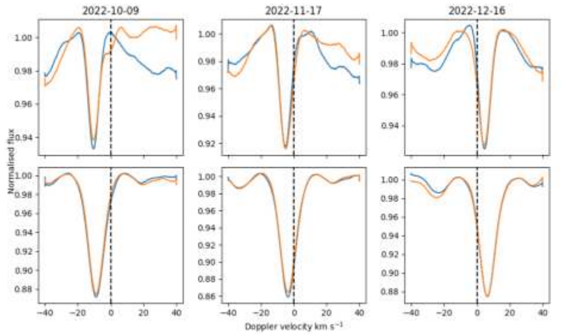

Figure 2. Upper part: Comparison between CO_2 profiles before (orange) and after (blue) the telluric removal. Dashed lines indicate 0 km s^{-1}, thus where the telluric signal is expected. Lower part: profiles of the reflected spectrum of the Sun. The absence of the telluric molecules in the solar spectrum makes the telluric contamination faint.

Cleaned spectra obtained for the six pointings performed in each observation were compared with each other to highlight spatial variations in the CO_2 signal. In particular, we computed and compared the Equivalent Width (EW) of each normalized profile. To avoid dependencies between results and computational method, we used two approaches to calculate the EW: i) fitting the CO_2 signal with a Gaussian curve and thus computing the EW as the area of the curve, and ii) considering the EW as the zero moment of the line profiles. Moreover, to exclude instrumental effects the EWs of the solar profiles were computed as well.

Preliminary Results and future development:

Due to the inclination of Mars respectively to Earth, the majority of the measurements fell within the Highlands (Figure 1). However, a few pointing captured the transition highlands-lowlands between Arabia Terra, Acidalia Planitia and the easternmost part of Tharsis. Both methods applied to calculate the EW allowed identifying spatial variation of the atmospheric Martian CO_2. Results of the two methods are concordant excluding methodological or instrumental errors. In particular, the preliminary analysis of the data showed that the highest EW values are referred to the measurements performed in correspondence of the transition highland-lowlands. In addition, latitudinal variations of the concentration of CO_2 were also detected over Tharsis and surrounding areas from north to south. This is of particular interest since Tharsis includes a huge variety of regional- and global-scale tectonic and volcanic features. Further studies are necessary to better frame the role of the causes (endogenic vs exogenic) responsible for the measured spatial variation of atmospheric CO_2.

References:

[1] Hauber E. et al. (2011) *JGR, 38.10.* [2] Sita M. and van der Lee S. (2022) *JGR*, *127.10.* [3] Fernando B. et al. (2023) *JCR, 4(9), 175* [4] Pieterek B. et al. (2024) *Icarus, 407, 115770* [5] Claudi R. et al. (2018) *SPIE Conf., 10702Z* [6] Harutyunyan, A., et al. (2018) SPIE Conf. 1070642 [7] Rainer, M., et al. (2018) SPIE Conf. 1070266 [8] Smette, A., et al. (2015) A&A, 576, A77 [9] Kausch, W., et al. (2015) A&A, 576, A78.

Acknowledgements:

Based on observations obtained at the Italian Telescopio Nazionale Galileo (TNG) through observing program A46TAC_22. The TNG is operated by the Fundación Galileo Galilei of the Italian Istituto Nazionale di Astrofisica (INAF).

TEKTITES/MICROTEKTITES FE OXIDATION STATE AND WATER CONTENT G. Giuli[1], [1]School of Science and Technology-Geology division, University of Camerino, Via Gentile III da Varano, 62032, Camerino (MC), I;

Introduction: Fe redox and water content of impact melt are important parameters as they can greatly affect melt density and viscosity which, in turn, affect the melt evolution and fate. In this contribution I briefly describe recent research on X-ray absorption spectroscopy (XAS) determination of Fe oxidation state and micro Fourier transform infrared spectroscopy (FTIR) determination of water content of tektites and impact glasses putting them in the context of previous research done with different techniques. In comparison with other techniques requiring large amount of samples (e.g. potassium dichromate titration, Mossbauer spectroscopy, Karl Fischer titration), XAFS and micro FTIR techniques allow to study both macroscopic samples of tek- tites as well as smaller microtektites giving the same error, making it possible to compare results between tektites and micro-tektites and, consequently, also to find differences between tektites and microtektites or between microtektites from different strewn fields.

Tektites and microtektites have been the subject of many geochemical studies in the past because of the glimpse they could provide on the formation conditions of impact melt. Despite they offer only a partial and limited view of the complexity of the processes operating during impact cratering and impact melt formation, still they represent the melt formed at the very initial stages of shock-metamorphism during impact and thus offer a precious window on the contact stage of impact cratering. Low $Fe^{3+}/(Fe^{2+}+ Fe^{3+})$ ratio and low water content are now commonly accepted to be characteristic of tektites and most microtektites [1-4]. These feature, together with isotopic signatures, can be fruitfully used to distinguish tektites/micro- tektites from terrestrial volcanic glasses.

Despite it could be tempting to use determined $Fe^{3+}/(Fe^{2+}+Fe^{3+})$ ratio and water content to constrain temperature and redox conditions during the first stages of impact melting, it must be kept in mind that, at least for microtek- tites, their iron oxidation state can be substantially modified during transport. This raises the question if microtektites should be considered the microscopic analog of tektites or if some differences may exist in their formation and/or trans- port mechanism.

Moreover, the fact that North American microtektite show an increase of the Fe oxidation state (within 3200 km distance from the source crater) whereas Australasian microtektites do not (within ca. 11,000 km distance from the putative crater location) suggest marked differences in the transport of these microtektites. The Fe redox state of a melt depends on oxygen fugacity, temperature, pressure, and melt composition. Moreover, also kinetics of Fe oxida- tion and its relation to temperature and composition of the melt (especially water content) must be taken into account. The relatively high range of Fe redox states found in NA microtektites, being not related to melt chemistry, could be possibly related to mechanisms acting during transport (e.g., in a more oxidizing medium than in the case of Australasian and Ivory Coast microtektites).

The medium in which tektites and/or microtektites travel can be an overlooked aspect of impact models. However it is the author opinion that a knowledge of the transport conditions of tektites and microtektites would greatly help in better deciphering their formation conditions. In this context, a larger dataset on Fe redox ratio and water content of microtektites, as well as new experimental constrains on Fe redox ratio and water solubility of silicate melts at extreme conditions, and on the kinetics of their variations, could help also to further improve physical models on melt formation and transport during impact cratering events.

References: [1] Fudali RF, Dyar MD, Griscom DL, Schreiber D (1987) Geochim Cosmochim Acta 51:2749–2756 ; [2]Giuli G, Pratesi G, Paris E, Cipriani C (2002) Geochim Cosmochim Acta 66:4347–4353; [3] Giuli G, Eeckhout SG, Cicconi MR, Koeberl C, Pratesi G, Paris E (2010a) In: Reimold WU, Gibson R (eds) Large meteorite impacts and planetary evolution IV. Geological Society of America Special Paper 465, Boulder, CO, USA, pp 645–652; [4]Giuli G, Pratesi G, Eeckhout SG, Koeberl C, Paris E (2010b) In: Reimold WU, Gibson R (eds) Large meteorite impacts and planetary evolution IV. Geological Society of America Special Paper 465, Boulder, CO, USA, pp 653–662; [5] Beran A, Koeberl C (1997) Meteorit Planet Sci 32:211–216;[6] Koeberl C, Beran A (1988) In: 18th Lunar and Planet. Sci. Conf., LPI-Cambridge University Press, 403–408;[7] Rochette P., Bezaeva N., Kosterov A., Gattacceca J., Masaitis V., Badyukov D.D., Giuli G., Lepore G.O. Beck P. (2019)Geosciences, 9, 225.

TARGET–PROJECTILE INTERACTION IN LARGE-SCALE IMPACTS ON EARTH: CLUES FORM THE AUSTRALASIAN MICROTEKTITES.

L. Folco[1,2], M. Masotta[1,2], (luigi.folco@unipi.it); [2]Dipartimento di Scienze ella Terra, Università di Pisa, Via Santa Maria, 53, 56126, Pisa, Italy; [2]CISUP, Università di Pisa, Lungarno Pacinotti 43/44, 56126 Pisa, Italy

Introduction: Microtektities (microscopic siliceous impact glass spherules) are high–velocity impact ejecta, distributed in strewn field extending for thousands of kilometres, that are generated by the melting and vaporization of the topmost layers of the Earth's continental crust during large-scale impacts of asteroidal/cometary bodies on Earth [1, 2, 3]. They are a natural laboratory for investigating the chemical-physical interactions between target and projectile. These are of crucial importance for understanding many aspects of the microtektite formation mechanism and - more in general - of the impact melting process [e.g, 4, 5].

Samples and Methods: Using a large geochemical database of Australasian microtektites (**Fig. 1**) available from the literature (n = 211; [6]), we have invetstigated the geochemical signature left by the chondritic impactor and its dependence on their geographic distribution. This signature has been recently identified in the high Ni contents (>100 µg/g Ni and up to 678 µg/g), i.e., well above upper crustal values (20 µg/g Ni; [7]) and corresponding to a chondritic impactor contamination up to ~5% by mass, in tens of Australasian microtektites [6].

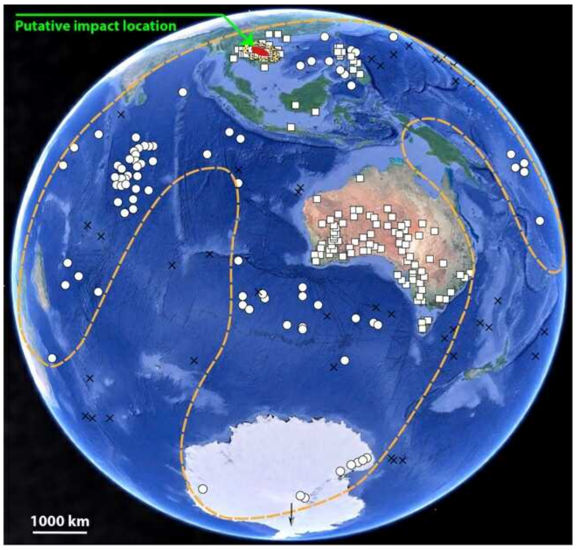

Fig. 1. The Australasian tektite/microtektite strewn field (modified after [6]). The find locations of tektites and microtektites are marked by squares and circles, respectively.

Results: The data set shows that impactor contamination decreases systematically with increasing distance from the putative impact location in Indochina (**Fig. 2**). Microtektites found within 3,000 km from putative impact location show Ni contents averaging 137±140 µg/g (range: 12 – 678 µg/g); those found at distances >3,000 km and <10,000 km in the Indian and Pacific Oceans have Ni contents averaging 34±23 µg/g (range: 7 – 92 µg/g); those found at distances >10,000 km in Antarctica have Ni contents averaging 5±3 µg/g (range: 1 – 17 µg/g, with the excpetion of one specimen with an anomalously high value of 56.8 µg/g reported by [8]). The Ni contents in microtektites found at distances in excess of 10,000 km are comparable to Earth's upper crust values. This indicates no impactor contamination, at difference to microtektites found closer to the putative impact location.

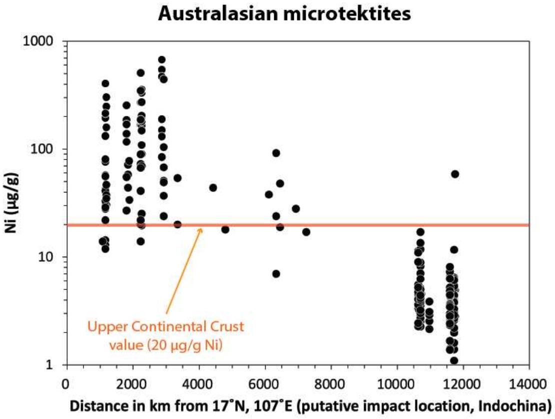

Fig. 2. Nickel concentrations (µg/g) versus distance (km) from the putative impact location in Australasian microtektites. Geochemical data set from [6]. Putative impavt location is from [10]. Ni concentration for Earth's upper continental crust is from [7]

Discussion: Qualitatively speaking, the longer the ejection distance, the highest the ejection velocity, the highest the stratigraphic level of the source material in the target. This implies that the parent liquids of the distant Australasian microtektites from Antarctica, devoid of impactor contamination and sourceed from the topmost layer of the target, formed first, with negligible physical-chemical interaction with the (chondritic) projectile. In turn, the parent liquids of the "proximal" microtektites from the seas surrounding Indochina and bearing a detectable impactor contamination formed (immediately) later, from the underlying stratigraphic layers, through significant mixing between target and projectile materials.

Conclusion: The lack of impactor contamination in early formed microtektite liquids is a relavent contraint for modelling microtektite formation in large scale impacts on Earth, requiring heating and melting prior to touch down of the impactor. Sufficient heat, in excess of the microtektite liquidus of about 1500 K could be provided by superheated compressed air (bow shock) and/or thermal radiation [9] at/from the front of the incoming fireball. This qualitative scenario appears in contrast to the most common view of microtektite heating and melting being caused by compression and adiabatic unloading during touch down.

References: [1] Artemieva, N. et al. (2002) Bull. Czech Geol. Surv. 77, 303–311. [2] Glass, B.P. and Simonson, B.M., (2013) *Distal impact ejecta layers. A record of large impacts in sedimentary deposits.* Springer, Heidelberg, New York, Dordrecht, London. Kitazato, K. et al. (2019) Science; [3] Rochette, P. et al. (2018) *Geology*, 46, 803–806. [4] Goderis, S. et al. (2017) *Geochim. Cosmochim. Acta*, 217, 28–50. [5] Hamann, C. et al. (2018) *Meteorit. Planet. Sci.* 53, 1594–1632.3. [6] Folco, L. et al. (2023) *Geochim. Cosmochim. Acta*, 360 (2023) 231–240. [7] Taylor, S.R. and McLennan, S.M. (1995) *Rev. Geophys.*, 32, 241–265. [8] van Ginneken, M. et al. (2018) *Geochim. Cosmochim. Acta* 228, 81–94. [9] Svetsov, V. et al. (2020) *Meteorit. Planet. Sci.* 55, 895–910. [10] Ma, p. et al. (2004) *Geochim. Cosmochim. Acta* 68, 3883–3896.

Acknowledgments: Transantartcic Mountains microtektite research at the University of Pisa is supported by the MUR-PNRA.

δ^{13}C VALUES OF THE LARGEST EXTRATERRESTRIAL MICRODIAMOND FOUND IN UREILITE NWA 6871 — IMPLICATIONS ON ITS ORIGIN.

O. Christ[1], A. Barbaro[2], G. Bragaggia[3], S. Gross[3], E. Thomassot[3,4], M.C. Domeneghetti[1], F. E. Brenker[2], and F. Nestola[5].
[1]Department of Earth and Environmental Sciences, University of Pavia, Pavia I-27100, [2]Geoscience Institute, Goethe-University Frankfurt, Altenhöferallee 1, 60438 Frankfurt, Germany, [3]Department of Chemical Sciences, University of Padova, Via Francesco Marzolo 1, 35131 Padova, Italy, [4]University of Lorraine, CNRS, CRPG, 15 Rue Notre Dame des Pauvres, 54500 Vandoeuvre-lès-Nancy, France, [5]Department of Geosciences, University of Padova, Via Gradenigo 6, 35131 Padova, Italy

Introduction: Ureilites are ultramafic achondrites consisting mainly of olivine and low-Ca pyroxene that are known for their significantly high carbon content in comparison to other achondrites [1]. All ureilites are assumed to originate from the same ureilite parent body (UPB) which has been destroyed by impact events [2]. Ureilitic carbon occurs mainly as graphite and diamond. Regarding the formation of diamond in ureilites the meteoritic community has not reached a point of consensus yet. Three major formation hypotheses have been proposed: (i) the formation deep inside the UPB [3], (ii) the direct transformation of graphite to diamond during a shock event [4], (iii) CVD processes [5]. Recently, the shock event(s) that destroyed the UPB was proposed to be the most likely scenario to form ureilitic diamond [6-10].

Although ureilitic diamonds have been studied in detail, their carbon isotopic composition has rarely been reported [12-18]. Most of these isotopic studies however, never analyzed solely diamond [12-15], only three publications report δ^{13}C values of “pure” diamond [16-18], of which one is a conference abstract [10], one is from 1970 without any sample characterization [16]. Only Miyahara et al. (2015) characterized the sample and reports δ^{13}C of ureilitic diamond [18]. Other studies focused solely on ureilitic graphite [19]. This shows the necessity for a new approach. Here we report a new method that involves the cleaning of ureilitic diamond of any accompanying graphite to produce clean δ^{13}C values of pure ureilitic diamond.

Sample: NWA 6871 is a highly shocked ureilite which was found in 2011 in Morrocco. The Meteoritical Bulletin describes it as “almost impossible cut”; a detailed petrological description including a description of carbon-bearing aggregates can be found in [11].

Methods: After localization by SEM, carbon-bearing aggregates (CBAs) have been extracted from the host meteorite and subsequently analyzed by SCXRD and micro-Raman spectroscopy (MRS). Identified larger CBAs were cleaned of graphite using a hydrothermal method usually used for gem diamonds. The removal of graphite was confirmed by repeated SCXRD and MRS measurements. Eventually, LG-SIMS was performed to collect δ^{13}C values of our diamonds.

Results: SCXRD revealed the presence of a single crystal diamond with a maximum length of 450 µm (Figure 1). In the diffractogram, the diamond shows stacking faults (lonsdaleite) [20], indicating a shock origin. Repeated SCXRD and MRS measurements confirmed the success of the cleaning process due to the absence of any graphite diffraction peaks or Raman bands. Carbon isotopic measurements yield a mean δ^{13}C value of -2.88 ± 0.42‰ ($n = 4$).

Figure 1: 450 µm sized microdiamond from NWA 6871. Microphotography by M. Chinellato.

Discussion: Compared to microdiamonds from the literature, the 450 µm sized microdiamond from NWA 6871 represents the largest extraterrestrial diamond found so far. In addition, it is the first time that a fully characterized ureilitic diamond has been analyzed regarding its carbon isotopic signature. Our data are similar to the few reported δ^{13}C values of ureilitic diamonds [16-18]. Comparing it to literature data of graphite [19], our data plots right between δ^{13}C values of graphite from coarse and fine-grained ureilites, whereof the latter have been interpreted as shock processed. Hence, upon shock graphite lost part of its lighter carbon isotopes and the remaining carbon atoms took part in the diamond formation.

Conclusions: Combining crystallographic and geochemical analyses, shows that ureilitic microdiamond was formed by shock. Hence, there is no necessity for a very large UPB to produce large diamonds. However, a comparison to graphite from the same ureilite must be made.

References: [1] Goodrich, C. A. (1992) *Meteoritics, 27.* [2] Rai, N. et al. (2020) *Geochem. Perspect.*

Lett., 14. [3] Urey. (1956) *ApJ, 124*. [4] Lipschutz, M. E. (1964) *Science, 143*. [5] Fukunaga, K. et al. (1987) *Nature, 328*. [6] Nestola, F. et al. (2020) *PNAS*, 117. [7] Barbaro, A. et al. (2020) *Minerals*, 10. [8] Barbaro, A. et al. (2021) *GCA*, 309. [9] Barbaro, A. et al. (2022) *Am. Min.*, 107. [10] Barbaro, A. et al. (2023) *EPSL*, 614. [11] Christ, O. et al. (2022) *Meteoritics & Planet. Sci., 57*. [12] Barrat, J.-A. et al. (2017) *EPSL, 478*. [13] Downes, H. et al. (2015) *Meteoritics & Planet. Sci., 50*. [14] Grady, M. et al. (1985) *GCA, 49*. [15] Hudon, P. et al. (2004) *LPSC XXXV,* Abstract #2075. [16] Russel, S. et al. (1993) *LPSC XXIV,* Abstract #2075. [17] Vdovykin, G. (1970) Space Sci. Rev., 10. [18] Miyahara, M. et al. (2015) *GCA, 163*. [19] Storz, J. et al. (2021) *GCA, 307*. [20] Németh, P. et al. (2014) *Nat. Commun,* 5.

A NEW PIEZOELETRIC CRYSTAL MICROBALANCE DEVICE AS A DUST ELECTROSTATIC COLLECTOR (DEC) IN THE MOON ENVIRONMENT.

Enrico Nardi[1,3], E. Palomba[1,2] , F. Dirri[1] , A. Longobardo[1,2], G. Massa[1,3], C. Gisellu[1,3], E. Zampetti[4].
[1]INAF-IAPS Rome, Italy, Via Fosso del Cavaliere, 100 Rome, (enrico.nardi@inaf.it); [2]ASI Space Science Data Center, Italy; [3]Sapienza University of Rome, Italy; [4]CNR-IIA, Via Salaria km. 29.300, 00016, Montelibretti, Rome, Italy.

Introduction and state of the art

In the context of the NASA-led Artemis program and the ESA lunar program, in recent years the world's space agencies and several private companies are planning to return to the Moon, thus allocating significant resources in the development of a lunar space program with the purpose of building a human outpost.

The Moon is a privileged location for space observations and investigation of fundamental questions related to the origin and evolution of our Solar System. Nevertheless, its environment can compromise instrument performance (e.g., dust, radiation bombardment from plasma and solar wind) and can also cause important problems for a potential human crew (i.e., vision obstruction, damage to spacesuits, obstruction of the respiratory tract). Knowledge of the lunar environment (in terms of physical properties, granulometry, electric charge) is thus of paramount importance in order to mitigate threats to both humans and instrumentation.

One of the main goals of the Artemis program is the measurement of the OH/H2O and organic-rich materials content on the lunar surface. Direct measurements of water abundance in a defined Moon region (e.g., Lunar South Pole) can help to understand:

- the mechanisms of water production and transport
- the impact history of the Moon and the role of small bodies (containing water, mineral hydrates and organic matter) in the inner early Solar System.
- lunar habitability, in view of in-situ long-duration human missions.

Since the Apollo Project, humanshave been exploring the lunar environment and its dust.
In 1972 the Lunar Ejecta and Meteorites (LEAM) Experiment [1] was deployed by the Apollo 17 astronauts on December 11, in order to characterize the lunar dust environment. Detecting the mass and velocity of lunar particles which entered the probe, the LEAM instrument demonstrated the presence of lunar dust slow-moving, highly charged particles.

In 2013, another NASA's spacecraft, Lunar Atmosphere and Dust Environment Explorer (LADEE), launched Lunar Dust experiment (LDEX) [2], which used collision ionization method to detect dust particles in the outer atmosphere of the Moon.

LDEX observed a permanently present dust cloud consisting primarily of ejecta produced from continual meteoroid bombardment of the lunar surface [3]. This data set provides the first dedicated measurement of the lunar dust environment for altitudes of ~3–250 km: since LDEX has not measured charged particles in this altitude range, it is assumed that they reach heights of less than 3 km [4].

In the same year, China's Chang' E-3 (CE-3) used a Solar Cell Probe (SCP) and a Sticky Quartz Crystal Microbalance (SQCM) to detect dust accumulation in landing site [5,6,7] and then in 2020 the China's Chang' E-5 (CE-5) lunar mission took place with the main task of collecting lunar samples using two probes (the reference probe and the measuring probe) obtaining information of paramount importance to try to better understand the levitation mechanisms and motion characteristics of lunar dust [8]. The SQCM data have not yet been published.

Physical processes on Moon surface

The Moon surface is exposed to solar radiation (which includes visible, ultraviolet and X radiation) as well as to solar wind, charged particles, galactic cosmic rays and high-speed micrometeorites. This can lead to different processes of dust charging:

- electron/ion collisions, that can produce negatively (low-energy collisions) or positively (high-energy collisions) charged grains;
- photoelectric emissions;
- contact charging with electron transfer.

The interaction of the lunar surface with UV radiation and plasma results in the emission and reabsorption of photoelectrons and/or secondary electrons at the walls of microcavities formed between neighboring dust particles below the surface, resulting in unexpectedly large negative charges and strong particle repulsions (Coulomb Force) sufficient to mobilize and lift off dust particles (**Figure 1**).

The electrostatic lofting that is supposed to occur on the lunar surface is expected to be the same phenomenon that occur on other bodies of the solar system, and in particular the reason of the absence of finer dust particles on atmosphereless small bodies; thus, the lunar surface is an excellent laboratory for studying the processes that may govern the evolution of airless planetary surfaces throughout the Solar System

The dynamics of charged dust in response to different electrical environments of airless bodies has been studied theoretically and with computer simulations, resulting in models of the phenomena, such as the "Patched Charge Model" [9], model that has been validated in laboratory [10,11].

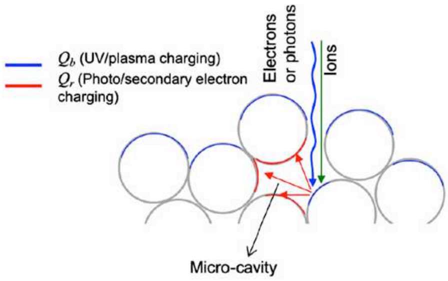

Figure 1. Patched Charge Model scheme

PCM instrument goals

In this framework, a new concept of PCM (Piezoeletric Crystal Microbalance) device aims at collecting and characterizing lunar particles by means of a capacitor able to attract them on crystals electrode for further analysis.

This instrument, called DEC (Dust Electrostatic Collector), is developed in the framework of EMM (Exploration of Moon and Mars) project, supported by the PNRR program, at Space Materials Laboratory (SMA-Lab) at INAF-IAPS whose basic concept will be demonstrated by reproducing the dust lofting on Moon surface in a dedicated facility.

The main goals of DEC instrument on the Moon are:

- to attract charge particles of dimensions ≤10 µm
- to assess the criticality of lunar levitating dust by measuring the electrical properties of the dust (i.e. charge-to-mass ratio).
- to improve the theoretical models predictions through comparison with the phenomenon reproduction in laboratory.

Secondary goals of DEC are mainly related to:

- Lunar dust physical properties
- Lunar dust granulometry
- Study and characterization of the charging and levitation processes.

The instrument core is a PCM (Piezoelectric Crystal Microbalance) which oscillates at a resonant frequency depending on the mass deposited on its sensible area [12].
The deposition process of these charged particles on the instrument would be favored by a particular type of design exploiting the effect of electric fields to attract the particles, a concept completely innovative and not yet applied in the field of microbalances.

The instrument will be capable of attracting charged dust grains by means of a variable Electric Field (EF), generated locally by the instrument itself. The application of this EF will break the equilibrium between the Electric and the Gravity Fields on the Moon, allowing the electrically charged dust grains to be attracted toward the microbalance and, in principle, by changing the local EF it will be possible to attract grains with different size and electric charge.

The design of the new facility and PCM setup is almost done and the project is in the development phase. The 2024 will be dedicated to the experimental phase to test the working principle of new PCM device in a simulated lunar environment.

Conclusion & future works

Building on DEC's breadboard heritage, the next focus will be the development of an in-situ instrument that will give a significant contribution to the study of the lunar soil and the processes that characterize it, thus allowing us to take the next step towards returning to the Moon.

The technological advances necessary to enable humans to return to the Moon and operate long-term and sustainably, will also pave the way to the next very ambitious goal: human exploration of Mars.

Acknowledgements

The DEC development is funded under the EMM project, supported by the PNRR Program.

References:

[1] Berg OE, Richardson FF, Burton H. 1973.*NASA SP* 330:16
[2] M. Horányi, Z. Sternovsky, M. Lankton, et al., Space Sci. Rev. 185 (2014) 93–113.
[3] Horányi, M., et al., *Nature* 522.7556 (2015): 324-326.
[4] Bernardoni, Edwin, Mihály Horányi, and Jamey R. Szalay. The Planetary Science Journal 4.2 (2023): 20.
[5] H. Zhang, Y. Wang, L. Chen, H. Zhang, et al., Sci. China Ser. ETechnol. Sci. 063 (2020) 520–527.
[6] D. Li, Y. Wang, H. Zhang, X. Wang, Y. Wang, Z. Sun, et al., Geophys. Res. Lett. 47 (2020).
[7] Li, Detian, et al. Journal of Geophysical Research: Planets 124.8 (2019): 2168-2177.
[8] Zhuang, Jianhong, et al., Sensors and Actuators A: Physical 320 (2021): 112564.
[9] Wang, X., et al., Geophysical Research Letters 43.12 (2016): 6103-6110.
[10] Orger, Necmi Cihan, et al. Advances in Space Research 63.10 (2019): 3270-3288.
[11] Schwan, J., et al. Geophysical Research Letters 44.7 (2017): 3059-3065.
[12] Sauerbrey, G. s.l. : Z. Phys. 155 206–222, 1959.

PRIMARY DUST LIFTING AND ELECTRIFICATION IN THE MAKGADIKGADI SALT PANS AS MARTIAN ANALOGUE.

G. Franzese[1] (gabriele.franzese@inaf.it), S. Silvestro[1], A. Martin-Ortega[2], G. Mongelluzzo[1], F. Franchi[3], H. Yizhaq[4], N. Andrés Santuiste[2], F. Esposito[1], C. Porto[1], C. I. Popa[1].
[1] *Osservatorio Astronomico di Capodimonte, Istituto Nazionale di Astrofisica, Napoli, Italy.*
[2] *Instituto Nacional de Técnica Aeroespacial (INTA), Ctra. Ajalvir km 4, Torrejón de Ardoz, Madrid, Spain*
[3] *Department of Earth and Environmental Sciences, Botswana International University of Science and Technology, Botswana*
[4] *Department of Solar Energy & Environmental Physics, BIDR Ben Gurion University, Sede Boker campus, 84990, Israel*

Introduction:

Dust embedded into the atmosphere represents one of the driving forces able to lead the planetary climate. Suspended grains can circulate across the globe for months, regulating the cloud lifecycle and the planet radiative budget, affecting so the thermal structure of the atmosphere and its chemical composition. In addition, mobilized sand and dust grains tend to acquire and hold a net charge that can lead to the generation of large electric fields inside the dust clouds. Considered that wind driven dust lifting is not limited to the Earth, the dust effect can be even more impactful on other bodies of the solar system, due to the lack of competing phenomena as water cycle and growth of vegetation. Beyond the others, Mars is for sure the planet where the contribution of dust is mainly visible and impacting the climate. The planet is continuously beaten by dust storms and devils that supply the atmospheric dust budget.

Despite being longly studied, dust lifting mechanisms still represent a challenge for the researchers, due to their intrinsic complexity [1]. For example, we are still unable to forecasting the occurrence of dust storm and devils, neither evaluate the amount of charge hold by the grains or the charges distribution inside the dust cloud. In turn, this prevents to comprehend the possible feedback that the E-field has on the lifting [2,3].

In order to resolve the questions still open in literature further data surveys and new sensors specifically developed are required. In this optic, our team has performed over the years extensive field campaigns in various martian analogue sites along our planet. This has been coupled with the design and development of various instrument devoted to the dust monitoring for planetary applications. The latter of this list is the MicroMED sensor, an Optical Particle Counter (OPC) designed to achieve the first direct characterization of martian airborne dust [4]. MicroMED is characterized by low dimensions and power consumption, making it suitable for both space application and deployment in harsh and isolated terrestrial environment. For this reason, we developed a terrestrial version of the sensor, identical in principle to its martian counterpart, but optimized to work at ambient pressure. This version is equipped with a controller able to operate the sensor autonomously following a preloaded schedule of activations.

We want here to present our last field survey in a martian analogue site on Earth, performed in the Kalahari Desert at the Makgadikgadi Salt Pans.

The main purposes of the campaign were:

- studying the local dust devil population and induced grain electrification,
- testing for the first time on field the MicroMED sensor.

The mission lasted along July and August 2023 and the final site is depicted in Fig. 1. We deployed a fully equipped meteorological station comprehensive also of sand mobilization monitoring sensors (Sensit) and Electric field probes. The final set up foreseen the monitoring of the E-field and wind speed and direction at three altitudes, besides the air and soil temperature. The station was completed by a camera system for the image survey and the MicroMED sensor. MicroMED provided the size distribution and concentration of the suspended dust every five minutes with a measurement rate of 5 MHz. All the sensors, except cameras and E-field were set to work day and night.

Preliminary results:

Along the whole campaign, the terrestrial version of the MicroMED sensor has proven its complete reliability for in situ operation. The acquired data will be useful to further improve the sensor and its operation routine, both for the terrestrial and planetary applications.

Final study site was characterized by a strong convective activity, with a rate of several dust devil occurring per hour during the activity peak. We observed tens of vortices, with few encounters directly crossing over the station.

As an example, Fig. 2 shows the image lapse of one of direct vortex encounters, while Fig. 3 presents the data relative to this encounter. In particular, the peak in the saltation activity and the correlated raising of the atmospheric electric field during the passage of the dust devil are depicted. The E-field is monitored at three different heights and all the signals closely mirror the saltation trend. As far as the authors know, these are the first reported data regarding dust devils vertical E-field profile.

Data are currently under analysis, but the acquired dataset will allow to greatly increase our comprehension of the electrification phenomenon, solving some of the limitation of the previous surveys [5].

References: [1] Harrison et al. (2016) *Space Science Reviews*, 1-47. [2] Kok et al. (2008) *Physical Review Letters*, *100*(1), 014501. [3] Esposito et al. (2016)

Geophysical Research Letters, *43*(10), 5501-5508 [4] Franzese et al. (2023) IEEE 2023 [5] Franzese et al. (2018) *Earth and Planetary Science Letters*, *493*, 71-81.

Fig. 1 The site location in the Makgadikgadi Pans.

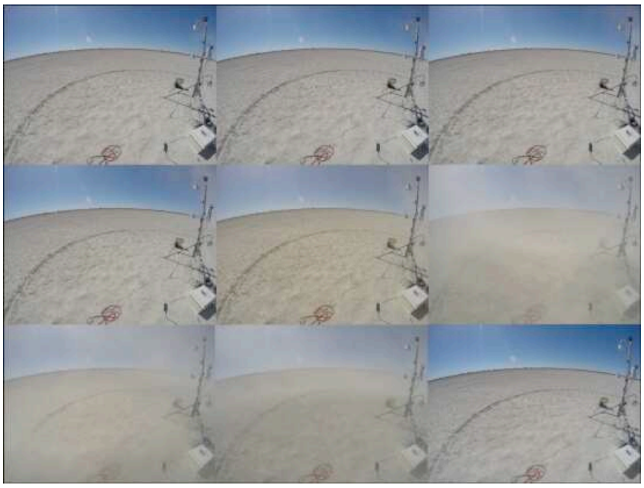

Fig. 2 The image sequence (from left to right, top to bottom) of a dust devil directly crossing our sensors.

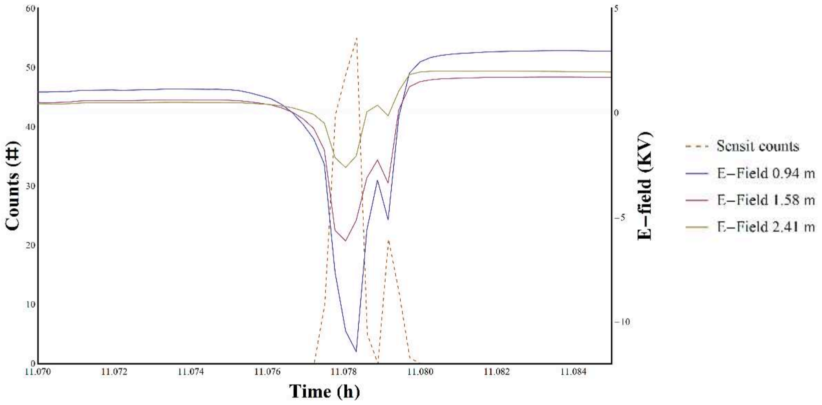

Fig. 3 The time series of the saltation and atmospheric electric field signals during a dust devil direct encounter.

FROM MICRO- TO METER-SCALE: NEW LABORATORY INVESTIGATIONS ON GRAIN SIZE AND MINERAL MIXING IN SUPPORT OF SPACE MISSION REMOTE SENSING INTERPRETATION.

G. Poggiali[1, 2], A. Wargnier[1], L. Fossi[2], S. Iannini Lelarge[3], J. Beccarelli[4], J.R. Brucato[2], M.A. Barucci[1], M. Pajola[5], M. Masotta [3,6], M. Matsuoka[7]
[1]LESIA-Observatoire de Paris, Université PSL, CNRS, Sorbonne Université, Université de Paris Cité, 92195 Meudon Principal Cedex, France (giovanni.poggiali@obspm.fr), [2] INAF-Astrophysical Observatory of Arcetri, Firenze, Italy, [3]Department of Earth Science, University of Pisa, Pisa, Italy, [4]CISAS, University of Padova, Italy, [5]INAF-Astronomical Observatory of Padova, Padova, Italy, [6]CISUP, Centro per l'Integrazione della Strumentazione Università di Pisa, Pisa, Italy, [7]National Institute of Advanced Industrial Science and Technology, Tsukuba, Japan

Introduction: Several Solar System bodies, like C-class asteroids and primitive small bodies, explored by past space missions or either target of new ones are characterized by dark surfaces. Despite many effort in understanding the spectroscopic behaviour of low albedo surfaces our knowledge is still incomplete. Dark surfaces are often linked to the presence of opaque material [1] or surface processes such as space weathering [2] or thermal alteration [3]. Therefore, the interpretation of remote sensing data could not be disjoint from an intensive laboratory work as a powerful tool to unveil the surface physical state and composition.

Among all the processes that can be simulated in the laboratory, analyzing complex mixtures of analogous materials stands out as pivotal for remote sensing interpretation. Yet, it also represents one of the most challenging investigations, particularly when multiple components are utilized. In this contribution, we present results from different works that share the common goal of studying how the mixing of different grain size and dark materials can affect the spectroscopic behaviour from near- to mid-infrared (1.25-25 µm).

Method: Here, two main works will be presented. The first involves the mixing of hydrated and anhydrous minerals components with different grain sizes [4]. The second concerns the mixing of basalts at different grain sizes with dark components [5].

For both works we developed a new protocol to mix two components with different grain sizes. The method passes through a series of steps including sieving and washing the minerals to separate each grain size and later the mixing the selected components. This procedure allows us to produce unique samples with a bigger grain size covered by a selected amount of small grains (Figure 1).

In the first work, we prepared several mixtures using 1 wt% and 5 wt% of hyperfine grain size (< 10 µm) of hydrated minerals and 95 wt% and 99 wt% of larger grain size (200–500 µm) of anhydrous minerals. We measured the IR reflectance spectrum of these mixtures in the range 8000–400 cm^{-1} (1.25–25 µm). Analysis of the spectroscopic features was carried out independently in two separated ranges covered by our measurements, in the NIR range we focused on the presence of the hydrated band at 2.7 µm and in the MIR range were we carried out an analysis of the most important spectroscopic features present in this wavelength range.

The second sample set includes four series of basaltic mix (feldspar and pyroxene), at different grain sizes from < 50 µm to 1000 µm, mixed with amorphous carbon at increasing weight percentages from 1% to 50%. We analysed several features on the spectrum of each mineral mixture: (i) near infrared slope; (ii) 2.7 µm OH-stretching band; (iii) Christiansen features; (iv) Reststrahlen band and Transparency feature.

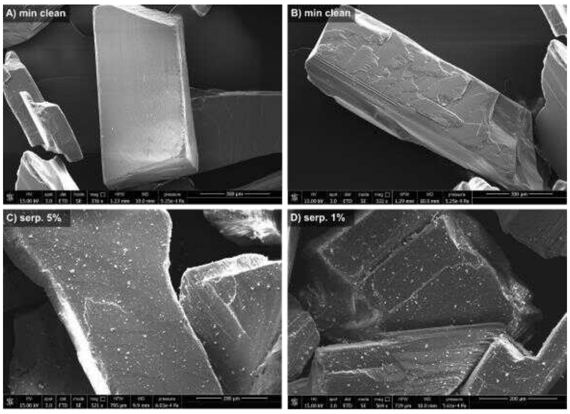

Figure 1. Secondary electrons SEM image of enstatite sample before (panels A and B) and after mixing with 5% and 1% of serpentine (panel C and D).

Results: Two main experimental works presented in two publications are showed in this contribution. In detail our results concern:

Hyperfine hydrated mineral mixing with coarse anhydrous minerals. Our experiments show how the addition of a hydrated component, which is minor in percentage and has a much smaller grain size, can lead to very remarkable changes in the NIR region especially in increasing the hydrated band depth at 2.7 µm (Figure 2), while slightly affecting the MIR region. The surface of many rocky bodies is covered with regolith, and these new laboratory data show how even a small amount of hydrated mineral in the composition can influence the overall final spectrum.

Dark component effect on different grain size bright minerals. Measurements presented in this work, for the first time taking into account a large wavelength range, point towards a critical effect of dark material but with a different outcome for each grain size of the brighter component of the mixture (Figure 3). Some of the most interesting results involved the slope trend of modification with dark material, in particular we observed an inversion between reddeding and blueing depending on the percentage of the mixture and the grain size. Moreover, we investigated also the different behaviour of several features such as: hydrated band at 2.7 µm, the Reststrahlen band and Transparency feature.

Conclusions: It is of paramount importance to improve our understanding of the spectroscopic changes induced by small variations in the mineral phases. This is pivotal for a correct interpretation of infrared data collected on planetary surfaces by space missions. The dataset that we assembled with our experiments will be a good support in the interpretation of upcoming data from the JAXA Phobos Martian Moon eXploration mission, as well as in understanding of previous data from dark surfaces in the Solar System like asteroids (162173) Ryugu and (101955) Bennu.

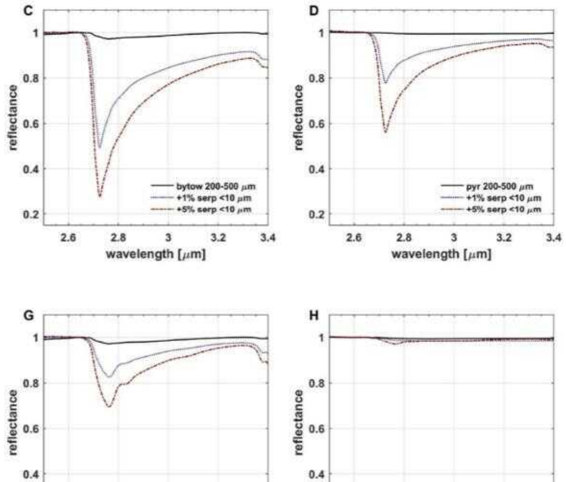

Figure 2. Detail of hydrated band around 2.7 µm for hydrated minerals serpentine (top panels) and montmorillonite (bottom panels) with grain size <10 µm mixed at 1 wt% (dotted blue line) and 5 wt% concentration (dash-dot red line) with: plagioclase bytownite (panel C, G) and iron sulfide pyrite (panel D, H). (Figure adapted from [4])

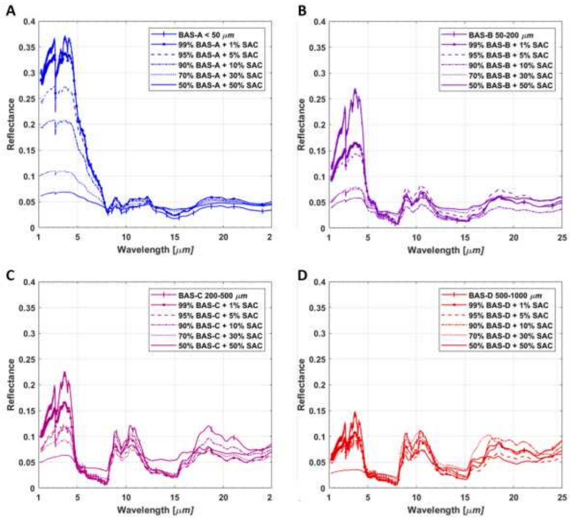

Figure 3. Infrared spectra of basaltic mixtures [BAS] at different grain sizes, <50, 50-200, 200-500 and 500-1000 µm, with addition in different proportions, from 1 to 50%, with synthetic amorphous carbon [SAC].

References: [1] Cloutis E. et al. (1990) *Icarus*, *84* (2), 315-333 [2] Hasegawa et al. (2022), *ApJ. Letters*, *939*, L9 [3] Lugassi, R, et al. (2015), *Geoderma*, *213*, 268-279 [4] Poggiali G. et al. 2023, *Icarus*, *394*, 115449 [5] Poggiali G. et al. 2023, *A&A* (under review)

THE RECOVERY OF THE MATERA METEORITE THANKS TO THE OBSERVATION OF THE 2023 VALENTINE'S DAY BOLIDE BY THE PRISMA FIREBALL NETWORK.

D. Barghini[1,2], A. Carbognani[3], D. Gardiol[1], S. Bertocco[4], M. Di Carlo[5], M. Di Martino[1], C. Falco[1] M. Morelli[6], G. Pratesi[7,8], W. Riva[1,9], R. Salerno[10], G. M. Stirpe[3], C. Volpicelli[1], and the PRISMA team, [1]INAF – Osservatorio Astrofisico di Torino, via Osservatorio 20, 10025 Pino Torinese (TO), dario.barghini@inaf.it, [2]Università degli Studi di Torino, Dipartimento di Fisica, Torino, [3]INAF – Osservatorio di Astrofisica e Scienze dello Spazio, Bologna, [4]INAF – Osservatorio Astronomico di Trieste, Trieste, [5]INAF – Osservatorio Astronomico d'Abruzzo, Teramo, [6]Museo Italiano di Scienze Planetarie, Fondazione Parsec, Prato, [7]Università di Firenze, Dipartimento di Scienze della Terra, Firenze, [8]INAF – Istituto di Astrofisica e Planetologia Spaziali, Roma, [9]Osservatorio Astronomico del Righi, Genova, [10]Meteo Expert, Cinisello Balsamo (MI)

Introduction: On 14/02/2023 (Valentine's Day) at 17:68:29 UT, the PRISMA network [1] detected a bright bolide (IT20230214) over the Puglia and Basilicata regions in Southern Italy. Since the network has not reached a dense coverage in this part of the country until today, only three cameras detected this event (ITPU01 – Castellanagrotte, ITPU03 – Tricase and ITAB01 – Vasto). The reconstructed tracks detected by these cameras are reported in Fig. 1.

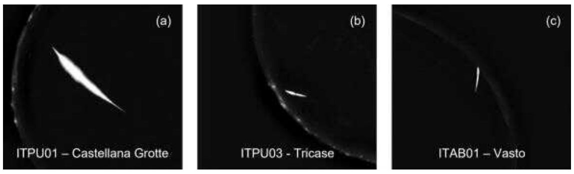

Figure 1. Images of the track of the IT20230214 bolide recorded by three all-sky cameras of the PRISMA network.

Triangulation: The analysis of the data collected by PRISMA allowed a detailed reconstruction of the IT20230214 event, and its three-dimensional trajectory is presented in Fig. 2. The bolide was detected from a starting altitude of 85.5 ± 0.1 km at an initial speed of 16.3 ± 0.1 km/s. It traversed the atmosphere for about 5.3 s at an inclination angle of 56.7 ± 0.3°, for a total trajectory length of 75.0 ± 0.1 km, arriving from the NNE direction and travelling towards SSW with an azimuth angle of 24.3 ± 0.1°. Projected on the ground, its trajectory began SW of Bari and ended NE of Matera, where the visible flight terminated at an altitude of 22.8 ± 0.1 km, while the meteoroid was travelling at a low speed of 3 ± 1 km/s.

Figure 2. Visualization on Google Earth of the reconstructed three-dimensional trajectory of the IT20230214 bolide (red dots) together with the position of the three PRISMA stations that detected the event (red pins).

Pre-atmospheric orbit: The computed preatmospheric heliocentric orbit of the IT20230214 meteoroid is plotted in Fig. 3. It has a eccentricity of 0.54 ± 0.02 and an inclination on the ecliptic plane of 14.5 ± 0.2°, with a semi-major axis of 2.10 ± 0.07 AU and its aphelion on the outer region of the Main Asteroidal Belt (represented as the grey shaded region of panel a). Together with a Tisserand's parameter of 3.51 ± 0.08, this points towards an asteroidal origin for the orbit of this meteoroid.

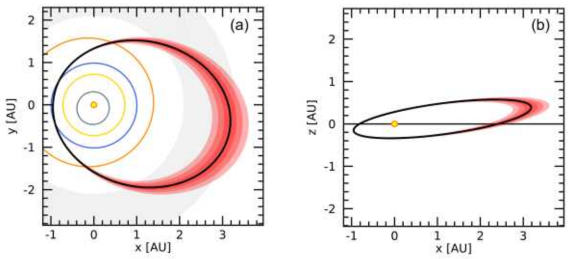

Figure 3. Heliocentric preatmospheric orbit of the IT20230214 meteoroid computed in this work. (a) Plot of the *(x, y)* ecliptic projection. (b) Plot of the *(x, z)* ecliptic projection. In both panels, the red shaded bands enclose the 1, 2 and 3σ confidence intervals.

Physical properties of the meteoroid: According to the results of the dynamic model developed within PRISMA [2] and applied to this case, the meteoroid had a preatmospheric speed 16.4 ± 0.2 km/s and an mass-to-section ratio (MSR) of 310–510 kg/m^2, corresponding to a preatmospheric mass in the range 5–21 kg and a preatmospheric size of 15–24 cm (considering 68% confidence intervals). A purely dynamic approach (considering the deceleration data only) suggests a residual meteorite mass of 0.6 ± 0.3 kg (7 ± 1 cm of size), while a photo-dynamic model (simultaneously fitting for the speed and magnitude data) results in a much more modest mass of 0.10 ± 0.04 kg (4.4 ± 0.7 cm).

Strewn-field: From these data, it was possible to estimate the probable area of fall of meteorite pieces using the Meteorite finder[1] software [3,4]. Similarly to the case of Cavezzo [5], the data of the wind speed and direction came from Meteo Expert. Figure 4 shows the extension of the strewn-field for frag-

---

[1] https://www.ict.inaf.it/index.php/31-doi/164-sw-2023-9

ments with a MSR of 75 kg/m^2 (red dots), comparable to the size of the final residue estimated from the photo-dynamic model (single-body flight). The area of fall is located north of the Matera city, in the Basilicata region. The effect of the wind drag caused the strewn-field to be shifted towards East compared to the geometrical prolongation of the trajectory. Adopting the same successful approach of the case of the Cavezzo meteorite, the Project Office (PO) of PRISMA prepared and disclosed a press release[2] on the morning of 16/02/2023, with a preliminary version of the strewn-field.

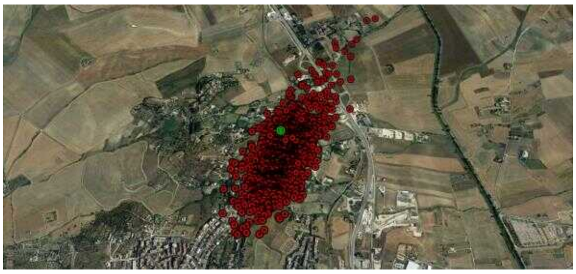

Figure 4. Map of the strewn-field for the IT20230214 event for meteorite pieces with a mass-to-section ratio of 75 kg/m^2 (red dots), with an overall extension of 2 x 0.5 km. The coordinates of the recovery of the fragments of the Matera meteorite are shown as the large green dot.

Figure 5. A picture from Google Earth of the house of the Losignore brother, where the green dots plot the position of the recovery of the main fragments.

Fig. 6: A picture of most of the fragments of the Matera meteorite. (http://www.prisma.inaf.it/index.php/2023/02/18/eccola-trovata-la-meteorite-di-san-valentino/)

Meteorite recovery: On the evening of 17/02/2023, the PRISMA PO was contacted by the brothers Mr. Gianfranco and Pino Losignore, who reported an interesting finding over their property (Fig. 5), located in Contrada Rondinelle on the municipality of Matera. The approximate coordinates of the recovery are 40°41'43.9"N and 16°35'4.2"E. They found a bunch of rocky fragments, of tens of grams of total mass, on the balcony of their house (Matera 1 on Fig. 5) and one tile of the pavement was damaged by what looked like a violent impact. We immediately recognized these fragments as freshly-fallen meteorite pieces. On the morning of the next day, it was also discovered that one fragment landed on the roof of their house (Matera 2) and damaged one solar panel, shattering its outer glass surface. Further searches in the neighbouring area led to the discovery of a third fragment, and a fourth one was recovered by two volunteers of the search campaign (Mr. Pierluigi Cox and Mrs. Silvia Yadira Padilla Leon). To date, the total recovered mass of the Matera meteorite is 117.5 g, distributed in 4 main specimens and dozens of small fragments from the impact on the balcony (see Fig. 6). This is compatible with the final mass estimated by the photo-dynamic model.

Meteorite analysis: The day after the recovery, all fragments were moved to the Istituto Nazionale di Fisica Nucleare - Laboratori Nazionali del Gran Sasso to measure their γ-activity with the HPGe detectors of the STELLA (Subterranean Low-Level Assay) facility, and the geochemical analysis of the meteorite was carried out at the Dipartimento di Scienze della Terra of the Università di Firenze. The analysis of the Matera meteorite will be sucject of a separate contribution to this conference.

References: [1] Gardiol D., et al (2019) *IMC Proc., 2019*, 81–86. [2] Barghini D. (2023) *PhD Thesis, UniTo*. [3] Carbognani A., et al. (2020) *EPJP, 135*, 255. [4] Carbognani A., et al. (2023) *Icarus, 408*, 115845. [5] Gardiol D., et al. (2021), MNRAS, 501, 1215–1227.

---

[2] http://www.prisma.inaf.it/index.php/2023/02/16/la-mappa-della-meteorite-di-san-valentino/

MULTI-ANALYTICAL INVESTIGATIONS OF TWO RYUGU PARTICLES.

M. Ferrari[1], L. Folco[2], E. Mugnaioli[2], S. De Angelis[1], A. Raponi[1], M. Masotta[2], E. Bruschini[1], R. Borriello[2], E. Ammannito[3], M.C. De Sanctis[1], M. Ciarniello[1], S. Stefani[1], G. Piccioni[1], E. La Francesca[1], L. Rossi[1] and M. Pedone[3]. [1]INAF-IAPS, Via del Fosso del Cavaliere 100, 00133, Rome, Italy (marco.ferrari@inaf.it); [2]Dep. Earth Science, University of Pisa, Via Santa Maria, 53, 56126, Pisa, Italy; [3]ASI, Via del Politecnico, 00133, Rome, Italy.

Introduction: The JAXA/Hayabusa2 mission collected 5.4 g of samples from two different sites (i.e., A and C) on the surface of the C-type asteroid (162173) Ryugu [1]. This asteroid is characterized by a low albedo and by the presence of hydrous and carbonaceous materials [2]. The Ryugu surface spectra collected by the Hayabusa2/NIRS 3 spectrometer reveal a narrow absorption feature at 2.72 μm [3] resembling that observed on the surface of Ceres by the Dawn/VIR spectrometer [4]. Laboratory analysis of returned grains revealed that Ryugu samples contain hydrated silicates, sulfides, oxides, carbonates, and organics. Ryugu particles display a close compositional match with the chemically unfractionated, but aqueously altered, CI chondrites [5], and represent the most uncontaminated and unfractionated extraterrestrial materials studied so far [6]. Spectroscopic observation revealed the presence of a band at 3.06 μm, indicating the possible presence of NH-bearing phases in most of the returned grains [7; 8].

With this work, using a multi-analytical approach, we aim to characterize two samples (C0091 and A0198) returned to Earth by the Hayabusa2 mission contributing to define the physical and mineralogical characteristics of the asteroid Ryugu and understanding the initial phases of the formation and evolution of the C-type bodies.

Experimental: The following laboratory analyses have been used to characterize the samples:

- VIS-IR imaging spectroscopy (0.4-5 μm) has been carried out with the SPectral IMager (SPIM) facility [9] on whole samples. Data allowed a first characterization of the mineralogic composition of their external surface, including an assessment of the presence of water, organic matter, and ammonium in addition to the minerals. Furthermore, by using the SPIM facility (i.e., the Dawn/VIR replica), we can perform a compelling comparison between the data collected on the samples with those provided by the Dawn/VIR spectrometer on Ceres, even if with a very different spatial scale;
- μ-FT-IR. We used this technique to obtain compositional information in the range 2.5-15 μm of some morphological features on the surface of the particles highlighting the spectroscopic differences with the particles' matrix.
- X-ray microscopy (XRM). This non-destructive technique has been used to obtain a high-resolution (submicron scale) 3D tomography of the samples, revealing their internal structure (including porosity and fracturing), as well as the morphology and composition of the individual grains contained in them; XRM data enabling the location of regions of interest (ROIs) within the samples to be analyzed by transmission electron microscopy (TEM);
- Raman μ-spectroscopy has been used to obtain compositional maps of the samples' surface at the micrometric scale;
- Focused ion beam-field emission gun-scanning electron microscopy (FIB-FEG-SEM) has been used to identify the main mineralogical phases and to extract the electron-transparent lamellae for TEM analyses;
- Transmission Electron Microscopy (TEM), electron diffraction, and energy-dispersive X-ray spectroscopy (EDS) have been used to identify amorphous materials, cryptocrystalline phases, and crystal defects through high-resolution techniques.

Results: The VIS-NIR spectra obtained with the SPIM facility on the surface of the two particles show the almost ubiquitous presence of a deep V-band centered at lengths slightly above 2.7 μm. In addition, absorptions near 3.4 μm and in the range 3.7-3.9 μm are detected in specific positions, returning an inhomogeneous surface composition at the scale of ~40 μm (SPIM pixel size). These absorption features can be related to the presence of phyllosilicates and carbonates, respectively.

In addition, at some specific points, the band at 3.06 μm indicates the presence of ammonium-bearing compounds.

The μ-Raman spectra acquired on the two particles are characterized by a high fluorescence background and by the presence of the Raman D and G-bands related to the presence of poorly ordered carbonaceous matter. The spectral parameters derived from the mathematical fitting of the acquired spectra as band positions, and band intensity ratio do not differ greatly between the two particles. Raman analysis identifies dolomite and calcite as the most common carbonates on both particles.

The two samples (A0198 and C0091) are characterized by a generally similar composition and also similar phase abundances. Energy Dispersive X-ray spectroscopic (EDX) data obtained using the FE-SEM confirmed the presence of hydrated silicates, sulfides (Ni-rich and Fe-rich), carbonates, phosphates, and oxides (mainly magnetite). Sulfides form dominantly euhedral grains (up to 5 µm in size), whereas oxides form submicrometric framboid, platy, or columnar structures. The internal distribution of silicates, sulfides, and oxides in the interior of the two samples, as revealed by XRM data, is rather homogeneous. Notably, sample C0091 displays a slightly smaller grain size and a slightly higher porosity compared to particle A0198.

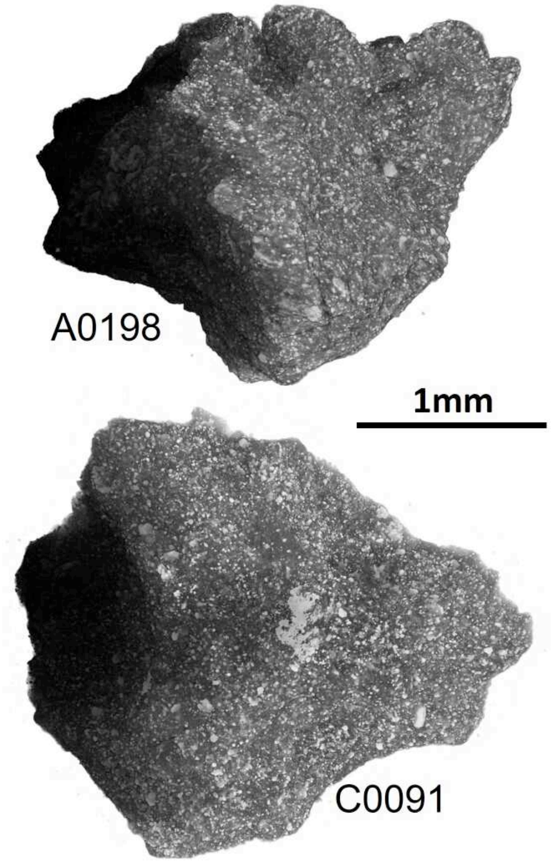

Fig.1 XRM images showing the distribution of sulfides and iron oxides on particle surfaces.

TEM/EDS and 3D Electron Diffraction investigations made on the three extracted lamellae (subsamples A0198-1-L1; A0198-1-L2 and A0198-1-L3) show that the matrix is mostly made of phyllosilicate flakes, with composition in-between serpentine and saponite, and amorphous carbonaceous matter. Crystals of sulfides, magnetite, apatite, and other minerals typical of low thermal alteration were also observed. Overall, the whole assemblage appears significantly porous.

Conclusions: To date, interpretation of remotely sensed data coupled with spectroscopic investigation of analogs has not enabled a full understanding of the mechanisms of aqueous alteration and the mineral assemblage of C-type objects. Furthermore, studies on meteorites have not provided morphological and compositional information on the mineral phases that preceded the alteration of their progenitor body. For this reason, spectroscopic measurements, and nanoscale mineralogical investigations on Ryugu returned samples represent a unique chance to definitively understand these processes.

Furthermore, this type of work is useful for establishing both a sequence of analyses capable of providing scientific answers to the pre-established objectives and for developing sample curation procedures that will be useful for studying future samples collected by sample return missions (e.g., OSIRIS-REx, MSR, and MMX).

References: [1] Watanabe, S. et al. (2019) Science; [2] Kitazato, K. et al. (2019) Science; [3] Kitazato, K. et al. (2021) Nat. Astron.; [4] De Sanctis, M.C. et al. (2015) Nature; [5] Yada, T. et al. (2021) Nat. Astron. [6] Ito, M. et al. (2022) Nat. Astron. [7] Pilorget, C. et al. (2022) Nat. Astron.; [8] Kebukawa, Y. et al. (2022) 53rd LPSC, #1271; [9] Coradini, A. et al. (2011) EPSC-DPS Joint meeting, #1043.

Acknowledgments: We are grateful to the ZEISS Group for making available their XRM Zeiss Xradia Versa 630 instrument and Regione Campania "in the field of the project in collaboration with the UE POR CAMPANIA FESR 2007/2013 0.0.2.1" for supporting the micro-FTIR measurements.

A new spectral parameter to detect olivines and pyroxenes: application to ordinary chondrites.

*G.Massa[1,2], A. Longobardo[1], E. Palomba[1], F. Dirri[1] and M. Angrisani[1,2]
[1]INAF Istituto di Astrofisica e Planetologia Spaziali, via Fosso del Cavaliere, 00133 Rome, Italy
[2]University of Rome “Sapienza”, Piazzale Aldo Moro 5, 00185 *Rome, Italy*
*email: giuseppe.massa@inaf.it.

Introduction: The meteorites are an important resource in order to understand the composition of the asteroids of the Solar System. The most common meteorites are the ordinary chondrites and they are thought to come from S-type asteroids. These meteorites are usually characterized based on their VNIR (from visible to near infrared) spectra, thanks to the presence of two strong absorption bands located at 1 and 2 µm (called BI and BII, repectively). Ordinary chondrites are silicate dominated, and their two main absorption bands are due to the presence of pyroxenes and olivines (Adams, 1974; Cloutis, et al., 1986; Cloutis, et al., 2015). OCs are subdivided on the basis of chemistry into three groups, the H, L and LL chondrites, for high total iron, low total iron and low total iron plus low metallic iron, respectively (Grady, 2014). To retrieve information about asteroids composition from their VNIR spectra, a comparison with meteorites spectra is necessary. The comparison is based on appropriate spectral parameters specifically defined and calibrated on the basis of meteorites’ composition. This calibration implies that the composition of a set of meteorites (e.g., OCs) is known (e.g., through XRD), and that its variations can be associated to variations in the spectral parameters. In Dunn, et al., 2010 and Cloutis, et al., 1986, the parameter used for the calibration of OCs are the band center at 1 µm (BCI), the band center at 2 µm (BCII), the band area ratio (BAR) and reflectance values at defined wavelengths. The relationships found were then used on remote spectra of asteroids to retrieve their composition.

The Hera mission and the ASPECT instrument: This work is in the context of the Hera mission. The Hera mission is under development in the Space Safety Program of the European Space Agency (ESA). The mission will follow the Double Asteroid Redirection Test (DART) mission (Michel, et al., 2018) and its launch is planned in October 2024. Around late December 2026, Hera will arrive near a binary system of asteroids composed of Didymos, that is the primary asteroid, and Dimorphos, i.e., Didymos’ moon, in the following referred to as Didymos system. Didymos is among a potentially hazardous asteroid with a minimum orbital intersection distance (MOID) is 0.04014 au (15.6 lunar distance) from the Earth (Okada, et al., 2022). Hera objectives are to investigate the subsurface and interior properties of the system and to study in detail the outcome of the kinetic impactor mission DART, thus providing extremely valuable information for asteroid impact threat mitigation, mining, and science purposes (Michel, et al., 2022). Due to the two prominent absorption bands at 1 and 2 µm in the spectra, it was found that Didymos is probably an Sq-type asteroid (Cheng, et al., 2018; De León, et al., 2010), so it is compositionally linked to the ordinary chondrite meteorites (Dunn, et al., 2013). Hera is equipped with the ASPECT (Asteroid Spectral Imager) VNIR spectrometer. It is a miniaturized hyperspectral imager extending from the visible up to shortwave infrared (SWIR) wavelengths (650-2500nm) using four different channels with a spectral resolution between 20-40 nm. The Asteroid Spectral Imager takes 2D snapshots at a given wavelength. When multiple snapshots are combined, a spectral datacube is formed, where the wavelength bands are separated in the time domain (Kohout, et al., 2018). The four channels of ASPECT are characterized by different sizes (pixels), 1024x1024, 640x512, 640x512, 1x1, for the VIS, NIR1, NIR2, SWIR channels respectively. The SWIR channel is a single pixel channel and thus is characterized of a very different spatial resolution compared to the others (Kohout, et al., 2018). This means that to have the best spatial resolution we have to focus on the first three channels (0.65-1.60 µm).

In this work we present the definition and calibration of a new spectral parameter that is defined on the 1 µm absorption band of silicates, that could help in retrieving information about Didymos composition.

Methods and Results: A first definition of a new parameter is based on the study of spectral features in binary mixtures. From literature it is known that the Band Area Ratio (BAR), that is the ratio between the area of the 2 and 1 µm band, is diagnostic for the abundance of olivine normalized to the abundance of *olivine* + *pyroxene* (Cloutis, et al., 1986; Dunn, et al., 2010; Palomba, et al., 2015).

In the case of a spectral dataset that only covers the 1 µm absorption band (such as ASPECT), we need a new parameter, based on the BAR concept, that would be sensible to the variation of olivine abundance. In this range we can define the band depth (BDI) as (Clark, et al., 1984):

$$BD = 1 - \frac{R_c}{R_{con}}$$

where R_c and R_{con} are the measured reflectance and the calculated continuum reflectance at the band center, respectively. We showed that this parameter is not related to the olivine abundance. In general, the extinction coefficient of the Fe^{2+} absorptions present in both olivines and pyroxenes is one order of magnitude lower in olivines than in pyroxenes.

Thus, the 1 µm feature is mainly due to pyroxenes unless they are only a minor component of the mixture (Cloutis, et al., 1986). We therefore used the BDI to retrieve a relation with the BAII both in binary mixtures of pyroxene and olivine and OCs studied in Dunn et al. 2010 (Figure 1).

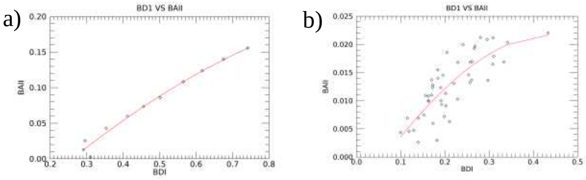

***Figure 1**: BAII vs BDI relation retrieved in binary mixtures (fig. a) of and OCs (fig. b). The red curves are the f(x) fit.*

The equation of the red curves in Figure 1 was then computed giving *BAII = f(BDI)*. Now we can calculate the BAII from the BDI. In this way, we can compute a new BAR that we will call AD1. In Figure 2 the scatterplot between AD1 and the olivine abundance in both binary mixtures and OCs is shown overlapped to the BAR values. The olivine abundance in OCs was measured thorugh XRD analysis.

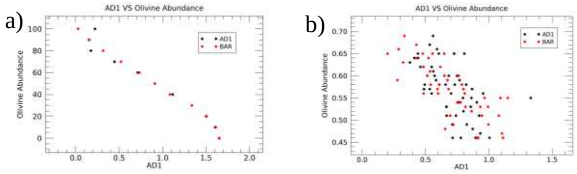

***Figure 2**: Scatterplot between AD1 and BAR vs olivine abundance in binary mixtures (fig. a) and OCs (fig.b). The red point are the BAR values while the dark ones are the AD1s.*

The HCP and LCP relative abundance HCP/(LCP+HCP) (High and Low Calcium Pyroxene) in OC meteorites is found to be centered at 0.76 with a standard deviation of 0.04, thus their effects on our parameter due to their relative variability is negligible.

Finally, we know that AD1 behaves as the BAR with respect to the olivine abundance.

The last step of this work was to compute the linear relation between AD1 and the olivine abundance that can be used to retrieve the olivine abundance of a spectrum that only covers the 1 µm range, as was done in Dunn et al. (2010) with the BAR. This linear relation was then applied to the dataset we used to calibrate our parameter. In Figure 3 the scatterplot between the olivine abundance calculated and measured is shown.

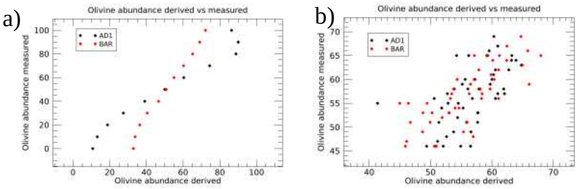

***Figure 3**: Scatterplot between the olivine measured and calculated through the parameter calibrated in this work (black points) and Dunn et al 2010 relation (red points) on binary mixtures (fig. a)) and OCs (fig. b).*

The root mean square deviation between the derived and measured abundance is 5% and 13% for the binary mixtures and 5% and 4% for the OCs, calculated with our calibration and Dunn et al. (2010) one, respectively.

Conclusions and future perspectives: This work showed the identification and calibration of a parameter that would allow the retrieval of the olivine abundance based only on the 1 µm absorption band. The important result is that the error on the measure obtained with our calibration on the OCs is very similar to the one obtained using Dunn et al. (2010) relation, with the advantage that we only need to know the 1 µm absorption band. This reinforces the reliability and importance of our parameter.

The future perspectives are:

1. To extend this application to other OCs spectra.
2. To identify possible influence of other variables (e.g., grain size, opaques, ecc..).

Acknowledgement: This work is funded through the ASI-UNIBO Agreement 2022-8-HH.0.

References

Adams, J. B. (1974). Journal of Geophysical Research 4829-4836. doi:https://doi.org/10.1029/JB079i032p04829

Cheng, A. F., & al. (2018). *Planetary and Space Science 157*, 104-115. doi:https://doi.org/10.1016/j.pss.2018.02.015

Clark, R. N., & Roush, T. L. (1984). *Journal of Geophysical Research: Solid Earth 89.B7*, 6329-6340. doi:https://doi.org/10.1029/JB089iB07p06329

Cloutis, E. A., & al. (1986). *Journal of Geophysical Research: Solid Earth, 91*(B11), 11641-11653.

Cloutis, E. A., & al. (2015). *Icarus 252*, 39-82. doi:https://doi.org/10.1016/j.icarus.2014.10.003

De León, J., & al. (2010). *Astronomy & Astrophysics 517* .

Dunn, T. L., & al. (2010). *Icarus 208.2*, 789-797. doi:https://doi.org/10.1016/j.icarus.2010.02.016

Dunn, T. L., & al. (2013). *Icarus 222.1*.

Grady, M. G. (2014). Atlas of meteorites. doi: https://doi.org/10.1017/9781139016308

Kohout, T., & al. (2018). *Advances in Space Research 62.8*, 2239-2244. doi:Feasibility of asteroid exploration using CubeSats—ASPECT case study.

Michel, P., & al. (2018). *Advances in Space Research 62.8*, 2261-2272.

Michel, P., & al. (2022). *The planetary science journal 3.7*, 160. doi:10.3847/PSJ/ac6f52

Okada, T., & al. (2022). *53rd Lunar and Planetary Science Conference., 2678*.

Palomba, E., & al. (2015). *Icarus 258*, 120-134. doi:https://doi.org/10.1016/j.icarus.2015.06.011

CHARACTERIZING PHYSICAL PROPERTIES OF METEOROIDS USING MACHINE LEARNING: A CASE STUDY USING HIGH-RESOLUTION OBSERVATIONS BY THE CANADIAN AUTOMATED METEOR OBSERVATORY.

M.Vovk[1], P. Brown[1], D. Vida[1], [1]Western University, London, ON, Canada (mvovk@uwo.ca, pbrown@uwo.ca, dvida@uwo.ca).

Introduction: Understanding the process of ablation and fragmentation of mm-sized meteoroids in the Earth's atmosphere is key to measuring their physical properties. These small particles can be used as proxies for their parent bodies, comets and asteroids, whose properties we often cannot measure directly. Furthermore, the physical properties of meteoroids are a key parameter used in satellite impact risk assessments, but they remain poorly known, with an uncertainty of an order of magnitude.

Currently, the majority of theoretical studies investigating faint meteors using either optical or radar instrumentation assume that meteoroids do not fragment [1] [2] [3] [4]. However, contemporary observations show that nearly 90% of faint meteors captured by high-resolution video cameras display significant fragmentation [5]. The model which does include fragmentation and successfully explains observations is called the erosion model and it assumes that meteoroids fragment by releasing 10-100 μm constituent grains which ablate independently [6]. However, this model is difficult to fit to data, requiring significant manual work to produce the fits. So far, automated fitting methods have been unsuccessful which leaves questions about the uniqueness of manual fits.

Aims: This study aims to apply the erosion fragmentation model in an automated and statistically sound way to high-resolution observations of meteors. This work uses the Perseids as a case study as they are observed in great numbers and should have similar physical properties, enabling method validation. The final products of this procedure are the inverted physical properties of meteoroids (bulk density, grain sizes, strength properties), and the meteoroid structural composition. In a first, this study aims to apply the model meteoroids to investigate their impact on meteoroid risk assessment and interactions with other planetary atmospheres, giving a model to base future mission instrumentation.

Methods: We use meteor observations from two state-of-the-art meteor observation instruments: (a) The telescopic mirror-tracking system that is a part of the Canadian Automated Meteor Observatory (CAMO) and achieves a 1 m measurement accuracy [7], and (b) The Electron Multiplying CCD (EMCCD) HNü 1024 cameras which observe meteors as faint as magnitude +8 [8]. Five Perseid meteors have been manually reduced and the erosion model has been manually fit to observations, forming a basis for the analysis. More are planned to be studied in the future. As a counterpart to the observations, a large synthetic data set of 1 million meteor observations has been generated using the erosion model and a wide range of meteoroid physical parameters. The observations were matched to synthetic observations using Principal Component Analysis (PCA) [11] in a Bayesian fashion, enabling estimating uncertainties of individual inverted physical properties. The PCA approach compares the observed characteristics of meteors such as the peak magnitude, heights of beginning and end, trail length, light curve shape, velocity, and deceleration. It is important to note that selecting the correct observed characteristics used in the PCA significantly impacts the results. The characteristics are required to accurately quantify the behavior of the meteoroid. 1000 synthetic meteors closest to the observations are selected by computing the similarity score provided by the PCA. The range of possible physical properties is then computed from the selected synthetic meteors.

Results: Our study provides initial insights into the physical characteristics of Perseid meteoroids. Our method measures a bulk density of Perseid meteoroids between 200 - 600 kg/m^3, consistent with previous findings [12]. The erosion coefficient, which regulates how much mass is released into grains, is confined to a range between 0.2 and 0.5 kg/MJ. The measured ablation coefficient of 0.01 - 0.03 kg/MJ is consistent with values expected for fast cometary objects [10]. The initial results also show that for the Persieds, factors like density, erosion, and ablation coefficients can be measured within a factor of two, with future work pointing to further improvement in accuracy.

Conclusions: This study performed the first automated and statistically sound model inversion of a meteoroid fragmentation model on high-resolution meteor observations. This novel approach is validated on the Perseids which showed consistent physical properties from one meteor to another, regardless of the meteoroid mass.

In the future, we will focus on sporadic meteoroids, with specific attention to those with velocities under 20 km/s which make the majority impacting satellites in Earth orbit [9].

References: [1] Öpik, E. J. *Interscience Publ. Inc.(New York),* 147, 1958. [2] Bronshten, V. A. *Springer*, 91-138, 1983. [3] Dawkins, Erin CM, et al. *Planetary and Space Science* : 105796 , 2023. [4] Pabari, Jayesh P., Srirag N. Nambiar, and Sonam Jitarwal. *Planetary and Space Science* 226: 105617, 2023. [5] D. Subasinghe, M. Campbell-Brown, and E. Stokan, *Monthly Notices of the Royal Astronomical Society*, vol. 457, pp. 1289–1298, 2016. [6] J. Borovicka, A. Milani, G. Valsecchi, and D. Vokrouhlick ́y, Eds., vol. 2. *Cambridge University Press*, 5, p. 107, 2007. [7] D. Vida, P. G. Brown, M. Campbell-Brown, R. J. Weryk, G. Stober, and J. P. Mc-Cormack, *Icarus*, vol. 354, 1, 2021 [8] P. Gural, T. Mills, M. Mazur, P. Brown, *Experimental Astronomy* 53:1085–1126, 2022. [9] D. Janches, A. A. Berezhnoy, A. A. Christou, G. Cremonese, T. Hirai, M. Horanyi, J. M. Jasinski, and M. Sarantos, *Planetary Science Journal*, 6, 2021. [10] Ceplecha, Z., Borovička, J., Elford, W. G., ReVelle, D. O., Hawkes, R. L., Porubčan, V., & Šimek, M. Space Science Reviews, 84(3/4), 327–471, 1998. [11] Dunteman, G. H. (1989) *Sage University Paper* (No. 69) [12] D. Vida, P. G. Brown, M. Campbell-Brown, A. Egal, Icarus, p.115842 , 2023. [12] Kikwaya, J.-B Campbell-Brown, M. and Brown, Peter, Astronomy and Astrophysics, 530, (2011).

Near Infrared Spectroscopy and Mass Spectrometry of Ammonium Salts at controlled P-T conditions

E. La Francesca[1], S. De Angelis[1], M.C. De Sanctis[1], E. Ammannito[2], M. Ciarniello[1], M. Ferrari[1], A. Raponi[1]
[1]Institute for Space Astrophysics and Planetology, IAPS-INAF, Via Fosso del Cavaliere, 100, 00133, Rome, Italy,
[2]Italian Space Agency, ASI, Via del Politecnico snc, 00133, Rome, Italy

Introduction: Solar System rocky and icy bodies are currently being studied as targets of many missions. Minor bodies such as asteroids and dwarf planets are being explored both with remote sensing and lander missions in the Main Belt and among near-Earth asteroids as well as with sample return missions.

Recent spectroscopic observations by Dawn mission at Ceres [1], Hayabusa2 at Ryugu [2] and OVIRS/OSIRIS-REx at Bennu [3] showed the presence of OH-bearing, hydrated and NH4-minerals (Ceres and Ryugu), which exhibit intense absorption bands in the 2.7-3.3 μm region in Visible-Near Infrared (VIS-NIR) reflectance spectra. Ammonia-rich compounds are known to be present also in outer solar system bodies such Pluto, Charon [4, 5] and Uranus' satellite Umbriel [6]. Laboratory work on planetary analogues at controlled conditions is a fundamental step in the pathway of the interpretation of mission data.

The purpose of this study is to provide the scientific community with experimental VIS-IR spectroscopy data of ammonium salts under controlled P-T conditions, which are critical for the interpretation of space mission data. Such measurements can give us clues about the stability of these materials on airless or faint atmosphere bodies.

Experimental setup and Samples: Measurements were performed in the IR 1÷6 μm range using the CAPSULA setup in use at IAPS CLAB [7]. A Bruker's FTIR, INVENIO model, was used; the detector was a liquid nitrogen cooled MCT (Mercury Cadmium Telluride), with spectral resolution 0.13 nm. The illumination source was the internal FTIR SiC lamp suitable for measurements up to the mid IR. The FTIR was equipped with two 19-fibers bundles to illuminate and to recollect the signal. Observation geometry was the standard i=30° and e=0°. Each fiber is characterized by an Indium Fluoride Glass (IFG- InF_3) with core/cladding diameter of 200/260 μm. The spatial spot on the sample (both illumination and recollection) is about 4 mm.

We focus our investigation on ammonium salts with different composition. In particular we started with ammonium carbonate, ammonium sulphate and ammonium chloride. Because these types of compounds can be hygroscopic, a vacuum/temperature treatment can help to remove adsorbed water from the environment.

Results: In fig.1 IR spectra of NH_4-chloride in high vacuum and at cryogenic temperatures (down to 50K) are displayed.

In fig.2 ammonium carbonate data in the 2.4 - 4.7 μm region are reported. No heating treatment was done. Ammonium carbonate is instable in vacuum, for this reason only a membrane pump was used and only a rough vacuum was achieved (3 mbar). The total measurements session duration was one week. Therefore, to preserve the sample during the night a static vacuum was maintained.

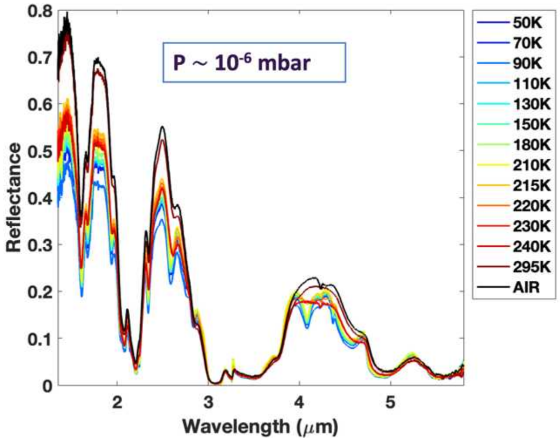

Figure 1: Spectra of Ammonium Chloride in high vacuum, in the 1-6 μm region. Deep red and black spectra are starting and ending treatment spectra, respectively.

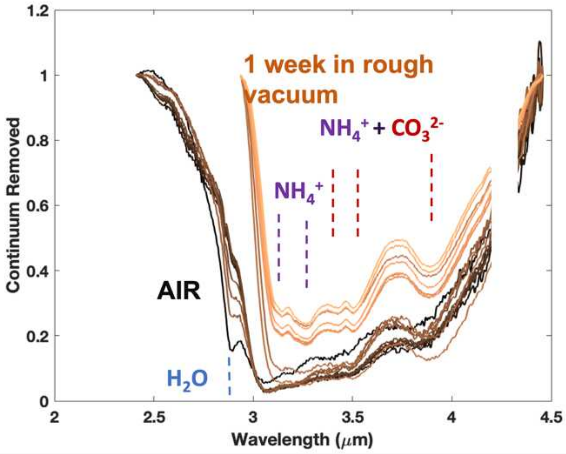

Figure 2: Spectra of Ammonium carbonate in range P amb down to 3 mbar, in the 2.4 - 4.7 μm region. Data are normalized for reflectance value at 2.43 μm. Deep red and black spectra are starting and ending treatment spectra, respectively.

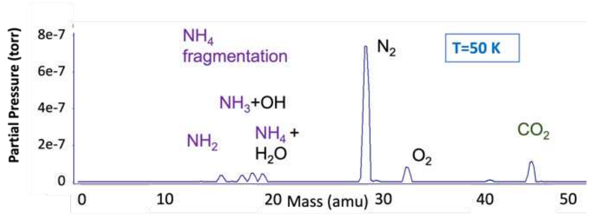

Figure 3: Mass Spectra of Ammonium carbonate in vacuum at T=50K.

The 3 μm region in ambient pressure measurement (Fig 2, black spectrum) is saturated because of both adsorbed water and ammonium absorption bands. After a week in a rough vacuum we can distinguish many NH_4 and CO_3^{2-} absorption bands, in the 3-4 μm region.
After 1 week in rough vacuum the sample quantity was considerably decreased, thus this species is extremely sensitive to low pressure. The observation of NH_4 carbonate on airless bodies could be justified thanks to low temperature effects or to specifical chemical bonding due to mixing with other materials, that could make it more stable.

In fig.3 the mass spectrum measured with NH_4 carbonate in vacuum and at 50K is shown. The peaks in the mass spectrum correspond to the principal volatile components involved in the process; namely the species that are being degassed during the process are N_2, O_2, CO_2, H_2O and the products deriving from NH_4 fragmentation.

Conclusions: IR spectroscopic measurements coupled with mass spectrometry prove to furnish a more comprehensive view and better characterize the investigated processes. In our study, mass spectra of ammonium carbonate at cryogenic temperatures (down to 50K) show how the degassing and decomposition process of NH_4 carbonate is slowed down at low temperatures with respect at ambient temperature conditions. This aspect is important to be kept in mind in order to infer the stability of such material on airless Outer Solar System bodies.

Acknowledgments: The experimental setup used has been funded in the framework of the Agreement ASI-INAF n.2018-16-HH.0.

References:

[1] De Sanctis M.C. et al., Nature Letter 528, 241-244, 2015. [2] Kitazato K., et al., Science, 364, 272-275, 2019. [3] Hamilton V.E., et al., Nature Astronomy, 2019. [4] Cook J.C., et al., Icarus 315 (2018) 30–45. [5] Cruikshank D.P. et al., 201, Icarus, 330, 155-168.[6] Cartwright R.J. et al., PSJ, 4:42 (28pp), 2023. [7] De Angelis S., et al. (2022): *16, EPSC2022-540.*

THE RADAR SIGNAL PROPAGATION THROUGH THE ICY CRUST OF JOVIAN MOONS

Turchetti, G. [1]*, Lauro, S. E. [1], Brin, A. [1], Cosciotti, B. [1], Mattei, E. [1], Pettinelli, E. [1]

[1] Mathematics and Physics Dept., Roma Tre University

*Corresponding author: Gabriele.turchetti@uniroma3.it

Introduction: The search for liquid water in the Solar System and beyond is one of the main goals of planetary exploration being water the fundamental ingredient for life as we know it. According to the current literature, several outer Solar System satellites like Europa, Enceladus, Titan, Ganymede, and Callisto host a planetary ocean (Hendrix et al., 2019). Therefore, probing these Ocean Worlds and investigating the chemical-physical properties of the water would provide information about their potential habitability. Ganymede, Callisto, and Europa are the targets of the missions JUICE (Jupiter Icy Moons Explorer) launched in April 2023 and Europa Clipper that will be launched in October 2024. In these missions the radar sounders RIME [2] (Radar for Icy Moons Explorations) and REASON [3] (Radar for Europa Assessment and Sounding: Ocean to Near-surface) will probe the interior of the Jovian icy moons using Radio waves to search for the ocean/ice interface or any signature of shallow liquid water inside the icy crusts.

Background: Radio Echo Sounding techniques (RES) has already been successfully employed to study subglacial lakes in Antarctica and Greenland [4][5] and to detect liquid water below the South Polar Layered Deposit (SPLD) on Mars [6][7]. With their cold icy crust, Galilean moons represent an ideal environment for RES surveys; in the frequency band of RIME and REASON (9 and 60MHz), very cold ice is known to generate very low attenuation allowing a very deep signal investigation. The inner ocean is expected to be more than 80 km deep, for Ganymede and Callisto [8] and in the first 10-15 km for Europa. In the latter, surface features also suggest the presence of shallow liquid water pockets [9][10]. Assessing the maximum penetration depth and the targets detectability in different scenarios will help interpreting the radar data. Several simulations have already been developed, considering different thermal gradients, ice composition, heating transport, and shell thickness [11]. However, recent studies have revealed the presence of different salts on Europa’s surface [12]. It is well known that salts, depending on concentration, distribution, and ice temperature, could strongly affect the dielectric properties of ice increasing the attenuation of radar signals and potentially preventing the detection of the ocean.

Methods: To investigate the effects of different salts in the icy crust on the propagation of the radar signals, we explored several possible scenarios by making simulations. To reproduce the condition of the missions JUICE and Europa Clipper in the simulations, we analysed the propagation of a 9MHz signal through an icy crust with the same characteristics of those of the satellites. We used the thermal gradients (figure 1) proposed by literature (e.g., Buffo et al. [13]), assuming the concentration of salts in the ice as homogeneous or variable. We explored a large set of Jovian moons icy crust configurations using as inputs the dielectric measurements of pure and doped ice collected in the EPP-Lab at Roma Tre laboratory. In this way we produced simulated radargrams (figure 2), the outputs of a radar analysis that show discontinuities of different materials in the crust of a planet or a satellite. These simulations allow us to understand, depending on the ice characteristics, at which depth we could detect liquid water beneath the surface and how any discontinuities of dielectric properties in the ice would appear in the data.

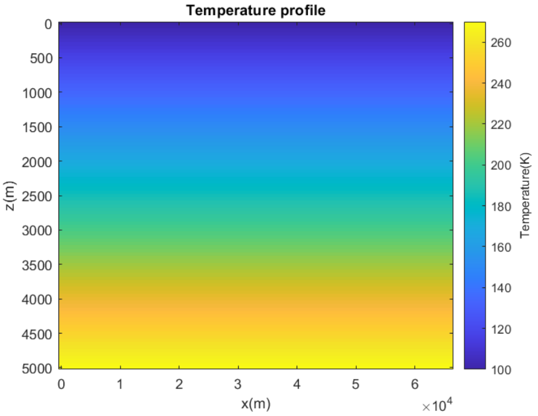

Figure 1: Temperature gradient of the icy crust of Europa, according to Buffo et al. [13], assuming the presence of a liquid water body. The vertical axis represents the depth, the surface is set at 0m, and a liquid water body is set at 5km.

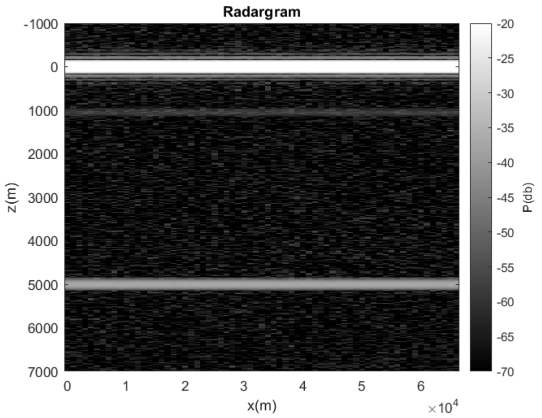

Figure 2: Icy crust simulated radargram collected with a signal of 1MHz bandwidth centered in 9MHz. The vertical axis represents the depth; the horizontal axis is the along-track distance covered by the spacecraft during data acquisition; the grayscale represents the power of the echoes collected by the radar that are linked to dielectric discontinuities of different materials. The stratigraphy, in this case, is formed by the surface, an icy layer of 1km doped with NaCl at the concentration of 10mM, an icy layer of 4 km doped with NaCl at the concentration of 0.1mM, and a liquid water body. The three electric discontinuities (surface at 0m, first-second ice layer at 1km, ice-water at 5 km) are clearly visible.

Conclusions: This work represents a starting point to assess the performance of RIME and REASON in a cold icy/salty crust and to provide synthetic radargrams to be compared with real data. The final goal of the study will be the production of a large dataset useful to understand under what conditions the water will be detectable inside/below the ice.

References

[1] Hendrix, A. R., et al. (2019) -The NASA roadmap to ocean worlds. In: Astrobiology, 19.1, 1-27.
[2] Bruzzone L. et al. (2013) -RIME: Radar for icy moon exploration. In: IEEE international geoscience and remote sensing symposium-IGARSS.
[3] Blankenship D. et al. (2018) - REASON for Europa. In: 42nd cospar scientific assembly 42: B5-3
[4] Siegert, M. J. (2018) -A 60-year international history of Antarctic subglacial lake exploration. In: J. Geol. Soc. Lond. 461, 7–21.
[5] Oswald, G. K. A. et al. (2008) -Recovery of subglacial water extent from Greenland radar survey data. In: J. Glaciol. 54, 94-106.
[6] Orosei, R. et al. (2018) -Radar evidence of subglacial liquid water on Mars *Sci., 361, 490-493*
[7] Lauro, S. E. et al. (2020) Multiple subglacial water bodies below the South Pole of Mars unveiled by new MARSIS data *Nature Astronomy, 5, 63-70*
[8] Heggy E. et al. (2017) -Radar probing of Jovian icy moons: Understanding subsurface water and structure detectability in the JUICE and Europa missions. In: Icarus 285: 237-251.
[9] Culberg R. et al. (2022) -Double ridge formation over shallow water sills on Jupiter’s moon Europa. In: Nature Communications 13.1
[10] Chivers C. J. ert al. (2023) -Stable Brine Layers beneath Europa’s Chaos. In: The Planetary Science Journal
[11] Kalousová, K. et al. (2017) -Radar attenuation in Europa's ice shell: Obstacles and opportunities for constraining the shell thickness and its thermal structure. In: Journal of Geophysical Research: Planets 122.3: 524-545.
[12] Trumbo S. K. et al., (2019) -Sodium chloride on the surface of Europa. In: Science advances 5.6:eaaw7123.
[13] Buffo J. J. et al., (2021) -Dynamics of a Solidifying Icy Satellite Shell. In: Journal of Geophysical Research: Planets

THE NEW A-CENTRAL MODEL FOR THE GEOMETRICAL CALIBRATION OF DAEDALUS LUNAR EYES FOR LAVA TUBE EXPLORATION.

E. Simioni[1], C. Pernechele[1] P. Martini[1], D. Scaccabarozzi[2], B. Saggin[3], D. Greggio[1], L. Lessio[1], P. Cambianica[1], A. Marchini[3], Wolfgang Erb[3], Monica Beghini[4,] , [1] Osservatorio Astronomico di Padova, Vicolo dell'Osservatorio 5, 35122 Padova, Italy (Emanuele.simioni@inaf.it),[2] Dipartimento di Meccanica, Politecnico di Milano, Polo Territoriale di Lecco, via G. Previati 1c, 23900, Lecco, Italy, [3]Università degli Studi di Padova, Dipartimento di Matematica "Tullio Levi-Civita", 35121 Padova, Italy, [4] DISMA, Dipartimento di Scienze Matematiche "Giuseppe Luigi Lagrange", 10129 Torino, Italy

Introduction: The possibility to explore the lunar subsurface by accessing lava tubes from skylights has been subject to an ESA's call for ideas in its Open Space Innovation Platform in the SysNova Lunar Caves system studies framework. The final aim is to enter and explore the skylight named Marius Hills Hole in Oceanus Procellarum (303.3°E, 14.2°N), which is believed to be an access point to a large underground void and represents a source of interest for the science community since Kaguya, Lunar Reconnaisance Orbiter (LRO) and Gravity Recovery and Interior Laboratory (GRAIL) missions have unequivocally underlined the presence of deep voids below the Lunar surface. These subsurface voids could be the base for long-term presence in human exploration framework [1] because: i) represent a natural shield against possible meteorite impacts, cosmic radiation, as well as extreme temperature variations (the equivalent radiation is the 0.3% of the total incident radiation on the surface); ii) are characterized by stable temperatures[2]; iii) could trap resources that are fundamental to human permanence, such as water.This overview could definitely change the paradigm of how approach future lunar exploration and open new doors to Martian exploration.

In this context, a robotic sphere named DAEDALUS (Descent and Exploration in Deep Autonomy of Lava Underground Structures) [3,4] has been selected for a subsequent ESA Concurrent Design Facility in order to descend and map the collapse pit, as primary objective, and, eventually, navigate and map the underground cave to confirm the preliminary results defined by the LROC NAC floor images in [3].

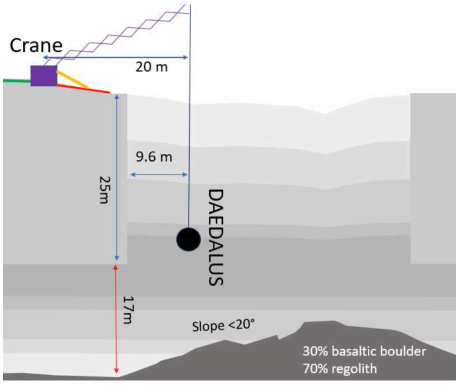

Fig 1: Scheme of the descending configuration in the Marius Hill skylight

For these reasons, the DAEDALUS is designed as a sphere and lowered into the pit using a robotic crane [5] system mounted on a dedicated rover (avoiding the sloping area before the void).

DAEDALUS CAM and other payloads:

The DAEDALUS robot has been designed to be equipped with environmental sensors, laser scanners and an optical instrument (DAEDALUS CAM) able to provide a 360 view of the vertical and subsurface environment and to retrieve as large amounts of data as possible. This is aimed both to answer scientific questions such as the morphology and composition of the lava layers outcropping in the vertical walls of the skylight, and to characterize in detail the morphology and assess the trafficability of the cave floor and eventual obstacles or hazards to plan further exploration.

The cameras are foreseen to capture a full view of the main void using natural illumination.

The DAEDALUS CAM is an optical camera composed of four Bifocal Panoramic Lenses (BPLs) [6] settled in a crossed configuration. A BPL (see top left panel in Fig. 2) is a lens which may record a panoramic field of view (FOV) of 360°x100° and, simultaneously, a round FOV of 20° with higher resolution (frontal field).

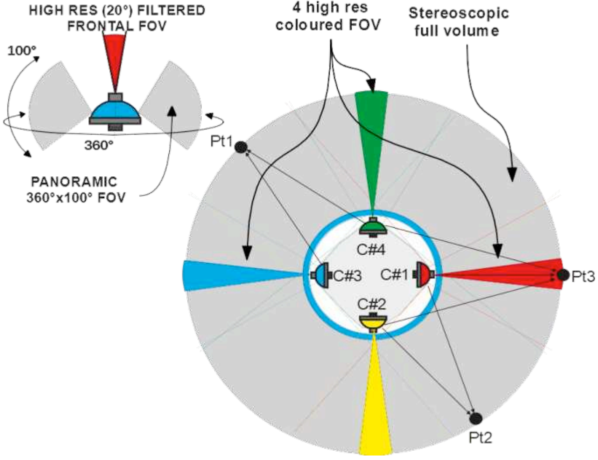

Fig. 2: BPL and Daedalus CAM concept.

The BPL main parameters are: a volume of 350 cm^3, a weight of 195 g, a power consumption of 4 W, a 2k x 2k format image sensors. The BPL provides an angular resolution of 0.1°/px (paraxial) in the panoramic field and about 0.03°/px in the frontal field.

Placing four of such BPLs, as shown in Fig. 3, the full volume surrounding the DAEDALUS CAM may be sampled in stereoscopic mode: all the points of the whole space around are viewed by at least two cameras (as ex. Pt1 and Pt2 in Fig. 2) in the panoramic field and, simultaneously, by the frontal (higher resolution) FOV.

The four colored higher resolution channels operate scientific recognition in four different pass-band filters allowing the monitoring of any rock structure and texture with high detail and providing an estimate of thermal stress induced micro fracturing as well as to perform a modal analysis of the distribution of clasts/phenocryst within a rock.

Pajload development: BPLs belong to Hyper-Hemispheric optical objectives. The geometrical calibration of this kind of lenses introduces many setup difficulties due to the extreme field of view. Different methods were developed to perform this kind of geometrical calibration in a limited ambient of a clean room and taking advantage of simple calibration chessboard. This is the case Scaramuzza model hystorically used by NASA for extensive cameras such as fisheye and panoramic lens.

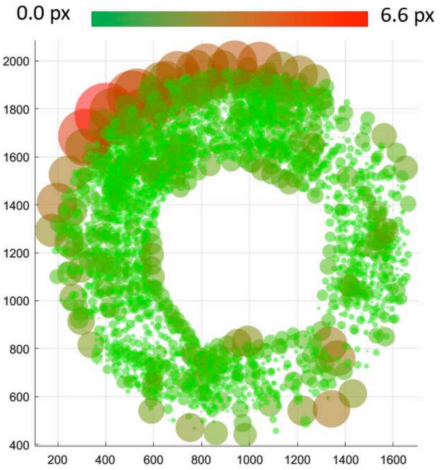

Fig 3: Residual of the riprojection [px] using classical panoramic calibration methods

Despite its efficiency, the Scaramuzza toolbox demonstrates to be ineffectual in the case of a hyper hemispherical lens due to modelistic limits in the approximation of the projection system introduced which does not conseider the acentrality of the system and does not fit with the real data in the external part of the field of view (as shown in Fig 3.). In particular this is linked to the pupil shift with respect to the zenith angle shown in red in Fig. 4.

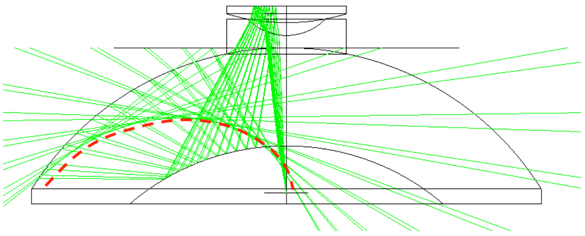

Fig. 4 the optical diagram of the BPL underling for all the chief rays (in green) the movement of the entrance pupil (in red)

New models have been develeped and tested at the INAF Padova laboratory to optimize the definition of the projective design, a strongly important task, considering its photogrammetric purpose. Results of this optimization (which underline the uniformity of the errors in the external region of the FOV) can be seen in Fig 5.

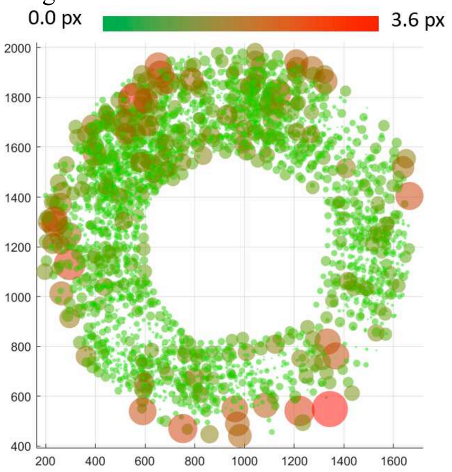

Fig 5: Residual of the riprojection [px] using novel panoramic calibration methods

DAEDALUS CAM images will be dewarped after downlink [8]. The same team involved in this challenging calibration is developing a FPGA-based exposure algorithm able to balance panoramic exposures to solve the illumination conditions.

Part of the team involved has developed, in the past years, the 3DPD [9], a stereo processing chain, capable of producing 3D reconstructions (DTM), starting from satellites' images. These photogrammetric activities are currently applied to the Martian images of CaSSIS and are the starting point for the future processing of the stereo pairs that will be acquired by the STC stereo camera [9] for the Bepi- Colombo mission.

Acknowledgments: This work is funded by ESA AO/2-xxx/20/NL/GLC, proposal TA 2-1739 OSIP Lunar Caves System Studies.

References: [1] Haruyama et al. (2012) (pp 139-163) Springer. [2] Tyler Horvath (2022) Geophysical Research Letters [3] Pozzobon et al. (2021), 52th LPSC, Abstract #1886). [4] Borrmann et al. (2021), 52th LPSC, Abstarct #2073. [5] Miaja et al., (2022), Acta Astronautica [6] Pernechele (2016), Opt Expr., 24(5), 5014. [7] Simioni et al. (2020),[8] C.Pernechele et al. (2023), this conference. [9] Simioni et al.(2021),

THE ANIME CUBESAT FOR NEAR-EARTH ASTEROIDS EXPLORATION.

Perna D.[1], Casalino L.[2], Fedele A.[3], Ivanovski S.[4], Lavagna M.[5], Pajola M.[6], Zannoni M.[7], Bechini M.[5], Belloni E. [5], Brienza D. [3], Cicala M.[3], Cremonese G.[6], Dotto E.[1], Ieva S.[1], Lasagni Manghi R. [7], Lucchetti A.[6], Manzari P. [3], Mazzotta Epifani E.[1], Natalucci S.[3], Prinetto J.[5], Simioni E.[6], Tortora P.[7], Zanotti G.[5]

[1] INAF - Osservatorio Astronomico di Roma, [2] DIMEAS - Politecnico di Torino, [3] Agenzia Spaziale Italiana, [4] INAF - Osservatorio Astronomico di Trieste, [5] DAER - Politecnico di Milano, [6] INAF - Osservatorio Astronomico di Padova, [7] CIRI Aerospace - Università di Bologna

Context: Interest in near-Earth asteroids (NEAs) has experienced rapid growth in recent decades for three primary reasons. Firstly, their proximity enables the exploration and investigation of small celestial bodies, down to the meter scale, thereby advancing our comprehension of the mechanisms involved in planetary formation. Secondly, this knowledge is crucial for mitigating the potential threat of their collision with Earth. Lastly, the near-future prospect of exploiting NEAs holds the potential to exponentially expand the natural resources available to humanity.

Ground-based observations of thousands of NEAs have unveiled the remarkable diversity within this population in terms of physical properties. So far, only a handful of NEAs have been visited by space missions: each of them has yielded unexpected discoveries and significant advancements in our understanding of planetary sciences.

The accomplishments of the NASA/JPL Mars Cube One mission in 2018 and of the ASI LICIACube mission in 2021 marked a new frontier in the exploration of the solar system using small satellites designed for deep-space missions.

In this context, the use of smallsats emerges as a fundamental strategy for exploring the vast diversity of physical properties exhibited by NEAs: this category of spacecraft offers unprecedented flexibility, compact size and relative ease of deployment, enabling more agile missions compared to traditional space probes.

Outline: Within the framework of the ALCOR program, the Italian Space Agency (ASI) is funding the “Asteroid Nodal Intersection Multiple Encounters (ANIME)” CubeSat Mission, with Phase A starting in November 2023. The aim is to develop a 12U CubeSat mission tailored for the exploration of multiple NEAs encountered during their transits through their orbital nodes. ANIME’s baseline mission profile encompasses flybys with two Potentially Hazardous Asteroids (PHAs) and a rendezvous with a small NEA with a size in the order of tens of metres. The selection of mission targets is based on their distinctive physical and orbital characteristics, rendering them exceptionally intriguing for both scientific research and planetary protection considerations.

The mission architecture is designed around flight-proven components, featuring a scientific payload comprising two RGB cameras and an onboard transponder for acquiring radio science data. By leveraging these components, ANIME aims to provide valuable insights into the latest theories concerning planetary formation scenarios. Noteworthy, such information will be also relevant for planetary protection purposes, as well as to assess a potential near-future exploitation of asteroid resources. Additionally, the mission seeks to validate critical technologies essential for CubeSat exploitation in deep space.

ESTABLISHING A COMMON GROUND FOR RADIATIVE TRANSFER IN EARTH AND PLANETARY ATMOSPHERES: RECENT EFFORTS

G. Liuzzi[1], D. Grassi[2], T. Maestri[3], G. Masiello[1], G. L. Villanueva[4], E. Papandrea[5], C. Serio[1], M. Martinazzo[3], V. Kofman[4,6], F. Biagiotti[2,7]. [1]Scuola di Ingegneria, Università degli Studi della Basilicata, Via dell'Ateneo Lucano 10, 85100 Potenza (PZ), Italy, giuliano.liuzzi@unibas.it, [2]INAF – Istituto di Astrofisica e Planetologia Spaziali (INAF-IAPS), Via Fosso del Cavaliere 100, I-00133, Rome, Italy, [3]Dipartimento di Fisica e Astronomia (DIFA), Università di Bologna, Via Irnerio 46, 40126 Bologna (BO), Italy, [4]NASA Goddard Space Flight Center, 8800 Greenbelt Rd., 20771 Greenbelt, MD, USA, [5]CNR, Istituto di Scienze dell'Atmosfera e del Clima (ISAC), Via Piero Gobetti 101, 40129 Bologna (BO), Italy, [6]American University, 4400 Massachusetts Avenue, 20016 Washington DC, USA, [7]Department of Physics, University of Rome "La Sapienza", Piazzale Aldo Moro 2, 00185 Rome, Italy.

Introduction: The last 20 years have seen the flourishing and development of a plethora of specialized radiative transfer codes for Earth science [1], [2] and related retrieval packages, which in most cases are specialized to accomplish specialized tasks. While most Earth retrieval packages are based on classical Optimal Estimation, they also are not uniform in notations and error characterization [3], making it challenging to compare their performances and specificity. On the side of radiative transfer, planetary sciences have benefited from the increasing availability of innovative line-by-line radiative transfer tools [4]–[6] which can be used on a variety of planetary bodies and atmospheres, and that incorporate updated spectral databases such as HITRAN [7]. In this work, we give an overview of the most recent innovations in radiative transfer for planetary science and Earth science, showing that important divergencies do exist in the treatment of spectroscopic parameters of gases, aerosols and surfaces. While, in many cases, these two branches of applications have grown apart, we elaborate pragmatic suggestions, guidelines and protocols to integrate elements from the two branches, with the objective of 1) simplifying codes used in Earth science and making them more flexible, and 2) get the planetary science community engaged with methods developed for Earth science.

Data and methods: The advent of new missions dedicated to the exploration of Earth radiation budget and to the spectroscopy of water vapor and trace gases, such as the Far infrared Outgoing Radiation Understanding and Monitoring (FORUM, [8]) and the Polar Radiant Energy in the Far-InfraRed Experiment (PREFIRE, [9]) have pushed community efforts to revise the specifics of the way in which radiative transfer on Earth is performed, since forthcoming missions are devoted to explore a spectral interval (100-600 cm^{-1}) that has not been observed from orbit thus far. We will focus on two aspects of this work: 1) the revision of the treatment of water vapor continuum, and 2) the way in which cloud properties are described and parameterized.

As for the continuum, the model that describes it most in use is the MT-CKD [10], which however is also tailored on the water vapor spectroscopic database as integrated in LBLRTM [11]. Recent works from the planetary science community [12] have demonstrated that the formalism of the continuum absorption can be expressed in terms of collision-induced absorptions (CIAs), which allows to treat the water vapor continuum in th same way as N_2-N_2, O_2-O_2, CO_2-CO_2 and other CIAs relevant to Earth and planetary science. We have integrated this new approach into a few of the radiative transfer codes most in use to analyze hyperspectral Earth observations (e.g., [13]) and demonstrated that CIAs formalism is effective and allows for a unified, simpler treatment of water self, foreign and other gases continuum on Earth.

As for clouds, we have recently proposed and implementing a new method [14] to provide fast simulations over the whole longwave spectrum, with high accuracy, particularly for optically thin scattering layers like cirrus clouds on Earth. Schemes of this kind can be particularly relevant when there is the need for fast computing of radiances in presence of clouds, and could be extended to several types of aerosols whose optical properties are known.

In the context of planetary science, another issue of importance regards the capability to retrieve atmospheric vertical profiles of temperature and other constituents of interest. Modern codes such as the Planetary Spectrum Generator (PSG, [4]) and ASIMUT [6] include this capability with specifics similar to those used in Earth atmospheric science. However retrievals of full vertical profiles with line-by-line codes can require significant computational resources and time. In this context, we show a new approach based on layer aggregation that can significantly reduce the required resources and maximize, at the same time, the information content extracted from the data. This approach, together with the ones illustrated above, opens the possibility to establish a common formalism across different planets, instruments and spectral intervals.

References:

[1] J. Vicent *et al.*, "Comparative analysis of atmospheric radiative transfer models using the Atmospheric Look-up table Generator (ALG) toolbox (version 2.0)," *Geoscientific Model Development*, vol. 13, no. 4, pp. 1945–1957, Apr. 2020, doi: 10.5194/gmd-13-1945-2020.

[2] H. H. Aumann *et al.*, "Evaluation of Radiative Transfer Models With Clouds," *Journal of Geophysical Research: Atmospheres*, vol. 0, no. 0, Jun. 2018, doi: 10.1029/2017JD028063.

[3] T. von Clarmann *et al.*, "Overview: Estimating and reporting uncertainties in remotely sensed atmospheric composition and temperature," *Atmospheric Measurement Techniques*, vol. 13, no. 8, pp. 4393–4436, Aug. 2020, doi: 10.5194/amt-13-4393-2020.

[4] G. L. Villanueva *et al.*, *Fundamentals of the Planetary Spectrum Generator*. 2022. Accessed: Jun. 07, 2022. [Online]. Available: https://ui.adsabs.harvard.edu/abs/2022fpsg.book.....V

[5] G. L. Villanueva, M. D. Smith, S. Protopapa, S. Faggi, and A. M. Mandell, "Planetary Spectrum Generator: An accurate online radiative transfer suite for atmospheres, comets, small bodies and exoplanets," *Journal of Quantitative Spectroscopy and Radiative Transfer*, vol. 217, pp. 86–104, Sep. 2018, doi: 10.1016/j.jqsrt.2018.05.023.

[6] A. C. Vandaele *et al.*, "Composition of the Venus mesosphere measured by Solar Occultation at Infrared on board Venus Express," *J. Geophys. Res.*, vol. 113, no. E5, p. 2008JE003140, May 2008, doi: 10.1029/2008JE003140.

[7] I. E. Gordon *et al.*, "The HITRAN2020 molecular spectroscopic database," *Journal of Quantitative Spectroscopy and Radiative Transfer*, p. 107949, Sep. 2021, doi: 10.1016/j.jqsrt.2021.107949.

[8] L. Sgheri *et al.*, "The FORUM end-to-end simulator project: architecture and results," *Atmospheric Measurement Techniques*, vol. 15, no. 3, pp. 573–604, Feb. 2022, doi: 10.5194/amt-15-573-2022.

[9] B. H. Kahn, B. J. Drouin, and T. S. L'Ecuyer, "Assessment of Sampling Sufficiency for Low-Cost Satellite Missions: Application to PREFIRE," *Journal of Atmospheric and Oceanic Technology*, vol. 37, no. 12, pp. 2283–2298, Dec. 2020, doi: 10.1175/JTECH-D-20-0023.1.

[10] E. J. Mlawer, V. H. Payne, J.-L. Moncet, J. S. Delamere, M. J. Alvarado, and D. C. Tobin, "Development and recent evaluation of the MT_CKD model of continuum absorption," *Philosophical Transactions of the Royal Society A: Mathematical, Physical and Engineering Sciences*, vol. 370, no. 1968, pp. 2520–2556, Jun. 2012, doi: 10.1098/rsta.2011.0295.

[11] S. A. Clough *et al.*, "Atmospheric radiative transfer modeling: a summary of the AER codes," *Journal of Quantitative Spectroscopy and Radiative Transfer*, vol. 91, no. 2, pp. 233–244, Mar. 2005, doi: 10.1016/j.jqsrt.2004.05.058.

[12] V. Kofman and G. L. Villanueva, "Absorption in exoplanet atmospheres: Combining experimental and theoretical databases to facilitate calculations of the molecular opacities of water," *Journal of Quantitative Spectroscopy and Radiative Transfer*, vol. 270, p. 107708, Aug. 2021, doi: 10.1016/j.jqsrt.2021.107708.

[13] G. Liuzzi, G. Masiello, C. Serio, S. Venafra, and C. Camy-Peyret, "Physical inversion of the full IASI spectra: Assessment of atmospheric parameters retrievals, consistency of spectroscopy and forward modelling," *Journal of Quantitative Spectroscopy and Radiative Transfer*, vol. 182, pp. 128–157, Oct. 2016, doi: 10.1016/j.jqsrt.2016.05.022.

[14] M. Martinazzo and T. Maestri, "The MAMA Algorithm for Fast Computations of Upwelling Far- and Mid-Infrared Radiances in the Presence of Clouds," *Remote Sensing*, vol. 15, no. 18, Art. no. 18, Jan. 2023, doi: 10.3390/rs15184454.

ITALIAN POTENTIAL CONTRIBUTION TO NASA URANUS FLAGSHIP AND NEW FRONTIERS 5 MISSIONS.

G. Sindoni[1], A. Olivieri[2], P. Tortora[3], M. C. De Sanctis[7], A. Ammannito[1], A. Amodio[2], D. Biccari[16], F Bovolo[4], L. Bruzzone[5], V. Della Corte[15], D. Durante[6], A. Genova[6], D. Grassi[7], F. Ferri[8], G. Lari[9], R. Lasagni Manghi[3], A. Longobardo[7], A. Lucchetti[10], G. Mitri[11], A. Mura[7], R. Orosei[12], M. Pajola[10], P. Palumbo[7], R. Pepe[2], G. Piccioni[7], G. Spada[13], A. Tiberia[1], F. Tosi[7], D. Turrini[14], M. Zannoni[3].

[1]Agenzia Spaziale Italiana, ASI HQ, Rome, Italy (giuseppe.sindoni@asi.it), [2]Agenzia Spaziale Italiana, Centro di Geodesia Spaziale, Matera, Italy, Rome, Italy, [3]University of Bologna, DIN, Italy, [4]Fondazione Bruno Kessler, Trento, Italy, [5]University of Trento, Trento, Italy, [6]Sapienza University of Rome, Italy, [7]INAF-IAPS, Rome, Italy, [8]Università degli Studi di Padova, CISAS, Padova, Italy, [9]University of Pisa, DM, Italy, [10]INAF-OAPD, Padova, Italy, [11]Università d'Annunzio, InGeo, Pescara, Italy, [12]INAF-IRA, Bologna, Italy, [13]University of Bologna, DIFA, Italy, [14]INAF-OATO, Torino, Italy, [15]INAF Osservatorio Astronomico di Capodimonte, Napoli, Italy, [16]NASA Jet Propulsion Laboratory, Pasadena, California, USA

Introduction:

With the release of the Planetary Science and Astrobiology Decadal Survey 2023–2032 [1], in the spring of 2022, a mission consisting of of an Orbiter and a Probe that would explore Uranus (UOP) was identified as the next priority Flagship project. This is intended to fill the gap in the current knowledge of the ice giants, carrying out a multi-year orbital tour of Uranus and its system, studying the planet’s interior, atmosphere, magnetosphere, satellites, and rings.

Moreover, NASA’s Science Mission Directorate (SMD) plans to release an Announcement of Opportunity (AO) to solicit New Frontiers (NF5) Program mission [2] investigations with the following schedule:

- Draft AO Text: Released on January 10, 2023
- Estimated Release of final AO: No earlier than 2026 (target)
- Estimated Proposal due date: 90 days after AO release.

In this context, the Science and Research Directorate (DSR) of the Italian Space Agency (ASI) was contacted by partners in the United States with the request for technical/scientific contributions, including hardware, to the several NF5 mission proposals being prepared.

Previous ASI collaborations on NASA missions

NASA and ASI have a long-standing collaboration on planetary exploration missions, which includes the provision of instruments and S/C subsystems and the invitation of Italian researchers to take part in the science teams. Examples of this virtuous collaboration are the NASA/ESA/ASI’s Cassini-Huygens to the Saturn system, NASA’s New Frontiers Juno to Jupiter, NASA’s Discovery Dawn to Vesta and Ceres, NASA’s MRO to Mars and NASA’s Discovery VERITAS to Venus.

Scientific instruments and associated science themes of interest for ASI and the Italian planetary science community

In the context of the Uranus Flagship and NF5 initiatives, ASI has expressed its interest in collaborating actively with NASA in providing scientific instruments with a substantial technological and flight heritage, that would enable science investigations relevant to the Giant Planets’ systems and small bodies. Here is a (non-exhaustive) list of the potential instruments, and associated science themes, that may be part of the Italian contributions to the NASA-led Uranus exploration endeavor and/or for the exploration of the Solar System through a NF5 mission:

Radio Science. ASI and its industrial partners have extraordinary experience in providing radio science instrumentation, e.g. with 3GM [3] on board of JUICE. A radio science experiment can characterize the internal structure (via two-way Doppler tracking) and the atmosphere (via one-way uplink radio occultations) of both planets and their largest moons. Moreover, ring occultations would enable retrieving ring particle size. Multiple close flybys of planets’ major satellites and small bodies can be used to determine their gravity fields and ephemerides, search for atmospheres (both the neutral and charged components), and probe their surfaces via bistatic radar experiments.

Visible and Near-Infrared Image-Spectroscopy. ASI has a long heritage with VIS-NIR spectroscopy on planetary missions. In particular, among last Italian successful spectrometers for the exploration of Giant Planets and small bodies we have VIR/Dawn [4] and JIRAM/Juno [5]. Moreover, Italy provided a strong contribution to the MAJIS/JUICE instrument [6].

In terms of Ice and Giant Planets’ atmospheric science, such an instrument would allow assessing the planet’s global energy balance of the planet, constraining the three-dimensional structure of clouds and, wind estimates from cloud tracking, temperature of the stratosphere, and studies of the vertical structure of the upper clouds. For the planets' moons, this would enable unveiling their surface composition by identifying and mapping various chemical species, notably volatiles, and organics. In terms of geological processes, multiple measurements (including tectonism, cryovolcanism, mass wasting, and impact cratering) can be accomplished.

Visible, multiband and high-resolution camera. The most recent example of an ASI-contributed VIS camera is JANUS [7], currently in-flight the ESA/JUICE spacecraft. To provide an understanding of planets' moons shapes, exo-and endogenic geological processes, as well as dynamical and compositional characterization of giant planets' atmosphere, capability and performances of an instrument similar to JANUS are required.

Radar Sounding. ASI has been contributing radar instrumentation on a variety of NASA missions, e.g. with SHARAD [8] on MRO mission. Ice is among the most transparent natural materials at frequencies used by radar sounders, and thus such instruments are expected to be effective in probing the moons of Giant Plantes and their outer icy or mixed rocky-icy shells. The possible detection of subsurface oceans would be beyond the penetration capabilities of any technically feasible radar sounder, according to current models which predict a crust thickness of hundreds of km, but stratigraphy within the outer shell could bear evidence of diapirism, convection, and other types of endogenic activity, both past and present.

Dust sensors. ASI heritage on dust sensors comes from the GIADA instrument [9] on boad the Rosetta ESA mission. GIADA was composed by 3 subsystems, microbalances, impact sensor and grain detector system. These all three measurement subsystems using the Rosetta GIADA heritage followed an improvement/development path allowing their use in different new space missions. The improved microbalance system, the VISTA instrument [10], was selected and part of the scientific payload on board ESA HERA mission; the impact sensor concept extend for hyper-velocity impacts allowed the development of DISC instrument unit [11] of the DFP payload onboard the ESA Comet Interceptor mission. These sensors can achieve the following goals in the context of the exploration of dusty/icy enviroments of giant planets' moons and comets: 1) Direct sensing of mass flux; 2) Indirect sensing of mass flux by measurement of particles/s/m^2 and size distribution; 3) Measurement of particles/s/m^2 and correlation with size distribution from model.

Atmospheric Structure Instrument for the entry probe. In-situ measurements during the entry and descent allow for investigating the atmospheric composition, structure, and dynamics down deep into the atmosphere. The instrument would consist of a multi-sensor package designed to measure the physical quantities characterizing Uranus' and Gas Giants atmosphere during the entry and descent of the probe into the planet. The key measurements will be the acceleration, pressure, temperature, and electrical properties all along the probe's descent into the atmosphere to investigate the atmospheric structure, dynamics, and electricity.

References:

[1] "Planetary Science and Astrobiology Decadal Survey 2023-2032: Public Release of the Survey Report". www.nationalacademies.org. Retrieved 2022-04-01.

[2] "New Frontiers 5 (NF5) – Announcement of Opportunity (AO)". https://newfrontiers.larc.nasa.gov/NF5/. 08/24/2023.

[3] Iess L. et al (2013). European Planetary Science Congress 2013, id.EPSC2013-491

[4] de Sanctis M. C. et al. (2011). Space Science Reviews, Volume 163, Issue 1-4, pp. 329-369.

[5] Adriani A. et al. (2017). Space Science Reviews, Volume 213, Issue 1-4, pp. 393-446.

[6] Piccioni G. et al. (2014). EGU General Assembly 2014, held 27 April - 2 May, 2014 in Vienna, Austria, id.10925.

[7] Palumbo P. et al. (2014). EGU General Assembly 2014, held 27 April - 2 May, 2014 in Vienna, Austria, id.10227.

[8] Seu R. et al. (2007). Journal of Geophysical Research, Volume 112, Issue E5, CiteID E05S05.

[9] Colangeli L. et al. (2007). Advances in Space Research, Volume 39, Issue 3, p. 446-450.

[10] Palomba E. et al. (2022). 16th Europlanet Science Congress 2022, id.EPSC2022-927.

[11] Della Corte V. et al. (2023). Advances in Space Research, Volume 71, Issue 8, p. 3457-3467.

TASTE - A CUBESAT MISSION TO DEIMOS. A. Meneghin[1], J.R. Brucato[1], V. Della Corte[2], M. Lavagna[3], G. Zanotti[3], J. Prinetto[3], M. Bechini[3], E. Belloni[3], F. De Cecio[3], A. Dottori[3], F. Fiore[4], G. Baroni[4], M. Citossi[4], F. Dogo[5], A. Fedele[6], M. Amoroso[6], S. Natalucci[6], [1]INAF - Osservatorio Astrofisico di Arcetri (andrea.meneghin@inaf.it), [2] INAF - Osservatorio astronomico di Capodimonte, [3]POLIMI - Dipartimento di Scienze e Tecnologie Aerospaziali, [4]INAF - Osservatorio Astronomico di Trieste, [5]Università degli Studi di Trieste, [6]ASI - Agenzia Spaziale Italiana.

Introduction: The Terrain Analyzer and Sample Tester Explorer (TASTE) is a CubeSat mission consisting of an orbiter capable of deploying a lander to explore the Martian moon Deimos. TASTE is funded by the Italian Space Agency (ASI) under the Alcor programme. The consortium, made up of INAF-OAA, INAF OAT and Politecnico di Milano, has successfully completed Phase A and is about to start Phase B.

Deimos was discovered in 1877 by Asaph Hall at the US Naval Observatory in Washington. Since then, Deimos has been studied only by Earth observation until the Mariner 9 mission in 1971. Further information was provided by the Viking orbiters in the late 1970s, the Soviet Phobos 2, NASA's Mars Global Surveyor, Europe's Mars Express and the UAE's Emirates Mars Mission (EMM).

The Japan Aerospace Exploration Agency (JAXA) plans to launch the Mars Moons eXploration (MMX) mission to visit both Martian moons and collect samples from the surface of Phobos for return to Earth.

Deimos and Phobos are considered key targets for understanding the origin and evolution of Mars and the terrestrial planets of the Solar System. To date, there is no clear consensus in the scientific community about the formation of the two moons [1]. There are two main hypotheses for the origin of the moons: they are thought to have been formed by a giant impact between Mars and a protoplanet, or they are captured asteroids [2].

TASTE Objectives: The high-level scientific objectives of the TASTE mission are to understand the origin of Deimos by combining both global morphology and composition from close orbit and local surface elemental, organic and mineralogical composition with a lander, complementing the expected results of the JAXA MMX mission [3].

TASTE will carry a suite of instruments on both the orbiter and lander submodules. The orbiter will carry a camera and an X- and γ-ray spectrometer, while the lander will carry a camera and the Surface Sample Analyser (SSA). In addition, the orbiter's radio will be used to collect gravity field data. All these instruments will work alone and in synergy to achieve the scientific objectives.

TASTE Mission: The TASTE mission will operate a 16U CubeSat consisting of a 12U orbiter and a 4U lander, which will be separated by a separation ring once in orbit around Deimos. The TASTE lander will have a tilt mechanism to reorient the lander on the surface of Deimos [4].

To reach the Martian environment, TASTE will have to be launched inside a carrier and released in the vicinity of Mars. TASTE will then be transferred to Deimos and inserted into quasi-satellite orbits (QSO), which have natural stability and ensure very low stationkeeping costs [5].

Two target QSOs have been identified: a large one (Mapping-1), at a distance of 27 to 37 km from the centre of mass of Deimos, which will serve as a stationing orbit for the "long-distance" science activities, and a small one (Mapping-2), with a size of 14x15 km, for the higher resolution imaging of the surface and the identification of the most suitable landing sites.

The lander will be released in a free-fall descent from a release point closer to the surface (100-1000 m), tilted on the surface if necessary, and anchored to the surface. At the end of the mission, the orbiter will be disposed of in accordance with planetary protection requirements.

TASTE Scientific Experiments: The scientific objectives of the TASTE mission are to define the global morphology and environment and the global elemental abundance from Mapping-1, the landing site morphology and texture from Mapping-2, the gravity field from both mapping orbits, and the organic content of the landing site by in-situ lander analyses.

The main experiments will be carried out with the SSA and the spectrometer.

The SSA, the payload that will enable the in-situ analyses, consists of the Sample Acquisition Mechanism (SAM), which acquires the samples from the surface, the Sample Extraction Chamber (SEC), where the liquid sample is extracted, and the Sample Analytical Laboratory (SAL), where the Lab-on-Chip (LoC) is placed and where the organic content of the samples is measured by fluorescence.

The orbiter will carry a miniaturised X-γ-ray spectrometer to characterise the elemental composition of the surface. The relative abundance of elements with atomic number ≤20 down to a few micrometres of the surface will be measured by fluorescent X-ray spectroscopy, using solar X-rays to excite the atoms of the elements. Gamma-ray spectroscopy of nuclear lines excited by galactic cosmic rays will also be used to assess the abundance of elements in the surface down to 10-20 cm. This instrument is a revision of the payload designed and under development in the HERMES-TP and HERMES-SP EC\MUR\ASI projects.

Conclusion: To date, the TASTE project has successfully completed Phase A. In this presentation, the scientific objectives and mission design to develop the CubeSat Cass applicability for scientific investigations in deep space low-gravity environments will be presented.

References:

[1] Rosenblatt et al., (2016), Nat. Geosci, 9, pp.581–583. [2] Murchie et al., (1999), JGR, 104 (E4), pp.9069-907. [3] Campagnola et al., (2018), Acta Astronautica, 146, pp. 409-417. [4] Tra-Mi Ho et al., (2017), Space Science Reviews, 208 (1-4). [5] Wallace et. al., (2012), Astrodynamics Specialist Conference, p. 5067.

THE VISTA INSTRUMENT ONBOARD MILANI CUBESAT FOR HERA MISSION.

F. Dirri[1], E. Palomba[1,2], A. Longobardo[1], C. Gisellu[1,3], D. Biondi[1], E. Nardi[1,3], E. Zampetti[4], D. Scaccabarozzi[5]
[1]INAF-IAPS Rome, Italy, Via Fosso del Cavaliere, 100 Rome, (fabrizio.dirri@inaf.it); [2]ASI Space Science Data Center, Italy; [3]Sapienza University of Rome, Italy; [4]CNR-IIA, Via Salaria km. 29.300, 00016, Montelibretti, Rome, Italy; [5]Politecnico di Milano, Polo Territoriale di Lecco, Via G. Previati 1c, Lecco, Italy

Hera Mission and Asteroids Target: Hera is a Planetary Defence Mission as a part of the world's first test of asteroid deflection and will perform a detailed post-impact survey of the target asteroid, Dimorphos. Hera/ESA Mission is performed in combination with DART/NASA Mission (Double Asteroid Redirection Test, a mission kinetic impactor test, which occurred in September 2022 that impacted Dimorphos surface) and is planned to launch in October 2024. Hera aims at demonstrating the new technologies from autonomous navigation around an asteroid to low gravity proximity operations, and investigate the Didymos binary system, including the assessment of its internal properties and the asteroid geophysics characterization [1]. Two CubeSats are included in Hera mother spacecraft: MILANI (developed by Tyvak International) and JUVENTAS (developed by GomSpace) will be deployed in the Close Proximity of the Didymos system: JUVENTAS will aim to the geophysical characterization of Dimorphos while MILANI, with two scientific payloads, aims at characterising the composition and dust environment of asteroid binary system.

MILANI CubeSat and Payloads Goals: The main mission objectives will leverage on MILANI payload instruments: ASPECT, a visible and near-infrared imaging spectrometer with four channels, i.e. VIS: 650-900nm, NIR1 channel: 850-1250nm, NIR2 channel: 1200-160 nm, SWIR channel: 1650-2500 nm and VISTA (Volatile In Situ Thermogravimetric Analyser), a dust detector (sensitivity: 4.4 ng/cm^2×Hz, saturation ~700µg/cm^2×Hz).

The main scientific goals of ASPECT are:

- ASP SG1: Global composition of the Didymos asteroid mapping;
- ASP SG2: Surface of the Didymos asteroid characterization;
- ASP SG3: Space Weathering and global shock effects on Didymos asteroid evaluation;
- ASP SG4: Local shock effect of Dimorphos caused by DART impact identification;

while, the main scientific goals of VISTA are:

- VIS SG1: dust particles detection smaller than 10µm;
- VIS SG2: characterization of volatiles and light organics;
- VIS SG3: Molecular contamination monitoring in support to MILANI and ASPECT hyperspectral imaging spectrometer.

VISTA Payload structure and working principle:

VISTA is a PCM-based device (Piezoelectric Crystal Microbalance) and converts the mass changes into fundamental resonance frequency variations (Sauerbrey equation [2]). The PCM sensor with customized heaters is capable of monitoring deposition and desorption/sublimation processes in vacuum [3], particles deposition and characterization by using Thermo-Gravimetric Analysis (TGA) [4].

VISTA Payload for HERA is composed by 3 different units: 1) two quartz crystals mounted in a sandwich-like configuration; 2) the Proximity Electronics (PE); 3) the Thermal Control System (TCS): two crystal-integrated and customized heaters (~35Ω) and a Thermo-Electric Cooler (TEC) to cool the sensor and facilitate the particles deposition.

The instrument was also tested in vacuum and cryogenic environment to monitor absorption/desorption and deposition/sublimation processes. The instrument is capable of monitoring particles lower than 5-10µm and sub-µm particles [5,6,7].
VISTA heritage comes from: ITT-Emits ESA Projects: 1) CAM (Contamination Assessment Microbalance), developed for "Evaluation of an in-situ Molecular Contamination Sensor for space use" (2014-2016) [8]; 2) CAMLAB (Contamination Assessment Microbalance for LABoratory) developed for "Development of a European Quart Crystal Microbalance" (2017-2019).

VISTA Model Philosophy and functionality test:

VISTA development for HERA started since 2020 up to 2023 (FM and FS delivery to Tyvak International) and included one Engineering Model_0 (EM0), one Engineering Qualification Model (EQM), one Flight Model (FM) and one Flight Spare (FS) (Figure 1). The EM_0 was electrically and mechanically representative of VISTA while the EQM, FM and FS present the same mechanical structure and electrical connections.

Figure 1. VISTA Model philosophy.

The Qualification and Acceptance tests on VISTA EQM, FM and FS have been performed at INAF-IAPS (Space Materials-Lab) and at PoliMI (Metro Space-Lab) in thermal vacuum chambers.

The test campaign included the:

1. Functionality tests (INAF)
2. Thermal vacuum tests (INAF) (Fig. 2)
3. Vibrational tests (PoliMI) (Fig. 3)

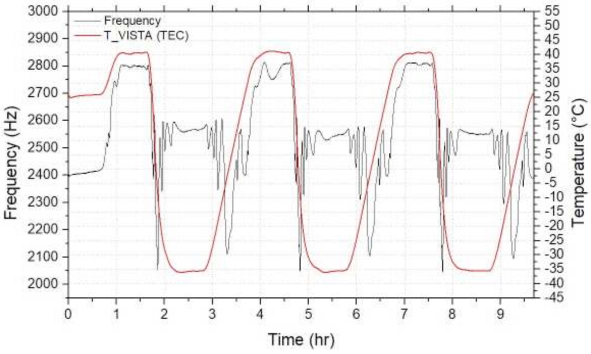

Figure 2. Thermal operative test of FS Acceptance Test campaign: three cycles are performed in the operative temperature range for acceptance (from -35°C to +40°C) with 30 minutes stabilization at each point.

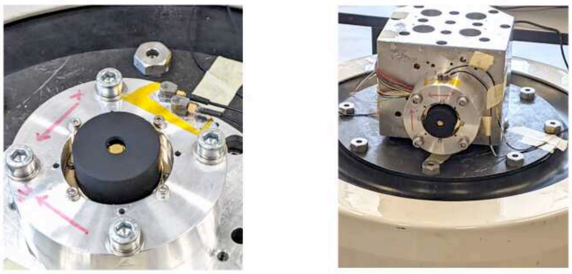

Figure 3. Mechanical Acceptance Tests VISTA-shaker interface for Y-axis tests (left) and X, Z-axes tests (right).

VISTA current status and operation during the close-range and experimental phases:

VISTA Payload is functioning in *passive* or *active modes* as following:

Accumulation mode (passive): this consists of passive collection of dust and volatiles on the microbalance. It will operate after MILANI deployment and science case, i.e. about 50 days of passive mode with a measurement rate of 1meas/10min continuously.

Heating mode (active): the microbalance can be warmed up to the volatile desorption temperature. This operational mode will follow the accumulation mode of the dust. The heating mode will be applied at the end of the four accumulation modes.

The measurement rate will replicate the calibration mode, in order to compare f vs T behaviour with and without deposited dust.

Cooling mode (active): the microbalance can be cooled down to favour the volatiles/compounds accumulation. This operational mode will be performed before the accumulation mode. The sensor head temperature will be decreased by 5-10°C with respect to VISTA base temperature.

The different operational modes are reported in Figure 5.

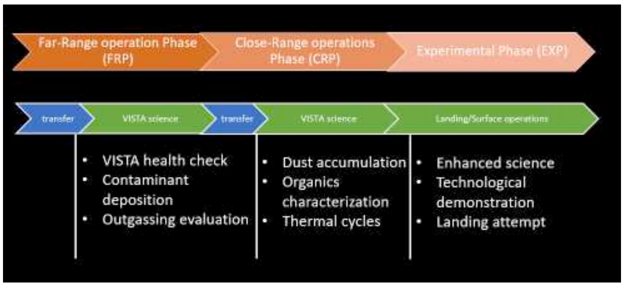

Figure 5. Operational modes of VISTA Payload in the FRP, CRP and Experimental Phases.

Currently, VISTA FM has been already integrated on MILANI CubeSat (November 2023) to perform the thermal and vibration cycles with the satellite (December 2023). During these tests, VISTA will be switched on different times for 20 minutes (*active modes*) in order to help the assessment of the molecular contamination due to the CubeSat and successively by Hera mother spacecraft.

References: [1] Michel P. et al. 2022. Planetary Science Journal 3:160; [2] G. Sauerbrey 1959, Z. Phys., 155, 206-222; [3] Dirri F. 2016, AMT, 9, 655-668; [4] Dirri F. 2018, IEEE Xplore Digital Library, pp. 150-154, doi: 10.1109/MetroAeroSpace.2018.8453532; [5] Palomba et al. 2016, OLEB, 46 (2-3); [6] A. Zinzi et al. 2011, S&A: A, 172, 504-510; [7] Zampetti, E. 2023, Sensors 2023, 23, 5682. https://doi.org/10.3390/s23125682; [8] D. Scaccabarozzi 2016, IEEE Xplore Digital Library, doi: 10.1109/MetroAeroSpace.2016.7573287.

PRELIMINARY PERFORMANCE ASSESSMENT OF CUSTOMIZED PIEZOELECTRIC CRYSTAL MICROBALANCES FOR SPACE APPLICATIONS.

C. Gisellu[1,2], F. Dirri[1], E. Palomba[1], A. Longobardo[1], E. Nardi[1,2], E. Zampetti[3], D. Scaccabarozzi[4], B. Saggin[4]; [1]INAF-IAPS, via del Fosso del Cavaliere 100, 00133 Rome (chiara.gisellu@inaf.it); [2]Università La Sapienza, Rome; [3]CNR-IIA, Montelibretti, SP35d, 00010 Monterotondo; [4]Politecnico di Milano, Polo Territoriale di Lecco, Via G. Previati 1/C, 23900, Lecco, LC.

Introduction: Piezoelectric Crystals Microbalances (PCM) are widely used sensors for measuring molecular contamination coming from outgassing sources in space in support to other instrument (e.g. spectrometers) and can be used to characterize the dust composition and particles deposition processes in different planetary environement. Furthermore, they are capable of detecting and measuring the presence of volatile compounds of astrobiological interest such as water and organics, in planetary samples with TG-Analysis. These measurements can be particularly relevant when performed on primitive asteroids or comets, or on targets of potential astrobiological interests, e.g. Mars [1].

This work presents a preliminary assessment of the performances of different PCM sensors, in order to demonstrate their capability of characterizing volatile compounds and simulant contaminants in vacuum chamber at low temperatures.

All the PCM sensors have been developed by an Italian Consortium composed by three Research Institutes: INAF-IAPS (National Institute of Astrophysics - Institute for Space Astrophysics and Planetology), CNR-IIA (National Council of Research – Institute of Atmospheric Pollution) and Politecnico di Milano and led by INAF-IAPS.

All the laboratory tests were performed at the Space Materials Laboratory at INAF-IAPS.

Working principle: The instrument core is a PCM whose frequency variations directly depends on the deposited sample mass on the crystal surface, according to Sauerbrey equation [2]:

$$\Delta f = -\frac{K_0 f^2}{A_0}\,\Delta m$$

where K_0 is a constant dependent on the piezoelectric material, A_0 is the sensor area and f is the resonance frequency. The working principle is shown in Figure 1.

The sensing part of the instrument is composed of two quartz crystals mounted in a sandwich-like configuration, one used as a reference and the other one exposed to the external environment (i.e., the sensing crystal).

By using customized heaters integrated on the crystals surface, the PCM is also capable of performing Thermo-Gravimetric Analysis (TGA), which is a widely used technique to perform thermal analysis of materials/compounds in order to detect and distinguish the volatile fraction and refractory ones by using deposition/sublimation and absorption/desorption rates. This special design of a built-in heater dramatically reduces the total mass and the power required to perform thermal cycles.

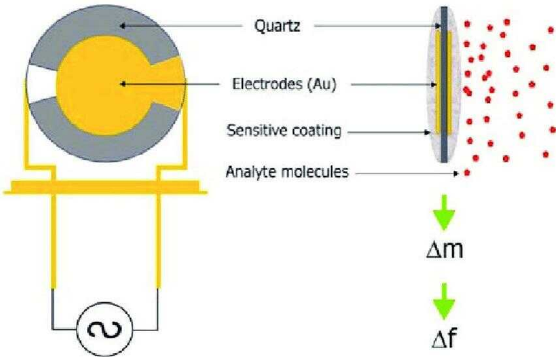

Figure 1. Working principle of a PCM. The particles are collected by the sensitive surface and the deposited mass is measured by frequency-mass relation.

The PCM is also equipped with a Thermoelectric Cooler (TEC), used to decrease the instrument temperature with respect to the external environment and enhance particles condensation. The instrument can also monitor particles lower than 5-10 µm and sub-µm particles [1].

Experimental setup for organic compounds/contaminants deposition: The PCM capability to detect contaminant depositions and to monitor the accumulation and desorption processes is verified by placing a Knudsen Cell containing an organic compound, used as a contamination source, placed in the Field Of View (FOV) of the sensing crystal.

A schematic of the setup used fot the deposition tests is shown in Figure 2. The PCM is mounted on a copper interface, in contact with a cold sink kept at -10°C, to enhance the molecules condensation on the crystal surface. The crystals are kept at a fixed temperature, in order to disentangle the frequency variation due to mass deposition and environmental parameters (e.g. temperature variations of the two crystals). The Knudsen Cell is heated from 50°C up to 100-130°C in 10°C steps.

The frequency is monitored during the tests and the deposited flux can be retrieved at each set point (Figure 3).

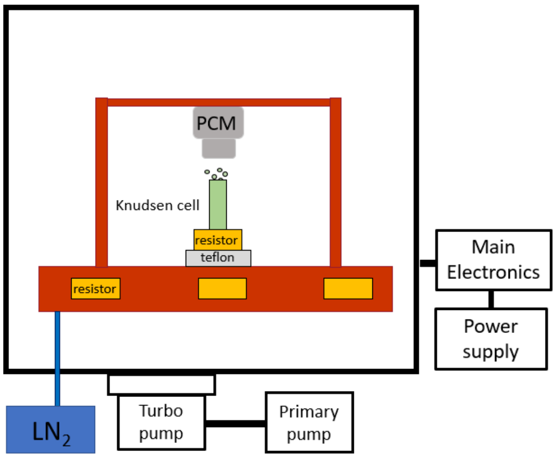

Figure 2. Schematic of setup for deposition/TGA tests.

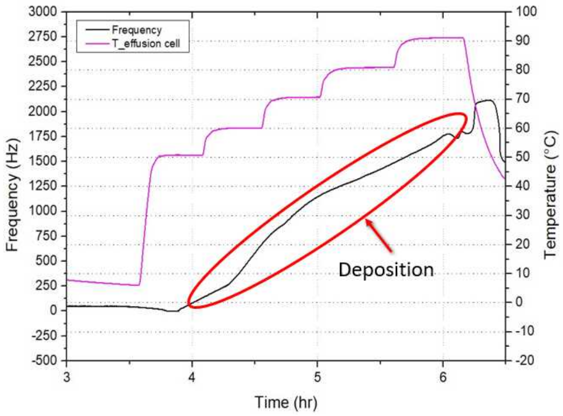

Figure 3. Deposition test from 50°C to 90°C.

After the deposition test, TGA cycles are then performed by heating the crystals by means of the built-in heaters. After the heating cycles, if the frequency returns to its initial value, all the deposited mass desorbed during the test.

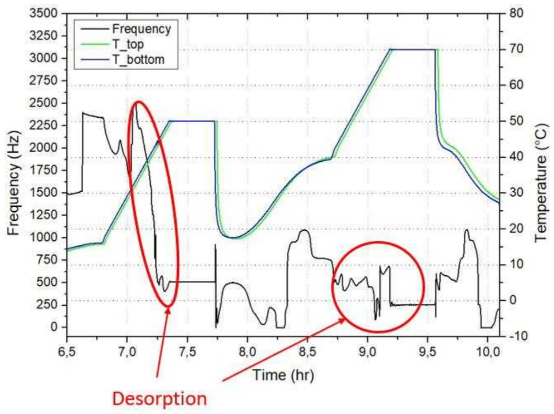

Figure 4. TGA cycles from 15°C to 50°C and from 40°C to 70°C.

Contaminant characterization: Two methods are then used to retrieve the enthalpy of sublimation by using the deposition rates, i.e. the Van't Hoff relation [3] or Langmuir relation [4]. Thus, by measuring two different deposition rates, k1 and k2, at two different close temperatures T1 and T2, it is possible to obtain the compound ΔH_{sub} by means of Van't Hoff relation or throughout the temperature range by using Langmuir relation.

The desorption rates from crystals surface are used as well to calculate the ΔH_{sub} and compare it with the ΔH_{sub} results obtained during the depositions/contamination processes.

Conclusions and future works:

Preliminary results are in good agreement with previous works. Further experiments will be performed with calibrated microspheres and meteorites <20 µm-particles size.

References: [1] E. Palomba et al (2016), OLEB, 46(2-3; [2] G. Sauerbrey (1959), Z. Phys., 155, 206-222; [3] S.W. Benson et al., 1968; [4] I. Langmuir, 1913.

NEO DATA MANAGEMENT: FROM AWARENESS TO OPERATIONS M. Giardino[1], A. Giunta[1], A. Zinzi[1], I. Di Pietro[1], E. Dotto[2], E. Perozzi[1] and the NEOROCKS Team. [1]Agenzia Spaziale Italiana, [2]INAF-Osservatorio di Roma.

Introduction: In the last 20 years the increasing focus at international level on the asteroid hazard has allowed to increase dramatically the NEO discovery rate, to perform on a regular basis impact monitoring by dedicated systems and to successfully develop and test mitigation techniques (e.g. deflection in space).
These achievements, although of great relevance, have urged planetary defence to address a gap still existing, i.e. complementing the NEO orbital data with exhaustive physical characterization. The importance of this issue has grown considerably as the NEO discoveries move toward objects of increasingly smaller size approaching our planet. In particular, tiny (meter size) meteorite-dropping bodies have been successfully identified when still in space and recovered on the ground. Tunguska-class objects (a few tens of meters) are still difficult to detect with a sufficiently long warning time and are likely to represent the next actual impact event. Within this framework the need for quick orbital and physical characterization linking up follow-up observations and data through a planetary defence rapid response system has been exhaustively addressed by the EU-H2020 NEOROCKS project [1] [2].

Data collection: While NEO orbital data are managed worldwide by the Minor Planet Center on behalf of the IAU, NEO physical properties are obtained as individual research outputs, thus following the usual scientific dissemination procedure (competitive proposals for telescope time, proprietary data periods, peer reviews, publication embargos etc.).
It is no surprise then that until now the only way for sharing worldwide NEO physical properties has been to collect them from the research articles appearing in the literature (formerly available at EARN – the Near-Earth Asteroid Research Node) or to access the repositories maintained on-line by individual research projects. The ESA NEO Coordination Centre (NEOCC) has indeed ingested the last updated version of EARN in its own orbital database thus allowing to perform queries on both physical and orbital data and plans to regularly update it. Even if this applies only to a fraction of the known NEO population and to some basic physical properties (e.g. rotation period, diameter, spectral type), it can be considered a first step toward a comprehensive NEO catalogue including both, dynamical and physical characterization. Yet the managent of physical properties data implies a rather cumbersome and lengthy procedure even when they are in a digital format because of the lack of standardization (similar to what ADES is for astrometry [3]).

In this respect it is worthwhile resorting to the EuroPlaNet Research Infrastructure, an initiative funded by EU Horizon 2020 programme with the aim of linking research institutions and companies active in planetary research in Europe and around the world [4]). Within the EuroPlaNet-2024 contract, the VESPA (Virtual European Solar and Planetary Access) portal has been deployed [5], which *"aims at building a Virtual Observatory for Planetary Science, connecting all sorts of data in the field, allowing for rapid data search and providing modern tools to retrieve, cross-correlate, and display data and results of scientific analyses."* The opportunity represented by EuroPlaNet for improving the NEO physical properties data management and dissemination has driven the design and the development of the NEOROCKS NEO physical properties database.

Physical properties database: Establishing and maintaining an European NEO catalogue - physical properties database is considered a major goal of the recently signed FFPA agreements between European Commission and ESA [6] within the framework of the EU SSA Programme [7]. Therefore, the NEOROCKS data model was designed according to the following state-of-the-art data management principles and standards:

- **EPN-TAP** (EuroPlaNet Table Access Protocol) is at the core of the data model providing the internationally adopted terminology;
- **FAIR** (Findable, Accessible, Interoperable, Reusable) principles ensure the long-term archive preservation and interoperability with other data centers;
- **IVOA** (International Virtual Observatory Alliance) improves the availability and the interoperability of astronomical data worldwide by defining the EPN-TAP standards and implementing the FAIR principles.

The NEOROCKS data model includes all the 47 mandatory EPN-TAP parameters that must be present (even if NULL) in any VO-compliant database . The EPN-TAP allows customization: optional parameters of interest for planetary science have been added to the data model as well as a set of additional parameters specifically for the NEO case. After the end of the NEOROCKS project in June 2023, the database is presently being integrated into the ASI Space Science Data Center, which provides the necessary HW/SW environment and experienced personnel. The visibility at international level is ensured by the long-standing SSDC experience in acquiring, managing, processing and disseminating the data produced by astronomical missions, following FAIR principles.

The next challenge is to populate and keep regularly updated the NEO physical properties database; this means to attract the scientific community to entrust the results of their research activities, as well as to ingest the data obtained by institutional programmes both on the ground and in space, through international agreements.

Conclusions and recommendations: The main conclusion that can be drawn is that the time has come for NEOs to be considered as a natural hazard that can be dealt with through operational monitoring and alert systems, involving when necessary civil protection actions. In this respect Europe is ready to play a prominent role because of the internationally recognized NEO community and the availability of a wide variety of existing assets: skilled amateur observatories, large telescopes ruled by national or international consortia (e.g. ESO), advanced orbit determination and impact monitoring systems (ESA NEOCC).

In order to do so, the adoption of standardized data management and data policy within the initiatives devoted worldwide to NEO physical and dynamical characterization is recommended.

In particular, supporting the maintenance and the evolution of the EuroPlaNet-compliant NEOROCKS physical properties database hosted at ASI SSDC will allow to timely face the sharp increase in the data flux coming from the next generation sky surveys and from space observatories.

Moreover, developing data analysis and management tools adopting the EPN-TAP standards [8] is likely to attract users and data to a unique physical properties database.

Finally, moving toward a European NEO data policy within the framework of the Open Science initiative [9] represents a key activity for fostering data exploitation.

References:

[1] Dotto E. et al. (2021) EPSC Abstracts. Vol. 15, EPSC2021-389, 202. https://doi.org/10.5194/epsc2021-38

[2] Perozzi E. et al. (2023) A Rapid Response Experiment Carried Out by the EU Neorocks Project. ESA NEO and Debris Detection Conference. NEOSST2-paper114.

[3] Chesley S.R., Hockney G.M., Holman M.J. (2017): American Astronomical Society, DPS meeting.

[4] EuroPlaNet Society: https://www.europlanet-society.org/.

[5] EuroPlaNet VESPA: http://www.europlanet-vespa.eu/

[6] Financial Framework Partnership Agreements (FFPA) ESA Vision. https://vision.esa.int/tag/ffpa/

[7] The EU Space Programme https://www.euspa.europa.eu/european-space/eu-space-programme.

[8] Erard S., et al "EPN-TAP: Publishing Solar System Data to the Virtual Observatory Version2.0" IVOA Recommendation 22 August 2022, https://www.ivoa.net/documents/EPNTAP/20220822/index.html"

[9] Horizon Europe Open Science: early knowledge and data sharing and open collaboration. https://op.europa.eu/en/web/eu-law-and-publications/publication-detail/-/publication/9570017e-cd82-11eb-ac72-01aa75ed71a1

Acknowledgements: NEOROCKS - The NEO Rapid Observation, Characterization and Key Simulations project is an Horizon 2020 EU-funded project under GA No 870403.

The NEOROCKS Team includes also S. Anghel, N. Ariani, M. Banaszkiewicz, S. Banchi, M.A. Barucci, F. Bernardi, A. Bertolucci, M. Birlan, B. Carry, A. Cellino, F. Colas, J. De Leon, A. Del Vigna, A. Dell'Oro, L. Dimare, P. Fatka, S. Fornasier, E. Frattin, P. Frosini, M. Fulchignoni, R. Gabryszewski, J. Huntingford, S. Ieva, J.P. Kotlarz, F. La Forgia, M. Lazzarin, J. Licandro, E. Mazzotta Epifani, A. Mediavilla, J. Nomen Torres, D. Perna, M. Popescu, P. Pravec, A. Rozek, N. Sanchez Ortiz, P. Scheirich, A. Sergeyev, C. Snodgrass, A. Sonka, C. Teodorescu, G.B. Valsecchi, P. Wajer.

VO-COMPLIANT PLANETARY ANALOGUE SPECTRAL CATALOGUES AT ASI-SSDC. A. Zinzi[1,2], M. Giardino[1,2], E. Bruschini[3], S. De Angelis[3], M. Ferrari[3], S. Fonte[3], A. Pisello[4], [1]Agenzia Spaziale Italiana, [2]Space Science Data Center, [3]INAF-IAPS, [4]Università degli Studi di Perugia.

Introduction: As planetary exploration missions advance, laboratory measurement of analogue and extraterrestrial specimens need to be more complex. A durable preservation and an efficient querying mechanism can leverage the reusability and accessibility of these data products.

This implies that not only the measurement techniques have to be adapted, but also the archival procedures have to be taken into account to easily find the needed data in the repository.

In order to adequately manage this task, in recent years, some standard protocols have been developed, in particular those regarding Virtual Observatory (VO) and the EPN-TAP (Europlanet-Table Access Protocol) [1] and, in some cases, already used for spectral libraries.

Exploiting the long-lasting experience of the Space Science Data Center (SSDC) in disseminating space datasets using international standard protocols, here we describe the still on-going work to develop a robust and VO-compliant database to expose spectral libraries both from the SSDC webpages and as a VO service. This methodology ensures the interoperability of the data service and maximises its findability across the worldwide community.

Spectral libraries considered: In a very first application to this method, we established the PVRG magmatic rocks spectra catalog (consisting of lab-made silicate rocks produced by the Petro-Volcanology Research Group of the University of Perugia) [2], using a single table and all parameters defined by the EPN-TAP protocol. This catalogue is still working and can be reached at the URL https://www.ssdc.asi.it/rockspectra/.

Subsequently we started working with a more complex dataset, generated by CLAB (Coradini LA-Boratory at IAPS-INAF) in support of the Rosalind Franklin rover/Ma_MISS instrument [3, 4]. This library comprises not only infrared spectra, such as the PVRG catalog, but also Raman spectra and hyperspectral cubes, Visible-Near-Infrared (VisNIR) spectral cubes and images of samples. In this context we adapted the datamodel developed for the previous catalog, in order to manage different types of data, but also including the “simple” spectral catalog already present.

Methodology: A set of metadata requirements was initially defined to correctly represent the different types of measurements involved. A data model was then designed and implemented. To populate the database, a dedicated web application was rapidly developed on top of the data model, following a low code approach. Finally, the CLAB catalog and the PVRG catalog were merged into a single data service and the GUI (graphical user interface) implementation to query and analyze the catalogs is currently ongoing.

Conclusion and future works: When at regime, the data model developed will allow an easy and powerful search inside the datasets. By the SSDC catalog pages users will be also allowed to look at the data and compare them, by means of advanced visualization procedures.

This would certainly improve the possibility of science return, considering also an increased visibility for the published resources derived by the compatibility with the public IVOA registry network.

References: [1] Erard, S. et al. (2022) IVOA Recommendation 22 August 2022, https://www.ivoa.net/documents/EPNTAP/20220822/index.html. [2] Pisello, A. et al. (2022) EPSC2022-539, 10.5194/epsc2022-539. [3] Vago, J. L et al. (2017) Astrobiology, 10.1089/ast.2016.1533. [4] De Sanctis, C. et al. (2017) Astrobiology, 10.1089/ast.2016.1541.

EUROPLANET GMAP: TOOLS, SERVICES, AND TRAINING SUPPORT FOR PLANETARYGEOLOGIC MAPPING.

R. Pozzobon[1,2], A. P. Rossi[3], M. Massironi[1], C. H. Brandt[3], G. Nodjoumi[3], M. Pondrelli[4], C. H. van der Bogert[5], L. Marinangeli[4], P.A. Tesson[6] , L. Penasa[7], A. Frigeri[8], C. Carli[8], F. Zambon[8], F. Altieri[8], B. Baschetti[1], A. Naß[9], M.D'Amore[9] and the GMAP Team.
[1]Dipartimento di Geoscienze, Padova, Università di Padova Italy, [2]Dipartimento di Fisica e Astronomia, Università di Padova, [3]Constructor University, Bremen, Germany,[4]Università d'Annunzio, Pescara, Italy, [5]WWU, Münster, Germany, [6]Kosmicznych Polskiej Akademii Nauk (CBK PAN), Warsaw, Poland, [7]INAF-OAPD, Padova, Italy, [8]INAF-IAPS, Roma, Italy, [9]DLR-PF, Berlin, Germany

Introduction: Geologic mapping plays a pivotal role in planetary exploration, initially pioneered and supported by USGS/NASA [1-3]. With the proliferation of international planetary missions and a growing number of anticipated human and robotic exploration endeavors, this effort has evolved into a global effort. Specific projects like Planmap [4, 5] contributed to this global undertaking. In recent years, the Europlanet research infrastructure [6] has introduced an initiative, Geological MApping of Planetary Bodies (GMAP) [7, 8], aimed at promoting European contributions to planetary geologic mapping. This involves providing guidance, tools, and training while enhancing existing Open-Source tools with either newly developed or adapted features [e.g., 9, 10]. The details of these resources are described herein.

Web Services: GMAP documents and collects existing mapping materials on its wiki [11] and employs a processing environment for basemap production using USGS ISIS [12] and NASA ASP [13], along with related libraries [14, 15], based on Jupyter-Hub [16]. Both code and documentation are accessible on the GMAP GitHub organization and its repositories [17]. An InvenioRDM [19, 20]-based data portal [18] is also at your disposal. Community mapping projects, selected and supported by the GMAP group, are listed on the GMAP wiki [11] and are set to contribute data to the portal, either directly or by providing metadata entries that point to long-term repositories like Zenodo [21]. GMAP explores data discovery communities within Zenodo [22]. The ongoing exploration of metadata harmonization and interoperability involves cross-searching with USGS Astropedia/PDS Annex [23]. Additionally, alternative data discovery options are in progress using ASI's Matisse tool [24].

Tools and mapping aids: Promotion of the Free and Open Source Software (FOSS) Geographic Information System (GIS) QGIS [25] is advocated in all GMAP activities. To streamline the mapping process, customized plugins [9, 10] have been created.

Training: GMAP's primary training initiative is its annual Winter School, usually conducted online in both live and asynchronous formats. Each edition is made entirely accessible for subsequent use [26, 27], with plans in place for the repurposing of materials, data, and documentation for additional workshops reaching up every year an increasing number of participants up to more than 400 in the 2023 edition with around 200 in real time.

Acknowledgments: Europlanet 2024 RI has received funding from the European Union's Horizon 2020 research and innovation programme under grant agreement No 871149.

References: [1] Williams, D. A. (2016). XXIII ISPRS, 41, 519. [2] Hauber, E., et al. (2019). doi: 10.1007/978-3-319-62849-3_5. [3] Skinner, J. A. Jr., et al. (2019) U.S. USGS Open-File Report 2019–1012,
doi: 10.3133/ofr20191012. [4] Rossi, A. P., et al. (2018) IAC 2018, #IAC-18,A3,1,12,x47635. [5] Massironi, M., et al. (2018), EGU Geophys. Res. Abs.,
20, #EGU2018-18106. [6] Europlanet (2023) https://www.europlanet-society.org/europlanet-2024-ri/ [7] Naß, A., et al. (2021) EPSC Abstracts, #EPSC2021-383. [8] GMAP web (2023) https://europlanet-gmap.eu. [9] Penasa, L., et al. (2020) EPSC #EPSC2020-1057, doi: 10.5194/epsc2020-1057, 2020 [10] Heyer, T., et al. (2023) doi:10.1016/j.pss.2023.105687 [11] GMAP wiki (2023) https://wiki.europlanet-gmap.eu [12] Laura, J., et al. (2023) ISIS, Zenodo, doi: 10.5281/zenodo.7644616. [13] Beyer, R., et al. (2018) ESS, 5, doi: 10.1029/2018EA000409. [14] Beyer, R. (2020) LPS LI, Abstract #2441. [15] Annex, A., Lewis, K. (2021) 5th PDW/PSIDA, Abs. #7003. [16] GMAP JupyterHub https://jupyter.europlanet-gmap.eu. [17] GMAP GitHub org. https://github.com/europlanet-gmap. [18] GMAP data portal https://data.europlanet-gmap.eu. [19] InvenioRDM https://inveniordm.docs.cern.ch. [20] Carson, M. B., et al. (2020) doi: 10.18131/g3-87fa-bg46. [21] CERN (2013) doi: 10.25495/7GXK-RD71. [22] GMAP Zenodo community (2023) https://zenodo.org/communities/gmap. [23] Hartke, M. A., et al. (2020) LPS LI, Abstract #2519. [24] Rognini, E., et al. (2022) EPSC Abstracts.

#EPSC2022-658. [25] QGIS Development Team (2023) https://qgis.org/. [26] GMAP Winter School access page (2024) https://www.planetarymapping.eu. [27] GMAP Winter School 2023 repo (2024) https://github.com/europlanet-gmap/winter-school-2024.

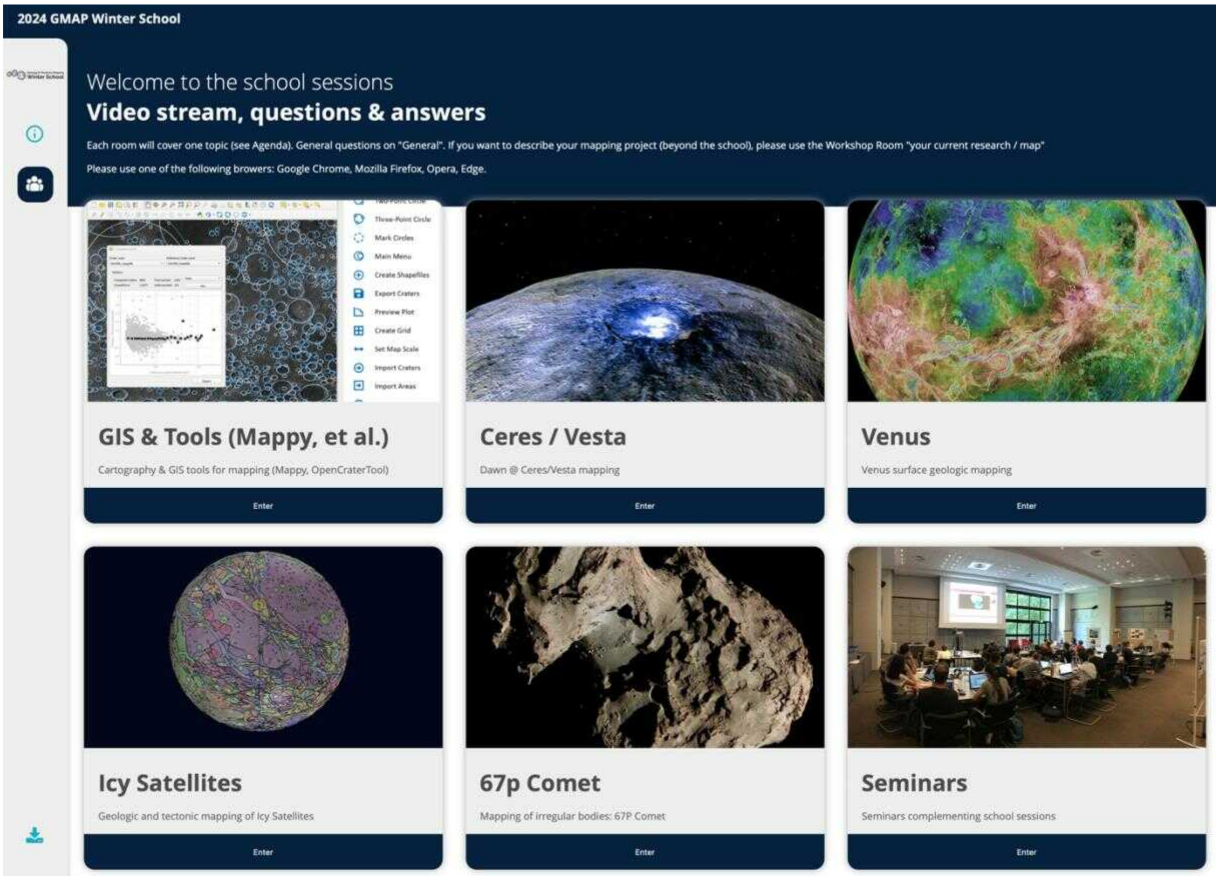

2024 GMAP Winter School

Welcome to the school sessions

Video stream, questions & answers

Each room will cover one topic (see Agenda). General questions on "General". If you want to describe your mapping project (beyond the school), please use the Workshop Room "your current research / map"

Please use one of the following browers: Google Chrome, Mozilla Firefox, Opera, Edge.

GIS & Tools (Mappy, et al.)

Cartography & GIS tools for mapping (Mappy, OpenCraterTool)

Ceres / Vesta

Dawn @ Ceres/Vesta mapping

Venus

Venus surface geologic mapping

Icy Satellites

Geologic and tectonic mapping of Icy Satellites

67p Comet

Mapping of irregular bodies: 67P Comet

Seminars

Seminars complementing school sessions

Figure 1: The 4th edition of the Planetary Mapping Winter School (22-26 January 2024) and the main platform page where the event is managed. The activities can be followed in real time or asynchronously and the training materials are hosted in Zenodo.

VENOM: Venture the ExtractioN of Organic Molecules – Preliminary design of the instrument.

G. Colombatti[1, 2], J.R. Brucato[3], A. Aboudan[2], C. Bettanini[1, 2], F, Ferri[2], A. Meneghin[3], G. Valentini[4], F. Ferranti[4] and the VENOM TEAM[1]
[1]DII - Università degli Studi di Padova (Giacomo.colombatti@unipd.it),
[2]CISAS “Giuseppe Colombo” – Università degli Studi di Padova, [3]INAF Arcetri- FI, [4]ASI - Rome

Exploring molecular biosignatures stands out as a primary objective in international exploration programs due to their capacity to offer more directly observable evidence of biogenicity compared to other types of biosignatures, where biological production is merely inferred. The detection of organic matter also plays a pivotal role in establishing habitability. Simple organic compounds serve as essential nutrients for life, and their presence on Solar System objects could serve as crucial evidence of actual habitability. Meanwhile, the identification of complex organic molecules may indicate traces of extinct life. Consequently, the in situ analysis with cutting-edge analytical techniques becomes imperative to extract, concentrate, and detect organic molecules and molecular biosignatures.

To detect biomarkers, a comprehensive sample preparation process is essential. This process involves liquefying the sample, filtering it to eliminate potential solid soil particles, desalting it, and concentrating it—an essential step to detect the target molecules at levels expected to be lower than one part per million. The ability to detect biomolecules across a broad range of molecular sizes and with unambiguous biotic origins would significantly enhance the robustness of the life detection strategy in space.

The VENOM instrument, in the Framework of the *Activities related to supporting the development of scientific projects in the area of Astrobiology of the Italian Space Agency*, relies on a powerful technique capable of detecting a diverse array of biogenic compounds, spanning from small biomolecules to large biogenic structures like cells.

Our objective is to develop an innovative, miniaturized lab-on-a-chip breadboard that serves as a highly-integrated, multiparametric, in situ platform. This platform will utilize immuno- and enzyme-assays to detect, identify, and assess biogenic compounds with a sensitivity reaching parts-per-billion. The intended application involves analyzing samples extracted from the surface of planets or moons. The design process will prioritize "flight readiness" to facilitate future development with the incorporation of additional components, ensuring compliance with all instrument requirements.

Key design considerations encompass the utilization of flight-qualifiable materials and components, especially for critical process components. The design aims for robustness in the face of sterilization procedures to meet planetary protection requirements, suitability for mission operational conditions and lifetime, as well as effective waste storage and scrubbing of post-operational blow-off.

Under the VENOM project, we propose expanding the range of biomarkers targeted, focusing particularly on significant ones such as adenosine monophosphate (AMP), adenosine triphosphate (ATP), DNA, RNA, lipopolysaccharides, lipoteichoic acid, nicotinamide, phosphoenolpyruvate, fatty acids, L- and D-amino acids, pigments, and hydrocarbons. These biomarkers are selected based on their relevance to "life as we know it," and if preserved on Mars or Europa and Enceladus, they could serve as highly diagnostic indicators of present or extinct life.

The instrument is designed to fulfill several key functions. Firstly, it must receive samples from outer space, ensuring their containment within a sealed environment. Following this, the instrument needs to facilitate fluid treatment and incorporate dedicated lines to deliver the treated fluid to the detection system. Figure 1 illustrates the schematic configuration of the instrument, depicting each subsystem or compartment.

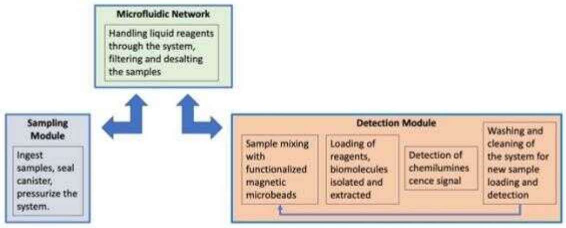

Figure 1. VENOM schematic design

The proposed instrument is a sophisticated Lab-on-Chip featuring integrated sensors and actuators that automate the execution of extraction, separation, and detection protocols. This device comprises three main components:

I. **Sampling Module**: This module is responsible for ingesting samples into the system.
II. **Microfluidic Network Module**: Dedicated to the handling of liquid reagents throughout the system, this module performs tasks such as filtering and desalting the sample.
III. **Detection Module**: Designed to detect and quantify the presence of biomarkers, this module

utilizes magnetic microbeads to isolate biomolecules and employs chemiluminescence for their detection.

This instrument is conceived to demonstrates a comprehensive and advanced capability to handle extraterrestrial samples, treat fluids, and detect biomarkers with precision.
The objective of the project is to develop a breadboard of VENOM for technology demonstration. The design of the entire system in its comprehensive and final configuration is aligned with the envisioned breadboard TRL5 maturity level.

The instrument is structured around a Main Frame that houses all its subsystems, with a baseline resembling the size of a 2U/3U cubesat.

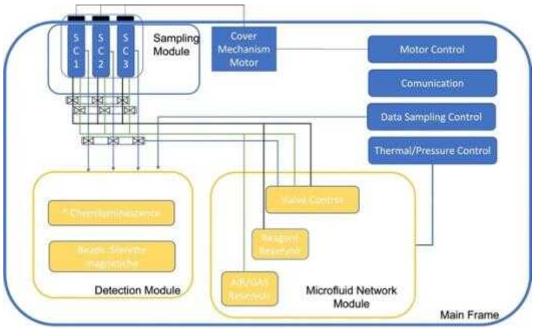

Figure 2. VENOM schematic modules

The Main Frame features a sealed structure designed to mechanically contain the Lab-on-Chip and microfluidics subsystems. This containment ensures that these components remain at room pressure (up to 1 atm), facilitating the conventional functioning of micro- and mini-fluidics and maintaining fluids in their normal liquid state. Throughout the project, the potential inclusion of sample preparation units into the sealed chamber will be subject to evaluation. The chamber itself will be equipped with a miniaturized pressurization system, serving to compensate for any eventual gas leakage during the journey or operation. Additionally, it can be utilized to pressurize the chamber once the instrument is positioned on the planetary target.

The sampling module is ingeniously organized as a carousel capable of accommodating various Sample Containers (SC). These SCs can be exposed to outer space in a single event or sequentially, enabling multiple uses. A straightforward rotating wheel mechanism is employed to open the cover of each preloaded SC and subsequently allow for the closure of the sample cylinder. Both the motor and the wheel are housed within the Sample Module, as depicted in Figure 3. This paper presents the preliminary activities carried out on the design of the main frame and on the Sample canister

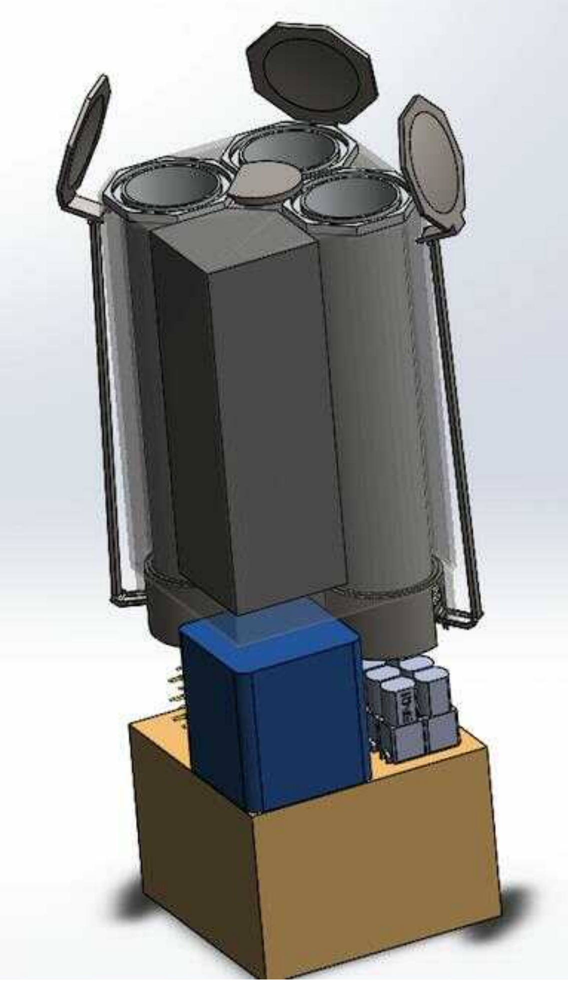

Figure 3. CAD showing the sample containers

Acknowledgemenst:
“Venture the ExtractioN of Organic Molecules (VENOM)” è un progetto selezionato dal ***bando ASI:*** *“Attività relative al supporto allo sviluppo di progetti/esperimenti scientifici nell’ambito dell’Astrobiologia” (prot.n. DC-DSR-UVS-2022-231), coordinato e supportato da ASI (Contratto di Finanziamento ASI n. 2023- 8-U.0, Codice Unico di Progetto (CUP) C13C23000360005).*

EXPLORE L-EXPLO & L-HEX: OPEN-SOURCE SCIENTIFIC APPLICATIONS FOR LUNAR CARTOGRAPHY.

Giacomo Nodjoumi[1], Javier Suárez-Valencia[1], Carlos Brandt[1], Angelo Pio Rossi[1], and the EXPLORE consortium.

[1]Constructor University Bremen, Campus Ring 1, Bremen, Germany (gnodjoumi@constructor.university),

Abstract

L-EXPLO and L-HEX are open-source Lunar scientific data applications (SDAs) developed under the H2020 EXPLORE project. They provide access to and enable advanced analysis of high-level data from Lunar missions, supporting a comprehensive range of analytical operations. Both applications are open-source backend-frontend docker services based on industry-standard specifications, deployable locally or remotely, making them widely accessible to users and easily integrated into existing scientific and operational workflows.

Introduction

Over the past decade, many planetary web-services have emerged [1-6], each offering unique visualization and processing capabilities. L-EXPLO and L-HEX [6] were developed with the goal of constructing a European service/platform dedicated to Lunar exploration. Several features distinguish our web-based platform from other services, mainly: its ability to handle multiple datasets, the exploration and processing of this data, support for 3D models/point clouds, 3DTiles, support for WMS/WMTS services, a customizable advanced processing API, integration with user data, and finally, the availability of customizable Deep Learning models.

L-EXPLO and L-HEX

The purpose of the SDA is to archive and provide access to a selection of high-level data from existing Lunar orbital missions, meaningful for surface characterization, geologic mapping, resource evaluation, and mission planning purposes.

In particular, the SDAs objectives include:

- Access to relevant high-level data from Lunar orbital missions.
- Perform analytical operations, such as image visualization, color-composites, hyperspectral summary products/spectral indexes visualization and generation [8].
- Building workflows (e.g. data selection, gathering, visualization, analysis, export, e.g. to GIS systems).
- Study global correlations with multiple datasets to improve existing geomorphological maps.
- Extraction of spectral indices and surface composition parameters, mainly from the Moon Mineralogical Mapper (M^3) data.
- Improve classification and segmentation algorithms for the lunar surface, and the detection of lunar landforms with Deep Learning models.
- (Upcoming Feature) Landing Site Characterization and Traverse Optimization, which will allow users to evaluate potential landing sites for future lunar missions based on comprehensive data from orbital and lander missions. This feature is currently under development and will be available soon.

Advantages and Impact

- Visualization: Create images and animations of lunar data, including spectral images, mineral maps, and topographic maps.
- Geologic and geomorphologic mapping support: Identify and map surface units.
- Spectral analysis and Spectral indices: Plot spectral profiles and/or compute advanced spectral indices to identify specific minerals and other features of the lunar surface.
- Landforms detection: Use Deep Learning to identify landforms such as craters and boulders.
- 3D model visualization.
- Traverses and mission planner (under development).

Deployment and Usage

The system's structure is built on widely used, well-explained, and open-source software. It's designed to be easy to customize and configure, and the user can even replace or change individual parts without affecting the whole system. The system uses the docker container architecture [9], which is known for being stable, widespread, and reliable. The frontend is built on top of TerriaJS [10]. The flowchart in Figure 1 shows the working scheme of this architecture.

Figure 1. Overall EXPLORE Lunar SDAs architecture with color-coded components, a) Processing (Yellow), geospatial web-services (Cyan), Advanced Under implementation (Dark Red),

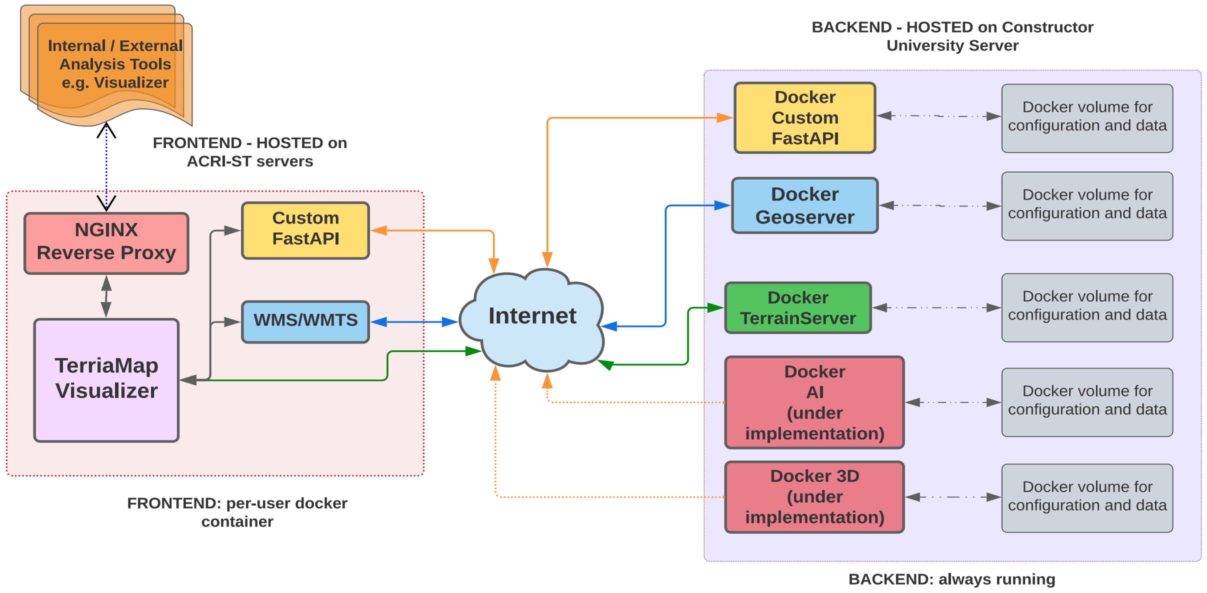

Our solution has been successfully tested on various Linux-based platforms, ranging from consumer laptop to high-end servers. The release version of the code is available via GitHub [11, 12].

The service has also been deployed as a web service at https://explore-platform.eu/. With prior registration, users can access the service and process data.

Conclusion:

The Explore SDA framework is developed using a combination of Open-Source tools, making it free to use, deploy, and upgrade. While science analysis-ready data (ARD) and foundational products are useful and increasingly popular, the ability to generate custom, documented, and reproducible high-level products beyond existing foundational resources is crucial for accelerating the mapping process and scientific analysis of the lunar surface. This approach can be easily adapted to other planetary bodies, requiring little modification from the existing Lunar SDAs.

References:

[1] Law, E. L. ; Day, B. H. ; Treks, S. S. (2020), NASA Moon Trek Applications in Lunar Science and Exploration, Lunar Surface Science Workshop, held 28-29 May, 2020 (Virtual). LPI Contribution No. 2241, id.5080

[2] Malaret, E. ; Robinson, M. ; Hash, C. ; Guasqui, P. ; Mauceri, C. ; Battisti, A. ; Malaret, V., (2022), Lunar QuickMap: Meeting The Challenge of Polar Exploration, Lunar Polar Volatiles Conference, held 2-4 November, 2022 in Boulder, Colorado. LPI Contribution No. 2703, 2022, id.5028

[3] Marco Figuera, R., Pham Huu, B., Rossi, A. P., Minin, M., Flahaut, J., & Halder, A. (2018). Online characterization of planetary surfaces: PlanetServer, an open-source analysis and visualization tool. Planetary and Space Science, 150, 141–156. https://doi.org/10.1016/j.pss.2017.09.007

[4] Oosthoek, J. H. P., Flahaut, J., Rossi, A. P., Baumann, P., Misev, D., Campalani, P., & Unnithan, V. (2014). PlanetServer: Innovative approaches for the online analysis of hyperspectral satellite data from Mars. Advances in Space Research, 53(12), 1858–1871. https://doi.org/10.1016/j.asr.2013.07.002

[5] https://adamplatform.eu

[6] A. Zinzi et al., 'MATISSE 2.0: The SSDC Webtool for Integrated Planetary Science Analysis', LPI Contributions, vol. 2549, p. 7018, 2021.

[7] https://explore-platform.eu/

[8] Zambon, F., Carli, C., Altieri, F., Luzzi, E., Combe, J.-P., Ferrari, S., Tognon, G., & Massironi, M. (2020). Spectral Index and RGB maps—Beethoven, Rembrandt basins on Mercury, Apollo basin and Leibnitz and Von Karman craters regions on the Moon (p. 57).

[9] D. Merkel, 'Docker: lightweight Linux containers for consistent development and deployment', Linux journal, vol. 2014, no. 239, p. 2, 2014.

[10] TerriaJS: https://terria.io/

[11] https://github.com/explore-platform/l-explo_l-hex_frontend

[12] https://github.com/explore-platform/l-explo_l-hex_backend-

THE TIANWEN2 MISSION AND THE DIANA INSTRUMENT

A. Longobardo[1], E. Palomba[1], F. Dirri[1], C. Gisellu[1,2], E. Nardi[1,2], D.Biondi[1], G. Massa[1,2], D. Scaccabarozzi[3], E. Zampetti[4], C. Martina[3], D. Kun[5], [1]INAF-IAPS, via Fosso del Cavaliere 100, 00133, Rome, Italy (andrea.longobardo@inaf.it), [2]Università La Sapienza, Rome, Italy; [3]Politecnico di Milano, Polo Territoriale di Lecco, Milan, Italy; [4]CNR-IIA, Montelibretti (RM); [5]CAS-SITP, Shangai, China

The Tianwen2 Mission: The CNSA's Tianwen2 mission [1] will study and sample the Kamo'oalewa near-Earth asteroid and then will rendezvous with the 311P/PANSTARRS main belt comet (MBC). The goals of the mission are to characterize NEAs and to explore for the first time a MBC, in particular to detect water traces and to understand their role in the water delivery to Earth.

The mission is expected to be launched in May 2025. It will reach and observe Kamo'oalewa in 2026, then it will land and collect sample of its surface. Asteroid samples will be brought back to Earth and then the Tianwen2 journey will continue toward 311P/PANSTARRS, that will be reached after 2032.

The mission payload includes multispectral cameras, a thermal emission spectrometer, an imaging spectrometer, a massa spectrometer, a magnetometer and a dust analyzer [1]. The dust analyzer is a suite of several sensors, including the DIANA (Dust Insitu ANAlyzer) instrument.

The DIANA instrument: The DIANA instrument is based on quartz crystal microbalance (QCM) technology and aims at detecting dust and its volatile content as well as at assessing the contamination issue.

The working principle is the conversion of crystals' oscillating resonant frequency to deposited mass, by means of Sauerbrey relation [2]. Crystals can be heated by built-in resistors [3] or cooled by a Thermo-Electric Cooler (TEC). This will enable Thermogravimetric Analysis (TGA), i..e, the study of mass variation as a function of temperature, which will allow measuring the abundance of volatile compounds of astrobiological interest (e.g., water, organics) in the cometary dust (heating mode) and revealing the occurrence of contaminants that could frost on the crystal (cooling mode).

DIANA includes:

- A sensor head (SH1), working at low temperature (i.e., 225-400 K), which will measure dust flux and the amount of physically adsorbed water, as well as assess the contamination issue during the Tianwen2 cruise phase. It consists of a quartz microbalance composed of a sensing crystal, a reference crystal, a TEC and the related Proximity Electronics, which converts the mechanical oscillation in a electric signal.
- A sensor head (SH2), working at high temperature (i.e., up to 500 K), which will measure dust flux and amount of organic components. The two quartz crystals (i.e., sensing and reference) have a different cut, which will allow reaching high temperatures without loss of piezoelectric properties. No TEC is included.
- A Main Electronics Unit, which reads the SH1 and SH2 frequencies and temperatures and sets the temperature ramp rate for TGA.

Table 1 lists the DIANA's SH1 and SH2 technical characteristics, while a sensor head is shown in Figure 1.

	SH1	**SH2**
Sensitivity (ng/cm^2)	4.4	17.6
Mass (g)	90	90
Volume (cm3)	100	100
Power (W)	1.5 (peak) 1 (average)	4.5 (peak) 2.5 (average)
Data rate (bit/meas)	78	114
Crystal Operating Temperature (K)	225-400	235-500

Table 1. DIANA's technical characteristics.

Figure 2. DIANA's SH2 Qualification Model

Operative modes: During the cruise stage, DIANA will work in *calibration mode*, consisting of heating and cooling cycles aimed at monitoring the frequency versus temperature variation. This activity will allow disentagling frequency variations due to mass deposition and those related to temperature changes. Moreover, cooling cycles will allow frosting of contaminant materials on the DIANA sensing crystals, that could be characterized by means of TGA.

When at 311P, DIANA will first work in *accumulation mode* to collect dust ejected from the comet and then in *heating mode* to measure the abundance of volatiles inside the dust (e.g., water, organics).

Development and testing: The DIANA's Qualification Model has been developed and successfully tested. Flight model is under development.

Mechanical tests consisted of sweep sine (in the frequency range from 5 to 100 Hz) and random (up to 17.7 g acceleration) vibrations.

Environmental tests demonstrated DIANA functionality when in conductive contact with a sink temperature between -55°C and 75°C.

Functionality tests demonstrated the frequency stability of SH1 and SH2 crystals (e.g., Figure 3), as well as the capability of built-in resistors to heat crystals up to 370 K (SH1) and 500 K (SH2), respectively with a temperature ramp rate comprised between 1 and 2 K/min.

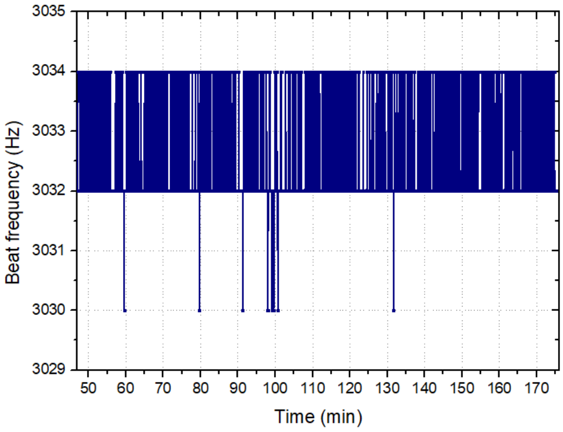

Figure 3. Frequency stability test of SH2. Frequency variations are within 2 Hz.

Acknowledgement: The DIANA development activities are funded by Italian Space Agency through the ASI-INAF Agreement 2022-27-HH.0

References:

[1] Zhang, X. et al. (2019), *LPSC abstracts*, 1045
[2] Sauerbrey, G. (1959), *Z. Phys*, 155, 206–222
[3] Palomba, E. et al. (2016), *OLEB*, 46, 273-281.

PANSHARPENING IN PLANETARY EXPLORATION STUDIES: DEVELOPMENT OF TOOLS AND APPLICATIONS.

A. Tullo[1], C. Re[1], G. Cremonese[1], B. Baschetti[2], Munaretto G. [1], R. La Grassa[1]. [1]INAF – Osservatorio Astronomico di Padova (Vicolo dell'Osservatorio, 5, Padova, Italy – adriano.tullo@inaf.it), [2]Department of Geosciences, University of Padova, Padova, Italy

Introduction: Despite modern technological developments, current technical limitations do not allow for a sensor characterised by both high spatial and spectral resolution. This implies that multispectral sensors do not reach the ground resolution of their panchromatic counterparts. Hence, missions or series of missions usually involve the presence of both instruments, considered complementary.

To overcome this division, the concept of pansharpening comes into play, which addresses the field of radiometric fusion to implement the ground resolution of the multispectral images based on the information acquired by panchromatic sensors.

In over forty years of development, more and more techniques have emerged using different approaches, mathematical and geometric, and recently through the application of neural networks [1].

Despite these developments, different complications and the lack of accessible tools have meant that pansharpening is rarely used in planetary exploration outside of Earth-observing.

In the present work, we report on the progress made in developing a dedicated set of tools that enable the application of different CS pansharpening [2] techniques and a preliminary performance evaluation in a series of case studies. These scenarios include the use of sensors data in Mars orbit and the preparation for use in the future Mercury observation.

Case studies and scientific outcomes: The ability to achieve higher resolution on the ground is an indisputable advantage on which several space missions have been based.

The primary investigations of the present studies were conducted with data from the Mars observing MRO HiRISE and TGO CaSSIS cameras [3][4].

Pansharpening allows the strengths of both instruments to be exploited in areas where the footprints of the two sensors overlap, a common occurrence for areas of high scientific interest.

The resulting data allow for a greater definition of the boundaries of geological units and the observation of limited-sized morphologies and features such as stratifications, exposed ice deposits, polar 'spiders' or furrows, and mud volcanoes.

Further tests were conducted with CRISM data from the MRO mission, implemented using the CaSSIS panchromatic filter. In this respect, pansharpening methods that preserve the spectrum could support compositional analyses and mitigate background noise.

In Mercury's case, the BepiColombo mission will soon allow observation of the surface with the three cameras of the SIMBIO-SIS instrument [5]: the VIHI hyperspectral sensor, the STC colour stereo camera and the HRIC high-resolution camera. The STC resolution (≈ 50 m/px) allows scaling ratios within the range of pansharpening applications for both the other cameras. In this case, pansharpening will be applied to implement the spectral information of VIHI based on STC panchromatic channels and to implement the filter colours of STC with the high ground resolution of HRIC (both an ≈10x increase in resolution).

Toolkit development and image alignment: Due to the lack of open-source or commercial tools adaptable to the purpose, dedicated tools have been developed. The tools were programmed in Python using open-source libraries.

Before applying radiometric transformations, it is crucial to ensure that the two images are accurately aligned. This step is performed manually with Georeferencing tools provided by GIS programs like QGIS or ArcGIS. However, the process is time-consuming and can be prone to errors caused by the operator. To address this issue, an automatic alignment methodology that utilises computer vision algorithms like SIFT and SURF is also under development and testing. These algorithms can identify significantly more tie points than a human operator could in a much shorter time.

Pansharpening Methods: Based on this principle, tools based on different CS pansharpening families have been developed and tested, showing different advantages and disadvantages depending on the application scenario.

They are based on pixel-wise transformation in which the multispectral data (MS) image space is projected into the panchromatic data (PAN) dimension and then moulded according to different radiometric fusion principles.

Despite the recent emergence of more articulated techniques, CS-based methods remain of great use and interest due to their ease of implementation and relatively low computational cost. These advantages make them suitable for managing heavy datasets such as those commonly handled in planetary exploration. Below is a partial list of the pansharpening methods added to the tools so far: *Brovey and MMSE Brovey* [6][7], *(G)IHS* [8], *ESRI* [9], *HPF, HPM* [1] and *Gram-Schmidt* (Fig.1) [10].

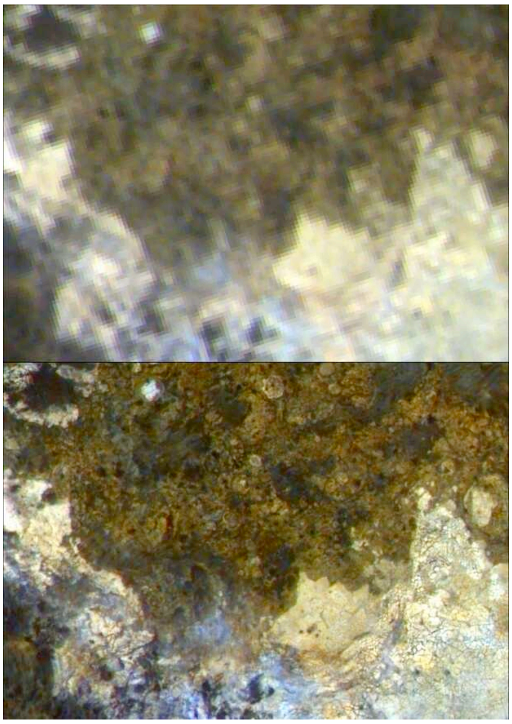

Fig.1 *Application of GS pansharpening on CaSSIS/HiRISE.*

Performance evaluation: Due to the lack of ground truths, visual inspection by professional operators is generally recognised as the principal benchmark for pansharpening methods [11]. Despite this, evaluation indices allow us to define the quality of products numerically and systematically. Because the performance of pansharpening algorithms is spectrally and spatially dependent, the qualities of pansharpened products are analysed here employing several indicators referring to both spectral deformation and structural image qualities: SAM, ERGAS, UQI, PSNR-B and SSIM [12][13]. Like the tools, the methodologies for extracting qualitative indices were deduced from the existing bibliography and programmed into dedicated Python tools.

Preliminary results on CaSSIS/HiRISE: The different nature of the approaches used leads to noticeably different results. Both visual analysis and evaluation indices (Tab. 1) tend to show similar findings: The simple Brovey, GIHS and ESRI methods, mainly dedicated to enhancing the results' details, show high SSIM values when compared to the HiRISE Pan image but tend to amplify and deform the spectral shape, showing relatively low indexes in spectral similarity indicators such as SAM and ERGAS. The HPM method shows the highest colour fidelity, achieving a SAM near the optimal value of 0 among the methods used, but does not achieve the same sharpening effect, generally showing more blurred details.

The MMSE Brovey and Gram-Schmidt methods confirmed to be the best reasonable compromise between spectral properties and features, showing low spectral error rates and a good SSIM and signal-to-noise ratio.

	ERGAS	SAM	PSNRB	UQI	l.r. MS SSIM	PAN SSIM
Brovey	52.270	**0.095**	33.714	0.116	0.194	**1.000**
ESRI	6.024	0.293	22.992	0.571	0.435	0.986
IHS	53.549	0.116	8.065	0.106	0.191	**1.000**
GIHS	2.361	0.114	38.601	0.923	0.596	0.986
HPF	1.698	0.097	52.338	**0.956**	0.693	0.886
HPM	**1.598**	**0.095**	**57.528**	**0.956**	0.813	0.936
Gram-Schmidt	1.806	0.099	38.893	**0.955**	0.593	0.998
MMSE Brovey	2.350	**0.095**	35.902	0.924	0.527	0.983

Tab.1 *Mean evaluation indices for the test dataset.*

Conclusions: Analysis of the results indicates that pansharpening shows considerable potential in the field of planetary sciences. Different methods lead to different results and must be weighted according to requirements. Different techniques make it possible to implement the resolution of details up to an order of magnitude and emphasise the colour rendition, favouring its use for mapping or photointerpretation.

Other methods allow the minimisation of spectral deformation, enabling their use in mineralogical and compositional characterisation studies.

The most delicate phase of the work is the preliminary alignment, to which the results are susceptible. The misalignment can lead to noticeable errors, so further developments are needed to simplify this part. In addition, future investigations will involve data derived from different sensors, allowing instruments to be adapted to an even wider range of instruments.

Acknowledgement: The study has been supported by the Italian Space Agency (ASI-INAF agreements no. 525 2017-03-17 and no.2017-47-H.0).

References: [1] Vivone G. et al. (2015). IEEE Trans. Geosc. Remote Sens., 53, 2565–2586. [2] Shettigara V. (1992). Photogramm. Eng. Remote Sens., 58, 561–567. [3] McEwen A. S. et al. (2007). J. Geophys. Res. Planets, _112_(E5). [4] Thomas N. et al. (2017). Space Sci. Rev. 212(3,4),1897–1944. [5] Cremonese G. et al. (2020). Space Sci. Rev. 216(5), 75. [6] Gillespie A. R. et al. (1987). Remote Sens. Environ., 22, 343–365. [7] Garzelli A. et al. (2008). IEEE Trans. Geosc. Remote Sens., _46_(1), 228–236. [8] Aiazzi B. et al. (2007). IEEE Trans. Geosc. Remote Sens. 45(10), 3230–3239. [9] Beene D. et al. (2022). Geographies, 2(3), 435-452. [10] Laben C. A. and Brower B. V., U.S. Patent 6 011 875, 2000. [11] Scarpa, G., & Ciotola, M. (2022) Remote Sens., 14(8), 1808. [12] Ranchin T. and Wald L. (2000). Photogramm. Eng. Remote Sens. 66(1), 49–61. [13] Yim C. and Bovik A. C. (2010). IEEE Trans. Image Process., 20, 88-98.

THE CONTRIBUTION AND THE FACILITIES OF THE GAL HASSIN ASTRONOMICAL CENTER IN PLANETARY SCIENCE – TOWARD A NETWORK OF WIDE-FIELD TELESCOPES IN SICILY.

A. Nastasi[1,3] and M. Di Martino[2], [1]Fondazione GAL Hassin – Centro Internazionale per le Scienze Astronomiche, Isnello (Via della Fontana Mitri, 90010 Isnello (PA), Italy. Email: alessandro.nastasi@galhassin.it), [2]INAF – Osservatorio Astrofisico di Torino (Via Osservatorio, 20, 10025 Pino Torinese (TO), Italy), [3]INAF – Osservatorio Astrofisico di Palermo (Piazza del Parlamento 1, 90134 Palermo, Italy).

Introduction: The GAL Hassin astronomical center, located in Isnello (Sicily), carries out educational and research activities since 2016 in many branches of planetary science through its robotic telescopes and international collaborations. Specifically, the center already hosts a 0.4m aperture, f/D=3.8 robotic telescope, called Galhassin Robotic Telescope (GRT, Fig.1). The GRT is extensively used to perform astrometric and multi-band photometric characterization of Solar System's minor bodies, especially Near Earth Objects (NEOs), to monitor exoplanet transits in support of the ESA ARIEL-ExoClock project, and to carry out optical observations of space debris and artificial satellites. The GRT has also been able to report some stellar occultation events from Trans-Nettunian Objects (TNOs).

The GRT is characterized by a large (82x82arcmin) field of view and a high pointing and tracking (up to 2°/sec) speed, and by an excellent time accuracy around 0.1 sec, key to provide accurate astrometry of fast-moving targets. The GRT has been designated with the observatory code "L34" by the IAU Minor Planet Center (MPC) in 2019.

The research capabilities of the center are expected to significantly increase in 2024 thanks to a 1m aperture, f/D=2.1 prime focus telescope, built by Officina Stellare: the Wide-field Mufara Telescope (WMT, Fig. 2). The WMT is already installed on Mount Mufara (1865 m altitude), about 10 km away from Isnello, and it is expected to become fully operational and remotely controlled by GAL Hassin within the first quarter of 2024. It will be used to perform accurate and deep observations of transients events and artificial objects in space. Thanks to its Spectral Instruments (SI) cryo-cooled camera, with a quantum efficiency >90%, it is expected to reach a magnitude limit of V ~ 21 within 60 sec exposure time. The WMT system is characterized by a very wide field of view of 150x150 arcmin and a maximum tracking speed of 6°/sec.

Finally, the WMT is equipped with the same GPS timekeeping system installed on the GRT, which guarantees an overall timing accuracy better than 0.01 sec. The WMT has been designated with the MPC Code "M57" in August 2023.

The WMT will represent a crucial facility to monitor and identify new potentially hazardous objects (PHOs) and their trajectories, and it will complement the activities of the largest telescopes which operate at other wavelength windows, in the framework of the multi-messenger astrophysics. Specifically, WMT's ability to perform accurate, multi-band photometry, will make it a facility complementary and of great support to the activities of the future ESA NEOSTEL (FlyEye) telescope, which will be installed on the same mountain, at few hundreds meters away, within the next few years.

Both WMT and GRT are located in the Madonie Park, an area less than 20 km from the northern coast of Sicily, which has superb astronomical conditions with very limited light pollution, more than 65% of clear nights per year and seeing conditions down to 1" for several hours per night. In addition, the relative low latitude (38°) makes this region an excellent place in Italy from where to observe the interesting events occurring close to the center of our Galaxy.

In my talk I will detail the results currently achieved by the GAL Hassin in the planetary science field thanks to the GRT, and the future goals which are expected to be reached with the upcoming WMT.

Figure 1. The Galhassin Robotic Telescope (GRT), hosted within the GAL Hassin astronomical center.

Figure 2. The Wide-field Mufara Telescope (WMT) installed on Mount Mufara, Sicily.